OCS Study MMS 2008-033

Empirical Weathering Properties of Oil in Ice and Snow

Project Number 1435-01-04-RP-34501

Final Report

For:

U.S. Department of the Interior
Minerals Management Service
Alaska Outer Continental Shelf Region
Anchorage, AK

By:

MAR, Incorporated
Rockville, MD

SL Ross Environmental Research Ltd.
Ottawa, ON

DF Dickins Associates Ltd.
La Jolla, CA

Emergencies Science and Technology Division
Ottawa, ON

October 2008

U.S. Department of the Interior
Minerals Management Service
Alaska Outer Continental Shelf Region

The Department of the Interior Mission

As the Nation's principal conservation agency, the Department of the Interior has responsibility for most of our nationally owned public lands and natural resources. This includes fostering sound use of our land and water resources; protecting our fish, wildlife, and biological diversity; preserving the environmental and cultural values of our national parks and historical places; and providing for the enjoyment of life through outdoor recreation. The Department assesses our energy and mineral resources and works to ensure that their development is in the best interests of all our people by encouraging stewardship and citizen participation in their care. The Department also has a major responsibility for American Indian reservation communities and for people who live in island territories under U.S. administration.

The Minerals Management Service Mission

As a bureau of the Department of the Interior, the Minerals Management Service's (MMS) primary responsibilities are to manage the mineral resources located on the Nation's Outer Continental Shelf (OCS), collect revenue from the Federal OCS and onshore Federal and Indian lands, and distribute those revenues.

Moreover, in working to meet its responsibilities, the **Offshore Minerals Management Program** administers the OCS competitive leasing program and oversees the safe and environmentally sound exploration and production of our Nation's offshore natural gas, oil and other mineral resources. The MMS **Royalty Management Program** meets its responsibilities by ensuring the efficient, timely and accurate collection and disbursement of revenue from mineral leasing and production due to Indian tribes and allottees, States and the U.S. Treasury.

The MMS strives to fulfill its responsibilities through the general guiding principles of: (1) being responsive to the public's concerns and interests by maintaining a dialogue with all potentially affected parties and (2) carrying out its programs with an emphasis on working to enhance the quality of life for all Americans by lending MMS assistance and expertise to economic development and environmental protection.

Empirical Weathering Properties of Oil in Ice and Snow

Project Number 1435-01-04-RP-34501

Final Report

For:

U.S. Department of the Interior
Minerals Management Service
Alaska Outer Continental Shelf Region
Anchorage, AK

By:

Ian Buist[2], Randy Belore[2], David Dickins[3], Dan Hackenberg[1], Alan Guarino[1] and Zhendi Wang[4]

[1]**MAR, Incorporated**
1803 Research Blvd., Suite 204
Rockville, MD

[2]**SL Ross Environmental Research Ltd.**
200-717 Belfast Rd.
Ottawa, ON

[3]**DF Dickins Associates Ltd.**
9463 Poole Street
La Jolla, CA

[4]**Emergencies Science and Technology Division**
Environment Canada
3439 River Road
Ottawa, ON

October 2008

This study was funded by the U.S. Department of the Interior, Minerals Management Service (MMS), Alaska Outer Continental Shelf Region, Anchorage, Alaska under Contract No. 1435-01-04-RP-34501, as part of the MMS Alaska Environmental Studies Program

TABLE OF CONTENTS

TABLE OF CONTENTS (continued)

TABLE OF CONTENTS (continued)

SECTION **Page #**

LIST OF TABLES

TABLE OF CONTENTS (continued)

SECTION **Page #**

LIST OF FIGURES

TABLE OF CONTENTS (continued)

TABLE OF CONTENTS (continued)

TABLE OF CONTENTS (continued)

EXECUTIVE SUMMARY

A considerable amount of field research was done in the 1970's and 1980's on first order physics of oil weathering in ice. Additional studies continued in the laboratory in the late 1980's and 1990's, but were generally limited to low-viscosity, low-pour point oils. It is now recognized that oil weathering is strongly dependent on the specific chemical composition and characteristics of individual crudes. The physical and chemical data required by modern state-of-the-art models are scarce, of poor quality, or nonexistent for oil-ice interaction.

The objective of this study was to generate experimental data to validate and refine weathering algorithms and computerized oil weathering models in the presence of ice and snow.

The emphasis for the research was extensive laboratory testing with meso-scale verification to investigate the fate, behavior and interactions of fresh crude oil spilled with first-year, land-fast sea ice. Six series of experiments were conducted over a four-year study:

1. Spreading on Ice and in Snow
2. Evaporation in Ice and Snow
3. Slick Thickness on Cold Water
4. Migration Rates through Brine Channels
5. Formation of Water-in-Oil Emulsions
6. Full Spill-Related Characterization of Crude Oil Samples

These experiments were conducted at three facilities:

i. An outdoor test facility near Ottawa, ON constructed using insulated, IBC shipping containers as the test tanks each containing 1 m^3 of salt water.
ii. An indoor, 11-m^3 wind/wave tank at SL Ross in Ottawa, ON specially modified: to incorporate a refrigerated cold air system to allow precise air temperature control to –30°C; to allow the growing of substantial thicknesses of sea ice; and, to generate under-ice water currents.
iii. The 10,000-m^3 Ohmsett Facility in Leonardo, NJ, outfitted with large-capacity industrial water chillers to ensure freezing water temperatures.

Four crude oils from the North Slope of Alaska, representing a wide range of physical properties, were used in the research: Alaska North Slope sales crude from Pump Station #1 on the TAPS pipeline, Northstar sales crude, Endicott sales crude, and Kuparuk sales crude. All the oil samples were collected in the fall of 2004.

The following algorithms are recommended, based on the best fit of the experimental data from the respective experiments to various theoretical equations.

Equilibrium Thickness of Oil on Quiescent Cold Water after Fay (1969)

$$h_\infty = \left(\frac{\rho^2 \nu D^3 V^2}{\sigma^2} \right)^{1/8}$$

Where: $h_\infty \equiv$ final slick thickness [cm]
V ≡ Volume of oil [g/cm^3]
D ≡ Molecular diffusivity of oil [cm^2/s]
≈ 1 x 10^{-4} cm^2/s
ν ≡ kinematic viscosity of oil [cm^2/s]
ρ ≡ density of water [g/cm^3]

Spreading on Cold Water Fay and Hoult (1971)

	One-dimensional	Axi-symmetric
Gravity-Inertia	$l = k_{1I}(\Delta g A)^{1/3} t^{2/3}$	$r = k_{2I}(\Delta g V)^{1/4} t^{1/2}$
Gravity-Viscous	$l = k_{1V}\left(\frac{\Delta g A^2}{\nu^{1/2}}\right)^{1/4} t^{3/8}$	$r = k_{2V}\left(\frac{\Delta g V^2}{\nu^{1/2}}\right)^{1/6} t^{1/4}$
Surface Tension-Viscous	$l = k_{1T}\left(\frac{\sigma^2}{\rho^2 \nu}\right)^{1/4} t^{3/4}$	$r = k_{2T}\left(\frac{\sigma^2}{\rho^2 \nu}\right)^{1/4} t^{3/4}$

	One-dimensional	Axi-symmetric
Gravity-Inertia	$k_{1I} = 1.5$	$k_{2I} = 1.14$
Gravity-Viscous	$k_{1V} = 1.5$	$k_{2V} = 1.45$
Surface Tension-Viscous	$k_{1T} = 1.33$	$k_{2T} = 2.30$

Where: $l \equiv$ the length of a 1-dimensional slick [cm]
$r \equiv$ the radius of a 2-dimensional slick [cm]
$k \equiv$ proportionality constants
$\Delta \equiv$ ratio of the density difference between water and oil to the density of water
$g \equiv$ acceleration of gravity [cm/s^2]
$A \equiv$ volume of oil per unit length normal to the direction of spread (initial thickness x initial length) [mL]
$V \equiv$ volume of oil [mL]
ν ≡ kinematic viscosity of water [cm^2/s]
ρ ≡ density of water [g/cm^3]
σ ≡ spreading coefficient, or net surface tension [g/cm s^2]
$= \sigma_{w/a} - \sigma_{w/o} - \sigma_{o/a}$

The reader is cautioned that neither of the above two algorithms incorporate the effects of wind, waves and oceanic turbulent eddies on oil slicks. These factors will break a slick up into many small patches, or slicklets, surrounded by clean water, and greatly increase the overall size of a slick and reduce the average final thickness.

Equilibrium Oil Thickness on Ice after Kawamura *et al*. (1986)

$$h_f = 0.04 V^{0.15} \mu^{0.24}$$

Where: $h_f \equiv$ final slick thickness [cm]
$V \equiv$ volume of oil [mL]
$\mu \equiv$ dynamic viscosity of oil [g/cm s]

Oil Spreading on Ice after McMinn (1971)

	One-dimensional		Axi-symmetric	
Gravity-Inertia	$l = k(gA)^{1/3}t^{2/3}$	**(12)**	$r = k(gV)^{1/4}t^{1/2}$	**(13)**
Gravity-Viscous	$l = k\left(\frac{\rho_o g A^3}{\mu}\right)^{1/5} t^{1/5}$	**(14)**	$r = k\left(\frac{\rho_o g V^3}{\pi^3 \mu}\right)^{1/8} t^{1/8}$	**(15)**

Where: $l \equiv$ the length of a 1-dimensional slick [cm]
$r \equiv$ the radius of a 2-dimensional slick [cm]
$k \equiv$ proportionality constants ≈ 1.0 for 1-D gravity viscous
$g \equiv$ acceleration of gravity [cm/s^2]
$A \equiv$ volume of oil per unit length normal to the direction of spread (initial thickness x initial length) [mL]
$V \equiv$ volume of oil [mL]
$\mu \equiv$ dynamic viscosity of oil [g/cm s]
$\rho_o \equiv$ density of oil [g/cm^3]
$\sigma_i \equiv$ spreading coefficient, or net surface tension of oil on ice [g/cm s^2]
$= \sigma (1-\cos \theta)$, where θ is the contact angle between ice and oil, assumed to be between 25° and 45° and σ is assumed to be 30 g/cms^2 after McMinn (1971)

Oil Spread in Snow after SL Ross and DF Dickins (1987)

$$r = \left(\frac{2K\rho_o g V}{\pi E^2 \mu}\right)^{1/4} t^{1/4}$$

Where: $K \equiv$ specific permeability of snow [cm^2]
$= 7.7 \times 10^{-2} d_o^2 e^{(-7.8\rho_s/\rho_i)}$
$d_o \equiv$ mean snow grain size [cm]
$E \equiv$ porosity (void fraction) of snow
$= (1-\rho_s/\rho_i)$
$\rho_s \equiv$ snow density [g/cm^3]
$\rho_i \equiv$ ice density [g/cm^3]

Stripping Velocity for Small Oil Forms under Ice adapted from Cox and Schultz (1980)

$$U_{th} = C_i\left(\frac{305.79}{88.68 - \mu_o}\right)$$

Where: U_{th} ≡ threshold ("stripping") velocity (cm/s)
μ_o ≡ oil viscosity in Poise
C_i ≡ under-ice roughness factor
= 1 for smooth, freshwater ice
= 2 for saline ice
= 3 for undulations under freshwater ice
= 4 for undulations under saline ice
= 6 for any refrozen rubble ice

Evaporation on Ice, Under Snow and Among Drift Ice after Stiver and Mackay (1983)

$$F_v = \ln\left[1 + \frac{BT_G}{T}\theta \exp\left(A - \frac{BT_0}{T}\right)\right]\frac{T}{BT_G}$$

Where: F_v ≡ volume fraction of the oil evaporated
T_0, T_G ≡ the intercept and slope of the modified ASTM distillation [°K]
T ≡ environmental ambient temperature [°K]
B, A ≡ dimensionless, oil-specific constants equal to the least-squares slope and intercept of a plot of the natural logarithm of the Henry's Law constant (H = Pv/RT, which is numerically equal to the slope of the tangent to the curve of a plot of F_v vs. □ at the given point) vs. T_b/T
T_b ≡ boiling point of weathered crude oil at atmospheric pressure [°K]
P ≡ vapor pressure of the weathered crude oil [Pa]
v ≡ liquid's molar volume [m^3/mol]
R ≡ gas constant 8.314 [Pa m^3/mol °K]
□ ≡ dimensionless evaporative exposure
= $kAt/V_0 = kt/x$
k ≡ mass transfer coefficient [m/s]
A ≡ area of slick [m^2]
t ≡ elapsed time since oil release [s]
V_0 ≡ initial volume of oil released [m^3]
x ≡ slick thickness [m]

And, for the mass transfer coefficient used to calculate □:

$$\frac{1}{k_T} = \frac{1}{k_a} + \frac{K_{oa}}{k_o} + \frac{x}{D_s}$$

Where: k_T ≡ overall mass transfer coefficient [m/s]
k_a ≡ air side mass transfer coefficient [m/s]
k_o ≡ liquid phase mass transfer coefficient [m/s]
K_{oa} ≡ air-oil partition coefficient
k_o/K_{oa} = 0.001 m/s
D_s ≡ diffusivity of oil vapor in snow [m^2/s]

$= 2 \times 10^{-5}\ m^2/s$

$x \equiv$ thickness of snow [m]

Emulsification in Drift Ice

At present there are no satisfactory algorithms to predict emulsification of oil slicks at sea. There are two basic reasons for this:

1. There is still a lack of understanding of the basic mechanisms by which emulsification occurs; and,
2. There is a basic lack of understanding how to measure and quantify the energy levels in various test tanks and the sea.

Until these issues are resolved, it is not fruitful to try to develop algorithms to predict emulsification rates at sea. The state of the art today is to conduct small-scale bench or tank tests with quantitatively evaporated oil samples at representative environmental temperatures to predict when oil will be come susceptible to forming stable emulsions. In open water conditions it is generally agreed that, once oil weathers to this state, emulsification will proceed to completion relatively rapidly, in a few hours. The results of the experiments reported here do not contradict this approach. There may be an effect of ice concentration on emulsification rate, but until the rate of emulsion formation in open water is understood and modeled, it is not possible to model the effects of drift ice on the processes.

Brine Channel Migration

It was not possible to develop algorithms for the rate of appearance of oil on the surface of melting ice in spring; however, the following key conclusions were formed from analyzing results from the migration study:

1. Oil viscosity/pour point/density play a major role in controlling the rate of migration in a given ice salinity.
2. Brackish ice provides fewer pathways for migration and slows down the surfacing rate with an effect equivalent to introducing sediment into the tanks.
3. It is not clear if the main effect observed in the sediment experiments is directly related to the presence of particle inclusions at the grain boundaries or the substantial cap of frazil ice in the upper layers of the sheet, providing no aligned brine channels for direct oil migration.
4. Regardless of oil type, water salinity or the presence of sediments, the difference in timing when most of the oil was exposed (80% or better) amounted to less than ten days. From an oil spill response point of view timing differences in migration rates due to these variables would likely be much more significant in the case of spills under much thicker ice in a true Arctic climate.

ACKNOWLEDGEMENTS

The authors would like to thank the following for their contributions to the study:

- BP Exploration Alaska and Alaska Clean Seas for providing and shipping the crude oil samples to Ottawa and Ohmsett.
- Dr. Dick Prentki for his role as Contracting Officer's Technical Representative (COTR) and for Ms. Caryn Smith as Project Inspector for MMS.

- The staff of MAR, Inc. at Ohmsett for their assistance with the large-scale emulsification and spreading tests
- Mr. Jake Morrison, Senior Technologist with SL Ross and Mssrs. Jason Colligan and Tim Partridge, university students employed by SL Ross who worked on the study.

1. PROJECT RATIONALE

The National Environmental Policy Act (NEPA) of 1969 (42 USC 4321-4347) requires that all Federal Agencies use a systematic, interdisciplinary approach that will ensure the integrated use of the natural and social sciences in any planning and decision making that may have an effect on the human environment. The Minerals Management Service (MMS) efforts in this direction include environmental impact statements, environmental assessment teams, studies that acquire and analyze marine environmental data, literature surveys, socioeconomic-analysis studies, public conferences, and special studies (toxicity studies, spill-trajectory analyses, etc.).

Oil spill weathering models are used in National Environmental Policy Act (NEPA) analysis as well as Oil Discharge Prevention and Contingency Plans (ODPCPs). The results of these models are used to estimate impacts in NEPA analysis as well as pre-planning for oil spill response. A modest amount of work in the field was done in the 1970's and 1980's on first order physics for oil weathering in ice. Additional studies have continued in the laboratory in the late 1980's and 1990's, but were generally limited to low viscosity, low pour-point oils. It is now known that oil weathering is strongly dependent on the specific chemical composition and characteristics of individual crudes. The physical and chemical data required by modern state-of-the-art models (such as the SINTEF oil weathering model used by MMS in Alaska) are scarce, of poor quality, or nonexistent for oil-ice interaction. Such models, therefore, ignore the more difficult aspects of oil-in-ice weathering. Sophisticated measurement techniques currently available enable precise measurements regarding oil evaporation, spreading, and dispersion in ice (as well as on ice) as a function of oil type and chemistry.

2. OBJECTIVE AND GOALS OF PROJECT

The objective of the research was to generate experimental data that could be used to validate weathering algorithms and computerized oil weathering models in the presence of ice and snow. More specifically the goals of the experiments were:

1. For low and high pour point oils, to measure emulsification, evaporation, spreading, under-ice movement, slick thickness, and oil composition in an ice field and in snow on top of sea ice.
2. To develop a database on oil weathering in ice fields for use in model validation.
3. Use these data in concert with other oil-ice weathering data to validate and enhance or develop new algorithms of oil weathering in ice.

The emphasis for the research was on extensive laboratory testing, with some meso-scale verification, of the fate, behavior and interactions of fresh crude oil spilled with first-year, land-fast sea ice.

3. HISTORICAL PERSPECTIVE

Following the *Torrey Canyon* spill in the English Channel in 1967, the scientific study of the behavior, fate and transport of oil spills at sea began in earnest (e.g., Fay 1969: Hoult and Fay 1971). In the early 1970's the beginning of development of the oil fields on the North Slope of Alaska spurred the study of oil spill behavior in cold climates and ice. The fate and behavior of spilled oil in ice-covered waters has been studied intensively in the United States, Canada and Norway during the past thirty-five years (e.g., McMinn, 1972; Nelson and Allen, 1982; Bobra and Fingas 1986; Vefsnmo and Johannessen 1992). Two of the largest field experiments in landfast sea ice took place in the Canadian Beaufort Sea in 1974/75 and 1979/80 (Norcor 1975; Dickins and Buist, 1981). The Norcor project involved eight spills of two different crude oils totaling 330 barrels under ice ranging in thickness from 17 to 70 inches. The later experiment in the same region simulated a sub-sea blowout by injecting compressed air and Prudhoe Bay crude oil under landfast ice (Dickins and Buist, 1981). Field spills under controlled conditions in pack or drift ice are more limited in scale, and have included a single set of experiments off the East Coast of Canada in 1986 (SL Ross and DF Dickins, 1987), and offshore trials in Norway (Vefsnmo and Johannessen, 1994).

These field studies in conjunction with numerous laboratory and tank tests, and actual arctic spill experiences have led to a good understanding of the basic processes controlling the behavior of fresh and emulsified crude oil, with and without gas, in a variety of ice conditions including landfast and broken pack ice. Dickins and Fleet (1992) present a comprehensive summary of all known references to date on the subject of oil-in-ice fate and behavior, including analytical studies, tank and basin tests, spills of opportunity, and experimental spills at sea. An excellent technical summary and critical review of many of the key research studies on oil fate and behavior in ice-covered waters was produced in the late 1990s by Environment Canada (Hollebone *et al.* 2000).

The following discussion summarizes the key processes governing the fate and behavior of oil spilled into ice-covered waters in the presence of different forms of sea ice. While many of the processes and countermeasures strategies are applicable to freshwater ice environments, the focus here is on saline conditions representative of the Arctic continental shelf regions (e.g., Chukchi Sea, Beaufort Sea, Barents Sea) and marginal ice zones and sub-Arctic areas such as the Bering Sea, Labrador Sea and Sea of Okhotsk. More process-specific reviews of the state of the art are given at the beginning of each report section describing the experiments conducted in this study.

The physical distribution and condition of spilled oil under, within or on top of the ice plays a major role in determining the potential environmental impacts of the spill and the most effective response strategies at different stages in the ice growth and decay cycle.

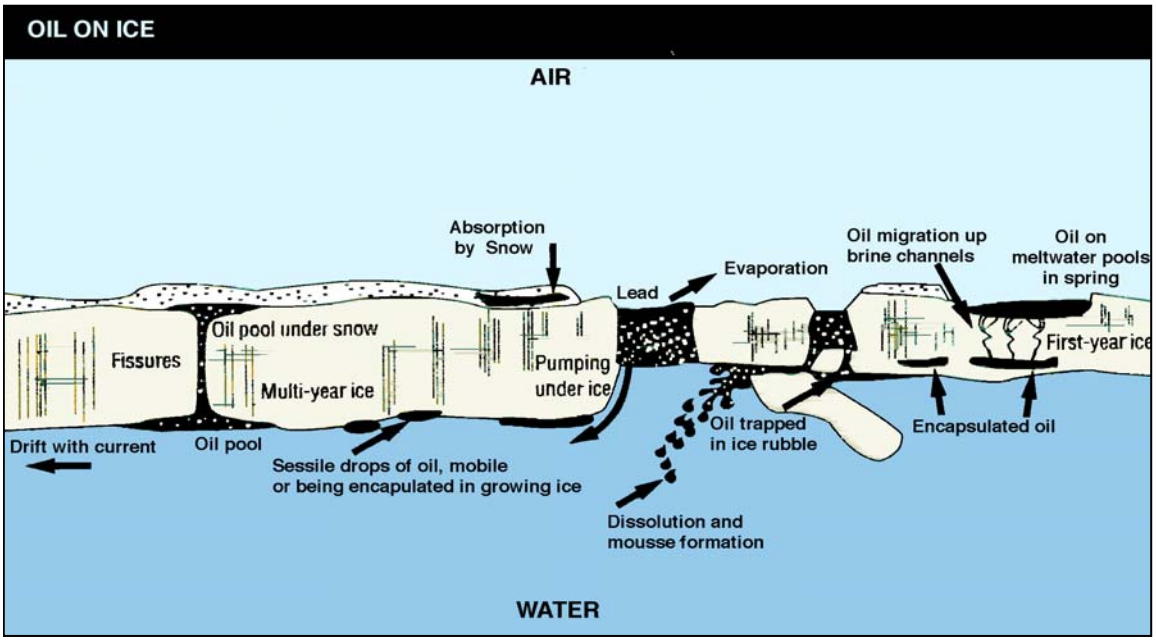

Figure 1. Illustration of Oil and Ice Processes

The fate and behavior of oil in ice-covered waters is governed by a number of important processes, several of which are illustrated above in Figure 1 (after Bobra and Fingas 1986) and discussed below.

3.1 Oil Spreading

Spreading in Pack or Drift Ice

In pack or drift ice, oil spills tend to spread far less and remain concentrated in greater thicknesses than in ice-free waters. In ice concentrations greater than "close pack" (over 6/10 of the sea surface ice covered), the ice floes themselves provide a high degree of natural containment and serve to physically limit oil spreading. As the ice concentrations become more open, the oil spreading gradually increases until it reaches close to an open water state in very open drift ice (3/10 and less). There are simple empirical models that predict the spreading of oil in broken ice by modifying the open water spreading (Figure 2) as a function of ice cover.

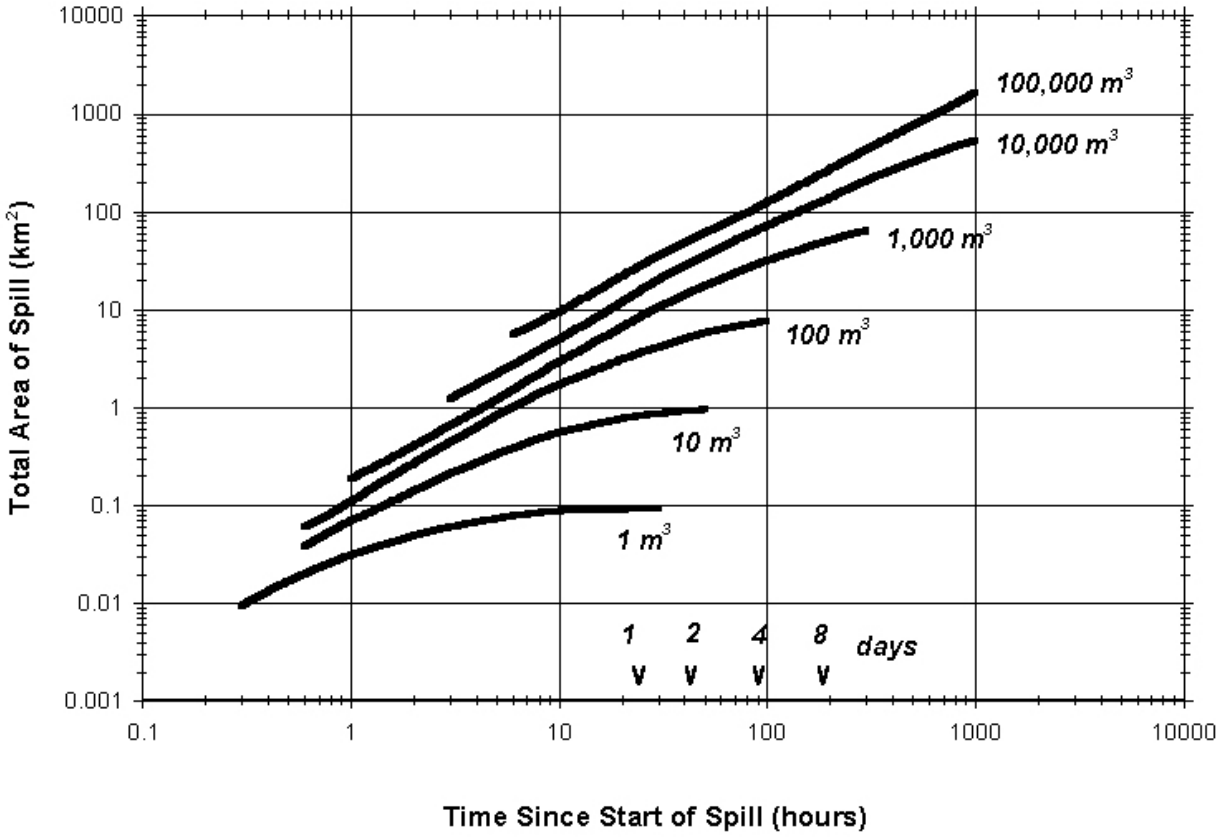

Figure 2. Predicted Spreading of Spills on Open Water

For example, a 100-m^3 spill in 6/10 ice cover after 10 hours would be estimated to have spread to 0.8 km^2 (2 km^2 from Figure 2 multiplied by 0.4 [1-6/10]).

Spreading Under Solid Ice

Even large spills (tens of thousands of barrels) of crude oil underneath of solid (or fast ice) will usually be contained within hundreds of meters from the spill source, depending on under-ice currents and ice roughness. Normal variations in "smooth" first-year ice thickness caused by snowdrifts on the surface provide large natural catchments to effectively contain oil spilled underneath the ice within a small area. Late-winter (April) under-ice storage capacities have been estimated to be as high as 400,000 barrels per km^2 from surveys of fast ice along the Alaskan North Slope (Kovacs *et al.,* 1981). Early winter values have been computed to be about a half as great, reflecting the smoother ice at that time. Sub-arctic regions with greater snowfalls would be expected to have a greater local variability in ice thickness earlier in the season. The implication is that any mid-winter spill under ice would be naturally contained within a relatively small area when compared to an identical volume spilled on open water.

As the natural containment increases with ice thickness, the area needed to contain a given spill volume decreases steadily throughout the winter, as illustrated in Figure 3.

The average oil layer thickness under the ice can range from several centimeters for spills in early winter to tens of centimeters in April for a spill under ice at the end of the ice growth cycle. The maximum oil thickness in the deepest pools could vary from 10 to over 30 cm, respectively. Actual values will depend on the local ice conditions at the time of the spill.

Natural variations in ice thickness comprise the most important physical characteristic limiting the spreading of oil from a sub-surface release. In the case of a small leak, the formation of a lip of new ice at the outer perimeter of the spilled oil will also act to further limit spreading in the case of unusually smooth ice (see following discussion).

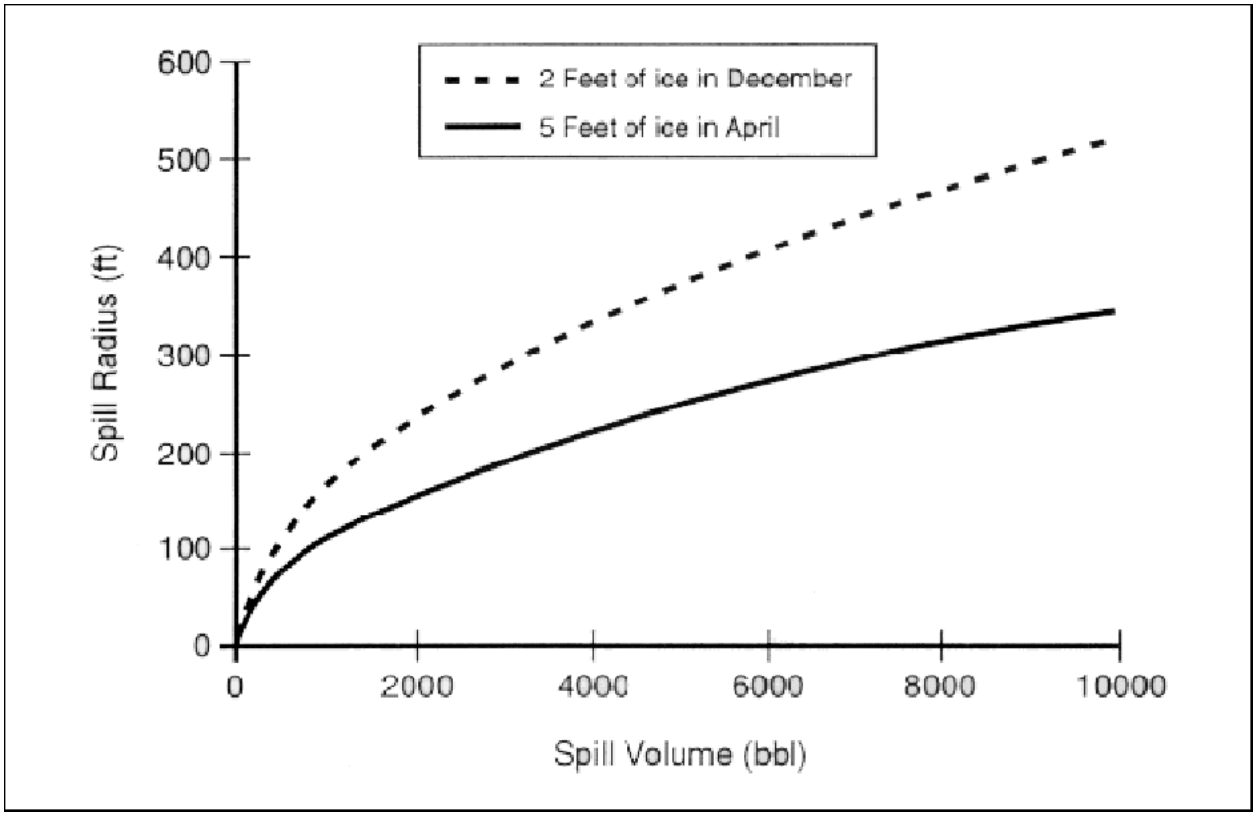

Figure 3. Predicted Radii of Spills of a Given Volume Spilled Under Landfast Ice (Dickins and Glover, 1996)

Spreading on Ice

The spreading of oil on ice is similar to spreading of oil on land. The rate of spreading is controlled by the density and viscosity of the oil, the final contaminated area being dictated by the surface roughness of the ice. Oil spilled on ice spreads much more slowly than on water and covers a smaller final area, thus slicks on ice tend to be much thicker than equivalent slicks on water. Figure 4 shows the final area of spills on ice as a function of spill size and ice roughness (after McMinn, 1972). Smooth first-year sea ice has a roughness in the 0.01 - 0.1 ft. range. Discrete ice deformation features such as rafting, rubble and pressure ridges can lead to localized increases in roughness up to tens of meters in elevation above sea level (in the case of extreme

grounded ridges along the seaward edge of the fast ice). Any oil spilled on the surface of rough ice may be completely contained in a thick pool bounded by ridge sails and ice blocks.

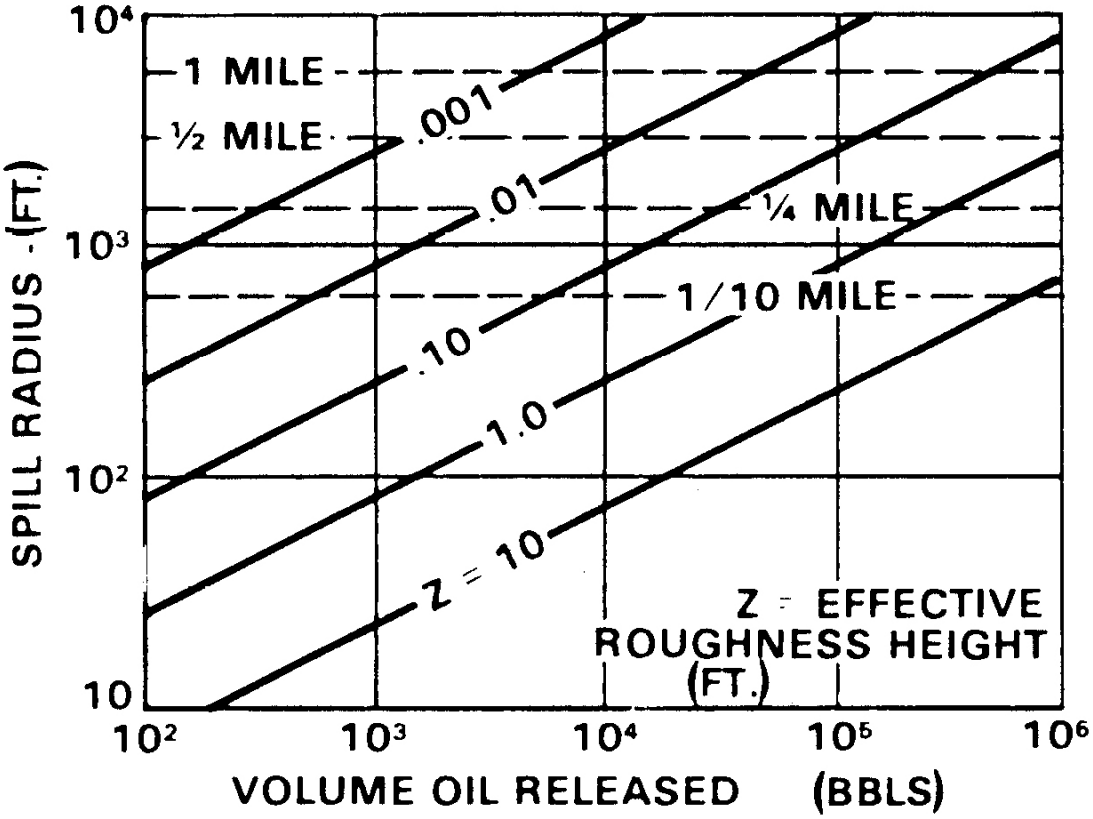

Figure 4. Predicted Spreading of Spilled Oil on Ice (McMinn 1972)

3.2 Oil Movement

Spills on and under ice will generally not move independently of the ice, but remain in the vicinity of the spill site; if the ice is drifting, the oil will drift with it. Winter under-ice currents in most Arctic near-shore areas are not sufficient to move spilled oil much beyond the initial point of contact with the ice under surface. Exceptions may be in areas with strong tidal currents. Several studies have determined that, with roughness values typical of undeformed first-year sea ice, the threshold current speed needed to initiate and sustain movement of an oil lens or pool along the ice under surface is approximately 20 cm/sec or ~ 0.5 knots (Cammaert, 1980; Norcor 1975; Rosenegger, 1975).

Under ice, in currents exceeding 0.5 knots, the rate at which oil moves is a complex function of oil and ice properties (Cox and Schultz 1981); it generally involves the progressive filling and draining of under-ice cavities with oil. In general, the oil is swept under the ice until it has filled enough under-ice cavities to account for the volume spilled. The volume of oil that can be retained by under-ice cavities decreases as the current speed increases; the speed at which oil

moves between cavities increases with increasing current speed and decreases with increasing oil viscosity. Under perfectly smooth ice oil will be moved along at 1.7 to 2.7 knots by two to three knot currents; under smooth sea ice with a roughness of 0.1 ft, two to three knot currents would move oil at a velocity of 1.4 to 2.1 knots (Cox and Schultz 1981, Wotherspoon and Swiss 1985).

Oil spilled among broken ice will move with the ice. Both the ice floes and the oil will move at a small percentage of the wind speed (SL Ross and DF Dickins 1987). A value of 3% is commonly used as a general rule to estimated drift speed, but ice floe-tracking experiments have shown that a value of 5 to 7% is not uncommon near shore (Tekmarine *et al.*, 1985). Due to the Coriolis effect, a turning angle of 10 to 20° to the right of the wind can be applied to better estimate the direction of oil moving with high concentrations of ice. Oil trapped in converging broken ice, will be thickened as the ice concentration increases; in extreme cases, rapid compression can force some of the oil in the water under or on top of adjacent floe edges. The majority of the oil, which was floating on the water or in slush ice between floes prior to compression, will be incorporated into the raised crushed ice edges as the floes contact and grind against one another under the wind-generated pressure.

3.3 Oil Weathering

The major weathering process that occurs for spills on ice or among broken ice is evaporation. Dispersion rates are very low in the presence of ice due the effective wave damping of the ice floes. Oil spilled under ice is quickly encapsulated by the growing ice sheet and does not evaporate or weather to any significant extent during the winter period (Norcor 1975, Dickins and Buist 1981). During the spring melt, the encapsulated oil is exposed on the ice surface in a close to fresh state, at which time normal evaporation will occur as the oil floats on melt pools.

At any time during the winter when oil appears on the surface from a trapped layer under or within the ice, it will be virtually fresh crude, even months after the spill occurred. Rates of oil evaporation in snow have been studied (SL Ross and DF Dickins 1988). Oil absorbed in and/or covered by snow evaporates at a significantly slower rate than a pool of the same oil on ice.

3.4 Oil Encapsulation and Migration

For a batch release of oil beneath a solid ice cover in winter, new ice will completely encapsulate the oil layer within 18 to 72 hours, depending on the time of year (Dickins and Buist, 1981). Oil spilled under the ice after May in the Arctic, or after April in sub-arctic regions, may not become encapsulated due to insufficient new ice growth before the onset of melt.

After the oil has spread under the ice and been encapsulated, it will remain trapped until the ice sheet has reached its maximum thickness, at which time a process of vertical migration through the opening brine channels will begin with the gradual warming of the ice sheet. The rate of vertical migration depends on the degree of brine drainage within the ice (a function of internal temperature), trapped oil pool thickness, and oil viscosity. During the period from freeze-up to mid-winter when the sheet is cooling and growing rapidly, there are very few passages, if any, for the oil to penetrate into the ice sheet. Vertical migration of the oil in this period is limited to

several centimeters of initial penetration through the porous skeletal layer (new ice crystals) at the ice/water interface.

As ice temperatures gradually increase, brine trapped between the columnar sea ice crystals begins to drain downward, leaving vertical channels for the oil to eventually rise to the surface. The first evidence of natural oil appearance on the surface has been observed as early as late May in experiments on the Beaufort Sea coast. In sub-arctic areas such as Labrador, this process will be advanced by about one month depending on air temperatures. Oil released beneath two meters of melting ice in one experiment on May 21 reached the ice surface within one hour (Norcor, 1975).

The rate of oil migration increases rapidly once daily air temperatures remain consistently above freezing. During the same experiment mentioned above, up to 50 percent of the oil originally trapped within the ice became exposed on the ice surface between June 10 and June 20. Oil slick thickness in the melt pools on the surface increased from 1 mm to over 10 mm during a one-week period. Figure 5 shows the timing of oil exposure as measured from three different experimental spills during the course of one winter (NORCOR 1975, Dickins and Buist 1981).

Natural melt of the ice from the surface down acts as a competing process to expose encapsulated oil. When this melt reaches the level where the ice was growing at the time of the spill, the oil is exposed. In most situations of a concentrated thick layer of fluid oil trapped in the ice, natural migration will bring most of it to the surface before the ice melts down to the oiled layer. Oil released subsurface in the presence of gas (e.g., blowout) may be distributed as fine droplets which surface much more slowly.

Once the oil reaches the ice surface, it lies in melt pools or remains in patches on the melting ice surface after the surface water on the ice has drained. Winds herd the oil into thicker layers against the edges of individual melt water pools.

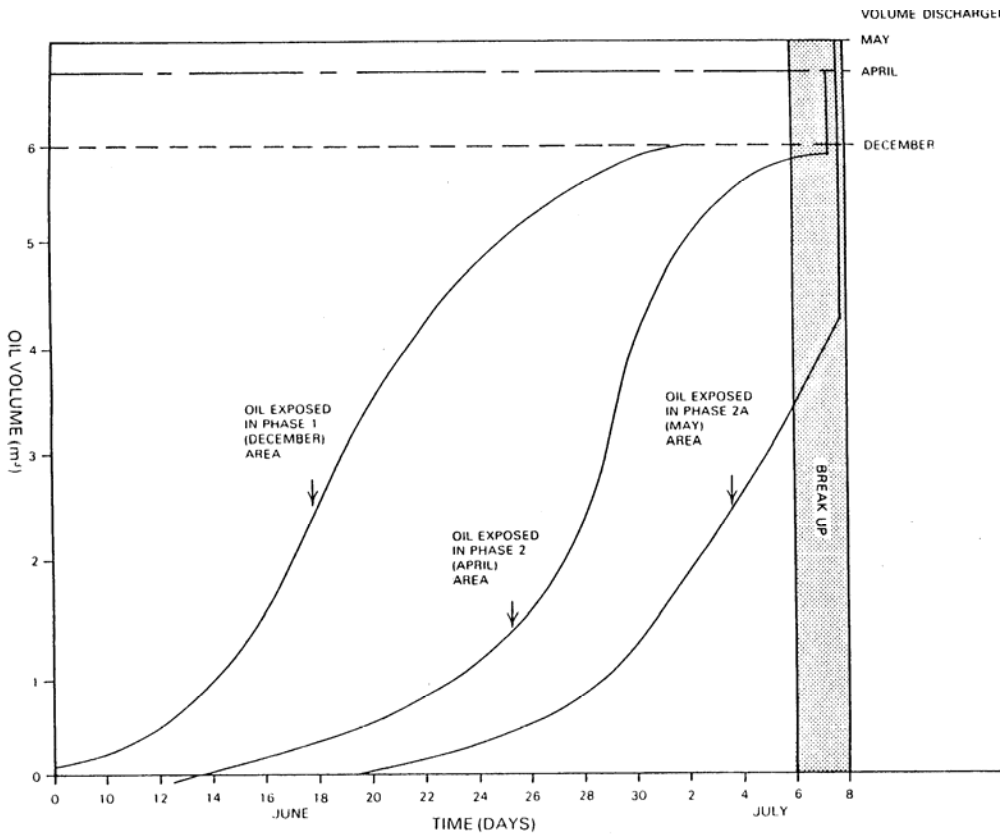

Figure 5. Rate of Oil Exposure From Beneath Sea Ice Originating From Three Simulated Sub-sea Blowouts (Dickins and Buist 1981)

4. GENERAL PROJECT METHODOLOGY

The study goals were achieved by conducting five series of small-scale experiments, over a period of three years, to generate data on:

1. Slick Thickness on Cold Water
2. Spreading on Ice and in Snow
3. Evaporation in Ice and Snow
4. Migration Rates through Brine Channels
5. Formation of Water-in-Oil Emulsions in Broken Ice

The experiments were preceded by a comprehensive spill-related characterization of fresh and wind tunnel weathered samples of each of the four crude oils utilized. The four crude oils were obtained from the North Slope of Alaska and represented a wide range of physical properties: Alaska North Slope sales crude from Pump Station #1 on the TAPS pipeline, Northstar sales crude, Endicott sales crude, and Kuparuk sales crude. The samples were collected in the fall of 2004 and used for all the experiments over the three-year experimental period.

These experiments were conducted at three facilities:

i. An outdoor test facility near Ottawa constructed using insulated, IBC shipping containers as the test tanks each containing 1 m^3 of salt water.
ii. An indoor, 11-m^3 wind/wave tank at the SL Ross Lab specially modified: to incorporate a refrigerated cold air system to allow precise air temperature control to –30°C; to allow the growing of substantial thicknesses of sea ice; and, to generate under-ice water currents.
iii. The 10,000-m^3 Ohmsett Facility in Leonardo, NJ, outfitted with large-capacity industrial water chillers to ensure freezing water temperatures.

4.1 Outdoor Test Tanks

An outdoor test facility was constructed just outside Ottawa for the purpose of conducting the brine channel migration experiments and the oil in snow spreading experiments (Figure 6). The facility was initially constructed using six new 1-m^3 IBC shipping containers (1.22m x 1.02m x 1.17m - L x W x H) with their tops removed as the test tanks.

The IBC containers were placed on a plywood base covering a leveled sand pad. Electrical resistance heating wire was buried in the sand to provide the capability to warm the bottom of the tanks, if necessary. Thermocouples were installed against the sides of the tanks and under some tanks to ensure that the sides and bottom of the tanks were not overly cold and to assess whether the bottoms of the tanks should be warmed. This was never required. The top aluminum frame members of each individual tank were covered with foam pipe insulation to prevent them from conducting cold down the sides of the tank, and then the space between the tanks was sealed with expanding foam insulation. The outside of the six tanks was insulated with 10 cm of rigid Styrofoam insulation. All the insulation was to minimize ice growing faster at the sides of the tanks than in the middle.

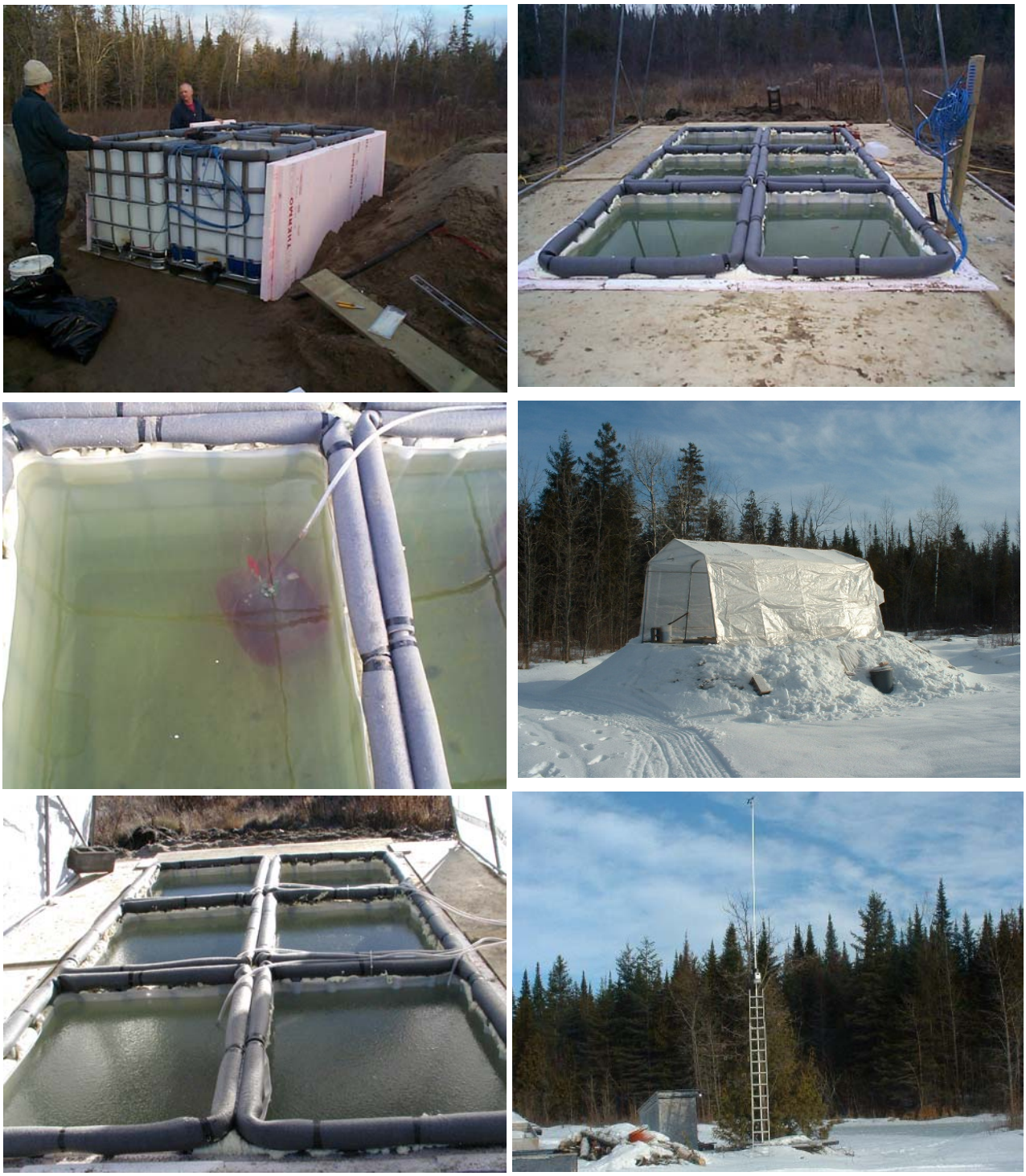

Figure 6. Construction of the Original 6-tank Outdoors Test Facility

Next, the tanks were buried up to their tops in sand. A walkway was installed around the tops of the tanks by placing plywood sheets on top of the sand berm. Finally, a portable shelter, consisting of a tubular steel frame with a plastic tarpaulin cover, was installed over the tanks to keep the snow off (to accelerate ice growth in winter) and shade the tanks (to slow ice melting in the spring). The ends of the shelter were left open to allow the air to circulate and keep the tank surface as cold as possible.

Three of the tanks were filled with 30‰ salt water (created by adding the appropriate weight of finely ground livestock feed salt to each of the containers as they were being filled with local well water) and three with 15‰. In 2005 another two tanks were added, for a total of eight, in order to study the effects of sediment on brine channel migration of oil during spring melt (see Section 11). In order to prevent pressure building up under the ice sheet as the ice grew downwards, causing the sheet to crack and over flood (a classic problem with growing ice in containers), under-ice pressure relief bladders were installed to prevent the ice from cracking as it grew downwards. These consisted of camping-type flexible plastic water containers filled with a 50:50 mix of RV anti-freeze and water that were weighted to sink. Plastic tubing was attached to the spouts of the bladders and directed the antifreeze squeezed from the bladders out of the tank to a collection tank located beside the test facility. A siphon break was incorporated into the tubing system to prevent the bladders from draining.

A Davis 6152 Wireless Pro2 weather station with base station and software was installed near the facility at a height of 9.1 m above grade to record the weather conditions.

4.2 Indoor Wind/Wave Tank

The insulated wind/wave tank located at the SL Ross laboratory in Ottawa is 11 m x 1.2 m x 1.2 m (L x H x W) and is normally filled with 35‰ salt water to a depth of 85 cm (Figure 7). One side of the tank is fitted with three large plate glass viewing windows. The temperature of the water in the tank is maintained at -1 to -1.5°C by a custom-built 11 kW water chiller. The tank water can also be circulated from one end of the tank to the other by a swimming pool filtration system used to clarify the water. Currents can be generated in the tank by installing a false floor and electric propeller system. For this project, a 4 kW, –40°C commercial air chiller capable of maintaining the air at –30°C with ± 1°C control was installed. It was sized to grow ice at a rate of 3 mm/hr on the water in the tank. Insulated panels were constructed to provide an airtight, removable cover for the tank. The air over the tank was recirculated from the downwind end of the tank via a 48-inch insulated duct that returned it to the inlet of the chiller. The air was blown over the top of the water/ice by a 200-m^3/min fan capable of maintaining wind speeds of 3 m/s. The fan was fitted with a flow laminator to minimize turbulence in the air above the water/ice. The chiller was also sized to allow 10% room-temperature makeup air to be drawn into the recirculation system so some chilled air could be wasted to the outdoors while conducting evaporation experiments, to prevent the buildup of oil vapors in the system. Ice sheets as thick as 40 to 50 cm could be grown in a few days. Realistic under-ice undulations were produced in the growing ice sheet using sections of rigid foam insulation placed at regular intervals across the tank once the ice sheet consolidates. Using a chainsaw to cut the sheet into rectangular blocks and rotating them in place in the midst of the freezing process could simulate rubble.

Figure 7. Indoors Wind/Wave Tank at SL Ross Laboratory Retrofitted to Grow Sea Ice

4.3 Ohmsett

The National Oil Spill Response Test Facility, called Ohmsett, (Figure 8) is the world's largest tow/wave tank and is specifically designed to evaluate the performance of equipment that detects, monitors and cleans up oil spills under environmentally safe conditions. The heart of the facility is the large outdoor, aboveground concrete test tank that measures 203 m long by 20 m wide, by 3.3 m deep. It is filled with 9.84 million liters of crystal clear water, and is maintained at oceanic salinity (35‰), through the addition of salt. Water clarity is maintained by the filtration and chlorinating systems. Spanning the tank are three bridges that move back and forth along the length of the tank on rails. The main and towing bridges move along the tank towing full-size spill response equipment through the water to simulate actual towing at sea or deployment in current at speeds up to 3.3 meters/sec. Simulated ocean wave conditions are created with a wave generating system and a wave dampening artificial beach. Waves up to one meter (3.3 feet) in height, as well as a simulated harbor chop, can be generated. Experiments can be viewed from the traveling bridges, the control tower, or underwater viewing windows on the side of the tank. The data collection and video systems record experiment results both above and below the water's surface. Ohmsett also has a Chemistry Laboratory and a Machine Shop.

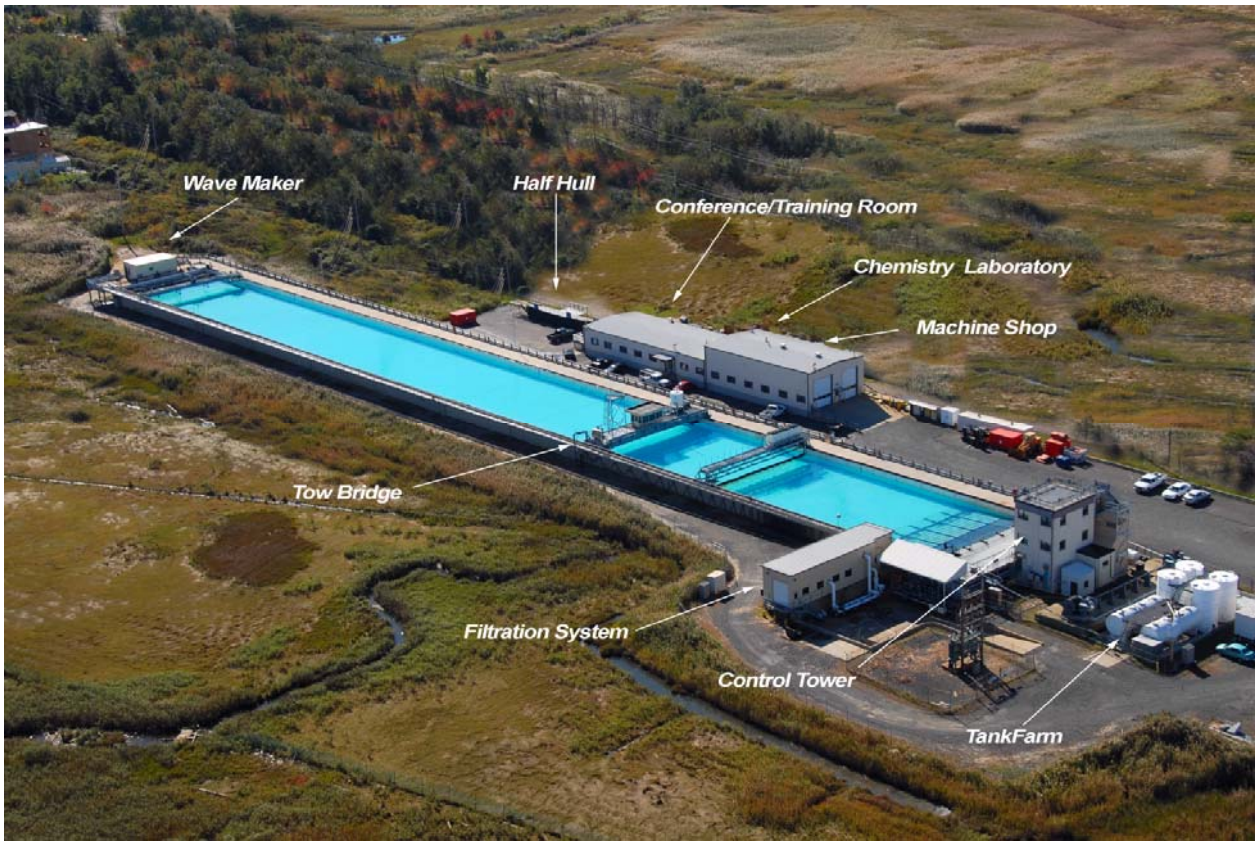

Figure 8. Aerial View of the Ohmsett Tank

In order for testing in ice conditions in Ohmsett to be feasible, the temperature of the 9,840 m^3 of tank water had to be maintained below a maximum of 0°C (above this temperature the ice will melt very rapidly) and above -1.7°C (the freezing point of 35‰ salt water). Ideally the water should be in the -1 to -0.5°C range, to preserve a test field of sea ice for as long as possible. A 525-ton portable industrial chiller was installed to cool the tank water. This system consisted of a chiller unit (condenser, evaporator, compressor, and heat exchanger utilizing refrigerant R-22) and an evaporative cooling tower to remove heat from the fresh water used to cool the condenser. The portable chiller was set up beside the filter area at the north end of the tank, and plumbed into the filter discharge piping. Tank water was taken from the filter discharge at 7.6 m^3/min (2000 gpm) directly through the chiller's heat exchanger, cooled an average of 1.1 to 1.7°C and returned to the piping that carried it to the south end, where it was reintroduced into the tank.

The ice for the tests at Ohmsett was obtained from Cold Regions Research & Engineering Laboratory (CRREL) using the following procedures. It requires four to five days to grow each sheet of ice in the CRREL Ice Engineering Basin (37 m x 9 m x 2.4 m deep) to a thickness of 20 to 25 cm. When the sheet reached the desired thickness it was cut with electric chainsaws into 1 m x 1.2 m slabs weighing in the order of 220 kg each. Once cut, the slabs were lifted and transferred to pallets. The slabs were stacked four deep on standard wooden pallets (Figure 9) giving a total pallet weight in the order of 900 kg. A layer of plastic sheeting was placed between the slabs to prevent their bonding together. Plastic banding was then used to secure the stack of slabs to the pallet.

The pallets were loaded onto refrigerated tractor-trailers for transport to Ohmsett. Using 45,000 lb as typical highway load limit for a refrigerated semi-trailer rig, a full load consisted of approximately 22 pallets. One sheet of ice grown at CRREL filled three refrigerated semi-trailers. Forklifts able to drive inside the trailers were used to load the pallets. On arrival at Ohmsett the pallets of ice were taken off the trucks with forklifts and placed in refrigerated ISO containers for storage until they were needed. The storage containers were maintained at a temperature of -15°C.

When required for the experiments, the pallets were removed from the refrigerated ISO containers and taken up to the tank deck by a forklift. The slabs of ice were manually slid off the pallets into the tank. Some slabs were chopped into smaller pieces to produce a range of sizes typical of real drift ice.

Figure 9. Ice for Experiments at Ohmsett

4.4 Report Layout

The report is organized by covering each of the series of experiments with its own stand-alone section, comprising a state of the art review on the specific subject area, methods, results, discussion, data analysis and algorithm selection. Section 5 details the characterization of the four crude oils. Section 6 deals with the spreading of oil on cold water and the cessation of spreading at an equilibrium thickness and Section 7 deals with the spreading of spilled oil on ice and in snow. Section 8 presents the experiments on movement of oil under ice by currents. Section 9 covers evaporation of spilled oil on ice at various sub-freezing temperatures and in a range of snow conditions. Section 10 details the experiments to examine the formation of water-in-oil emulsions in drift and pack ice fields subjected to swell, both small-scale in the laboratory wind/wave tank and mid-scale at Ohmsett. Finally, Section 11 documents the experiments to quantify brine channel migration rates as a function of oil, ice salinity and sediment load. Section 12 summarizes the findings of the study.

5. CRUDE OIL CHARACTERIZATION

5.1 Introduction

Understanding the key spill-related properties of specific oils is an important component of pre-spill planning. Physical and chemical properties will not only directly affect the fate and behavior of the spilled oil, but also the suitability and effectiveness of most spill-response techniques. The physical properties of spilled oil at ambient conditions and their rate of change in the environment will often define the Window of Opportunity for various countermeasures. For instance, dispersants are most effective on low- to medium-viscosity oils, and *in situ* burning is generally not possible once stable emulsions have formed.

5.2 Evaporation

The oil characterization tests required 4 L of fresh crude oil. The oil was reconstituted by heating to above 45°C and vigorously mixing the sample. This ensured that all waxes, resins or asphaltenes that may have precipitated during exposure to cold were re-dissolved.

The oil was then divided into three aliquots. Two aliquots were weathered in a small wind tunnel: one for two days and one for two weeks and weighed periodically. This is typically equivalent to a few hours and a few days at sea. Approximately 900 mL of the fresh crude was poured into two metal trays to a depth of 2 cm for this purpose. In addition, the fresh oil is subjected to a modified American Society for Testing and Materials (ASTM) distillation (ASTM D86, modified in that both liquid and vapor temperature are measured) in order to obtain two oil-specific constants for evaporation prediction purposes. A Gas Chromatograph Simulated Distillation (GC SIMDIS) was also performed with each fresh crude in order to use the evaporation results in certain computer models. Further details on the GC SIMDIS procedures may be found in Section 5.3 below.

Evaporation is correlated using Evaporative Exposure (θ – after Stiver and Mackay 1983), a dimensionless time unit calculated by:

$$\theta = \frac{kt}{x} \qquad \textbf{(1)}$$

Where: k ≡ a mass transfer coefficient [m/s] (determined experimentally in the laboratory wind tunnel by measuring the weight loss of a tray of toluene)
t ≡ elapsed time [s]
x ≡ oil thickness [m]

5.3 Physical Property Methods

The fresh and weathered oil samples were subjected to the analyses outlined in Table 1 to determine their physical properties, particularly how the properties changed with evaporation and temperature. A brief explanation of why each property is important to spill behavior, and response, follows.

Table 1. Test Procedures for Oil Physical Property Analysis

Property	Test Temperature(s)	Equipment	Procedure
Density	0° and 15°C	Anton Paar Densitometer	ASTM D4052
Viscosity	0° and 15°C	Brookfield DV III+ Digital Rheometer c/w Cone and Plate	Brookfield M/98 211
Interfacial Tension	Room temperature	CSC DuNouy Ring Tensiometer	ASTM D971
Pour Point	N/A	Koehler Cloud and Pour Point Apparati	ASTM D97
Flash Point	N/A	Pensky-Martens Closed Cup Flash Tester	ASTM D93
Emulsification Tendency/Stability	0° and 15°C	Rotating Flask Apparatus	(Mackay and Zagorski 1982, Hokstad and Daling 1993)

Density

Density, the mass per unit volume of the oil (or emulsion), determines how buoyant oil is in water. The common unit of density is grams per milliliter (g/mL). The density of oil increases with weathering and decreases with increasing temperature. Density affects the following processes:

- Sinking - if the density of the oil exceeds that of the water it will sink;
- Spreading - in the early stages of a spill, more dense oils spread faster;
- Natural dispersion - more dense oils disperse more easily; and,
- Emulsification stability - dense oils form more stable emulsions.

Viscosity

Viscosity is a measure of the resistance of oil to flowing, once it is in motion. The common unit of viscosity is the centi-Poise (cP); the SI unit is the milli-Pascal second (mPas), which is numerically equivalent to the centi-Poise. The viscosity of oil increases as weathering progresses and decreases with increasing temperature. Viscosity is one of the most important properties from the perspective of spill behavior and affects the following processes:

- Spreading - viscous oils spread more slowly;
- Natural and chemical dispersion - highly viscous oils are difficult to disperse;
- Emulsification tendency and stability - viscous oils form more stable emulsions; and,
- Recovery and transfer operations - more viscous oils are generally harder to skim and more difficult to pump.

Interfacial Tension

Interfacial tension is a measure of the surface forces that exist between the interfaces of the oil and water, and the oil and air. Chemical dispersants work by reducing the oil/water interfacial tension to allow a given mixing energy (i.e., sea state) to produce smaller oil droplets. Emulsion breakers also work by lowering the oil/water interfacial tension; this weakens the continuous layer of oil surrounding the suspended water droplets and allows them to coalesce and drop out of the emulsion. Interfacial tensions (oil/air and oil/water) are fairly insensitive to temperature, but are affected by evaporation. Interfacial tension affects the following processes:

- Spreading - interfacial tensions determine, in part, how fast an oil will spread and whether the oil will form a sheen;
- Natural and chemical dispersion - oils with high interfacial tensions are more difficult to disperse naturally, chemical dispersant work by temporarily reducing the oil/water interfacial tension;
- Emulsification rates and stability; and,
- Mechanical recovery - oleophilic skimmers (e.g., rope-mop and belt skimmers) work best on oils with moderate to high interfacial tensions.

Pour Point

The pour point is the lowest temperature (to the nearest multiple of 3°C) at which crude oil will still flow in a small test jar tipped on its side. Near, and below this temperature, the oil develops a yield stress and, in essence, gels. The pour point of an oil increases with weathering. Pour point affects the following processes:

- Spreading - oils at temperatures below their pour points will not spread on water;
- Viscosity - an oil's viscosity at low shear rates increases dramatically at temperatures below its pour point;
- Dispersion - an oil at a temperature below its pour point may be difficult to disperse; and,
- Recovery, transfer and storage - crude oil below its pour point may not flow towards skimmers or down inclined surfaces in skimmers, and at temperatures significantly below its pour point, may present storage/transfer challenges.

Flash Point

The flash point of oil is the temperature at which the oil produces sufficient vapors to ignite when exposed to an open flame or other ignition source. Flash point increases with increasing evaporation. It is an important safety-related spill property.

Emulsification Tendency and Stability

The tendency of crude oil to form water-in-oil emulsions (or "mousse") and the stability of the emulsion formed are measured by two numbers: the Emulsification Tendency Index (Zagorski and Mackay 1982, Hokstad and Daling 1993) and the Emulsion Stability (adapted from Fingas *et al.* 1998). The Emulsification Tendency Index is a measure of the oil's propensity to form an emulsion, quantified by extrapolating back to time = 0 the fraction of the parent oil that remains (i.e., does not cream out) in the emulsion formed in a rotating flask apparatus over several hours. If a crude oil has an Emulsification Tendency Index between 0 and 0.25 it is unlikely to form an emulsion; if it has a Tendency Index between 0.25 and 0.75 it has a moderate tendency to form emulsions. A value of 0.75 to 1.0 indicates a high tendency to form emulsions. Recently the Emulsion Stability assessment used by SL Ross has been changed to reflect the four categories suggested by Fingas *et al.* 1998. Emulsion types are selected based on water content, emulsion rheology and the visual appearance of the emulsion after 24 hours settling. The four categories, and their defining characteristics, are:

1. Unstable – looks like original oil; water contents after 24 hours of 1% to 23% averaging 5%; viscosity same as oil on average
2. Entrained Water – looks black, with large water droplets; water contents after 24 hours of 26% to 62% averaging 42%; emulsion viscosity 13 times greater than oil on average
3. Meso-stable – brown viscous liquid; water contents after 24 hours of 35% to 83% averaging 62%; emulsion viscosity 45 times greater than oil on average
4. Stable – the classic "mousse", a brown gel/solid; water contents after 24 hours of 65% to 93% averaging 80%; emulsion viscosity 1100 times greater than oil on average

Both the Tendency Index and Stability generally increase with increased degree of evaporation. Colder temperatures generally increase both the Tendency Index and Stability (i.e., promote emulsification). Emulsion formation results in large increases in the spill's volume, enormous viscosity increases (which can reduce dispersant effectiveness), and increased water content (which can prevent ignition of the slicks and in situ burning). If emulsions with water contents in excess of 50% form in the test apparatus, their rheology (viscosity as a function of time and shear rate) is measured.

The results of the analyses performed on the various oil and emulsion samples are usable in all of the major oil spill models worldwide, including ADIOS, the SINTEF/IKU OWM, ASA's WOSM and the SL Ross Oil Spill Model. The data can be combined with each particular model's property change prediction equations to permit accurate estimates of the changes in the physical and chemical characteristics of the slick with time and changing conditions

5.4 Chemical Property Methods

The Emergencies Science and Technology Division (ESTD) of Environment Canada provided detailed chemical analyses of crude oil samples, both fresh and weathered, in support of the project.

Crude oil is an extremely complex mixture of hydrocarbons. Oil hydrocarbons range from small, volatile compounds to very large, non-volatile compounds. Oil hydrocarbons are generally classified by their structures, including saturates, olefins, aromatics, resins, and asphaltenes.

Saturates are a group of hydrocarbons composed of only carbon and hydrogen with no double carbon-carbon bond. They are the predominant hydrocarbon classes that comprise crude oil. Saturates include straight chain, branched chain, and cyclo alkanes (paraffins).

1. Normal alkanes (normal paraffins) ranging from C_5 to C_{40} are often the most abundant constituents in many oils. Large *n*-alkanes ($>C_{18}$) are often referred to as waxes.
2. Isoalkanes are hydrocarbons containing branched carbon chains. They are also a major group of constituents of oil. Five most abundant and important oil isoprenoid compounds are farnesane (I-C_{15}: 2,6,10-trimethyl-dodecane), trimethyl-tridecane (I-C_{16}), norpristane (I-C_{18}: 2,6,10-trimethyl-pentadecane), pristane (I-C_{19}: 2,6,10,14-tetramethyl-pentadecane) and phytane (I-C_{20}: 2,6,10,14-tetramethyl-hexadecane).
3. Cycloalkanes consist of rings of carbon atoms joined by single atomic bond. The most abundant cycloalkanes (also called naphthenes) are the single-ring cyclopentane (C_5H_{10}) and cyclohexane (C_6H_{12}), and their alkylated (from C_1 to C_{14}) homologues alkylcyclopentanes and alkyl-cyclohexanes).
4. Terpanes and steranes are branched cyloalkanes consisting of multiple condensed five- or six-carbon rings. They have been increasingly used in recent years as marker compounds for source identification and differentiation of oils, and monitoring the weathering and degradation process of oil hydrocarbons under a wide variety of conditions.

Alkenes, commonly referred to as olefins, are partially unsaturated straight-chain hydrocarbons characterized by one or two double carbon-to-carbon bonds in their molecules. Concentrations of olefins are generally very low in crude oils. Significant amounts of olefins are found only in some refined products.

Aromatic hydrocarbons are cyclic, planar compounds that are stabilized by a de-localized π-electron system. Important sub-classes of the aromatics include:

1. Mono-aromatic ring group consisting of BTEX (the collective name of benzene, toluene, ethylbenzene, and the *o*-, *m*-, and *p*-xylene isomers) and other alkyl-substituted benzene compounds (C_n-benzenes). The alkylbenzenes are useful for evaluating weathering behavior, potential toxicity, composition, and concentration changes of oil in the short term following a spill.
2. Polycyclic aromatic hydrocarbons (PAH). The PAHs are often broken into two subgroups, a list of 16 unalkylated compounds ranging from 2-ring to 5-ring compounds on the US EPA priority lost, and five families of alkylated PAH homologues based on the naphthalene (N), fluorene (F), phenanthrene (P), chrysene (C) and dibenzothiophene (DBT). The last, DBT, is a sulphur-substituted PAH, but is convenient to group with the other four families for toxicological and forensic uses. The US EPA PAH priority compounds are of wide interest for environmental quality measurements. The five alkylated homologus series are characteristic of petroleum-based materials and have a wide variety of uses including assessment of toxicological and environmental impacts, oil fate in the environment, and oil forensics and identification.

Resins include heterocyclic hydrocarbons (such as sulfur, oxygen, and nitrogen containing PAHs), phenols, acids, alcohols, and monoaromatic steroids. Because of their polarity, these compounds are more soluble in polar solvents. Sulfur is often a very abundant element in

petroleum and may be present in several forms, including elemental sulfur, hydrogen sulfide, mercaptans, thiophenes (thiophene and its alkylated homologues), and dibenzothiophenes (dibenzothiophene and its alkylated homologues). The sulfur content in crude varies from near zero for "sweet" oils to 6% by weight for some "sour" heavy oils. Most organic nitrogen hydrocarbons in crude oils are present as alkylated aromatic heterocycles with a predominance of neutral pyrrole and carbazole structures over basic pyridine and quinoline forms. They are chiefly associated with high boiling fractions, and much of the nitrogen in petroleum is in the asphaltenes. Oxygen reacts with hydrocarbons to form various oxygen-containing hydrocarbons, such as phenols, cresols, and benzofurans. Compared to PAHs, the concentrations of these nitrogen and oxygen containing compounds are generally very low.

Asphaltenes are a class of very large and complex compounds, precipitated from oils in laboratory by addition of excess *n*-pentane (or *n*-heptane by some definitions). Despite a considerable volume of relevant analytical data, very little is known about molecular configuration of asphaltenes. From X-ray diffraction patterns of solid asphaltenes, it has been inferred that crystallographic organization can be represented by an asphaltenes "macromolecule", in which clusters of partly ordered aromatic matter and carrying aliphatic chains of varying length are associated in micelles or particles. If abundant in oil, they have a significant effect on oil behavior.

Materials and Instruments

Distilled chromatographic solvents were used without further purification. Calibration standards used for the determination of individual and total petroleum hydrocarbons include *n*-alkane standards from C_8 to C_{34} including pristane and phytane purchased from Restek, polycyclic aromatic hydrocarbon (PAH) standards from Restek and Sigma Aldrich. The verification standards include Prudhoe Bay (PB 13.1 % evaporated) and a 16 PAH mixture from Chiron S.A., Norway for quality assurance.

Oil Sample Preparation and Fractionation for Chemical Analysis

This process is illustrated in Figure 10. Approximately 0. 800 gram of crude oils are accurately weighed, dissolved in hexane, and made up to the final volume of 10.00 mL. The final concentrations of the oils are ~80 mg/mL.

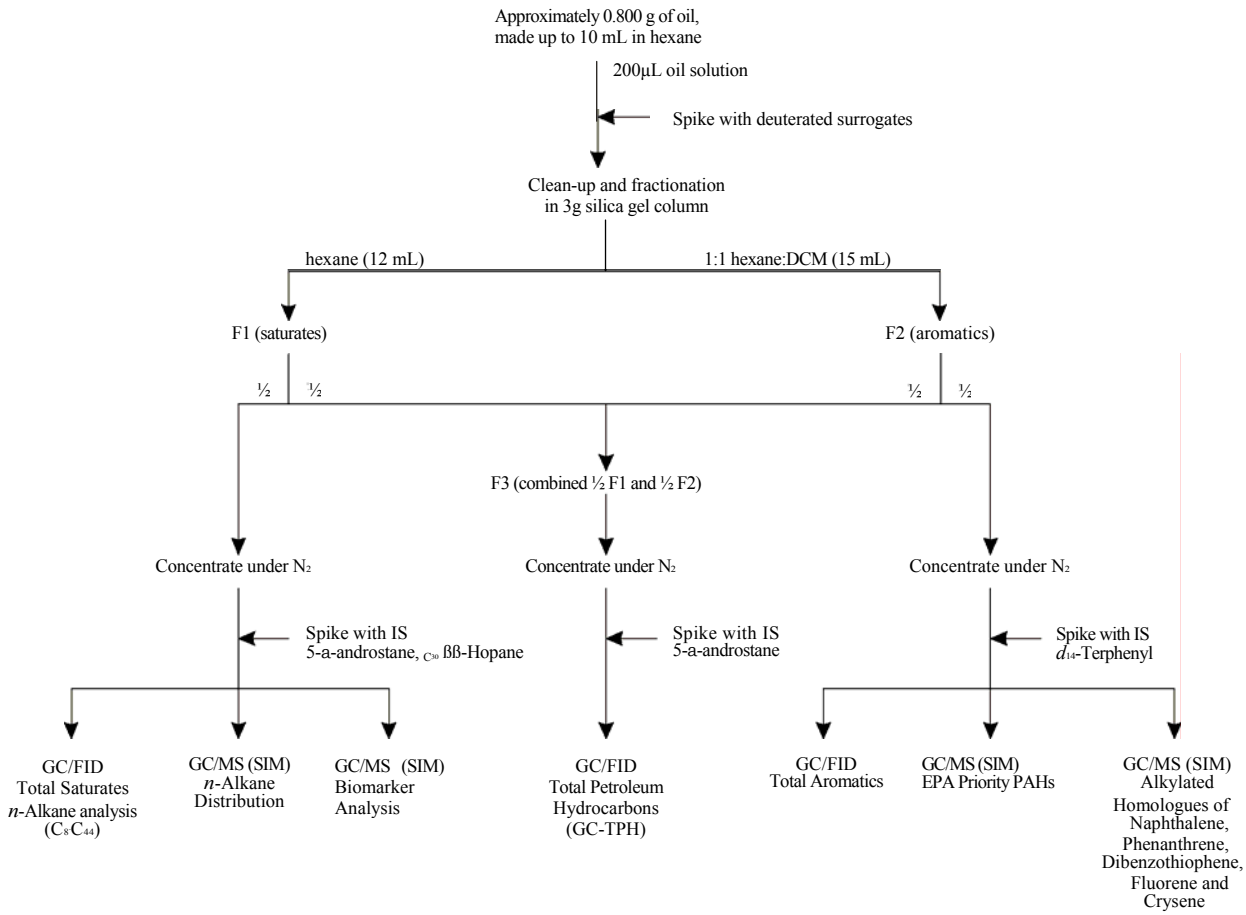

Figure 10. Oil Analysis Protocol

A chromatographic column with a PTFE-stopcock (10.5 mm I.D. x 200 mm length) is plugged with borosilicate glass wool at the bottom, and serially rinsed with methanol, hexane and dichloromethane, and allowed to dry. The column is dry-packed with 3 grams of activated silica gel with tapping to settle the silica gel, and topped with about 1.0 cm anhydrous sodium sulphate. The column is conditioned with 20 mL of hexane, and the eluent is discarded. 200 µL of oil-in-hexane solutions containing approximately 16 mg of oil are spiked with appropriate surrogates (100 µL 200 ppm of *o*-terphenyl and 100 µL of mixture of deuterated acenaphthene, phenanthrene, benz[a]anthracene, and perylene, 10 ppm each), and then quantitatively transferred into the preconditioned 3-g silica gel microcolumns using an additional 3 mL of hexane to complete the transfer. All eluent up to this point is discarded. Hexane (12 mL) and 50% dichloromethane (DCM) in hexane (v/v, 15 mL) are used to elute the saturate and aromatic hydrocarbons, respectively. For each sample, half of the hexane fraction (labeled F1) is used for analysis of aliphatics, *n*–alkanes, and biomarker terpane and sterane compounds; half of the 50% DCM fraction (labeled F2) is used for analysis of alkylated homologous PAHs and other EPA priority unsubstituted PAHs; the remaining halves of the hexane fraction and 50% DCM fraction are combined into a fraction (labeled F3) and used for the determination of the total GC-detectable petroleum hydrocarbons (TPH) and the unresolved complex mixture of hydrocarbons (UCM). These three fractions are concentrated under a stream of nitrogen to appropriate volumes (~0.8 mL), spiked with appropriate internal

standards (100 µL of 200 ppm 5-α-androstane and 100 µL of 10 ppm C_{30}-ββ -hopane, 100 µL of 10 ppm terphenyl-d_{14}, and 100 µL of 200 ppm 5-α-androstane for F1, F2, and F3 respectively), and then adjusted to an accurate pre-injection volume (1.00 mL) for GC-FID and GC-MS analyses.

Determination of Total Petroleum Hydrocarbons (GC-TPH) and Individual *n*-Alkanes and Isoprenoids by GC-FID

Analyses for most of the sample *n*-alkane distributions (*n*-C_8 through *n*-C_{44}, plus pristane and phytane) and TPH were performed on an HP 5890 gas chromatograph equipped with a flame-ionization detector (FID) and an HP 7673 auto-sampler. A 30 m x 0.32 mm i.d. (0.10 µm film thickness) DB-5HT (high temperature) fused-silica capillary column was used. The injector and detector temperature are set at 290 and 325°C. The oven temperature program employed is: 2 min hold at 40°C, ramp to 340°C at 25°C/min, and 15 minutes hold at 340°C. A 1 µL aliquot is injected in the splitless mode with a 1-min purge-off.

For 15 samples analyzed in 2006, an Agilent GC equipped with a FID detector and a HP 7683 auto-injector was used. The column used was DB-5 high temperature (30m x 0.25 mm id, 0.10 um film thickness).The carrier gas was helium (2.5 mL/min).

GC-FID analysis provides a baseline resolution of *n*-alkanes from *n*-C_8 to *n*-C_{41}. Quantitation of the analytes was based on the internal standard compound, 5-α-androstane.

The concentrations of individual *n*-alkanes, selected isoprenoids such as pristane and phytane, and total petroleum hydrocarbons are determined by high resolution capillary GC-FID using the following equation:

$$Concentration\ (\mu g / g) = 2 \times \frac{A_S\, W_{IS}\, D}{A_{IS}\, RRF\, W_S} \qquad \textbf{(2)}$$

Where:

A_S ≡ Response for the analyte in the sample, units of instrument response (area counts, peak height, detector current).
A_{IS} ≡ Response for the internal standard in the sample, units same as A_s.
W_{IS} ≡ Amount (g) of internal standard added to the sample.
D ≡ Dilution factor (dimensionless).
W_S ≡ Weight of sample (g).

Note that F1 and F2 are split in half for analyses, so the final concentration of individual analytes must be multiplied by 2. Prior to sample analysis, the instrument is calibrated using a standard solution, which is composed of C_8 through C_{34} *n*-alkanes, and 5-α-androstane as the internal standard. A 5-point calibration is established demonstrating the linear range of the analysis. The

relative response factor (RRF) for each hydrocarbon component is calculated relative to the internal standard. Total GC detectable petroleum hydrocarbons (TPH), defined as the sum of resolved plus unresolved aliphatic and aromatic hydrocarbons, is quantified by the internal standard method using the baseline corrected total area of the chromatogram. The RRF used for the determination of TPH is the average of the *n*-alkane relative response factors over the entire analytical range.

Determination of Hydrocarbon Group Constituents (SARA Analysis)

The asphaltene and resin mass fractions of an oil or oil product are determined gravimetrically. The asphaltene precipitation is a minor variation on the procedure of ASTM method D2007. The saturate fraction (F 1) and aromatic fraction (F2) are calculated by mass-balance from the total petroleum hydrocarbon measurement.

A 100 mL quantity of *n*-pentane is added to a pre-weighed sample of approximately 5g of oil. The flask is shaken well and allowed to stand for 30 minutes. The sample is filtered through a 0.45-µm membrane using a minimum of rinsings of *n*-pentane. The precipitate is allowed to dry then weighed. The weight of the precipitate as a fraction of the initial oil sample weight is reported as the percentage asphaltenes.

The filtrate from the precipitation, the "maltene" fraction, is recovered and made up to 100 mL with *n*-pentane. A 15-g, 1-cm diameter column of activated silica gel is prepared. A 1-cm layer of sodium sulphate protects the top of the column. A 5-mL aliquot of the maltene fraction is loaded onto the column. A 60-mL volume of 1:1 (v:v) benzene:hexane is eluted through the column and discarded. A 60-mL volume of methanol, followed by a 60-mL volume of dichloromethane are eluted through the column and combined. The methanol/dichloromethane fractions are reduced by rotary evaporation and blown down to dryness under nitrogen. The mass fraction of this dried eluent, compensating for the volume fraction used, is reported as the percentage of resins in the sample. Measurements are repeated three times for each sample and the means are reported as the final values.

Determination of Polycyclic Aromatic Hydrocarbons (PAHs) by GC-MS

Analyses of target PAH compounds including 5 alkylated PAH homologous groups and other EPA priority PAHs, were performed on an Agilent 6890 GC equipped with an Agilent 5973 mass selective detector (MSD). System control, acquisition and analysis were performed using Agilent G1701 BA MSD ChemStation. A 30 m x 0.32 mm i.d. (0.25 µm film thickness) HP5MS fused-silica capillary column is used. The chromatographic conditions are as follows: carrier gas, helium (1.0 mL/min); injection mode, splitless; solvent delay, 4 minutes; injector temperature, 280°C; MSD heater and source temperature, 280 and 230°C, respectively. The temperature program employed for biomarkers and alkylated PAHs is: 50°C hold for 2 min, then ramp at 6°C/min to 300°C and hold for 17 minutes. Prior to sample analysis, the GC-MS is tuned with perfluorotributylamine (PFTBA).

GC-MS analysis was performed in selected ion monitoring (SIM) mode to quantify the target compounds and to improve detection limits. The concentrations of the individual PAH and biomarker compounds were determined based on the internal standard of d_{14}-terphenyl.

Quantitation of target PAHs including alkylated PAH homologues and other EPA priority PAHs is performed on GC-MS in SIM mode with RRFs for each compound determined during instrument calibration. The ions monitored are 128, 142, 156, 170, and 184 for alkyl homologues of naphthalene; 178, 192, 206, 220, and 234 for phenanthrene alkyl series; 184, 198, 212, and 226 for dibenzothiophene alkyl series; and 166, 180, 194 and 208 for fluorene alkyl series. The RRF for target PAH compounds are calculated from authentic standards. PAH alkyl homologues are quantified by using the straight baseline integration of each level of alkylation. Although the alkylated homologue groups can be quantified using the RRF of the respective unsubstituted parent PAH compounds, it is preferable to obtain the RRFs directly from alkylated PAH standards, if they are commercially available. In this project, the RRFs obtained from 1-methylnaphthalene, 2-methyl-naphthalene, 2,6-dimethyl-naphthalene, 2,3,5-trimethyl-naphthalene, and 1 -methyl-phenanthrene are used for quantitation of 1 -methyl-naphthalene, 2-methylnaphthalene, C_2-naphthalene, C_3-naphthalene, and C_1-phenanthrene in oil, respectively. The RRFs of 2,3,5-trimethyl-naphthalene and 1-methyl-phenanthrene are used for quantification of C_4-naphthalene, and C_2-, C_3-, and C_4-phenanthrenes respectively. The selection criteria for the integration and reporting of each alkylated homologue are based primarily on pattern recognition and the presence of selected confirmation ions.

Determination of BTEX and Alkyl Benzene Compounds by GC-MS

The BTEX and other alkyl substituted benzene components in oils are identified from mass spectral data, comparison of GC retention data with reference standards, and calculation of retention index values and comparison with those reported in the literature.

The BTEX and alkyl-benzenes are quantitated by GC/MS using an internal standard method. Strict quality control measures are used in order to guarantee the precision and accuracy of analytical data. The GC/MS is carefully maintained and tuned daily to achieve the required sensitivity. Prior to sample analysis, the instrument is calibrated using a standard solution that is composed of 5 BTEX compounds, 6 C_3-benzene compounds, 2 C_4-, 2 C_5-, 1 C_6- and 1 C_7-benzene compounds. The internal standard used is d_{10}-ethylbenzene.

Oil samples are directly weighed and dissolved in *n*-pentane to an approximately concentration of 2 mg/mL for GC/MS analysis. It is important to note that there is no solvent evaporation and concentration step, which may result in the loss of BTEX compounds. To achieve improved precision and accuracy of analytical data, the following refinements are implemented in addition to the routine quality control measures:

1. The oil solutions in vials are tightly capped to avoid any possible loss of volatile BTEX compounds, and are then put in a refrigerator for 30 minutes to precipitate the asphaltenes to the bottom of the vials in order to void performance deterioration of the column due to introduction of asphaltenes.
2. C_3-benzenes in oil are quantified using the RRF directly obtained from the respective individual C_3-benzene standards instead of using the RRF obtained from benzene or C_1/C_2 substituted benzenes.

Concentrations of each component are computed using the predetermined RRF relative to the internal standard, using the formula:

$$Concentration\ (\mu g / g) = \frac{A_S\, W_{IS}\, D}{A_{IS}\, RRF\, W_S}, \qquad \textbf{(3)}$$

Where:

$A_S \equiv$ Response for the analyte in the sample, units of instrument response (area counts, peak height, detector current).

$A_{IS} \equiv$ Response for the internal standard in the sample, units same as A_s.

$W_{IS} \equiv$ Amount (g) of internal standard added to the sample.

$D \equiv$ Dilution factor (dimensionless).

$W_S \equiv$ Weight of sample (g).

Determination of Simulated Boiling Point Distribution and Wax Content by GCFID

This analysis is performed on an Analytical Controls SIMDIS analyser, a modified Hewlett-Packard 5890 series II gas chromatograph. The system has a custom cryogenically-cooled inlet and a customized high-temperature column. Reference and calibration mixtures are run according to Analytical Controls specifications.

Oil samples are made up as 2% (m/m) solutions in carbon disulphide. An aliquot of 0.5 µL is injected into the inlet. The inlet temperature program runs from 40°C to 430°C a 70°C per minute. The oven temperature program runs from -20°C for 1 min, ramp at 10°C/min to 430°C, and hold for 3 minutes at this final temperature. The flame ionization detector operates at 430°C. The Analytical Controls Software outputs a series of simulated boiling point ranges as a function of temperature and can produce a "wax report" for the relative abundances of all *n*-alkanes in the oil sample.

Simulated distillation (SIMDIS or SimDist) fast and simple analytical technique used to simulate a true boiling point (TBP) distillation, a complex process requiring large apparatus and long time periods. The distillation is simulated by gas chromatography on a non-polar column. During the measurement, the temperature of the chromatographic column is increased to drive out the heavier, higher-boiling components of the oil. By following a set temperature program, as described in ASTM D2887, for example, the GC chromatograph can be correlated to the true boiling point distribution. This is accomplished by comparing the elution times of 30-50 standard compounds with their known boiling points.

One major advantage of the GC technique is that a GC column is orders of magnitude more efficient at distillation than that of a TBP distillation apparatus. This means that lower temperatures are needed in a GC system than in a TBP or even in an atmospheric equivalent boiling point (AEBP) distillation. Thus, lower temperatures are used on the GC simulated distillation than are necessary in a true distillation column. The 430°C final temperature on the gas chromatograph correlates to an equivalent true boiling point of 650°C.

It's important to not be confused by the temperatures at which the GC operates and those of the final TPB-correlated mass fraction distribution. The only place in the report the GC oven temperatures are mentioned in the report is in the methods section, so that the results may be repeated. All other temperatures on the tables and graphs for the boiling point distributions are the TBP equivalents.

Though they may appear related in the table of results for a SIMDIS, the unresolved-complex mixture, cumulative boiling point mass fraction, wax, and resin contents all measure different characteristics of the oil and are not easily comparable.

Cumulative Boiling Point Distribution: The cumulative mass fraction is that portion of oil that will boil to vapor below a specified temperature. The cumulative distribution is the cumulative mass fractions as a function of increasing boiling point. The boiling point distributions of crude oils and petroleum products may be in a range from 30 °C to 700 °C.

UCM: An unresolved complex-mixture of hydrocarbons in the gas chromatogram of oil. The UCM is the "envelope" or hump area between the solvent baseline and the base of resolvable peaks.

Waxes: Waxes are predominately straight chain saturates with melting points above 20 °C (generally, the n-alkanes C18 and heavier).

Resins: This is the name given to a large group of polar compounds in oil. These include heterosubstituted aromatics, acids, ketones, alcohols and monoaromatic steroids. Because of their polarity, these compounds are more soluble in polar solvents, including water, than the non-polar compounds, such as waxes and aromatics, of similar molecular weight. They are largely responsible for oil adhesion.

5.5 Physical Property Results

The four crude oils used in this study were:

- Alaska North Slope (ANS) crude obtained from the Trans-Alaska Pipeline System at Pump Station 1 on 10/20/04 at 8:00 am
- Endicott sales crude obtained 10/15/04 at 4:30 pm
- Kuparuk sales crude obtained 10/22/04 at 11:00 am
- Northstar sales crude obtained 10/24/04 at 11:00 am

The results of the physical property tests are summarized in Tables 2 through 5. Complete data may be found in Appendix A.

ANS Crude

ANS is the crude shipped through the TAPS pipeline to Valdez for transshipment by tanker to markets in the Lower 48 and overseas. The sample used in this study was of medium-gravity (31.2°API), low viscosity (10 mPas at 15°C), low pour point (-21°C) and would not emulsify when fresh at either 0° or 15°C. The ANS crude evaporated quite rapidly in the wind tunnel at an average temperature of 18°C, losing 30.8% of its initial volume from a 2-cm thick slick in 2 days and 38.2 % in two weeks. After 2 days exposure the pour point had increased to 3°C, resulting in a significant increase in viscosity at 0°C and the onset of non-Newtonian rheology. The loss of

light ends also allowed the crude to form "entrained water"[1] emulsions at 0°C with water contents of 29 to 44%.

Endicott Crude

Endicott is the processed sales crude from the Endicott oil field located about 10 miles east of Prudhoe Bay. The oil is produced from two artificial gravel islands connected by a causeway. Endicott sales crude is sent 24 miles by pipeline to Pump Station 1 for blending with the other North Slope crudes to make up ANS. The sample used in this study was of moderately heavy gravity (22.2°API), moderately-high viscosity (205 mPas at 15°C), high pour point (12°C) and would not emulsify when fresh at 15°C; but did form an entrained water emulsion at 0°C. The Endicott crude evaporated quite slowly in the wind tunnel at an average temperature of 16°C, losing only 0.8% of its initial volume from a 2-cm thick slick in 2 days and 5.3 % after two weeks. The loss of light ends also allowed the crude to form "entrained water"[2] emulsions at 15°C with a water content of 29%.

Kuparuk Crude

Kuparuk is the processed sales crude from the Kuparuk River oil fields on the western flank of the Prudhoe Bay oil field that is sent 24 miles by pipeline to Pump Station 1 for blending with the other North Slope crudes to make up ANS. The sample used in this study was of moderately heavy gravity (22.2°API), medium viscosity (81 mPas at 15°C), low pour point (-21°C) and would not emulsify when fresh at either 15°C or 0°C. The Kuparuk crude evaporated at a moderate rate in the wind tunnel at an average temperature of 18°C, losing 9.5% of its initial volume from a 2-cm thick slick in 2 days and 20.3% after two weeks. The loss of light ends did not promote the formation of emulsions with the Kuparuk crude at either 0° or 15°C.

Northstar Crude

Northstar is the processed sales crude from the Northstar artificial island located 6 miles offshore, 12 miles northwest of Prudhoe Bay. The oil is sent first by sub-sea pipeline, then by overland pipeline to Pump Station 1 for blending with the other North Slope crudes to make up ANS. The sample used in this study was of light gravity (40.9°API), low viscosity (2.1 mPas at 15°C), low pour point (<-21°C) and would not emulsify when fresh at either 15°C or 0°C. The Kuparuk crude evaporated at a high rate in the wind tunnel at an average temperature of 17°C, losing 43.7% of its initial volume from a 2-cm thick slick in 2 days and 52.0% after two weeks. After 2 weeks exposure the pour point had increased to 3°C, resulting in a significant increase in viscosity at 0°C and the onset of non-Newtonian rheology. The loss of light ends did not promote the formation of emulsions with the Northstar crude at either 0° or 15°C.

[1] Looks black, with large water droplets; water contents after 24 hours of 26% to 62% averaging 42%; emulsion viscosity 13 times greater than oil on average.

[2] Looks black, with large water droplets; water contents after 24 hours of 26% to 62% averaging 42%; emulsion viscosity 13 times greater than oil on average.

Table 2. Physical Property Results Summary for ANS Crude

Spill-related properties ANS Crude

Evaporation (Volume %)	0	30.8	38.2
Density (g/cm^3)			
0 °C	0.877	0.930	0.940
15 °C	0.870	0.920	0.930
Dynamic Viscosity (mPa.s) at 100 s^{-1}			
0 °C	17.6	1791	3582
15 °C	10.2	164	374
Kinematic Viscosity (mm^2/s)			
0 °C	20.0	1925	3809
15 °C	11.8	179	402
Interfacial Tension (dyne/cm)			
Oil/ Air	27.3	32.1	33.4
Oil/ Seawater	18.8	24.6	31.8
Pour Point (°C)			
	-21	3	9
Flash Point (°C)			
	-10	67	75
Emulsion Formation-Tendency and Stability @		0 °C	
Tendency Index	Very unlikely	Very likely	Very likely
Stability	Unstable	Entrained	Entrained
Water Content	0%	44%	29%
Emulsion Formation-Tendency and Stability @		15 °C	
Tendency Index	Very unlikely	Very likely	Very likely
Stability	Unstable	Unstable	Entrained
Water Content	0%	20%	29%

ASTM Modified Distillation

Evaporation (% volume)	Liquid Temperature (°C)	Vapour Temperature (°C)
IBP[1]	87	33
5	146	94
10	177	126
15	206	155
20	237	181
25	271	210
30	305	250
40	365	308
50	421	351

Weathering Model

$$Fv = \frac{\ln[1 + (C_1/Tk)\theta\exp(C_2 - C_3/Tk)]}{(C_1/Tk)}$$

where: Fv is volume fraction of oil evaporated
θ is evaporative exposure
Tk is environmental temperature (K)

C_1 = 5321
C_2 = 2.70
C_3 = 3340

[1] IBP means Initial Boiling Point

Table 3. Physical Property Results Summary for Endicott Crude

Spill-related properties Endicott Crude

Evaporation (Volume %)	0	0.8	5.3
Density (g/cm^3)			
0 °C	0.932	0.935	0.937
15 °C	0.921	0.924	0.925
Dynamic Viscosity (mPa.s) at 40 s^{-1}			
0 °C	1984	2699	3895
15 °C	205	247	342
Kinematic Viscosity (mm^2/s)			
0 °C	2128	2885	4156
15 °C	222	267	370
Interfacial Tension (dyne/cm)			
Oil/ Air	32.8	33.1	34.7
Oil/ Seawater	27.0	35.2	39.0
Pour Point (°C)			
	12	15	15
Flash Point (°C)			
	44	52	55

Emulsion Formation-Tendency and Stability @ 0 °C			
Tendency Index	Very likely	Very likely	Very likely
Stability	Entrained	Entrained	Entrained
Water Content	39%	39%	43%
Emulsion Formation-Tendency and Stability @ 15 °C			
Tendency Index	Very unlikely	Very unlikely	Very likely
Stability	Unstable	Unstable	Entrained
Water Content	0%	13%	29%

ASTM Modified Distillation

Evaporation (% volume)	Liquid Temperature (°C)	Vapour Temperature (°C)
IBP	217	161
5	254	204
10	289	242
15	325	272
20	356	302
25	375	325
30	397	346
40	424	374
50	439	383

Weathering Model

$$Fv = \frac{\ln[1 + (C_1/Tk)\theta\exp(C_2 - C_3/Tk)]}{(C_1/Tk)}$$

where: Fv is volume fraction of oil evaporated
θ is evaporative exposure
Tk is environmental temperature (K)

C_1 = 19740
C_2 = 41.70
C_3 = 16121

Table 4. Physical Property Results Summary for Kuparuk Crude

Spill-related properties Kuparuk Crude

Evaporation (Volume %)	0	9.5	20.3
Density (g/cm^3)			
0 °C	0.930	0.952	0.964
15 °C	0.921	0.943	0.956
Dynamic Viscosity (mPa.s) at 30 s^{-1}			
0 °C	211	1536	8300
15 °C	81.0	351	1391
Kinematic Viscosity (mm^2/s)			
0 °C	227	1613	8609
15 °C	88.0	372	1455
Interfacial Tension (dyne/cm)			
Oil/ Air	31.1	32.2	32.9
Oil/ Seawater	19.6	22.0	25.3
Pour Point (°C)			
	<-21	<-21	-9
Flash Point (°C)			
	-5	28	100
Emulsion Formation-Tendency and Stability @		0 °C	
Tendency Index	Very unlikely	Very unlikely	Very unlikely
Stability	Unstable	Unstable	Unstable
Water Content	13%	29%	0%
Emulsion Formation-Tendency and Stability @		14 °C	
Tendency Index	Very unlikely	Very unlikely	Very unlikely
Stability	Unstable	Unstable	Unstable
Water Content	0%	17%	0%

ASTM Modified Distillation

Evaporation (% volume)	Liquid Temperature (°C)	Vapour Temperature (°C)
IBP	147	37
5	210	69
10	254	94
15	291	133
20	318	155
25	344	168
30	373	186
40	413	211
50	434	285

Weathering Model

$$Fv = \frac{\ln[1 + (C_1/Tk)\theta\exp(C_2 - C_3/Tk)]}{(C_1/Tk)}$$

where: Fv is volume fraction of oil evaporated
θ is evaporative exposure
Tk is environmental temperature (K)

C_1 = 5090
C_2 = -1.44
C_3 = 3076

Table 5. Physical Property Results Summary for Northstar Crude

Spill-related properties North Star Crude

Evaporation (Volume %)		0	43.7	52.0
Density (g/cm^3)				
0 °C		0.836	0.878	0.889
15 °C		0.821	0.868	0.877
Dynamic Viscosity (mPa.s)	at 230 s^{-1}			
0 °C		3.6	36.1	204
15 °C		2.1	14.4	24.4
Kinematic Viscosity (mm^2/s)				
0 °C		4.4	41.1	229
15 °C		2.6	16.6	27.8
Interfacial Tension (dyne/cm)				
Oil/ Air		27.5	30.5	31.9
Oil/ Seawater		22.2	21.8	23.4
Pour Point (°C)				
		<-21	0	3
Flash Point (°C)				
		-10	90	122
Emulsion Formation-Tendency and Stability @			0 °C	
Tendency Index		Very unlikely	Very unlikely	Very unlikely
Stability		Unstable	Unstable	Unstable
Water Content		0%	0%	0%
Emulsion Formation-Tendency and Stability @			15 °C	
Tendency Index		Very unlikely	Very unlikely	Very unlikely
Stability		Unstable	Unstable	Unstable
Water Content		0%	0%	0%

ASTM Modified Distillation

Evaporation (% volume)	Liquid Temperature (°C)	Vapor Temperature (°C)
IBP	135	100
5	150	116
10	168	132
15	174	138
20	184	148
25	204	165
30	223	186
40	269	230
50	314	278

Weathering Model

$$Fv = \frac{\ln[1 + (C_1/Tk)\theta\exp(C_2 - C_3/Tk)]}{(C_1/Tk)}$$

where: Fv is volume fraction of oil evaporated
θ is evaporative exposure
Tk is environmental temperature (K)

C_1 = 4310
C_2 = 8.60
C_3 = 4708

5.6 Chemical Property Results

The results of the chemical property analyses are summarized in Tables 6 through 14. Complete data may be found in Appendix B.

Table 6. Total Petroleum Hydrocarbons (GC-TPH)

	Northstar Pipeline			Endicott Blend		
	Fresh	2-day	2-week	Fresh	2-day	2-week
GC-TPH (mg/g)	717	819	817	646	643	637
GC-TSH/GC-TPH (%)	74.6	74.2	74.0	63.4	62.8	62.7
GC-TAH/GC-TPH (%)	25.4	25.8	26.0	36.6	37.2	37.3
Resolved peaks/TPH (%)	34.8	26.3	24.1	21.2	21.0	19.9
UCM/GC-TPH (%)	65.2	73.7	75.9	78.8	79.0	80.1
	ANS from PS1			Kuparuk Blend		
	Fresh	2-day	2-week	Fresh	2-day	2-week
GC-TPH (mg/g)	601	635	573	566	551	520
GC-TSH/GC-TPH (%)	69.6	67.0	65.7	65.6	64.1	64.1
GC-TAH/GC-TPH (%)	30.4	33.0	34.3	34.4	35.9	35.9
Resolved peaks/TPH (%)	24.9	17.7	16.0	16.0	16.0	16.0
UCM/GC-TPH (%)	75.1	82.3	84.0	84.0	84.0	84.0

T

SH:

total GC-detectable saturated hydrocarbons; TAH: total GC-detectable aromatic hydrocarbons.
UCM: unresolved complex mixture of hydrocarbons.

Table 7. Hydrocarbon Group Determinations (SARA)

	Northstar Pipeline			Endicott Blend		
	Fresh	2-day	2-week	Fresh	2-day	2-week
Saturates (w/w%)	72.1	69.9	65.3	50.3	49.8	48.9
Aromatics (w/w%)	24.6	24.4	23.0	29.1	29.5	29.0
Resins (w/w%)	3.2	5.7	11.7	15.5	15.6	16.6
Asphaltenes (w/w%)	0.0	0.1	0.0	5.1	5.2	5.5
	ANS from PS1			Kuparuk Blend		
	Fresh	2-day	2-week	Fresh	2-day	2-week
Saturates (w/w%)	59.3	54.2	48.7	54.4	51.8	47.3
Aromatics (w/w%)	25.9	26.7	25.4	28.5	29.0	26.5
Resins (w/w%)	11.0	14.1	20.5	8.5	10.2	15.9
Asphaltenes (w/w%)	3.8	5.0	5.5	8.5	9.0	10.3

Table 8. VOCs: BTEX and Alkylated Benzene Compounds in Northstar and Endicott

	Northstar Pipeline			Endicott Blend		
Component (mg/g oil)	Fresh	2-day	2-week	Fresh	2-day	2-week
BTEX group						
Benzene	2.416	0.003	0.002	0.269	0.211	0.132
Toluene	7.813	0.013	0.006	4.714	3.717	2.504
Ethylbenzene	1.627	0.004	0.001	1.231	0.951	0.606
m- & *p*-Xylene	6.003	0.021	0.002	4.331	3.471	2.411
o-Xylene	2.608	0.017	0.001	1.849	1.515	1.108
Sum	**20.47**	**0.057**	**0.012**	**12.39**	**9.864**	**6.761**
C_3-alkylbenzenes						
Isopropylbenzene	0.372	0.006	0.000	0.278	0.239	0.172
Propylebenzene	0.679	0.025	0.000	0.545	0.506	0.352
3- & 4-Ethyltoluene	2.671	0.152	0.002	1.578	1.407	0.955
1,3,5-Trimethylbenzene	0.938	0.085	0.001	0.579	0.479	0.360
2-Ethyltoluene	0.699	0.059	0.000	0.533	0.466	0.343
1,2,4-Trimethylbenzene	4.081	0.443	0.004	2.493	1.611	1.162
1,2,3-Trimethylbenzene	0.306	0.052	0.000	0.247	0.221	0.167
Sum	**9.747**	**0.823**	**0.008**	**6.253**	**4.930**	**3.511**
C_4- to C_6-alkylbenzenes						
Isobutylbenzene	0.131	0.021	0.000	0.077	0.069	0.050
1-Methyl-2-Isopropylbenzene	0.066	0.019	0.000	0.042	0.038	0.061
1,2-Dimethyl-4-ethylbenzene	0.524	0.275	0.002	0.275	0.251	0.168
Amylbenzene	0.084	0.077	0.006	0.101	0.097	0.072
n-Hexylbenzene	0.111	0.148	0.069	0.114	0.120	0.094
Sum	**0.916**	**0.539**	**0.078**	**0.610**	**0.575**	**0.446**
Total	**31.13**	**1.419**	**0.098**	**19.26**	**15.37**	**10.72**

Table 9. VOCs: BTEX and Alkylated Benzene Compounds in ANS and Kuparuk

	ANS from PS1			Kuparuk Blend		
Component (mg/g oil)	Fresh	2-day	2-week	Fresh	2-day	2-week
BTEX group						
Benzene	2.784	0.007	0.001	0.808	0.124	0.005
Toluene	7.627	0.150	0.059	2.345	0.694	0.062
Ethylbenzene	1.492	0.052	0.002	0.518	0.145	0.007
m- & *p*-Xylene	4.754	0.222	0.007	2.090	0.621	0.034
o-Xylene	2.160	0.156	0.004	1.156	0.413	0.028
Sum	**18.82**	**0.588**	**0.073**	**6.917**	**1.998**	**0.136**
C_3-alkylbenzenes						
Isopropylbenzene	0.362	0.036	0.000	0.164	0.065	0.003
Propylebenzene	0.596	0.072	0.001	0.232	0.091	0.008
3- & 4-Ethyltoluene	1.891	0.283	0.008	0.881	0.408	0.032
1,3,5-Trimethylbenzene	0.592	0.127	0.004	0.388	0.175	0.019
2-Ethyltoluene	0.628	0.120	0.004	.346	0.163	0.020
1,2,4-Trimethylbenzene	2.808	0.489	0.019	1.395	0.677	0.081
1,2,3-Trimethylbenzene	0.281	0.076	0.003	0.152	0.088	0.014
Sum	**7.158**	**1.204**	**0.041**	**3.559**	**1.668**	**0.177**
C_4- to C_6-alkylbenzenes						
Isobutylbenzene	0.093	0.015	0.001	0.062	0.034	0.005
1-Methyl-2-Isopropylbenzene	0.116	0.017	0.001	0.032	0.020	0.004
1,2-Dimethyl-4-ethylbenzene	0.323	0.164	0.017	0.233	0.166	0.032
Amylbenzene	0.098	0.070	0.014	0.042	0.040	0.025
n-Hexylbenzene	0.100	0.104	0.057	0.061	0.064	0.038
Sum	**0.730**	**0.370**	**0.089**	**0.429**	**0.324**	**0.104**
Total	**26.71**	**2.162**	**0.204**	**10.90**	**3.990**	**0.417**

Table 10. PAH Distributions of Northstar and Endicott

		Northstar Pipeline			Endicott Blend		
		Fresh	2-day	2-week	Fresh	2-day	2-week
Akylated PAH (µg/g oil)							
Naphthalene	C0-N	933	732	49.7	1022	1025	845
C1-N		3355	3924	2562	3289	3516	3065
C2-N		4017	5342	6229	3554	3950	3688
C3-N		3356	4578	5942	2956	3253	3245
C4-N		1690	2352	3172	1725	1839	1846
Sum		**13351**	**16928**	**17956**	**12546**	**13582**	**12689**
Phenanthrene	C0-P	307	421	597	334	347	355
C1-P		676	931	1306	742	773	801
C2-P		765	1062	1486	881	916	955
C3-P		637	878	1191	780	806	823
C4-P		333	489	684	531	550	579
Sum		**2718**	**3782**	**5263**	**3268**	**3392**	**3514**
Dibenzothiophene	C0-D	69.1	99	141	287	299	303
C1-D		138	198	287	522	542	561
C2-D		185	268	375	748	792	833
C3-D		128	184	261	648	681	706
Sum		**521**	**749**	**1064**	**2206**	**2314**	**2403**
Fluorene	C0-F	155	210	280	130	140	138
C1-F		309	425	586	336	342	349
C2-F		424	579	804	494	529	547
C3-F		403	613	797	505	557	604
Sum		**1291**	**1827**	**2466**	**1465**	**1568**	**1639**
Chrysene	C0-C	45.4	60.5	78.9	67.1	69.2	70.9
C1-C		93.1	117	153	115	118	122
C2-C		127	171	224	157	162	174
C3-C		103	156	204	140	145	152
Sum		**369**	**505**	**660**	**479**	**494**	**519**
Total alkylated PAHs (µg/g)		**18250**	**23789**	**27409**	**19963**	**21350**	**20764**
C2-N/C1-N		1.45	1.42	1.27	1.40	1.39	1.36
Ratios of C3-D isomers		1.00:0.44:0.18	1.00:0.44:0.18	1.00:0.46:0.19	1.00:0.67:0.31	1.00:0.67:0.32	1.00:0.67:0.32
Ratio of C1-P isomers		0.80	0.80	0.81	0.72	0.72	0.72
(C2D/C2P):(C3D/C3P)		0.24:0.20	0.25:0.21	0.25:0.22	0.85:0.83	0.86:0.84	0.87:0.86
C0N:C1N:C2N:C3N:C4N		0.55:1.98:2.38 :1.99:1.00	0.31:1.67:2.27 :1.95:1.00	0.02:0.81:1.96 :1.87:1.00	0.59:1.91:2.06 :1.71:1.00	0.56:1.91:2.15 :1.77:1.00	0.46:1.66:2.00 :1.76:1.00
∑N:∑P:∑DBT:∑F:∑C		4.91:1.00:0.19 :0.47:0.14	4.48:1.00:0.20 :0.48:0.13	3.41:1.00:0.20 :0.47:0.13	3.84:1.00:0.67 :0.45:0.15	4.00:1.00:0.68 :0.46:0.15	3.61:1.00:0.68 :0.47:0.15
EPA Priority List (µg/g oil)							
Biphenyl		264	351	334	257	280	257
Acenaphthylene		16.6	25.2	26.2	16.1	18.7	17.6
Acenaphthene		9.6	12.8	16.9	9.89	15.5	14.7
Anthracene		2.63	4.46	6.87	2.86	3.56	3.09
Fluoranthene		3.13	4.74	4.83	6.82	3.75	3.50
Pyrene		11.8	16.6	24.6	9.30	10.5	10.0
Benz(a)anthracene		4.41	5.63	9.52	5.74	7.14	7.04
Benzo(b)fluoranthene		3.78	5.23	7.03	9.10	9.71	9.92
Benzo(k)fluoranthene		0.12	0.06	0.25	0.29	0.24	0.14
Benzo(e)pyrene		11.7	15.3	22.7	19.2	19.1	20.1
Benzo(a)pyrene		2.09	2.41	3.81	2.93	3.17	2.44
Perylene		0.90	1.08	1.46	0.75	1.16	0.95
Indeno(1,2,3cd)pyrene		0.00	0.00	0.00	0.00	0.00	0.00
Dibenzo(a,h)anthracene		1.06	1.31	1.79	2.23	2.36	2.32
Benzo(ghi)perylene		1.60	1.97	3.21	7.08	6.99	6.55
Total EPA Priority PAHs		**334**	**448**	**463**	**349**	**382**	**356**
TOTAL PAHs (µg/g oil)		**18584**	**24237**	**27872**	**20312**	**21732**	**21120**

Table 11. PAH Distributions of ANS and Kuparuk

		ANS from PS 1			Kuparuk Blend		
		Fresh	2-day	2-week	Fresh	2-day	2-week
Akylated PAH (µg/g oil)							
Naphthalene	C0-N	740	514	94.6	550	464	158
C1-N		2281	2240	1250	1692	1741	1237
C2-N		2677	2965	2502	2296	2484	2428
C3-N		2303	2672	2652	2217	2534	2666
C4-N		1413	1588	1668	1500	1615	1844
Sum		**9414**	**9979**	**8167**	**8255**	**8838**	**8332**
Phenanthrene	C0-P	210	233	253	201	227	253
C1-P		484	536	582	475	535	598
C2-P		594	668	785	681	706	819
C3-P		526	572	651	608	638	740
C4-P		335	392	423	388	416	471
Sum		**2149**	**2401**	**2695**	**2353**	**2522**	**2881**
Dibenzothiophene	C0-D	128	142	155	133	149	165
C1-D		256	292	312	309	347	386
C2-D		469	518	561	706	786	861
C3-D		409	460	499	732	814	947
Sum		**1263**	**1413**	**1527**	**1880**	**2096**	**2358**
Fluorene	C0-F	82.7	93	92.7	56.8	60.8	69.1
C1-F		204	235	259	189	201	221
C2-F		340	383	422	354	405	457
C3-F		376	413	469	422	497	549
Sum		**1002**	**1124**	**1243**	**1021**	**1164**	**1296**
Chrysene	C0-C	36.5	41.0	45.8	34.4	38.5	44.0
C1-C		65.3	74.4	87.9	71.0	77.5	85.2
C2-C		107	114	122	106	124	136
C3-C		90.7	106	116	95.3	108	113
Sum		**299**	**335**	**372**	**307**	**348**	**378**
Total alkylated PAHs (µg/g)		**14127**	**15253**	**14005**	**13815**	**14968**	**15245**
C2-N/C1-N		1.39	1.39	1.25	1.43	1.41	1.31
Ratios of C3-D isomers		1.00:0.62:0.31	1.00:0.64:0.31	1.00:0.63:0.31	1.00:0.71:0.37	1.00:0.72:0.37	1.00:0.71:0.37
Ratio of C 1-P isomers		0.79	0.78	0.80	0.86	0.87	0.86
(C2D/C2P):(C3D/C3P)		0.79:0.78	0.78:0.80	0.71:0.77	1.04:1.20	1.11:1.28	1.05:1.28
C0N:C1N:C2N:C3N:C4N		0.52:1.61:1.89 :1.63:1.00	0.32:1.41:1.87 :1.68:1.00	0.06:0.75:1.50 :1.59:1.00	0.37:1.13:1.53 :1.48:1.00	0.29:1.08:1.54 :1.57:1.00	0.09:0.67:1.32 :1.45:1.00
∑N:∑P:∑DBT:∑F:∑C		4.38:1.00:0.59 :0.47:0.14	4.16:1.00:0.59 :0.47:0.14	3.03:1.00:0.57 :0.46:0.14	3.51:1.00:0.80 :0.43:0.13	3.50:1.00:0.83 :0.46:0.14	2.89:1.00:0.82 :0.45:0.13
EPA Priority List (µg/g oil)							
Biphenyl		139	141	108	89.6	97.4	88.1
Acenaphthylene		13.4	14.5	13.1	12.5	13.6	13.6
Acenaphthene		9.16	9.0	8.25	7.72	8.81	9.16
Anthracene		1.89	2.91	1.54	1.76	2.27	2.29
Fluoranthene		2.67	2.75	3.12	2.69	3.18	3.82
Pyrene		7.12	8.2	8.50	7.13	7.40	8.19
Benz(a)anthracene		3.90	5.14	5.57	4.95	5.94	6.03
Benzo(b)fluoranthene		4.21	4.87	5.62	4.99	5.26	6.00
Benzo(k)fluoranthene		0.23	0.23	0.26	0.51	0.38	0.47
Benzo(e)pyrene		9.10	9.6	11.3	8.06	8.52	10.3
Benzo(a)pyrene		1.98	2.25	2.27	2.62	2.61	3.31
Perylene		2.14	2.42	2.78	6.19	6.93	7.47
Indeno(1,2,3cd)pyrene		0.00	0.00	0.00	0.00	0.00	0.00
Dibenzo(a,h)anthracene		1.09	1.21	1.22	1.54	1.58	1.67
Benzo(ghi)perylene		3.10	3.23	3.83	3.81	3.64	4.46
Total EPA Priority PAHs		**199**	**207**	**175**	**154**	**167**	**165**
TOTAL PAHs (µg/g oil)		**14326**	**15459**	**14180**	**13969**	**15135**	**15410**

Table 12. Simulated Distillation (SIMDIS) and Wax Content

Cumulative Mass Fraction (%) by Cut-point Temperature

	Endicott Blend			Northstar Pipeline		
BP(°C)	Fresh	2-day	2-week	Fresh	2-day	2-week
40	0.1			2.1		
60	1.0			3.5		
80	1.6	0.2	0.2	9.9	0.1	0.1
100	2.0	0.5	0.5	15.5	0.1	0.1
120	3.1	1.4	1.2	20.9	0.1	0.1
140	4.9	2.9	2.4	26.1	0.2	0.1
160	6.7	4.6	3.8	31.8	0.4	0.1
180	8.9	6.6	5.4	37.0	1.8	0.1
200	11.1	8.8	7.2	41.5	5.3	0.2
250	18.3	16.2	14.0	53.1	22.3	11.0
300	27.1	25.8	23.8	64.2	41.5	32.2
350	37.1	36.9	35.2	74.5	59.2	52.7
400	47.1	47.9	46.6	82.1	72.4	68.0
450	57.8	59.6	58.7	88.0	82.6	79.9
500	67.0	69.5	68.9	92.0	89.8	88.3
550	75.2	78.1	77.8	94.8	94.5	93.8
600	82.0	85.0	85.0	96.5	97.4	97.2
650	87.9	90.7	90.8	97.5	97.4	99.2
$\sum n$-C_n (%res. sat)	3.646	4.179	4.098	9.643	4.51	5.361
$\sum C_{18}$+ (%wax)	1.774	2.308	2.391	1.255	1.823	2.439
$\sum$UCM (%unres.)	96.4	95.8	96.1	90.4	94.5	93.9

	ANS from PS1			Kuparuk Blend		
BP(°C)	Fresh	2-day	2-week	Fresh	2-day	2-week
40	3.7	0.2		1.2	0.4	0.2
60	5.7	1.1		1.7	1.5	1.2
80	10.5	1.8	0.1	3.5	2.5	1.8
100	13.8	2.0	0.1	5.0	3.0	1.9
120	17.0	2.2	0.2	6.6	3.6	2.0
140	20.3	2.4	0.2	8.4	4.3	2.1
160	23.8	3.0	0.2	10.6	5.2	2.3
180	27.1	4.1	0.3	13.0	6.5	2.6
200	30.2	6.3	0.6	15.5	8.4	3.1
250	38.5	16.2	7.3	23.7	16.4	9.0
300	47.0	28.0	20.2	33.2	26.6	19.7
350	55.6	39.8	33.9	43.0	37.2	31.2
400	63.2	50.4	46.0	51.9	46.9	41.9
450	70.7	60.8	57.9	60.8	56.6	52.4
500	76.9	69.4	67.6	68.5	65.1	61.8
550	82.5	77.1	76.0	75.6	73.3	70.7
600	87.2	83.4	82.8	81.6	80.3	78.4
650	91.3	88.9	88.5	86.9	86.7	85.4
$\sum n$-C_n (%res. sat.)	3.682	2.111	2.276	1.034	0.708	0.592
$\sum C_{18}$+ (%wax)	0.533	0.855	1.315	0.324	0.365	0.497
$\sum$UCM (%unres)	96.5	98.0	95.0	94.7	99.3	99.6

Table 13. *n*-Alkane Distributions of Northstar and Endicott

***n*-Alkane Component**	Northstar Pipeline			Endicott Blend		
(mg/g oil)	Fresh	2-day	2-week	Fresh	2-day	2-week
n-C_8	10.8	0.02	0.00	1.41	1.64	1.24
n-C_9	12.2	0.29	0.00	2.67	2.68	1.97
n-C_{10}	11.1	3.01	0.01	3.25	2.87	2.19
n-C_{11}	11.0	9.15	0.38	3.46	3.36	2.53
n-C_{12}	10.32	13.3	5.20	3.68	3.68	2.98
n-C_{13}	9.32	14.2	12.0	3.71	3.75	3.25
n-C_{14}	8.79	14.4	15.7	3.50	3.74	3.38
n-C_{15}	8.43	13.8	15.9	3.61	3.83	3.84
n-C_{16}	7.53	12.3	14.2	3.56	3.62	3.70
n-C_{17}	6.81	11.2	13.2	3.37	3.58	3.65
Pristane	3.81	6.17	7.25	2.19	2.20	2.26
n-C_{18}	5.46	8.99	10.5	3.22	3.30	3.46
Phytane	2.54	4.07	4.74	1.56	1.57	1.67
n-C_{19}	4.59	7.62	8.72	2.94	2.98	3.07
n-C_{20}	4.17	6.67	7.83	2.98	3.03	3.05
n-C_{21}	3.65	5.75	6.62	2.93	2.98	3.04
n-C_{22}	3.09	5.15	5.83	2.90	2.90	2.99
n-C_{23}	2.40	3.83	4.58	2.77	2.80	2.86
n-C_{24}	1.79	2.64	3.11	2.74	2.75	2.84
n-C_{25}	1.03	1.71	1.96	2.36	2.44	2.47
n-C_{26}	0.66	1.18	1.30	2.39	2.47	2.56
n-C_{27}	0.35	0.64	0.74	1.95	1.99	2.00
n-C_{28}	0.29	0.41	0.46	1.57	1.59	1.62
n-C_{29}	0.00	0.00	0.00	1.37	1.45	1.46
n-C_{30}	0.00	0.00	0.00	1.01	1.01	1.02
n-C_{31}	0.00	0.00	0.00	0.77	0.82	0.82
n-C_{32}	0.00	0.00	0.00	0.64	0.65	0.67
n-C_{33}	0.00	0.00	0.00	0.59	0.61	0.64
n-C_{34}	0.00	0.00	0.00	0.61	0.64	0.68
n-C_{35}	0.00	0.00	0.00	0.48	0.52	0.56
n-C_{36}	0.00	0.00	0.00	0.27	0.29	0.32
n-C_{37}	0.00	0.00	0.00	0.24	0.26	0.30
n-C_{38}	0.00	0.00	0.00	0.25	0.26	0.27
n-C_{39}	0.00	0.00	0.00	0.19	0.20	0.22
n-C_{40}	0.00	0.00	0.00	0.15	0.16	0.20
n-C_{41}	0.00	0.00	0.00	0.12	0.13	0.14
n-C_{42}	0.00	0.00	0.00	0.07	0.08	0.10
n-C_{43}	0.00	0.00	0.00	0.04	0.05	0.06
n-C_{44}	0.00	0.00	0.00	0.03	0.04	0.05
TOTAL	**130**	**146**	**140**	**71.5**	**72.9**	**70.1**
C_{17}/PRISTANE	1.79	1.82	1.81	1.54	1.63	1.61
C_{18}/PHYTANE	2.15	2.21	2.21	2.07	2.10	2.07
PRISTANE/PHYTANE	1.50	1.52	1.53	1.41	1.40	1.36
Odd Alkanes	59.7	68.1	64.0	33.6	34.4	32.9
Even Alkanes	64.0	68.0	64.2	34.2	34.7	33.3
CPI	0.93	1.00	1.00	0.98	0.99	0.99

Table 14. *n*-Alkane Distributions of ANS and Kuparuk

***n*-Alkane Component (mg/g oil)**	ANS from PS1			Kuparuk Blend		
	Fresh	2-day	2-week	Fresh	2-day	2-week
n-C_8	5.72	0.22	0.00	2.14	0.56	0.04
n-C_9	6.42	0.68	0.00	2.42	0.84	0.07
n-C_{10}	5.48	1.84	0.06	2.22	1.07	0.14
n-C_{11}	5.58	4.08	0.51	2.50	1.76	0.49
n-C_{12}	5.19	5.47	2.22	2.58	2.33	1.24
n-C_{13}	4.55	5.77	4.31	2.38	2.38	2.03
n-C_{14}	3.88	5.14	4.72	1.89	2.19	2.07
n-C_{15}	3.87	5.07	5.22	1.85	2.04	2.20
n-C_{16}	3.35	4.41	4.42	1.64	1.73	1.88
n-C_{17}	3.16	4.19	4.37	1.64	1.73	1.96
Pristane	2.08	2.72	2.74	0.98	1.03	1.15
n-C_{18}	2.77	3.55	3.66	1.42	1.56	1.67
Phytane	1.39	1.77	1.79	0.74	0.81	0.85
n-C_{19}	2.40	2.99	3.12	1.21	1.32	1.47
n-C_{20}	2.19	2.84	2.90	1.11	1.20	1.31
n-C_{21}	2.04	2.66	2.67	0.94	1.08	1.17
n-C_{22}	1.86	2.49	2.54	0.92	0.95	1.08
n-C_{23}	1.74	2.29	2.36	0.82	0.86	0.95
n-C_{24}	1.57	2.01	2.11	0.74	0.77	0.84
n-C_{25}	1.41	1.83	1.89	0.70	0.71	0.79
n-C_{26}	1.39	1.75	1.85	0.65	0.63	0.74
n-C_{27}	1.07	1.40	1.42	0.54	0.57	0.58
n-C_{28}	0.86	1.11	1.12	0.42	0.46	0.49
n-C_{29}	0.80	1.07	1.07	0.43	0.47	0.49
n-C_{30}	0.57	0.68	0.70	0.28	0.31	0.33
n-C_{31}	0.45	0.55	0.57	0.23	0.25	0.26
n-C_{32}	0.31	0.42	0.42	0.19	0.18	0.21
n-C_{33}	0.26	0.34	0.33	0.11	0.12	0.13
n-C_{34}	0.29	0.38	0.37	0.12	0.13	0.14
n-C_{35}	0.22	0.29	0.30	0.10	0.11	0.12
n-C_{36}	0.14	0.16	0.15	0.07	0.08	0.09
n-C_{37}	0.11	0.15	0.14	0.06	0.07	0.08
n-C_{38}	0.12	0.14	0.13	0.05	0.06	0.07
n-C_{39}	0.07	0.10	0.10	0.04	0.04	0.05
n-C_{40}	0.06	0.08	0.08	0.03	0.03	0.03
n-C_{41}	0.05	0.06	0.06	0.02	0.02	0.02
n-C_{42}	0.04	0.05	0.04	0.00	0.00	0.00
n-C_{43}	0.03	0.04	0.03	0.00	0.00	0.00
n-C_{44}	0.03	0.03	0.02	0.00	0.00	0.00
TOTAL	**73.5**	**70.8**	**60.5**	**34.2**	**30.5**	**27.2**
C_{17}/PRISTANE	1.51	1.54	1.59	1.67	1.68	1.70
C_{18}/PHYTANE	2.00	2.01	2.04	1.92	1.93	1.95
PRISTANE/PHYTANE	1.50	1.54	1.53	1.33	1.27	1.35
Odd Alkanes	34.2	33.6	28.5	16.0	14.4	12.9
Even Alkanes	35.8	32.8	27.5	16.5	14.2	12.3
CPI	0.96	1.02	1.03	0.97	1.01	1.04

6. OIL SPREAD ON COLD WATER AND EQUILIBRIUM THICKNESS

The purpose of this task was to determine the effect of oil properties (primarily pour point and viscosity) on the spreading and equilibrium thickness of crude oil on cold water both in the lab and at Ohmsett.

6.1 State of the Art

Fay and Hoult (1971) presented the classic treatment of oil spreading, based on Fay's (1969) theory. They postulated three spreading regimes based on a balance of the various forces acting on a slick on water. Glaeser and Vance (1971) performed a series of one-dimensional spreading tests with Prudhoe Bay crude on a melt pool and compared the results to Fay's theory. They observed that the slick stopped spreading before it thinned to sheen: an equilibrium slick thickness was reached. Fazal and Milgram (1979) showed in a series of small experiments that evaporation of oil can affect its spreading and explained the thick/thin phenomenon in crude oil spreading on water. Tebeau *et al.* (1984) performed a series of experiments to investigate spreading on cold water and among broken ice. SL Ross and Energetex (1986) conducted a series of one-dimensional spreading tests with several different oils and found that Fay's equation did not reasonably predict the results and suggested a "viscosity correction factor". SL Ross and DF Dickins (1987) proposed substituting oil viscosity for water viscosity in the Fay spreading models to better predict viscous oil spreading. SL Ross and DMER (1988) conducted a series on one-dimensional spreading tests with waxy and non-waxy oils at 5° and 10°C. They concluded that oil viscosity should be substituted for water viscosity in Fay's equations and that if the pour point of oil approaches ambient water temperature, spreading will cease. Timco and Davis (1995) performed a series of axi-symmetric spreading tests with paraffin oil, a waxy crude and a light crude on cold water and in ice with waves and wind.

6.2 Methods

Two types of experiments were conducted for this task: one-dimensional spreading tests in the wind/wave tank and axi-symmetric spreading tests in metal pans. Tests were repeated at 0°, 5° and 10°C. In addition, during the emulsification experiments at Ohmsett, two larger-scale one-dimensional spreading tests were conducted.

One-dimensional Tests

A series of four graduated bottomless troughs open at one end was suspended in the tank for the one-dimensional tests (Figure 11). These troughs were constructed using 2.4-m long, 10-cm wide strips of painted steel flashing material. A wooden strip stiffened the two outside trough edges and served as a graduated length scale for the photographic data analysis. The bottom edges of the strips were mounted in wooden spacers placed every 60 cm to keep the strips spaced evenly apart along their entire length. One end of the trough bundle was closed with a slotted wooden end piece into which the metal sides were sealed with silicone (Figure 12 – taken during spreading on ice tests when the troughs were frozen in an ice sheet). The other end of the trough was open. The oil was initially retained at the closed end of the trough by a series of removable rubber dams. For the open water tests, the trough bundle was suspended at either end using threaded rods hanging down from beams spanning the tank walls. The depth that the troughs

were immersed in the water (approximately 4 cm) was adjusted using the threaded rods. After each test the troughs were wiped down thoroughly with clean sorbent pads.

The oils (initial slick thicknesses of 1 cm and 2 cm were employed) were released at the same time by removing the four dams simultaneously. The spread of the oils down the troughs was recorded using an overhead digital video camera. When the thick portion of the slick had stopped spreading, pre-weighed 3-cm diameter circles of sorbent pad were placed on the slick at three distances down the trough and used to collect all the oil under the circle. If one sorbent circle was insufficient to recover all the oil, a second was placed exactly where the first had been and the amount of oil was calculated using the sum of the weights of the two. The thickness of the oil under a sorbent circle was estimated by determining the net weight of oil in the sorbent(s), converting the oil mass to volume by dividing by the fresh oil density at the ambient temperature (0°, 5° and 10°C) then dividing the oil volume by the surface area of the 3-cm diameter sorbent circle.

The spreading rate was measured as follows:

1. Still digital images were obtained from the digital video at fixed times after the dams were raised to release the oil;

Figure 11. One-Dimensional Spreading Tests Apparatus in Indoor Tank

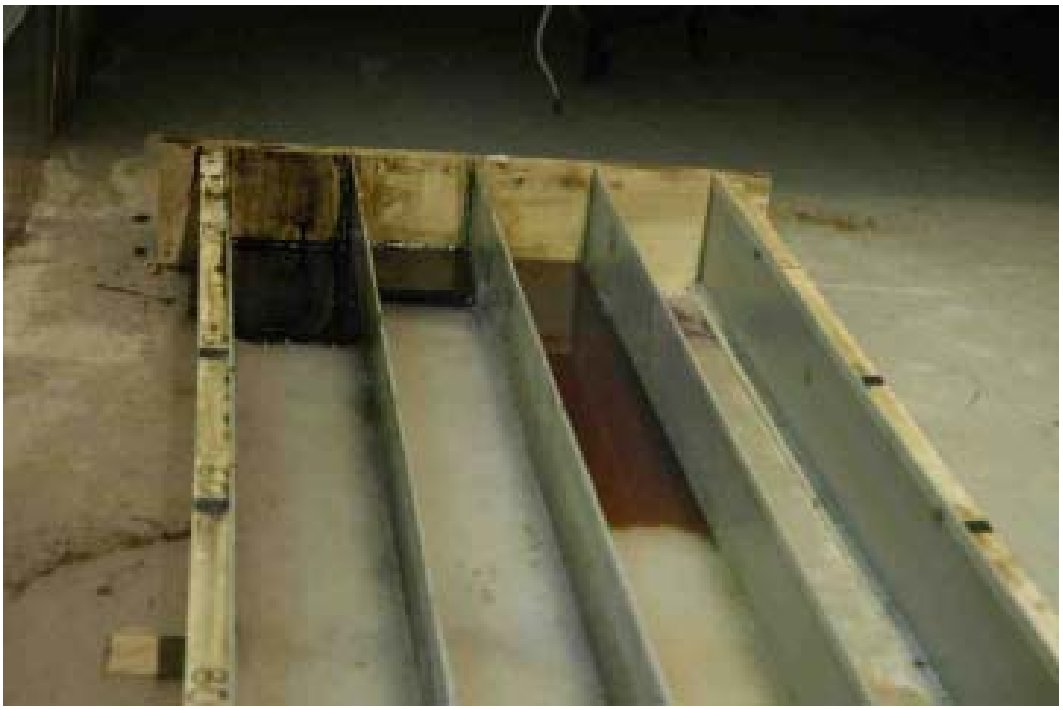

Figure 12. Close-up of Sealed End of One-Dimensional Spreading Tests Apparatus (in ice)

2. The still images were analyzed using image software to determine the distance from the origin of the leading edge of each slick. This was measured in pixels, and then converted to centimeters using a calibration for the digital photograph.
3. This produced a table of distance vs. time for each individual experiment.

Two-dimensional Tests

The axi-symmetric spreading tests were conducted in two 1 m x 1 m x 10 cm metal pans (Figure 13) partially filled with tank water floating side-by-side in the wind/wave tank (for temperature control). Before each test the pans were thoroughly cleaned to obtain a pristine air/water interface.

Volumes equivalent to 1- or 2-cm thickness were placed in a 10-cm diameter metal ring placed at the center of the pan. The oil was released by lifting both rings by hand at the same time (Figure 14). Once the oil had stopped spreading the 3-cm sorbent circles were used, as described above, to estimate the slick thickness at three radii out from the release point at the center of the slick.

The spreading rate was measured as follows:

1. Still digital images were obtained from the digital video at fixed times after the rings were raised to release the oil;
2. The still images were analyzed using image software to determine the area of each slick. This was measured in square pixels, and then converted to square centimeters using a calibration scale for the digital photograph.
3. The average radius of the slick was calculated assuming the slick was a circle.

4. This produced a table of radius vs. time for each individual experiment.

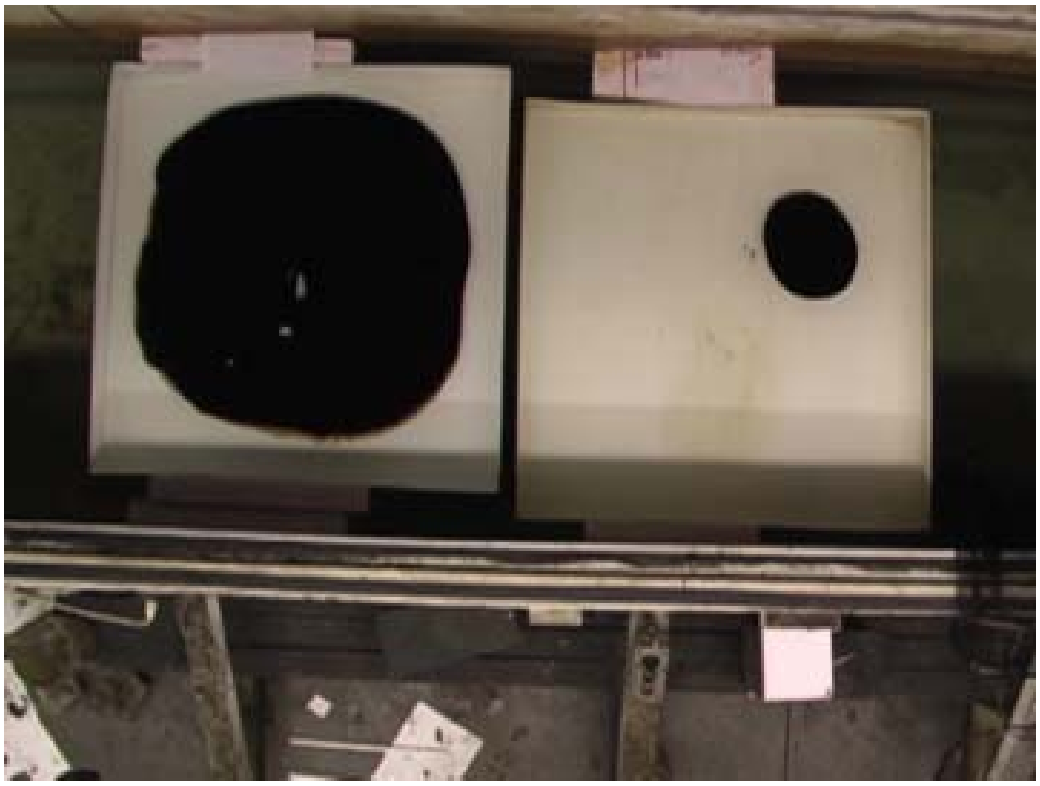

Figure 13. Metal Pans Floating in Indoor Tank Used for Axi-symmetric Spreading Tests

Figure 14. Releasing Oil by Hand from Metal Rings in Center of Pans

6.3 Results

The results of the spreading tests are presented here graphically. All the data may be found in Appendix C.

Equilibrium Thickness Measurements

One-dimensional Tests. The equilibrium thickness measured at given locations down the spreading troughs is given in Figures 15 through 17.

Two-dimensional Tests. The equilibrium thickness measured at given locations in the spreading pans is given in Figures 18 through 20.

Spreading Measurements

One-dimensional Tests. The slick spreading measured in the troughs is given in Figures 21 through 23. Note that the datasets for the Northstar crude are much shorter in time span than the others. As the Northstar oil thinned it became translucent and the leading edge of the slick became impossible to distinguish against the dark water on the video.

Two-dimensional Tests. The slick spreading measured in the pans is given in Figures 24 through 26. Note that the abrupt reduction in spread is caused by the slick the walls of the pans

6.4 Discussion and Algorithm Selection

The classic treatment of oil spreading on water was proposed by Fay (1969) and refined by Fay and Hoult (1971). In their theory there are two spreading forces (gravity and surface tension) that are opposed by two resistances (inertia and viscosity). By equating the forces with a resistance, they developed two sets of three spreading equations; one set for 1-dimensional spreading (such as down a trough) and one set for 2-dimensional, or axi-symmetric spreading:

	One-dimensional		**Axi-symmetric**	
Gravity-Inertia	$l = k_{1I}(\Delta g A)^{1/3} t^{2/3}$	**(4)**	$r = k_{2I}(\Delta g V)^{1/4} t^{1/2}$	**(5)**
Gravity-Viscous	$l = k_{1V}\left(\frac{\Delta g A^2}{\nu^{1/2}}\right)^{1/4} t^{3/8}$	**(6)**	$r = k_{2V}\left(\frac{\Delta g V^2}{\nu^{1/2}}\right)^{1/6} t^{1/4}$	**(7)**
Surface Tension-Viscous	$l = k_{1T}\left(\frac{\sigma^2}{\rho^2 \nu}\right)^{1/4} t^{3/4}$	**(8)**	$r = k_{2T}\left(\frac{\sigma^2}{\rho^2 \nu}\right)^{1/4} t^{3/4}$	**(9)**

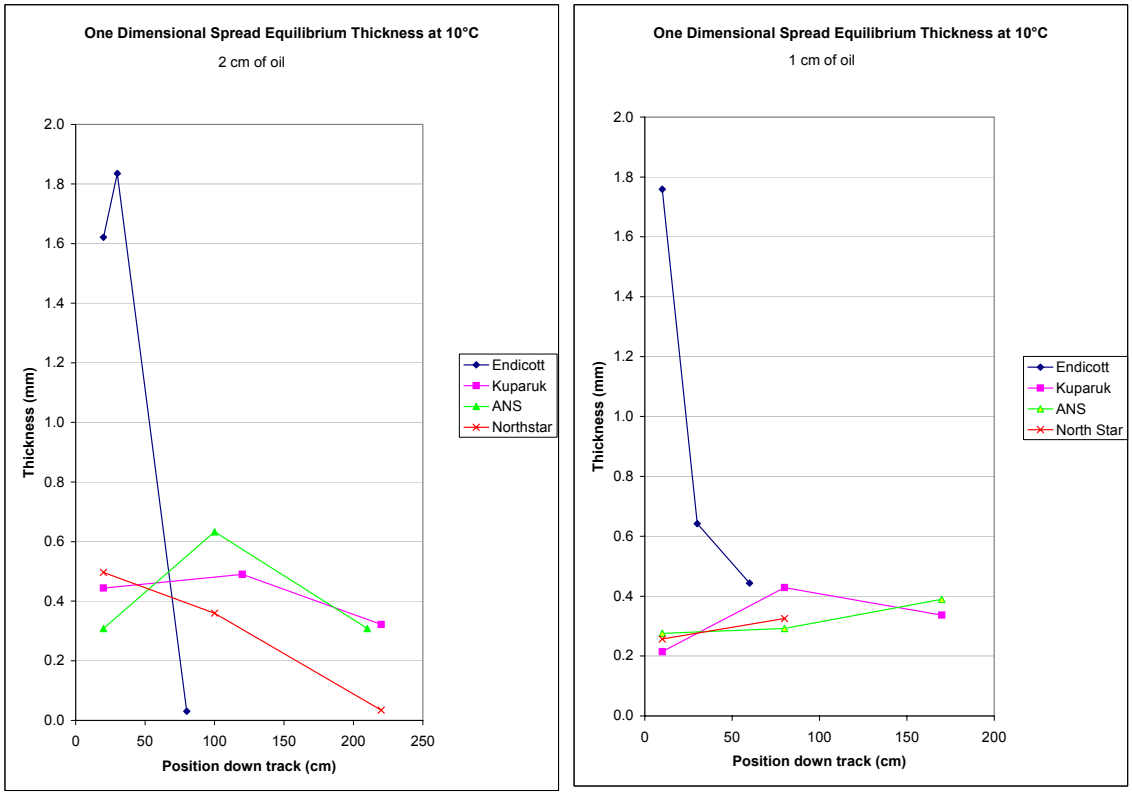

Figure 15. One-dimensional Equilibrium Thickness Results at 10°C

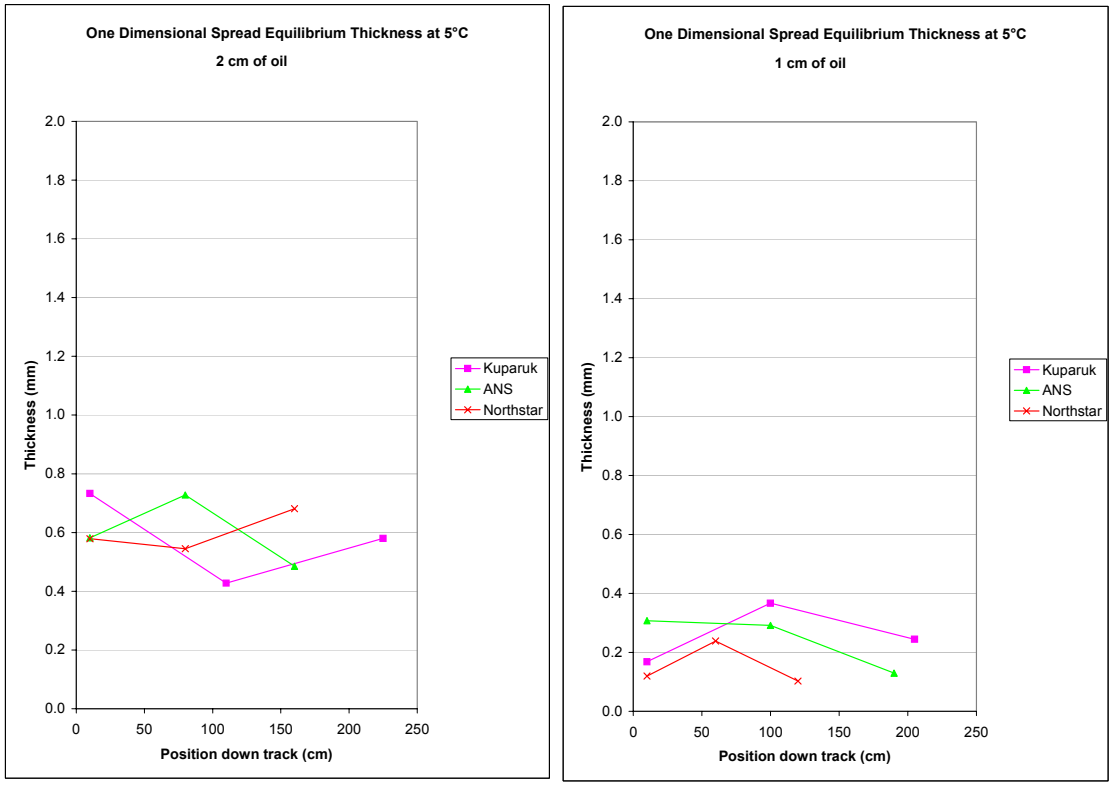

Figure 16. One-dimensional Equilibrium Thickness Results at 5°C

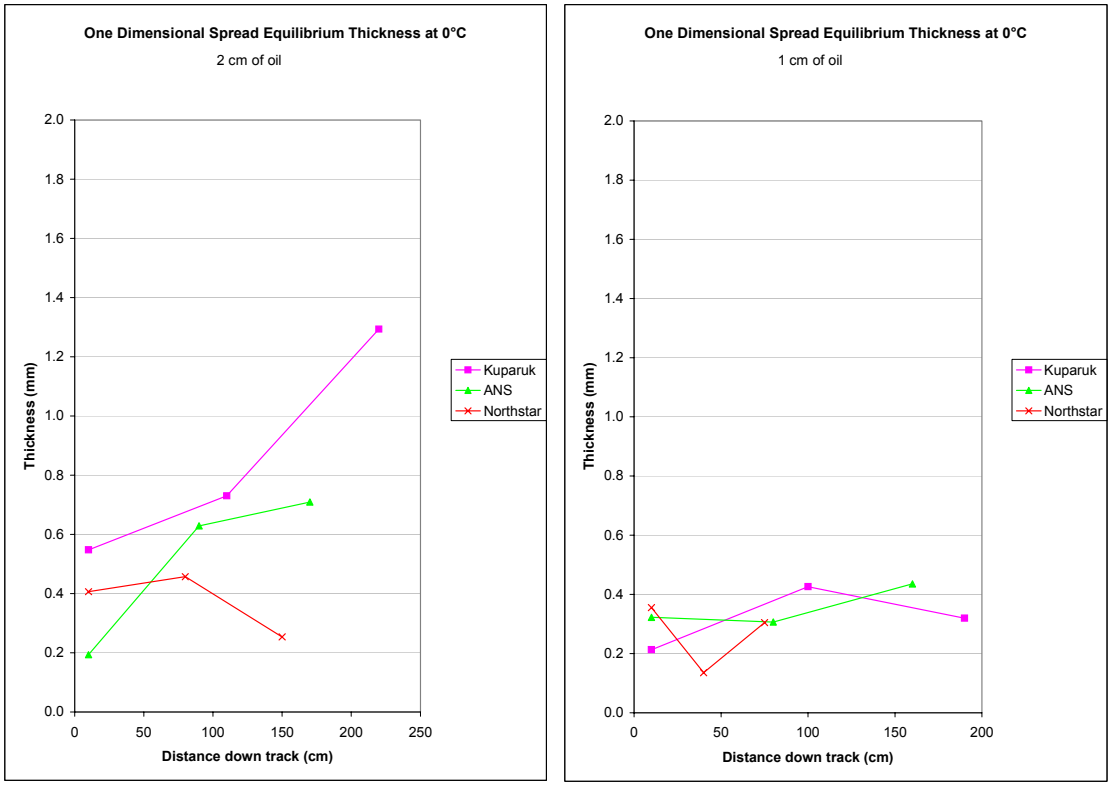

Figure 17. One-dimensional Equilibrium Thickness Results at 0°C

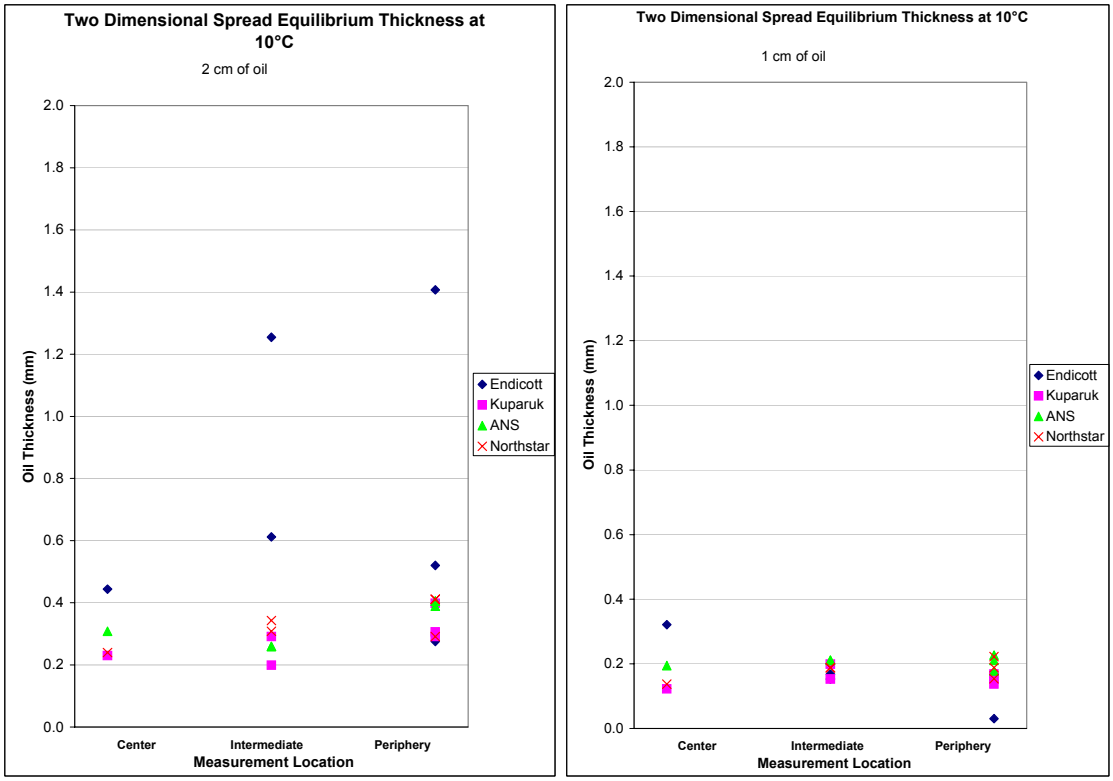

Figure 18. Two-dimensional Equilibrium Thickness Results at 10°C

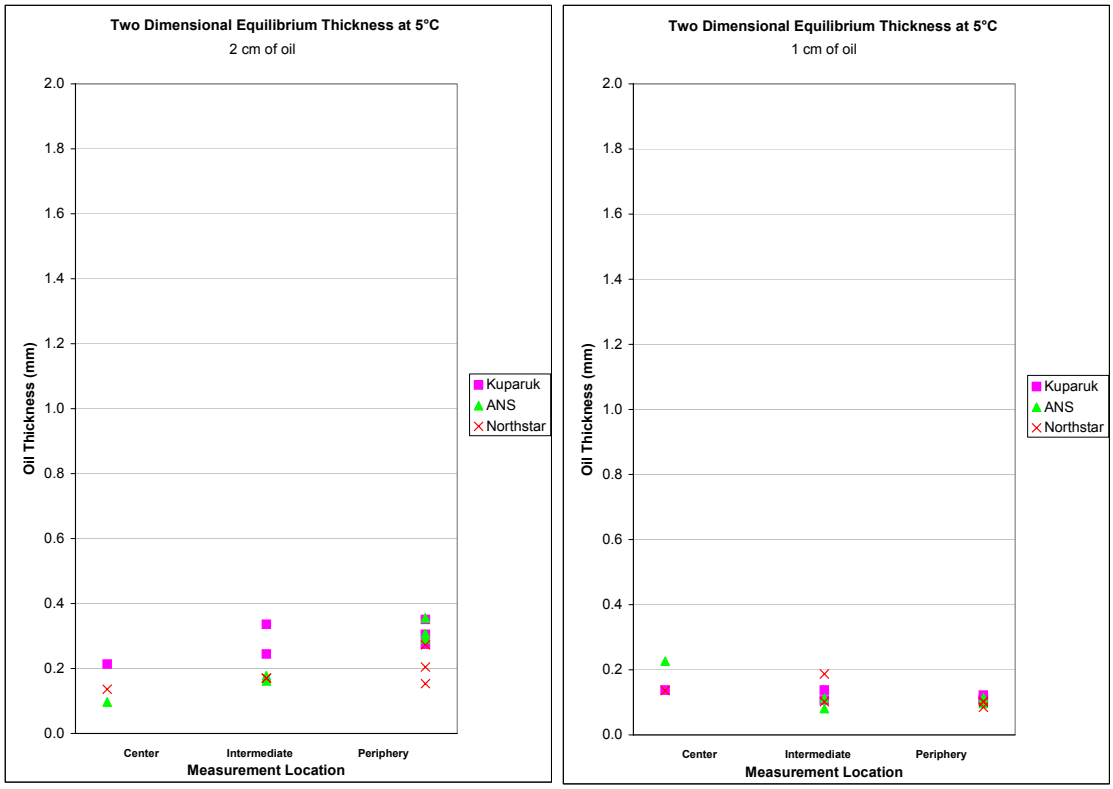

Figure 19. Two-dimensional Equilibrium Thickness Results at 5°C

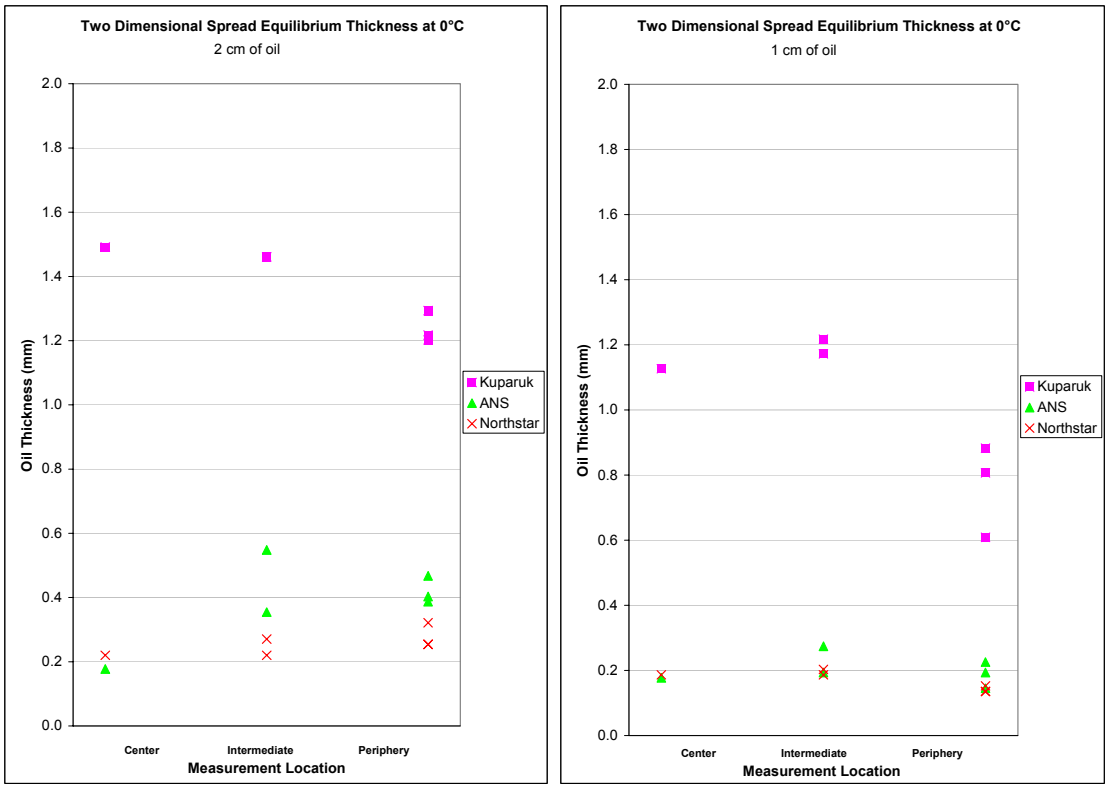

Figure 20. Two-dimensional Equilibrium Thickness Results at 0°C
(NB. Data for 1and 2 cm slick of Kuparuk at 0°C is suspect)

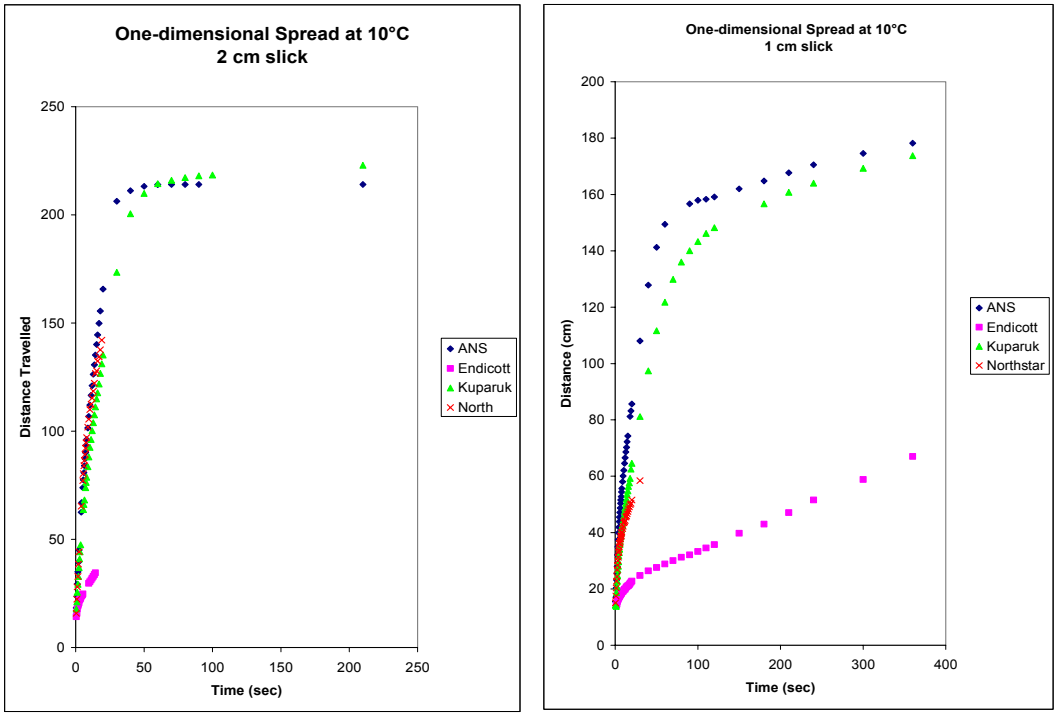

Figure 21. One-dimensional Spreading Results at 10°C

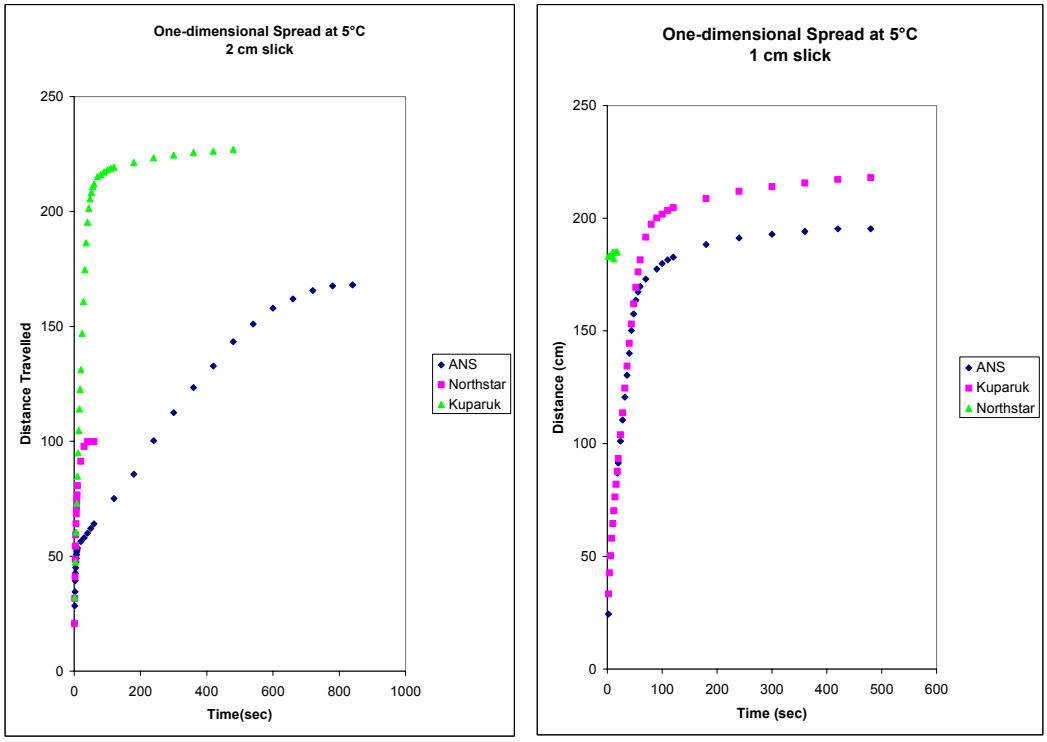

Figure 22. One-dimensional Spreading Results at 5°C

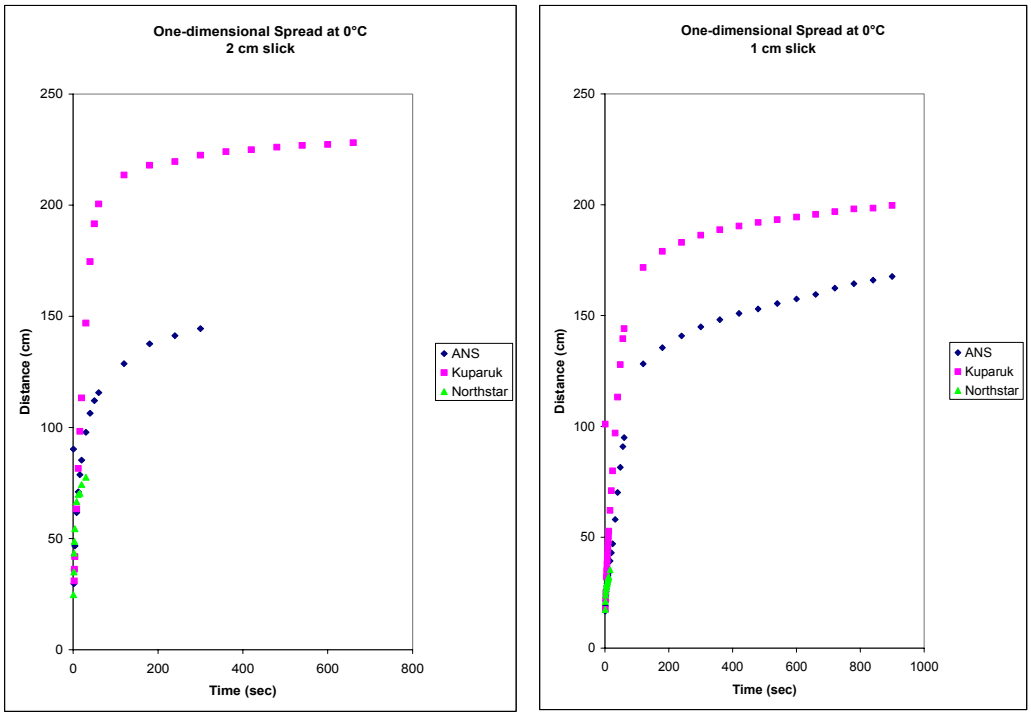

Figure 23. One-dimensional Spreading Results at 0°C

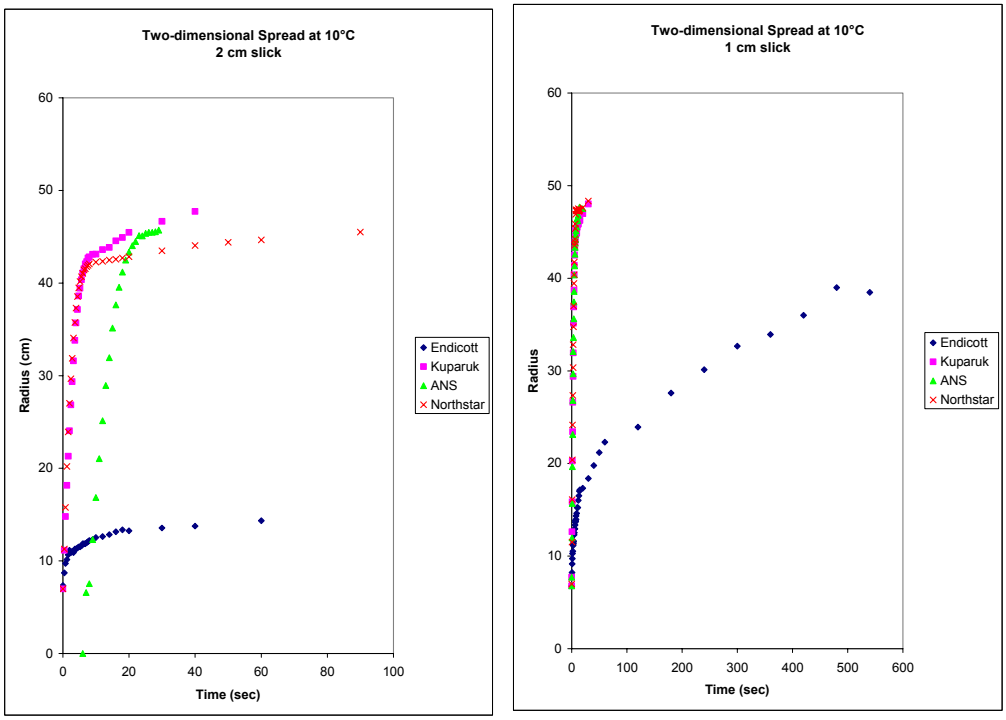

Figure 24. Two-dimensional Spreading Results at 10°C

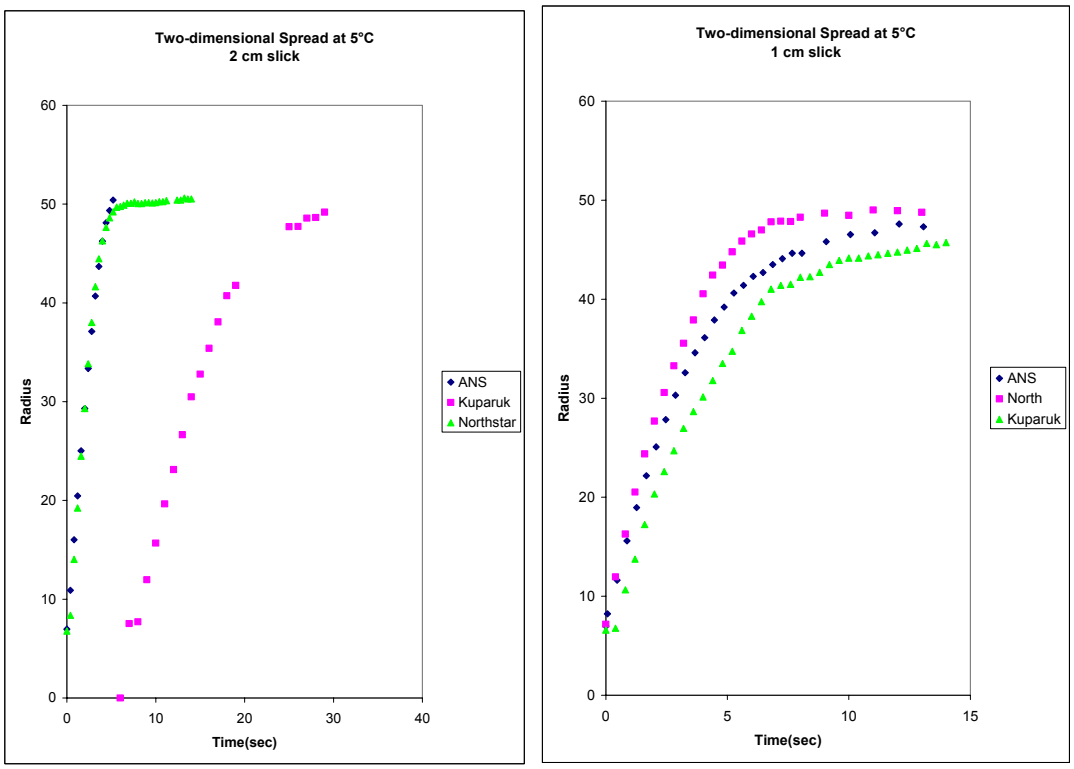

Figure 25. Two-dimensional Spreading Results at 5°C

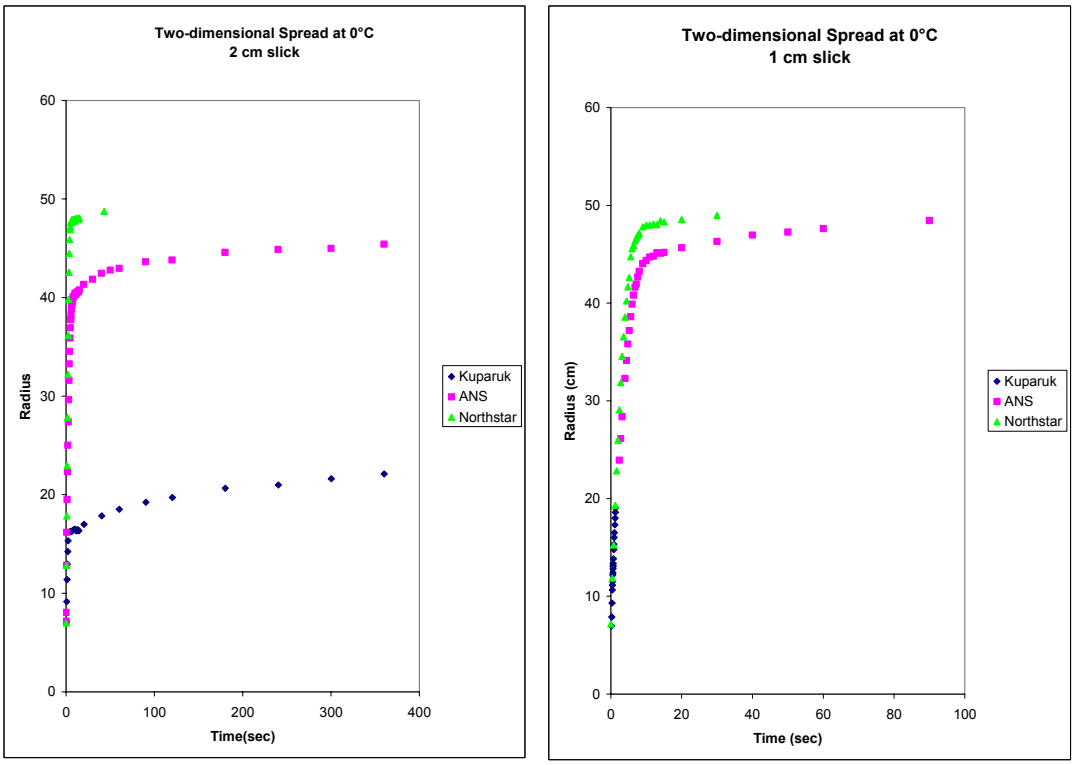

Figure 26. Two-dimensional Spreading Results at 0°C
(NB. Data for 1 and 2 cm slick of Kuparuk at 0°C is suspect)

Where: $l \equiv$ the length of a 1-dimensional slick [cm]
$r \equiv$ the radius of a 2-dimensional slick [cm]
$k \equiv$ proportionality constants
$\Delta \equiv$ ratio of the density difference between water and oil to the density of water
$g \equiv$ acceleration of gravity [cm/s^2]
$A \equiv$ volume of oil per unit length normal to the direction of spread (initial thickness x initial length) [mL]
$V \equiv$ volume of oil [mL]
$\nu \equiv$ kinematic viscosity of water [cm^2/s]
$\rho \equiv$ density of water [g/cm^3]
$\sigma \equiv$ spreading coefficient, or net surface tension [g/cm s^2]
$= \sigma_{w/a} - \sigma_{w/o} - \sigma_{o/a}$

Fay and Hoult (1971) give the following values for the proportionality constants:

	One-dimensional	**Axi-symmetric**
Gravity-Inertia	$k_{1I} = 1.5$	$k_{2I} = 1.14$
Gravity-Viscous	$k_{1V} = 1.5$	$k_{2V} = 1.45$
Surface Tension-Viscous	$k_{1T} = 1.33$	$k_{2T} = 2.30$

Fay (1969) also derives a formula for predicting the slick thickness below which the spreading is dominated by surface tension forces. For a thick slick surrounded by sheen, or a slick on a bounded surface (such as the spreading pans used in this study), this transition thickness can be considered the equilibrium thickness of the thicker portions of the oil:

$$h_c = \sqrt{\frac{\sigma}{(\rho - \rho_o)g}} \qquad \textbf{(10)}$$

Where: $h_c \equiv$ critical transition thickness [cm]
$\rho_o \equiv$ density of oil [g/cm^3]

Fay (1969) proposed an equation for the maximum length scale of a slick; based on the presumption that diffusion of soluble components through the slick into the water column eventually causes the spreading coefficient (or net interfacial tension) to decline to 0. This equation, rewritten to estimate final slick thickness, is:

$$h_\infty = \left(\frac{\rho^2 \nu D^3 V^2}{\sigma^2} \right)^{1/8} \qquad \textbf{(11)}$$

Where: $h_\infty \equiv$ final slick thickness [cm]
$V \equiv$ Volume of oil [g/cm^3]
$D \equiv$ Molecular diffusivity of oil [cm^2/s]
$\approx 1 \times 10^{-4}$ cm^2/s

Table 15 gives the predicted slick thickness from the equations 10 and 11. The volumes of oil used in equation 11 were those for the 2-D spreading experiments.

Table 15. Predicted Final Slick Thickness Using Fay's (1969) Equations

									Using Equation 10.			Using Equation 11.						Using Equation 11 modified by viscosity factor.					
												h_∞ [mm]						h_∞ [mm]					
	Interfacial Tension		Density			Kinematic Viscosity			h_c [mm]			2 cm thickness = 250 mL			1 cm thickness = 125 mL			2 cm thickness = 250 mL			1 cm thickness = 125 mL		
Oil	o/w	o/a	0°C	5°C	10°C	0°C	5°C	10°C	0°C	5°C	10°C	0°C	5°C	10°C	0°C	5°C	10°C	0°C	5°C	10°C	0°C	5°C	10°C
ANS	18.8	27.3	0.877	0.875	0.872	20.1	16.8	14.1	4.3	4.2	4.2	0.33	0.33	0.33	0.27	0.27	0.27	0.48	0.47	0.46	0.40	0.39	0.38
Endicott	32.8	27	0.932	0.929	0.925	2128.8	1001.4	472.0	3.5	3.4	3.3	0.42	0.42	0.42	0.35	0.35	0.35	1.09	0.99	0.90	0.92	0.83	0.76
Northstar	27.5	22.2	0.836	0.831	0.826	4.3	3.6	3.1	3.4	3.3	3.3	0.34	0.34	0.34	0.29	0.29	0.29	0.41	0.40	0.39	0.35	0.34	0.33
Kuparuk	31.1	19.6	0.930	0.927	0.924	226.8	165.4	120.7	5.0	4.9	4.8	0.35	0.35	0.35	0.29	0.29	0.29	0.68	0.66	0.63	0.57	0.55	0.53

It is clear when comparing Figures 15 through 20 with Table 15 that the thicknesses predicted by Equation 10 are an order of magnitude too large; however, the thicknesses predicted by Equation 11 are of the correct magnitude, except for the Endicott crude at 10°C (Figures 15 and 18). This is because the Endicott crude, when fresh, has a Pour Point of 12°C, and thus quickly develops an internal yield stress, gels and ceases spreading when released on 10°C water. At 0°C, where the Kuparuk crude has a significantly higher viscosity that the other two crudes (the Endicott crude, because it did not spread at 10°C was not tested at the lower temperatures), its final slick thickness was also higher than predicted by Equation 11 (Figures 17 and 20). The final set of predictions is Equation 11 multiplied by the ratio of oil viscosity to water viscosity raised to the power ⅛. This factor is equivalent to using the oil kinematic viscosity in Equation 11 rather than the water viscosity (SL Ross and Energetex 1986, SL Ross and DMER 1987, and SL Ross and DF Dickins 1987). This factor considerably improves the predicted final thickness to better fit the experimental data. It must be kept in mind that the use of a single value of viscosity to represent a non-Newtonian fluid, such as the Endicott oil at 10°C, introduces another considerable source of error into the predictions. With this in mind, Equation 11 with the viscosity factor included seems to reasonably predict the final slick thickness for the crude oils. The modified Equation 11 correctly predicts that there is little difference in the final slick thickness (on the order of 0.5 mm) for the three relatively fluid crudes and a significantly higher final thickness for the gelled oil (Endicott at 10°C). The Kuparuk oil 2-D experiment at 0°C resulted in a much higher thickness than predicted: this is believed to be due to the fact that the Kuparuk crude was inadvertently left uncovered in the metal ring overnight to cool and was thus likely much more viscous than the fresh oil. Equation 11 also correctly predicts that a smaller oil volume results in thinner equilibrium slicks.

The reader is cautioned that Equation 11 does not incorporate the effects of wind, waves and oceanic turbulent eddies on oil slicks. These factors will break a slick up into many small patches, or slicklets, surrounded by clean water, and greatly reduce the average final thickness.

Fay and Hoult (1971) derived a method for non-dimensionalizing 1-D spreading data in order to confirm their theory with experimental data. Figures 27 through 29 shows the data from the trough spreading experiments on water plotted using their technique and Figures 30 through 32 show the 2-D spreading data in the non-dimensionalized form rederived for the 2-D equations.

The solid line in each figure is the theoretical prediction of Fay and Hoult (1971) for the Gravity-Inertia and Gravity-Viscous spreading regimes using the properties of ANS crude.

In general, both sets of data fit the theory quite well. The exceptions are:

- In Figures 27 and 30 (1-D and 2-D spreading at 10°C) the Endicott data falls significantly below the theoretical curve, and the non-dimensionalized plots of the other oils. The slope of the Endicott data is also different than for the others, more so in the 2-D experiments. This is likely due to the temperature being lower than the crude's Pour Point, thus creating non-Newtonian flow behavior in the oil. The Endicott crude experiments were only completed at 10°C: at lower temperatures the oil had gelled into a semi-solid that did not start to spread, due to the onset of a significant yield stress.
- The Kuparuk 2-D spreading experiments at 0°C gave significantly lower results than the other two oils. This is probably due to the oils evaporating overnight after inadvertently being left uncovered while they equilibrated to the test temperature (see also the equilibrium thickness discussion above).

The spreading data support the theory of Fay (1969) and Fay and Hoult (1971) that the oil spreading on water is not dependent on the viscosity of the oil, only the viscosity of the layer of underlying water set in motion by the spreading oil slick. Despite considerable effort devoted to determining if oil viscosity played a role in the spreading rate (see Appendix C), as postulated by SL Ross and Energetex (1986), SL Ross and DF Dickins (1987) and SL Ross and DMER (1988) no improvement in the correlations could be made (excepting, of course, for the gelled Endicott crude). In fact, there are quite a few instances where the Kuparuk crude (the most viscous of the three fluid oils) spread faster than the other two, considerably less viscous crudes.

One reason for this apparent contradiction with the earlier research may be that, in those studies, the spreading experiments were conducted in shallow troughs with a bottom and two sealed ends filled with only a few centimeters of water. The oil spreading over this water would initially create the layer of water moving with the spreading slick as envisioned by Fay (1969); however, the water layer could only grow to a few millimeters thickness before it began to be affected by the bottom of the trough. This would cause viscous resistance to the oil spreading force of gravity to change, which could have been interpreted by the researchers as an effect of oil viscosity. In the experiments here, in troughs with no bottom and the downward end open, the data fits Fay's viscous dissipation theory quite well, with the difference in oil spreading rates accounted for adequately by differences in crude oil density (excepting of course, for the high Pour Point Endicott crude).

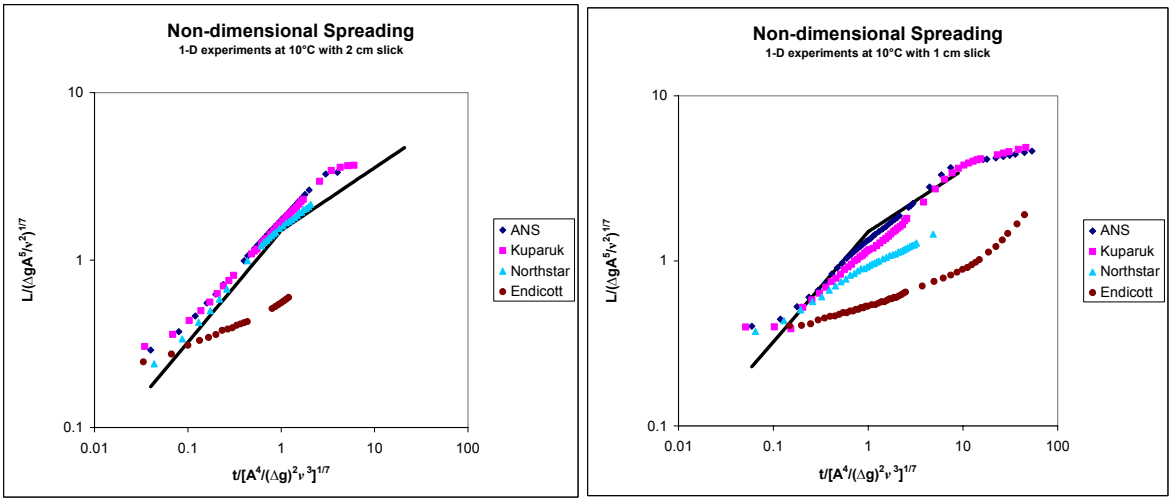

Figure 27. 1-D Spreading Data at 10°C in Non-dimensional Format

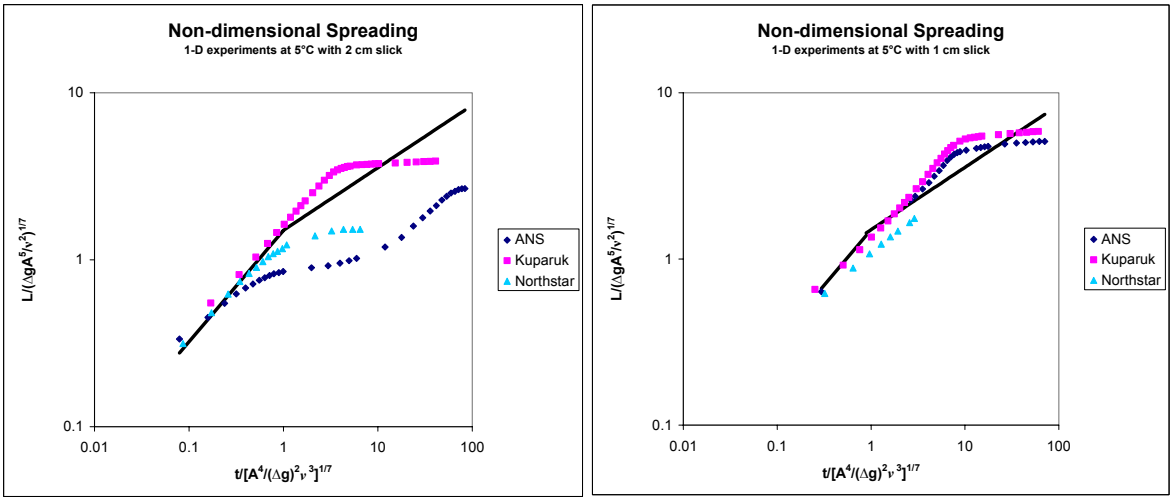

Figure 28. 1-D Spreading Data at 5°C Plotted in Non-dimensional Format

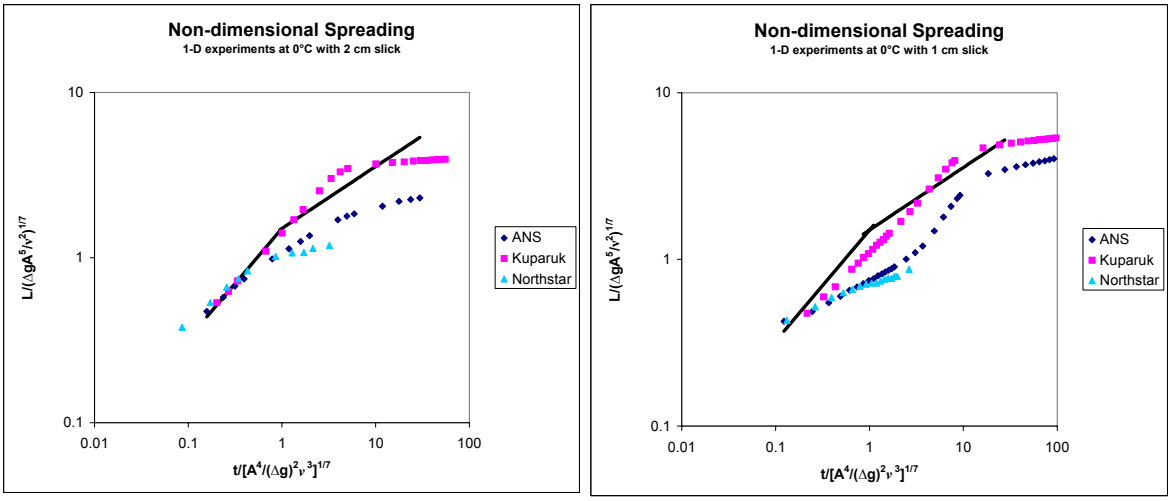

Figure 29. 1-D Spreading Data at 0°C Plotted in Non-dimensional Format

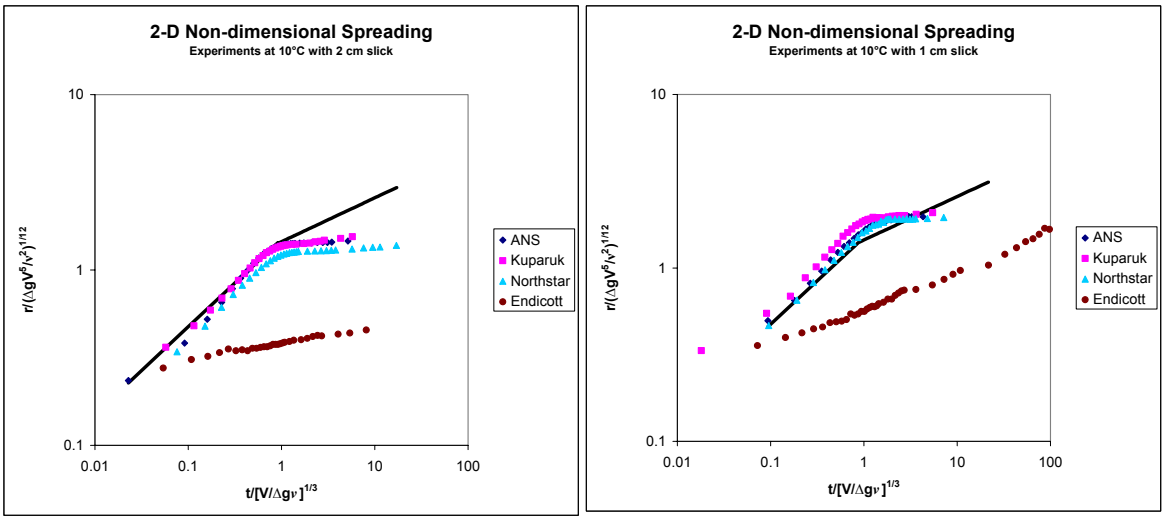

Figure 30. 2-D Spreading Data at 10°C Plotted in Non-dimensional Format

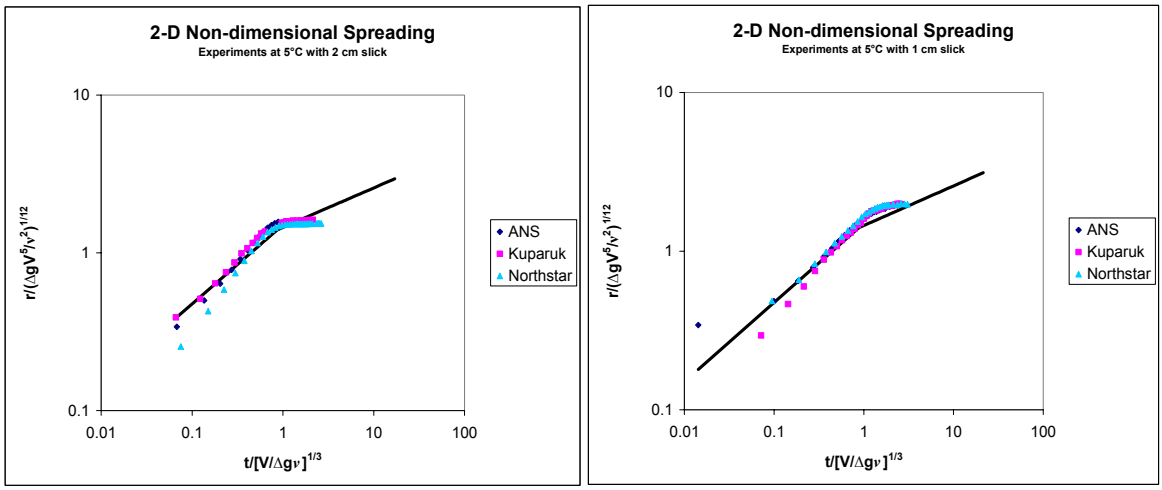

Figure 31. 2-D Spreading Data at 5°C Plotted in Non-dimensional Format

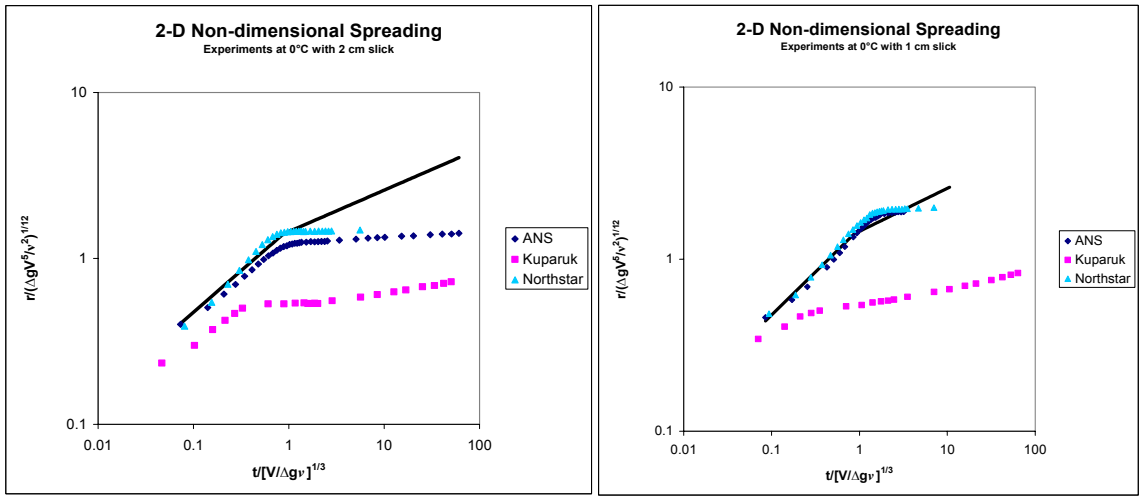

Figure 32. 2-D Spreading Data at 0°C Plotted in Non-dimensional Format
(NB. Data for 1 and 2 cm slick of Kuparuk at 0°C is suspect)

Larger-scale Experiments at Ohmsett

During the emulsification in broken ice experiments at Ohmsett, two larger-scale one-dimensional spreading tests with Kuparuk and Northstar crude at 0°C were performed. A spreading "trough" was created at one side of the using containment boom. The "trough was 3 m wide and 30 m long. The oil (120 L) was initially contained in an area 3 m wide and 1.8 m long by a barrier at the start of the "trough" to give an initial thickness of 2.15 cm. The oil was released by lifting the barrier and timing the spread of the oil down the trough past measured marks on the tank with a stopwatch. Figure 33 shows the results plotted in non-dimensional format compared to the same data from the lab tests. The two data sets for the Kuparuk crude are very similar; however, the data from the spreading test with the Northstar crude at Ohmsett is quite different. This is because, prior to the experiment beginning, some of the oil leaked past the barrier and second, because a wind had sprung up that was blowing down the "trough". This caused the Northstar oil to be advected down the "trough" as well as spreading down the "trough", thus the steeper slope of the Ohmsett data points.

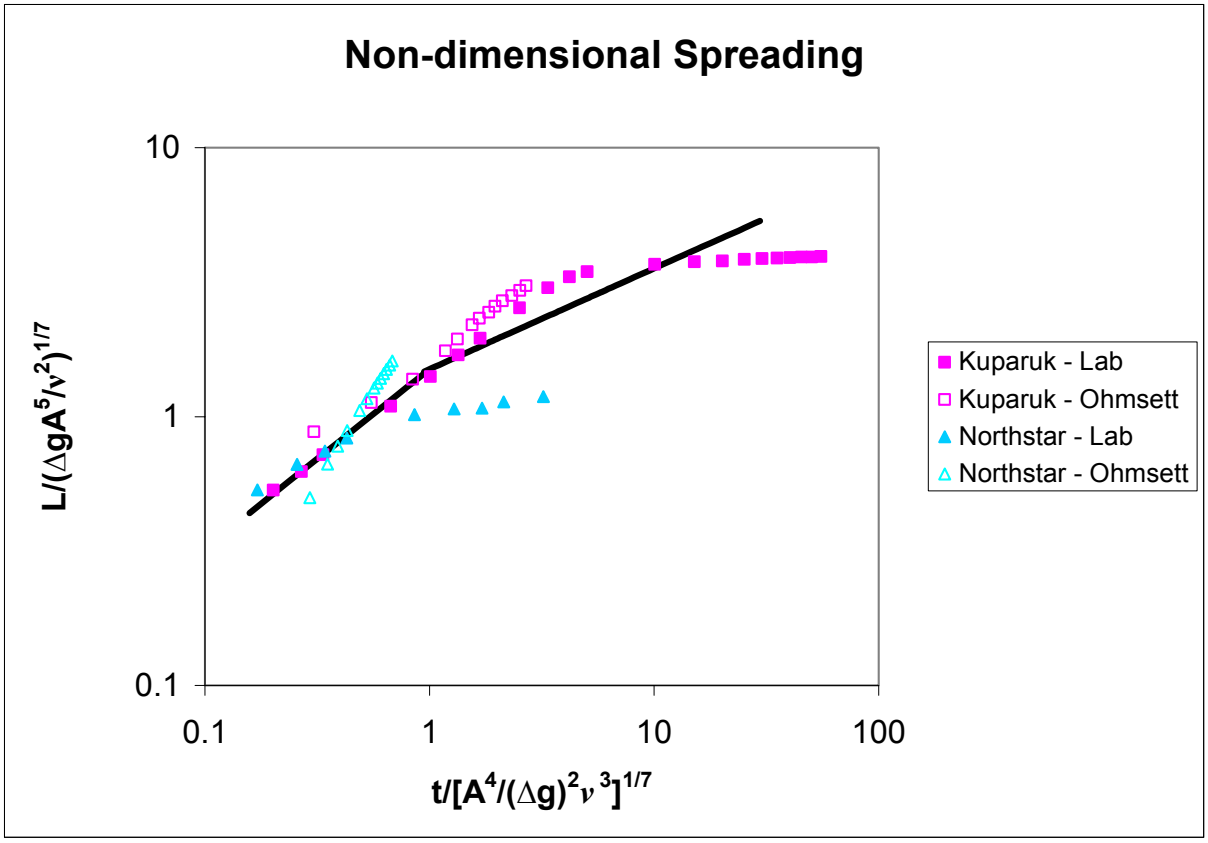

Figure 33. Comparison of Large- and Small-scale Spreading Data

7. OIL SPREADING ON ICE AND SNOW

The purpose of this task was to determine the effect of oil properties (primarily pour point and viscosity) on the spreading of crude oil on ice in the lab and on snow at the outdoor test facility.

7.1 State of the Art

Oil Spreading on Ice

Fay and Hoult (1971) presented the classic treatment of oil spreading, based on Fay's (1969) theory. Glaeser and Vance (1971) present the results of a series of oil (diesel and North Slope crude) spreading experiments on sea ice near Barrow, AK. McMinn (1972) reports on a second series of releases of North Slope crude oil (some on snow-covered sea ice and some on bare lake ice) undertaken near Port Clarence in January 1972 and correlates the data using a modification of the Fay spreading model. Chen *et al*. (1974) conducted a series of radial spreading experiments on freshwater ice grown in a cold room with five different, low-pour point crudes and correlated the results with a gravity-viscous spreading regime model after Fay.

Oil Spreading on Snow

Glaeser and Vance (1971) present the results of a series of oil (diesel and North Slope crude) spreading experiments in snow on sea ice near Barrow, AK. McMinn (1972) reports on a second series of releases of North Slope crude oil (some on snow-covered sea ice) undertaken near Port Clarence in January 1972 and correlates the data using the Fay spreading model. Mackay *et al*. (1975) report on a series of small-scale laboratory and larger field studies of the behavior of oil spilled on snow on terrain. Kawamura *et al*. (1986) carried out a series of experiments on the spreading of different chemicals, including mineral oils, in different types of snow, and correlated the results using Darcy's Law. SL Ross and DF Dickins (1988) conducted mid-size experiments to measure oil spreading in snow on ice. Bech and Sveum (1991) report on a series of five large experiments with 1 m^3 each of diesel or crude released onto or under snow on sea ice.

7.2 Spreading on Ice Methods

Only one-dimensional spreading experiments were conducted for this task. Tests were repeated at -1°, -10° and -20°C.

One-dimensional Tests

A series of four graduated bottomless troughs open at one end was frozen into the surface of a 35‰ ice sheet in the tank for the one-dimensional tests (Figure 34). These troughs were constructed using 2.4-m long, 10-cm wide strips of painted steel flashing material. A wooden strip stiffened the two outside trough edges and served as a graduated length scale for the photographic data analysis. The bottom edges of the strips were mounted in wooden spacers placed every 60 cm to keep the strips spaced evenly apart along their entire length. One end of the trough bundle was closed with a slotted wooden end piece into which the metal sides were sealed with silicone (Figure 35). The other end of the trough was open. The oil was initially retained at the closed end of the trough by a series of removable rubber dams that sealed against the sides of the trough and against the ice sheet. After each test the troughs were wiped down thoroughly with clean sorbent pads.

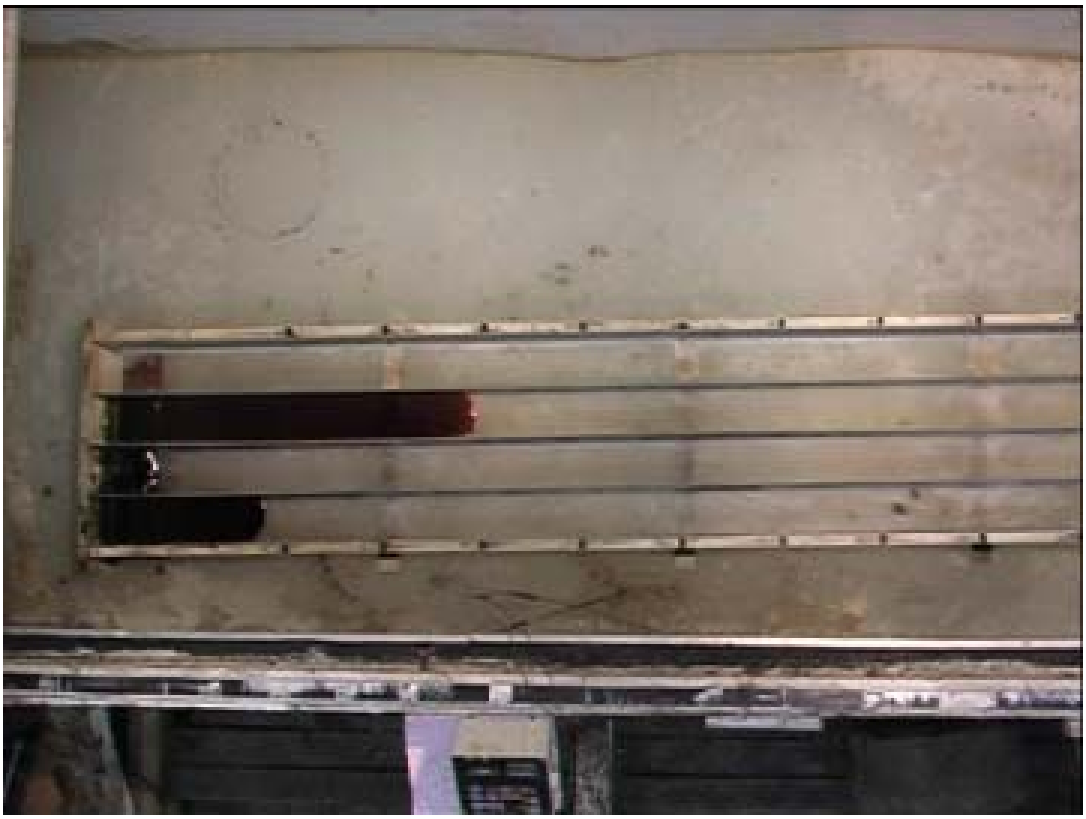

Figure 34. One-dimensional Spreading Tests Apparatus Frozen in Ice Sheet in Indoor Tank

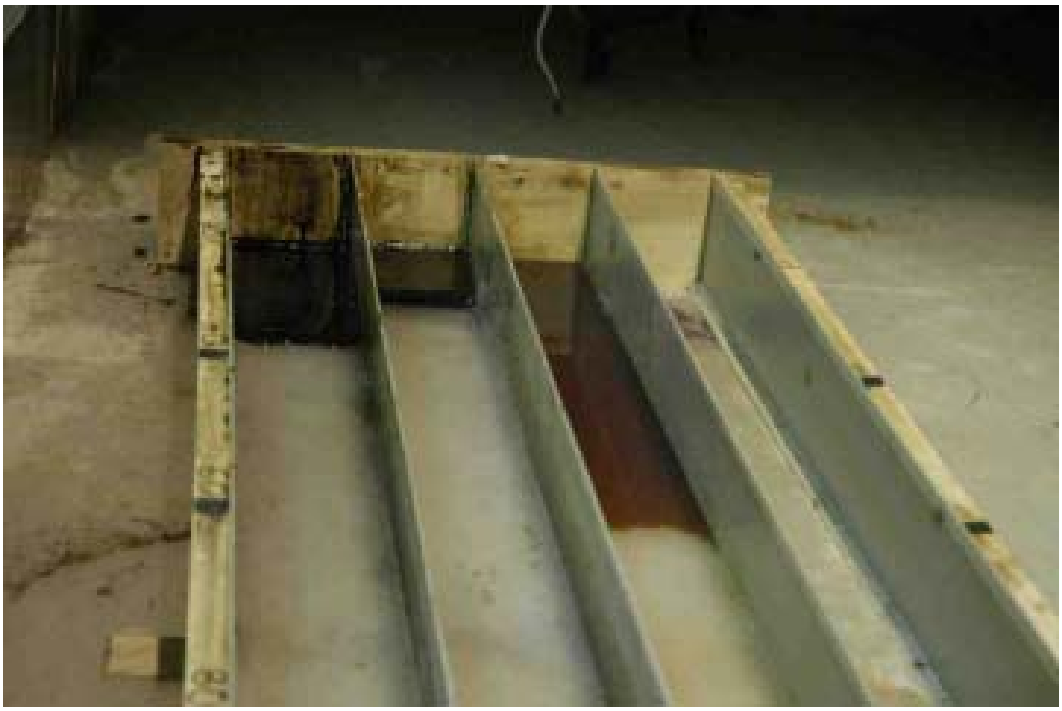

Figure 35. Close-up of Sealed End of One-dimensional Spreading Tests Apparatus in Ice

The oils (initial slick thicknesses of 1 cm and 2 cm were employed) were released at the same time by removing the four dams simultaneously. The spread of the oils down the troughs was recorded using an overhead digital video camera. When the slick had stopped spreading, pre-weighed 3-cm diameter circles of sorbent pad were placed on the slick at three distances down the trough and used to collect all the oil under the circle. If one sorbent circle was insufficient to recover all the oil, a second was placed exactly where the first had been and the amount of oil was calculated using the sum of the weights of the two. The thickness of the oil under a sorbent circle was estimated by determining the net weight of oil in the sorbent(s), converting the oil mass to volume by dividing by the fresh oil density at the ambient temperature (-1°, -10° and -20°C) then dividing the oil volume by the surface area of the 3-cm diameter sorbent circle.

The spreading rate was measured as follows:

1. Still digital images were obtained from the digital video at fixed times after the dams were raised to release the oil;
2. The still images were analyzed using image software to determine the distance from the origin of the leading edge of each slick. This was measured in pixels, and then converted to centimeters using a calibration for the digital photograph.
3. This produced a table of distance vs. time for each individual experiment.

7.3 Spreading on Ice Results

The results of the spreading tests on ice are presented here graphically. All the data may be found in Appendix D.

Equilibrium Thickness Measurements

One-dimensional Tests. The equilibrium thickness measured at given locations down the spreading troughs is given in Figures 36 through 38.

Spreading Measurements

One-dimensional Tests. The slick spreading measured in the troughs is given in Figures 39 through 41.

7.4 Spreading on Ice Discussion and Algorithm Selection

The classic treatment of oil spreading on ice was proposed by Glaeser and Vance (1971) and McMinn (1972). In their theory there are two spreading forces (gravity and surface tension) that are opposed by two resistances (inertia and oil viscosity) after Fay (1969) and Fay and Hoult (1971). By equating the forces with a resistance, they developed a set of spreading equations for 2-dimensional, or axi-symmetric spreading on ice. For this study, the equivalent 1-dimensional spreading equations were derived. McMinn (1972) postulated that, on real sea ice with roughness on the order of 2.5 cm, that slicks would never thin to where surface tension would be a significant spreading force, thus:

	One-dimensional		Axi-symmetric	
Gravity-Inertia	$l = k(gA)^{1/3} t^{2/3}$	**(12)**	$r = k(gV)^{1/4} t^{1/2}$	**(13)**
Gravity-Viscous	$l = k\left(\frac{\rho_o g A^3}{\mu}\right)^{1/5} t^{1/5}$	**(14)**	$r = k\left(\frac{\rho_o g V^3}{\pi^3 \mu}\right)^{1/8} t^{1/8}$	**(15)**

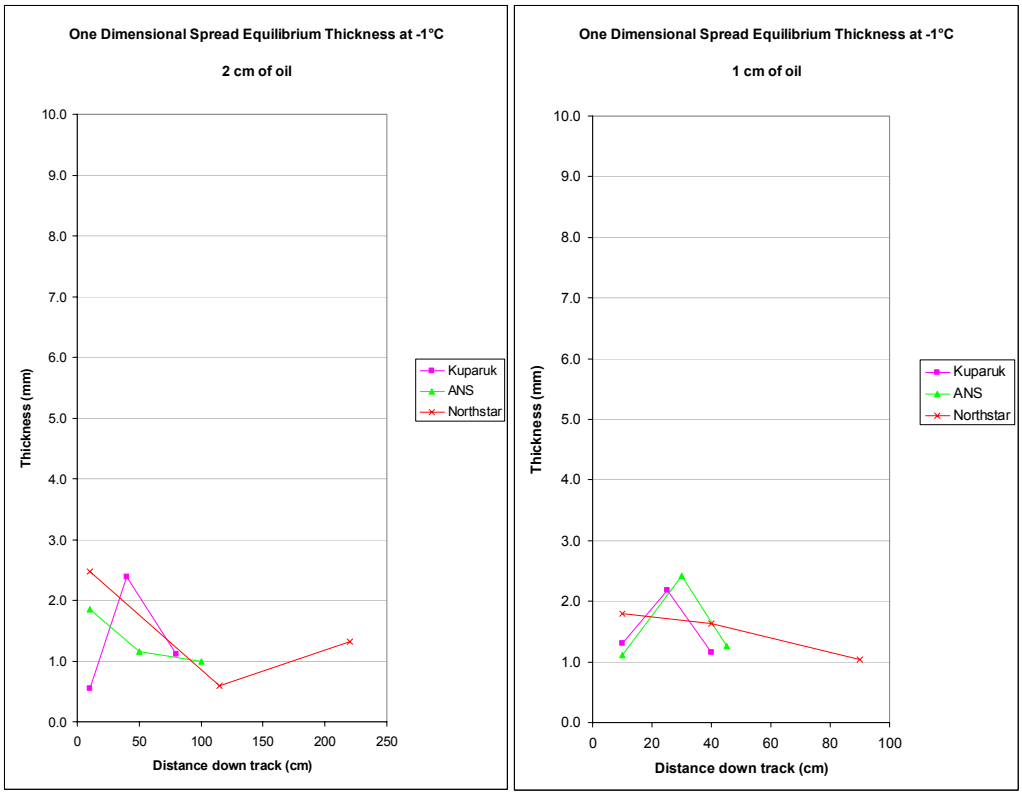

Figure 36. One-dimensional Equilibrium Thickness on Ice at -1°C

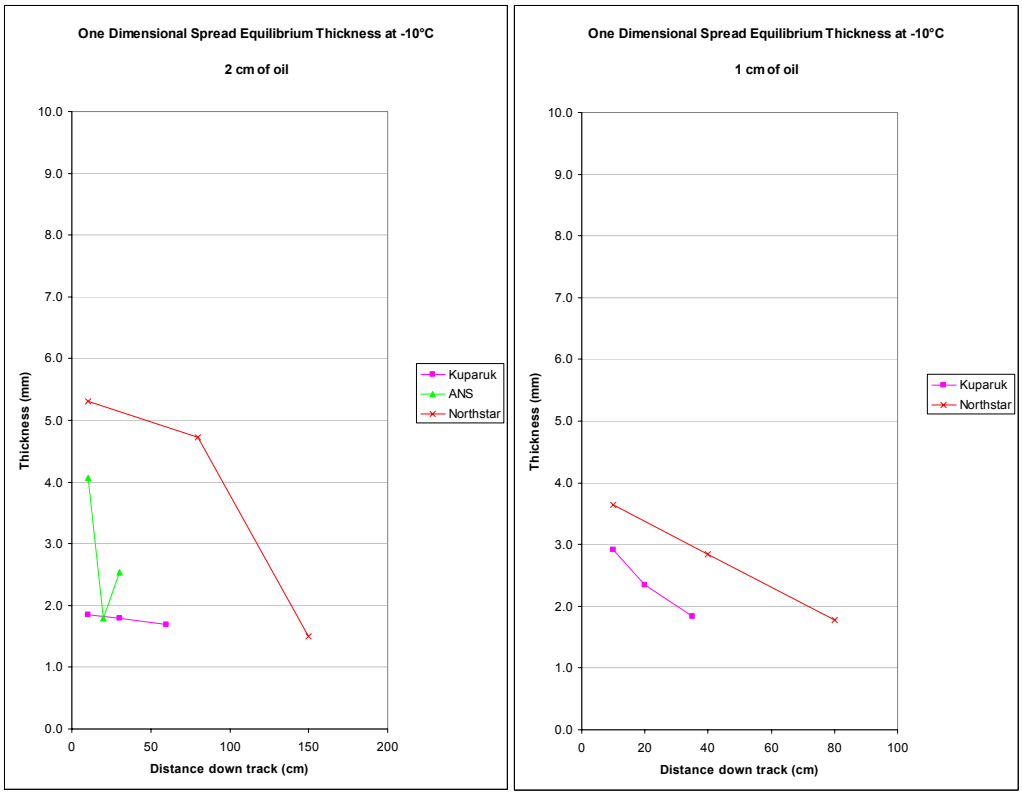

Figure 37. One-dimensional Equilibrium Thickness on Ice at -10°C

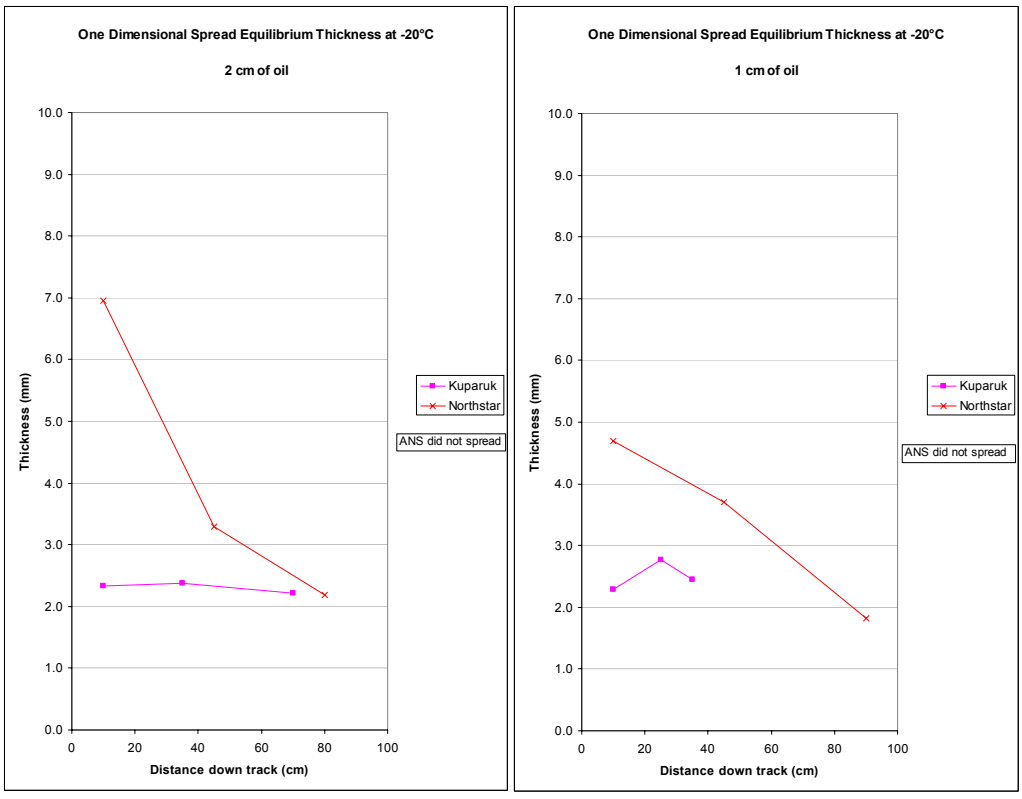

Figure 38. One-dimensional Equilibrium Thickness on Ice at -20°C

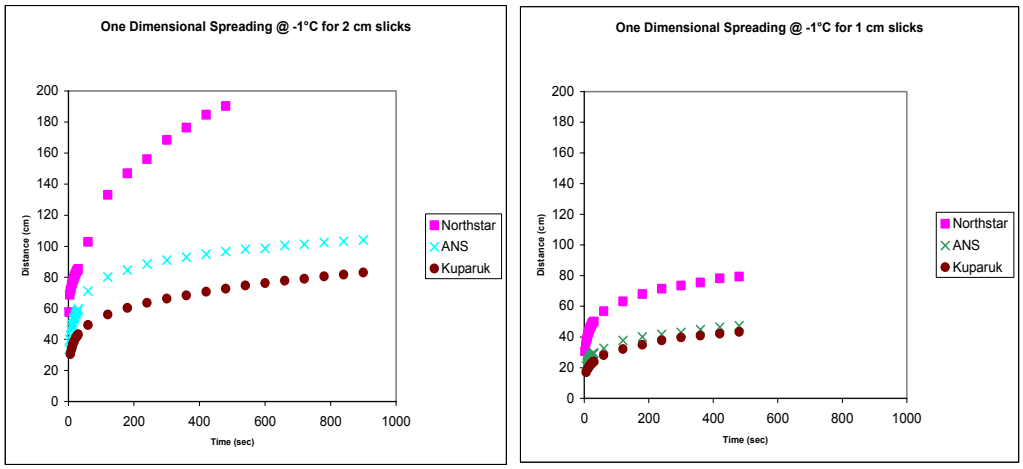

Figure 39. One-dimensional Spreading Results on Ice at -1°C

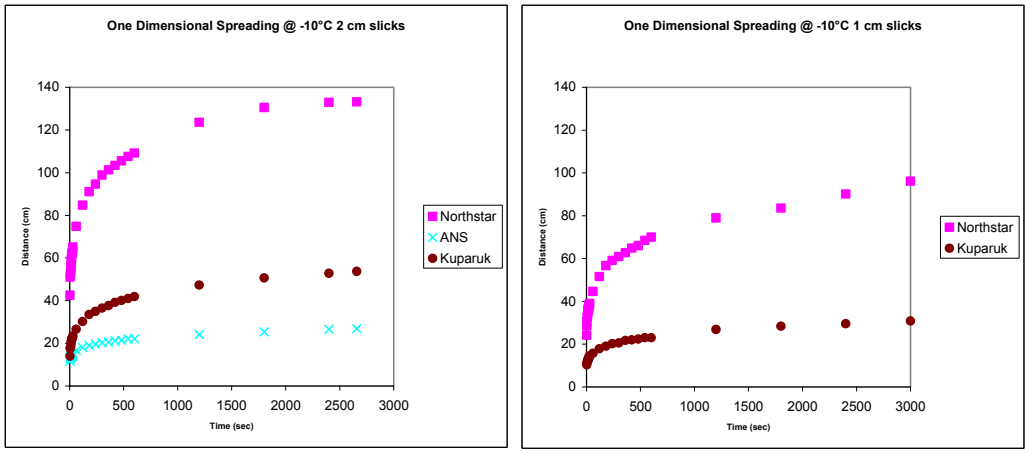

Figure 40. One-dimensional Spreading Results on Ice at -10°C

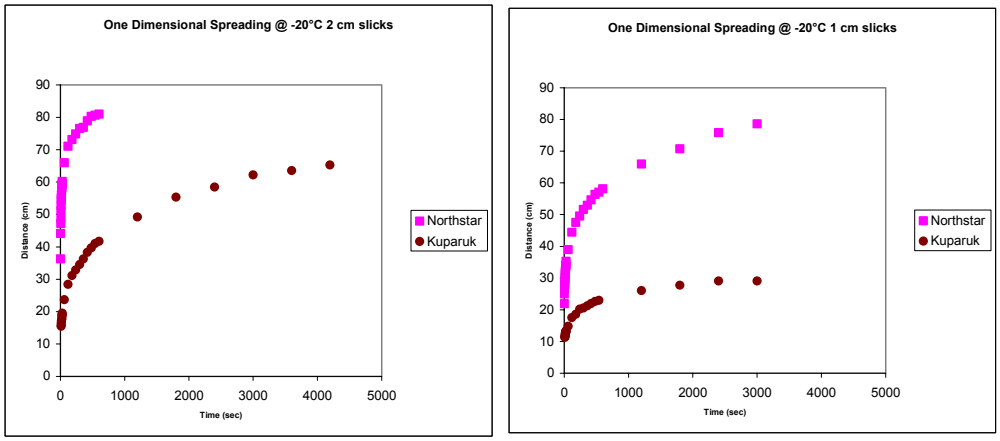

Figure 41. One-dimensional Spreading Results on Ice at -20°C

McMinn (1972) also derives a formula for predicting the slick thickness below which the spreading is dominated by surface tension forces:

$$h_{ci} = \sqrt{\frac{2\sigma_i}{\rho_o g}} \qquad \textbf{(16)}$$

Where: $h_{ci} \equiv$ critical transition thickness on ice [cm]
$\rho_o \equiv$ density of oil [g/cm^3]

Where: $l \equiv$ the length of a 1-dimensional slick [cm]
$r \equiv$ the radius of a 2-dimensional slick [cm]
$k \equiv$ proportionality constants
$g \equiv$ acceleration of gravity [cm/s^2]
$A \equiv$ volume of oil per unit length normal to the direction of spread (initial thickness x initial length) [mL]
$V \equiv$ volume of oil [mL]
$\mu \equiv$ dynamic viscosity of oil [g/cm s]
$\rho_o \equiv$ density of oil [g/cm^3]
$\sigma_i \equiv$ spreading coefficient, or net surface tension of oil on ice [g/cm s^2]
$= \sigma (1-\cos\theta)$, where θ is the contact angle between ice and oil, assumed to be between 25° and 45° and σ is assumed to be 30 g/cm s^2 after McMinn (1971)

Kawamura *et al*. (1986) studied the spreading of chemicals, including mineral oils, on ice and developed the following relationship for final slick thickness in cm:

$$h_f = 0.04 V^{0.15} \mu^{0.24} \qquad \textbf{(17)}$$

Table 16 gives the predicted slick thickness from equations 16 and 17. Note that the Endicott did not spread at -1°C, thus it was not tested at the colder temperatures. The ANS crude barely spread at -10°C, and did not spread at -20°C.

Table 16. Predicted Slick Thickness on Ice at Various Temperatures

	Interfacial Tension		Density			Kinematic Viscosity			hc [mm] using Equation 16			hc [mm] from Eqn 16 x visc ⅛			hc [mm] from Eqn 17		
Oil	o/w	o/a	-1°C	-10°C	-20°C	-1°C	-10°C	-20°C	-1°C	-10°C	-20°C	-1°C	-10°C	-20°C	-1°C	-10°C	-20°C
ANS	18.8	27.3	0.878	0.883	0.888	20.7	28.5	40.7	2.1	2.1	2.1	3.7	3.8	4.0	1.8	1.9	2.1
Endicott	32.8	27	0.933	0.94	0.947	2474.1	9591.5	43265.0	1.3	1.3	1.3	6.5	7.6	9.2	5.7	7.9	11.3
Northstar	27.5	22.2	0.837	0.845	0.855	4.5	6.2	8.7	2.0	2.0	2.0	3.1	3.2	3.3	1.2	1.3	1.4
Kuparuk	31.1	19.6	0.93	0.935	0.941	241.7	426.8	802.7	1.8	1.8	1.8	4.8	5.2	5.6	3.2	3.7	4.3

When comparing Figures 36 through 38 with Table 16 it can be seen that the thicknesses predicted by Equation 16 are of the correct magnitude at -1°C (except for the Endicott crude which gelled at all test temperatures); however, at the lower temperatures the equilibrium thickness increases, which is not a trend predicted by Equation 16. The second set of predictions is Equation 16 multiplied by the ratio of oil viscosity to water viscosity raised to the power ⅛

(after SL Ross and Energetex 1986, SL Ross and DMER 1987, and SL Ross and DF Dickins 1987). This factor predicts the correct trend of increasing equilibrium thickness with decreasing temperature but does not improve the fit to the experimental data. In particular, the ANS crude has partially gelled at -10°C and would not spread at -20°C. The final prediction of Equation 17 is somewhat better, since it implicitly includes viscosity and correctly predicts the trend of increasing thickness with decreasing temperature. It must be kept in mind that the use of a single value of viscosity to represent a non-Newtonian fluid (i.e., a crude oil at a temperature near its Pour Point), such as the Endicott oil at -1°C, introduces another considerable source of error into the predictions. Neither theory is satisfactory; however this is not a great problem since, as noted by McMinn (1971), the scale of the surface roughness for real sea ice is on the order of 3 cm, and this will dictate the equilibrium slick thickness on ice, not oil-related factors.

Fay and Hoult (1971) derived a method for non-dimensionalizing 1-D spreading data in order to confirm their theory with experimental data. Figures 42 through 44 show the data from the trough spreading experiments on ice plotted using the non-dimensionalized form rederived for 1-D spreading on ice.

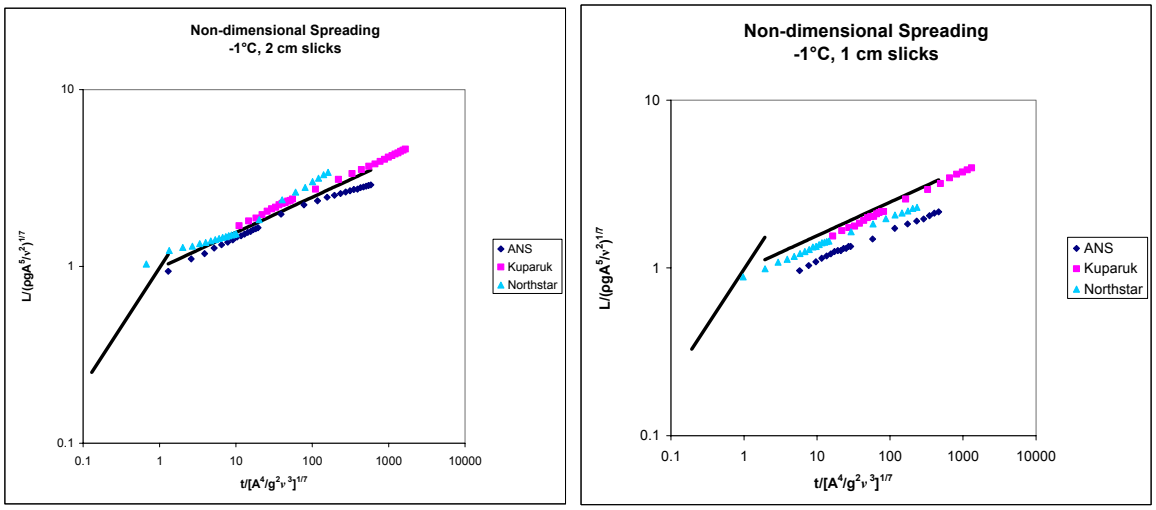

Figure 42. Non-dimensional Spread on Ice at -1°C

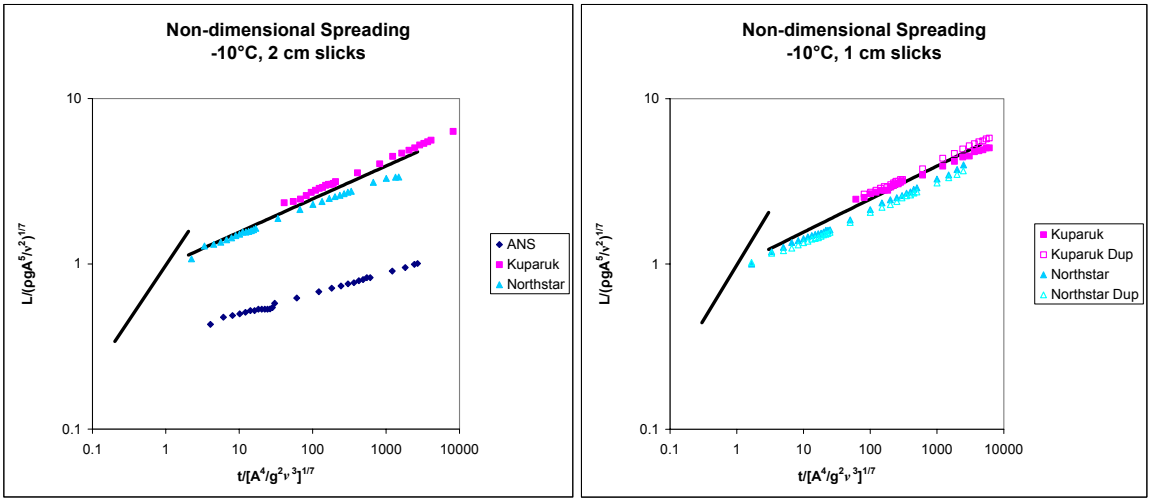

Figure 43. Non-dimensional Spread on Ice at -10°C

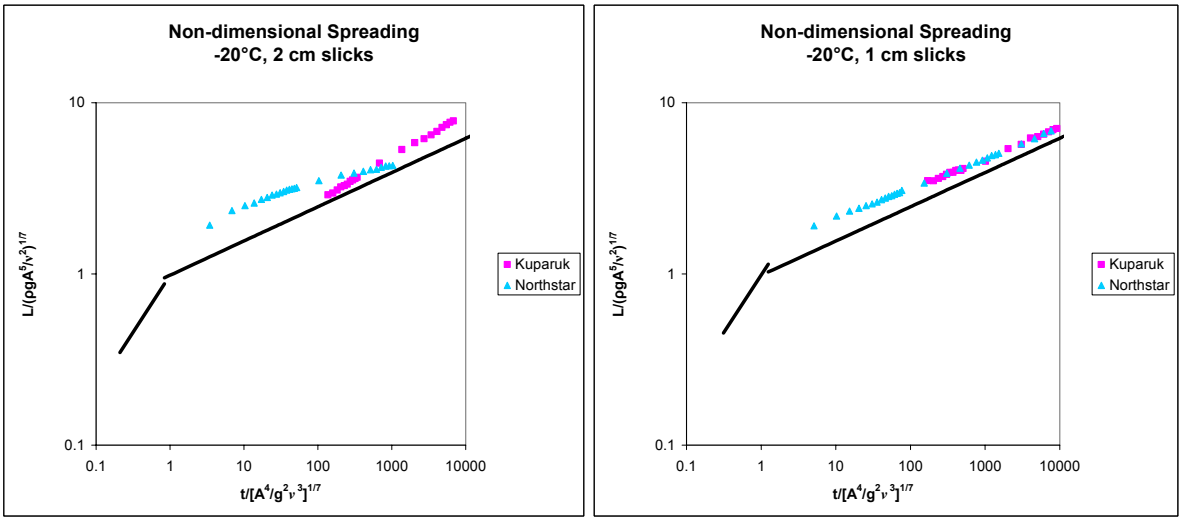

Figure 44. Non-dimensional Spread on Ice at -20°C

In general, the data fit the theory quite well with the value of *k* appearing to be 1. The Endicott crude did not spread at -1°C, due to its Pour Point of 12°C, and was not included in the tests at colder temperatures. At -10°C, a 2-cm slick the ANS crude spread very sluggishly and a 1-cm slick did not spread at all. While cooling to the ambient temperature the oil must have evaporated enough to raise it's Pour Point to near -10°C.

7.5 Spreading on Snow Methods

The spreading on snow experiments were mostly conducted on the frozen surface of the outdoor test tanks. The cover over the tanks was removed to allow natural snow to accumulate to different thicknesses (Figure 46) as depicted. One series, in February 2007, was carried out on

freshly snow-covered ice grown in 1-m^2 pans on the ground beside the outdoor tanks. This was done so as not to oil the surface of the larger outdoor tanks that were being used for brine channel migration studies at the time.

Prior to each experiment, collecting a snow sample of known volume in a pre-weighed sealable container, then re-weighing the container determined the density of the snow and the temperature and depth of the snow-ice interface was measured. The crystals were characterized by examining them on a snow crystal card (Figure 45) shown below, with a magnifying glass.

Figure 45. Snow Crystal Card

Next, a line of holes on 10-cm centers was cored to the ice surface in the snow with a small-diameter tube along three radii out from the middle of each test area. The purpose of these holes was to see when the oil spreading under the snow reached a given radius. A funnel, supported on three thin metal legs was then placed over the middle hole and a pre-weighed amount of fresh oil was poured as quickly as possible from a 4-L Jerry can into the funnel and onto the snow. The pour was timed and the appearance of oil in the bottom of the holes recorded. Each experiment was also videotaped. When the spreading had stopped, a thin strip of sorbent was pushed into the oil layer to the ice surface and withdrawn. The depth of the oil layer on the strip was measured with a ruler and recorded.

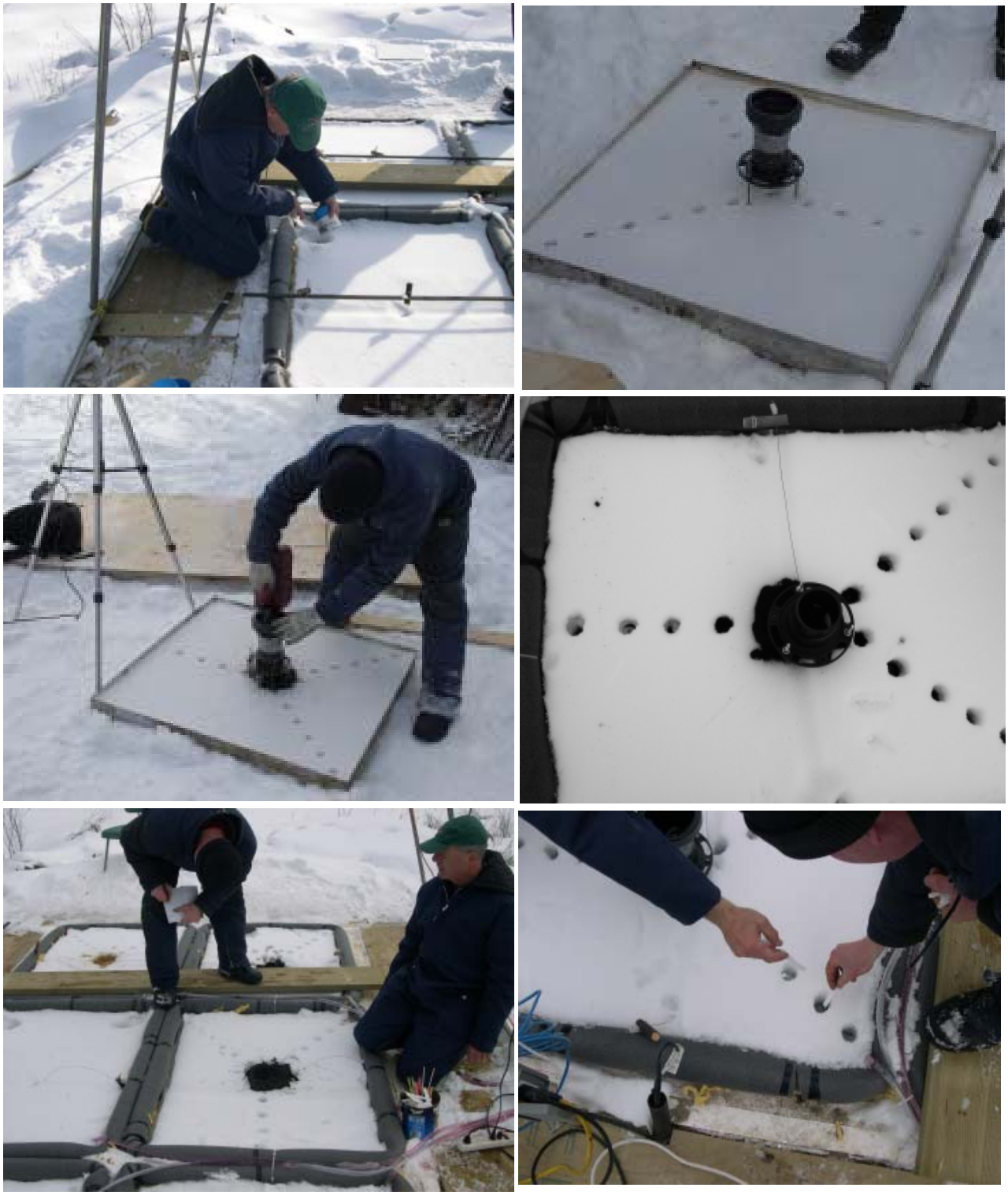

Figure 46. Spreading in Snow Experimental Methods

7.6 Spreading on Snow Results

The results of the spreading tests on ice are presented here graphically. All the data may be found in Appendix D.

Equilibrium Thickness Measurements

One-dimensional Tests. The equilibrium thickness measured at given radii in each snow plot is given in Figures 47 and 48. No Slick thickness measurements were made in the tests in 2007.

Spreading Measurements

One-dimensional Tests. The slick spreading measured in the troughs is given in Figures 49 and 50. Note that the time scale on the x-axis is different for each graph.

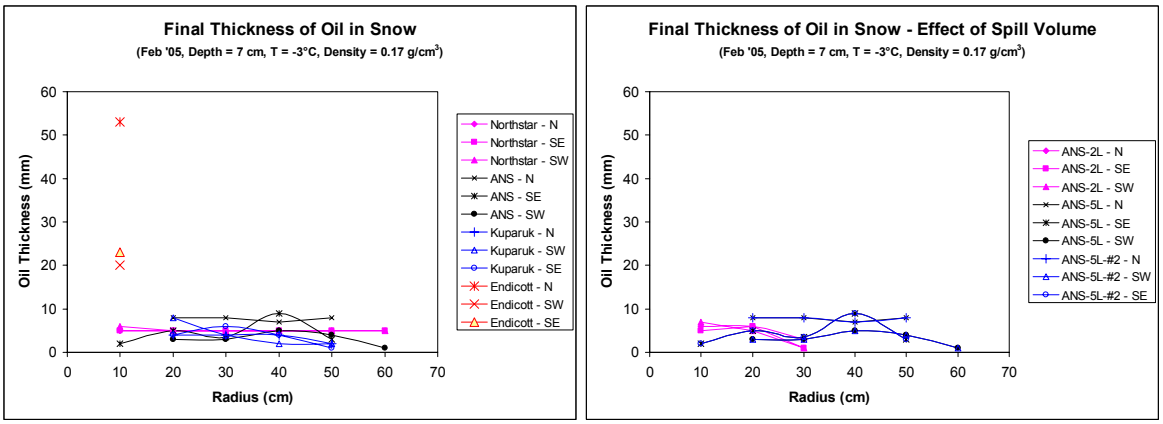

Figure 47. Final Thickness of Oil in Snow in February 2005 Tests

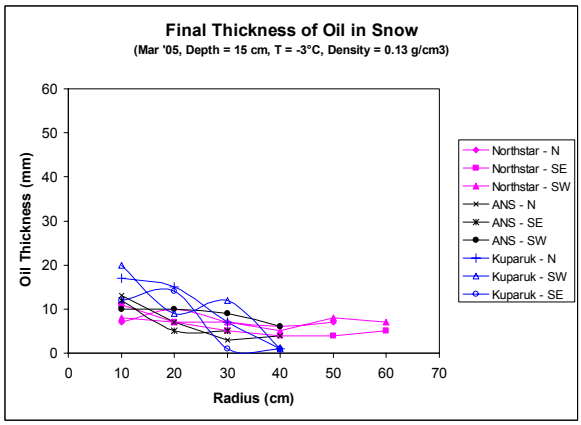

Figure 48. Final Thickness of Oil in Snow in March 2005 Tests

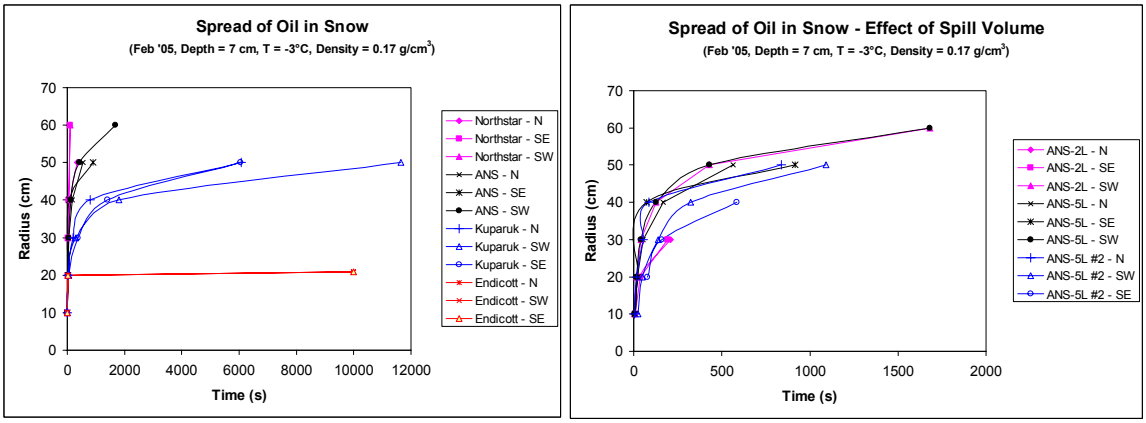

Figure 49. Spreading of Oil in Snow in February 2005 Tests

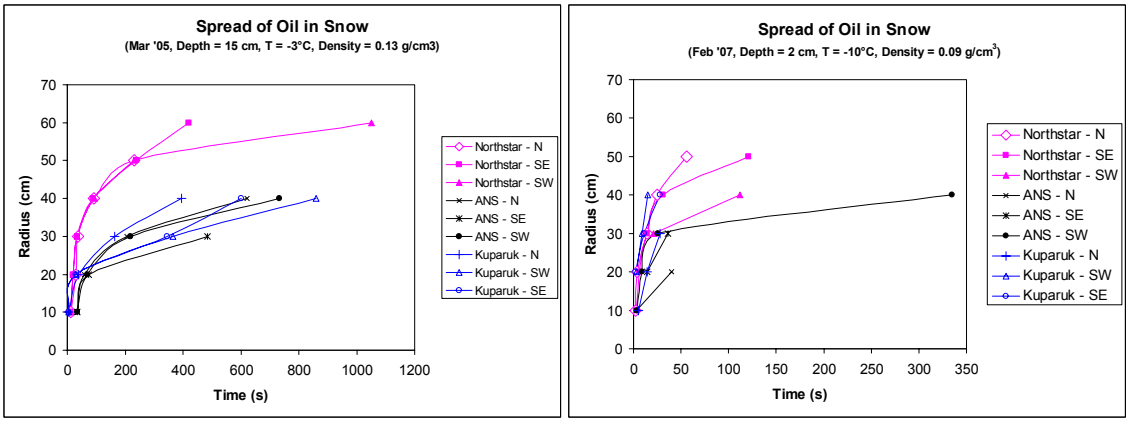

Figure 50. Spreading of Oil in Snow in March 2005 and February 2007 Tests

7.7 Spreading on Snow Discussion and Algorithm Selection

SL Ross and DF Dickins (1988) reviewed all the work on oil spreading in snow up to that point in time (primarily Glaeser and Vance 1971, McMinn 1972, Chen *et al.* 1974, NORCOR 1975, Mackay *et al.* 1975 and Kawamura *et al.* 1986) and proposed, and verified with mid-scale experiments and other's historical data, the following equation for 2-D horizontal spreading of oil in snow from an instantaneous release:

$$r = \left(\frac{2K\rho_o g V}{\pi E^2 \mu} \right)^{1/4} t^{1/4} \qquad \textbf{(18)}$$

Where: $K \equiv$ specific permeability of snow [cm^2]
$= 7.7 \times 10^{-2} d_o^2 e^{(-7.8\rho_s/\rho_i)}$
$d_o \equiv$ mean snow grain size [cm]
$E \equiv$ porosity (void fraction) of snow
$= (1-\rho_s/\rho_i)$
$\rho_s \equiv$ snow density [g/cm^3]
$\rho_i \equiv$ ice density [g/cm^3]

Figures 51 through 53 show the data for each of the three experiments plotted against the prediction of Equation 18. The data fit the prediction quite well, with the following exceptions:

- In the February 2005 experiments the Endicott oil, with a pour point of 12°C, spread out on top of the snow for a short distance, then gelled into a thick, semi solid (Figure 47).
- In the February 2007 experiments at –10°C, the Kuparuk oil also spread rapidly over the surface of the thin snow layer and stopped suddenly.
- In many of the experiments the initial data has a different slope, since these data were taken while the oil was still pouring from the container, and fit a different model (SL Ross and DF Dickins 1988) for spreading in snow from a continuous release.

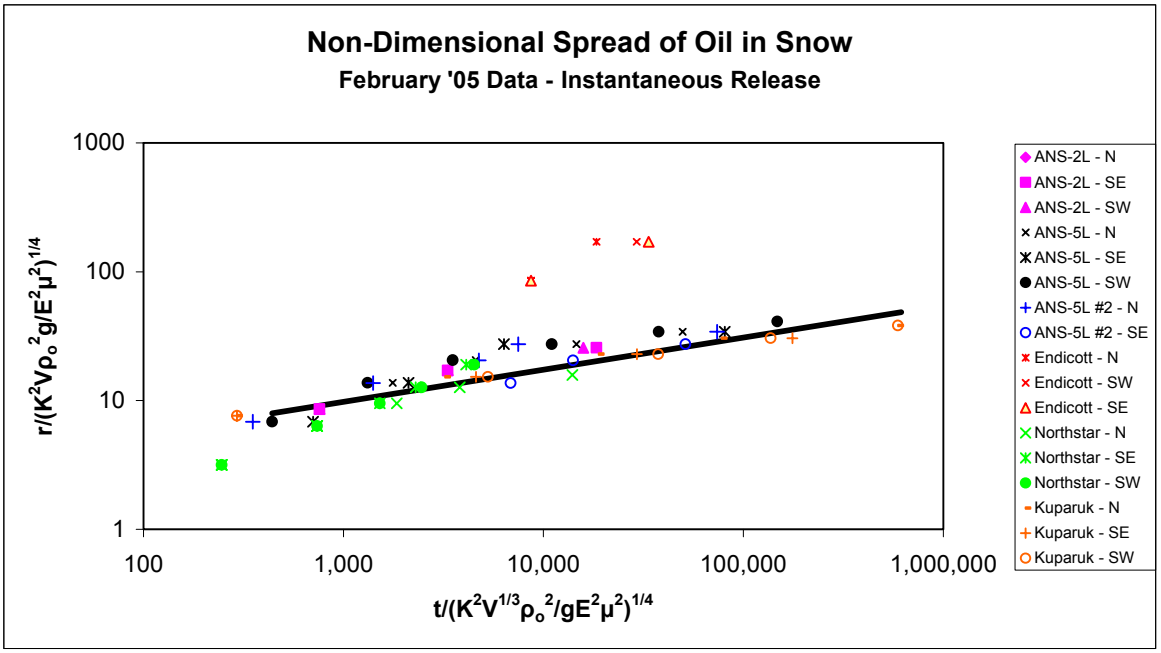

Figure 51. Non-dimensional Spreading in Snow Data From February 2005 Experiments

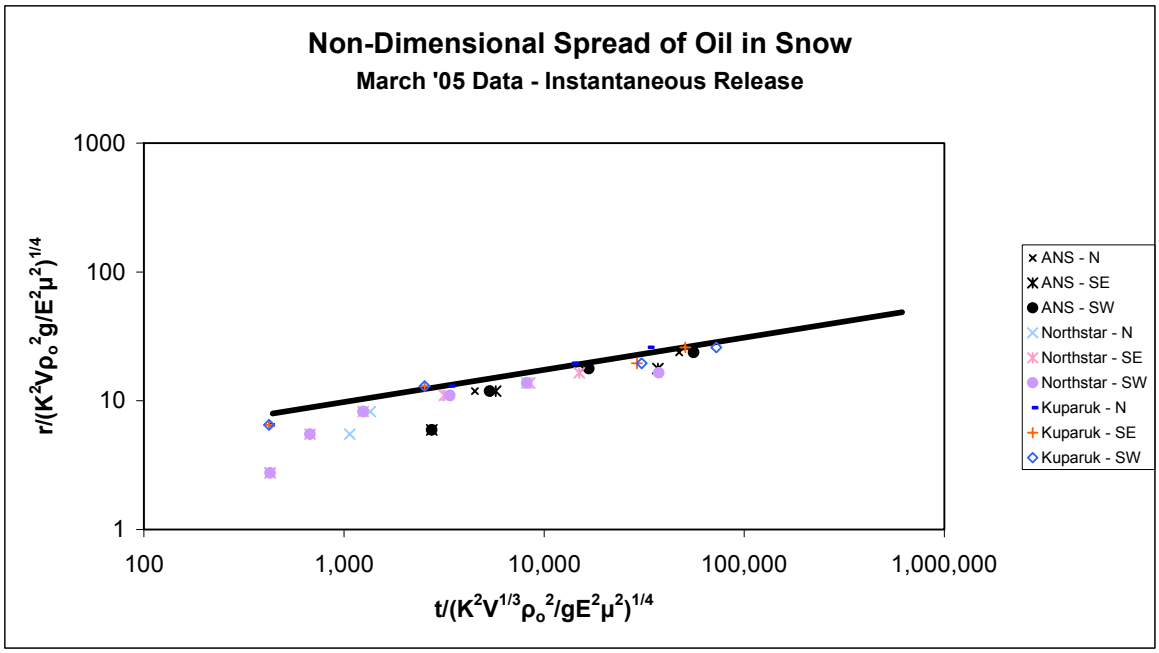

Figure 52. Non-dimensional Spreading in Snow Data From March 2005 Experiments

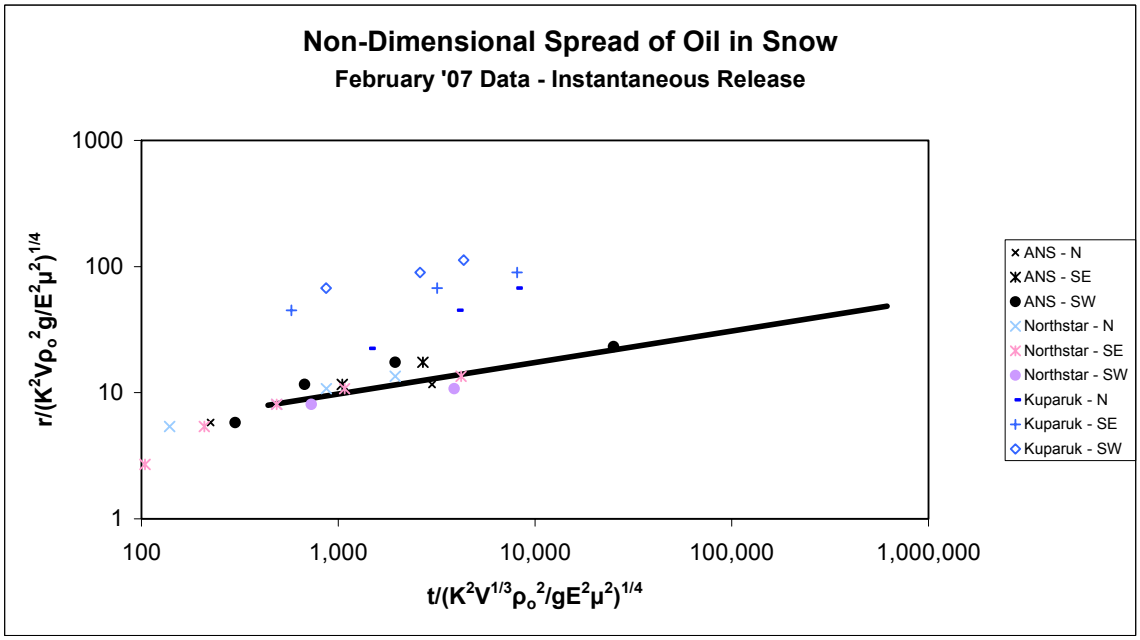

Figure 53. Non-dimensional Spreading in Snow Data from February 2007 Experiments

8. MOVEMENT OF OIL UNDER ICE BY CURRENTS

These experiments were undertaken to quantify the movement of crude oil spilled under sea ice with particular attention paid to the effect of oil properties and under-ice roughness on the minimum water velocities required to start moving small oil droplets and blobs under ice (i.e., the "stripping" velocity). The focus of the experiments was on small oil forms, as might be deposited from a sub sea blowout or pipeline leak, as opposed to larger pools of oil. There was a need identified to explore salinity as an independent variable in the spreading and advection of crude oil under ice, especially as vast areas off the Alaskan North Slope are characterized by brackish water (10 to 15‰) which in turn leads to sea ice with significantly lower salinity. The goal was to perform parametric experiments in order to explore potential salinity effects involving changes to the composition of the small-scale, soft, bottom roughness associated with the porous skeletal layer at the sea ice water interface. (This bottom roughness is in the size range of mm, and is not present to the same degree in fresh water ice.) The skeletal (SK) layer as depicted in Figure 54, can absorb a substantial amount of oil, and may lead to an increased threshold velocity to initiate movement (effectively increasing the static break-away friction) as well as requiring increased current speeds to maintain downstream oil movement.

8.1 State of the Art

There have been a large number of laboratory studies of oil spreading and movement under ice – this review focuses on those experiments that involved measuring the stripping velocity, or initial movement from rest, of oil in an ice flume or in the field. Moir and Lau (1975) report a series of tests using Plexiglas ice "keels" in a flume to determine failure velocities for slicks beneath an ice surrogate (expanded foam insulation sheets covered with vinyl). Chen *et al*. (1976) and Tsang and Chen (1978) report on a series of experiments to measure the velocity of oil under river ice, and possible deflection techniques. Uzner *et al.* (1978) report a series of flume experiments to measure the stripping velocity and advection of oil slicks. This is considered the seminal study on the effects of under-ice currents on oil movement. Smooth, freshwater ice was used in the flume, along with crude oil and No. 2 fuel oil. Cox and Schultz (1980) and (1981) report on experiments in the same flume to assess the advection of oil under ice in the presence of large, under-ice roughness features. Cammaert (1980) describes a series of tests to determine the stripping velocity of oil spilled with natural gas under sea ice as a function of under-ice undulation amplitude. Puskas *et al.* (1987) and Puskas and McBean (1986) report a series of experiments in a flume with fresh and saltwater ice conducted to determine the drag coefficient of oil slicks under ice and the effects of oil and ice parameters. Three crude oils were tested.

The influence of ice salinity on under-ice oil spreading (stripping velocity, roughness effects, etc.) has not been studied in any systematic manner. One of the key references used to predict the threshold current velocities needed to initiate and sustain movement of oil under sea ice (Uzner *et al.* 1979) was based on the use of freshwater ice sheets to perform the experiments (with different degrees of superimposed artificial roughness). Malcolm and Cammaert (1981) used a saline ice cover (salinity not specified) but focused entirely on the effect of gas entrapped in thin ice areas on the oil spreading behavior. Puskas *et al.* (1987) and Puskas and McBean (1986) report a separate series of experiments in a flume with fresh and saltwater ice carried out to determine the drag coefficient of oil slicks under ice and the effects of oil parameters. Hollebone *et al.* (2000) plotted the two sets of test data. The comparison indicates a significantly lower

velocity for slicks beneath ice grown from 30‰ salt water than under fresh water ice at a given current. No experiments were conducted with ice grown from brackish water and no data on stripping velocity is presented.

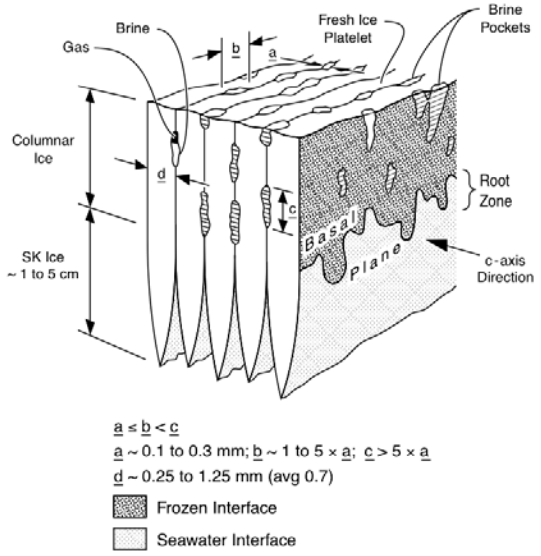

Figure 54. Model of the Sea Ice Crystal Structure, Showing the Transition From Columnar Ice to the Skeletal (SK) Layer at the Bottom of an Ice Sheet

8.2 Methods

The experiments were carried out in the wind/wave tank in the SL Ross lab beneath ice sheets grown to simulate real under-ice surfaces, which feature gentle undulations and a soft crystalline underside (Figure 55 and 56). A series of parametric studies was carried out, varying oil type, water salinity, under-ice roughness, and current speed.

The first step in readying the tank for the tests was to install a false bottom in order to generate currents under the ice sheet. This was accomplished by constructing a rectangular tunnel out of plywood that was placed in the bottom of the middle 5 m of the tank (the tunnel only extended under the middle of the tank to allow the water to turn and flow in the opposite direction at each end). The tunnel was 38 cm high and just narrower than the tank width (1.1 m). A 5-speed electric boat motor was placed at one end of the tunnel, with its propeller pushing water into the one end of the tunnel. This caused the water between the bottom of the ice sheet and the top of the tunnel to flow towards the electric motor. A Sontek ADV-11000 10-MHz acoustic Doppler velicometer was used to measure the under-ice currents. It was inserted into a hole in the ice sheet just downstream of the test area with the sensor at a depth of 13 cm below the ice pointing directly upstream. A laptop computer was used to record and process the water velocity data.

A series of measurements were taken under a typical, smooth ice sheet before the experiments in order to document the current regime at steady state for each motor speed setting. The results are given in Figure 57. The bottom right-hand graph compares the centerline water velocities

measured at each motor setting. Unfortunately, it was not possible to position the ADV closer than about 5 cm from the ice sheet, tank sides or the top of the tunnel.

For most of the experiments, the under-ice oil began to move just after the motor speed was increased. Therefore, it was necessary at the beginning of each series of experiments with a particular ice sheet and salinity, to record the water velocity during the transient period of acceleration after a motor speed change. The time that a particular oil form began to move after the motor speed was increased was determined from the video, and thus by comparing that time with the transient velocity record for that speed change, it was possible to estimate the water velocity at the time the oil began to move.

Finally, a series of "telltales" were frozen into holes drilled 10 cm apart in the ice sheet so that the movement of oil beneath the sheet could be timed, a ¼-inch thick aluminum plate holding a plastic tube and a disposable plastic syringe to inject oil under the ice was installed and an oil recovery slot was cut in the ice sheet just downstream of the ADV current meter.

Three types of ice sheets (Figure 56) were created for each salinity of water tested (0, 15 and 30‰):

1. An undisturbed sheet with a level underside;
2. An undulating sheet, created by placing slabs of rigid Styrofoam insulation across the width of the tank spaced about 1.2 m apart to simulate the effects of snow drifts on the underside of natural; ice sheets; and,
3. A rubble sheet, created by cutting a fully-grown ice sheet into rectangles ranging in dimension from 10 cm to 25 cm and randomly rotating some of the blocks manually to create an artificial rubble field extending below the bottom of the ice sheet.

For a typical set of four experiments (varying oil type), the first step was to record the transient water velocity changes for each increase in motor speed setting. This involved collecting a 60-second "burst" of data with the ADV starting just before the speed change. Then the motor was stopped and the tank allowed to stop circulating. Next, about 50 mL of the fresh candidate oil was injected under the ice sheet. Typically the oil would break up into a mix of small, spherical droplets, medium-sized spherical and oblong drops and larger blobs, all floating against the under-ice surface. For the tests involving undulating and rubble ice sheets the oil forms would invariably move under their own buoyancy to the highest point of the ice near the injection tube. Then the video and ADV laptop readout would be started and the motor turned on to speed 1. Once the water circulation was steady, as determined by the laptop velocity readings and no oil movement was detected, the motor setting was increased. This was repeated until one or more oil forms began to move. Once in motion, the velocity of the oil was measured by timing its movement past the telltales. Once the highest motor speed had been reached and the oil had been flushed into the recovery slot, it was removed using strips of sorbent, then the motor was shut off and the tank allowed to calm before repeating the process with the next oil.

Figure 55. Indoor Tank Setup for Oil Movement Under Ice Experiments

Figure 56. Various Ice Sheets Used in Experiments on Oil Movement Under Ice

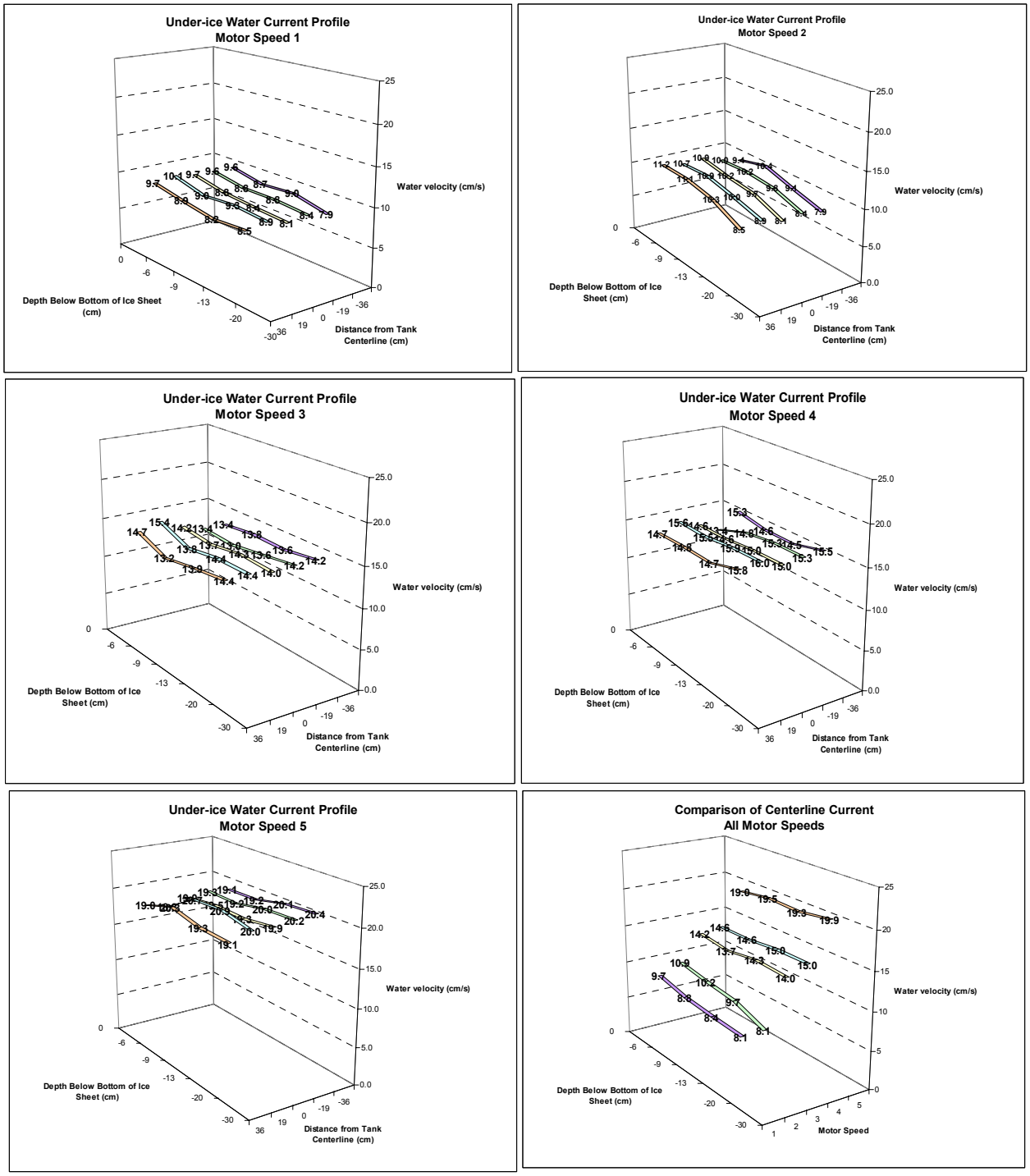

Figure 57. Under-ice Water Velocity Profiles For Five Motor Speeds

8.3 Results

Figures 58 and 59 summarize the results of the experiments. Full data may be found in Appendix E. Each graph gives the "stripping" velocity (the data point on the x-axis) and the speed at which the specific oil form (denoted by crude type and form size) moved under the ice, once in motion.

The dashed line is the least-squares correlation of all the measured oil speeds with the measured water velocity.

The graphs are arranged such that the first row is the results of all the experiments under smooth ice, with the freshwater ice on the left, the 15‰, or brackish water ice in the middle, and the 35‰ seawater tests on the right. The second row is the results of the tests under undulating ice sheets and the third row gives the results for the rubble ice sheets. Note that the scale of the y-axis is different for each row: 0 to 5 cm/s for the smooth ice tests, 0 to 10 cm/s for the undulating ice experiments and 0 to 20 cm/s for the rubble experiments.

8.4 Discussion and Algorithm Selection

Several trends are apparent:

- The "stripping' velocity was in the 4 to 6 cm/s range under the smooth, freshwater ice (as reported by Uzuner *et al.* 1979 and Cox and Schultz 1980). There was no significant effect of oil properties on the "stripping" velocity under freshwater ice for the small oil forms tested. The speed at which the oil forms moved under the freshwater ice, once started, was approximately 10 to 20% of the measured current speed, with no apparent correlation between oil form size or crude type with speed. The exception was the medium and larger oil Endicott crude forms that moved at only 2 to 4% of the current.

As the freshwater under-ice roughness increased (moving down the column of graphs) the "stripping" velocity increased dramatically. Beneath undulating freshwater ice the "stripping" velocity ranged from 5 to 20 cm/s and the crude properties appeared to have an effect. The Northstar crude began to move at currents of 4 to 9 cm/s, the ANS and Kuparuk started to move in currents of 10 to 14 cm/s and the Endicott began to move at currents of 17 to 20 cm/s. The speed at which the oil forms moved, once started, ranged from 10 to 30% of the current speed, with the least-squares correlation giving a 20% factor. Under the refrozen rubble ice the "stripping" velocity increased again, with measured values ranging from 16 to 30 cm/s. Once moving the oil forms moved at about 6 cm/s, with no apparent effect of oil type or current speed.
As the salinity of smooth ice increased (moving right along the row of graphs), the "stripping" velocity also increased. Under brackish ice, the large forms of ANS and Kuparuk began to move at a current of about 5 cm/s; however, the other oil forms did not begin to move until much higher velocities, in the range of 9 to 19 cm/s. Beneath 35‰ ice the situation was similar; there did not seem to be a significant effect of increasing the salinity from brackish to seawater on the "stripping" velocity. Not surprisingly, there was no significant observable effect of salinity on the speed of the oil forms after they had begun moving.

There appears to be a similar effect of increasing salinity causing increasing "stripping" velocity beneath the undulating ice sheets. From freshwater ice to brackish water ice there appears to be a slight increase in "stripping" velocity. Although there appears to be a large increase from brackish ice to 35‰ ice, this may be an artifact of the data processing. Inadvertently, no transient water velocity measurements (immediately after a motor speed change) were recorded under the 35‰ ice sheet and the current speeds were estimated from the 15‰ transient current data set. As such, the data for the 35‰ undulating ice must be treated as less reliable.

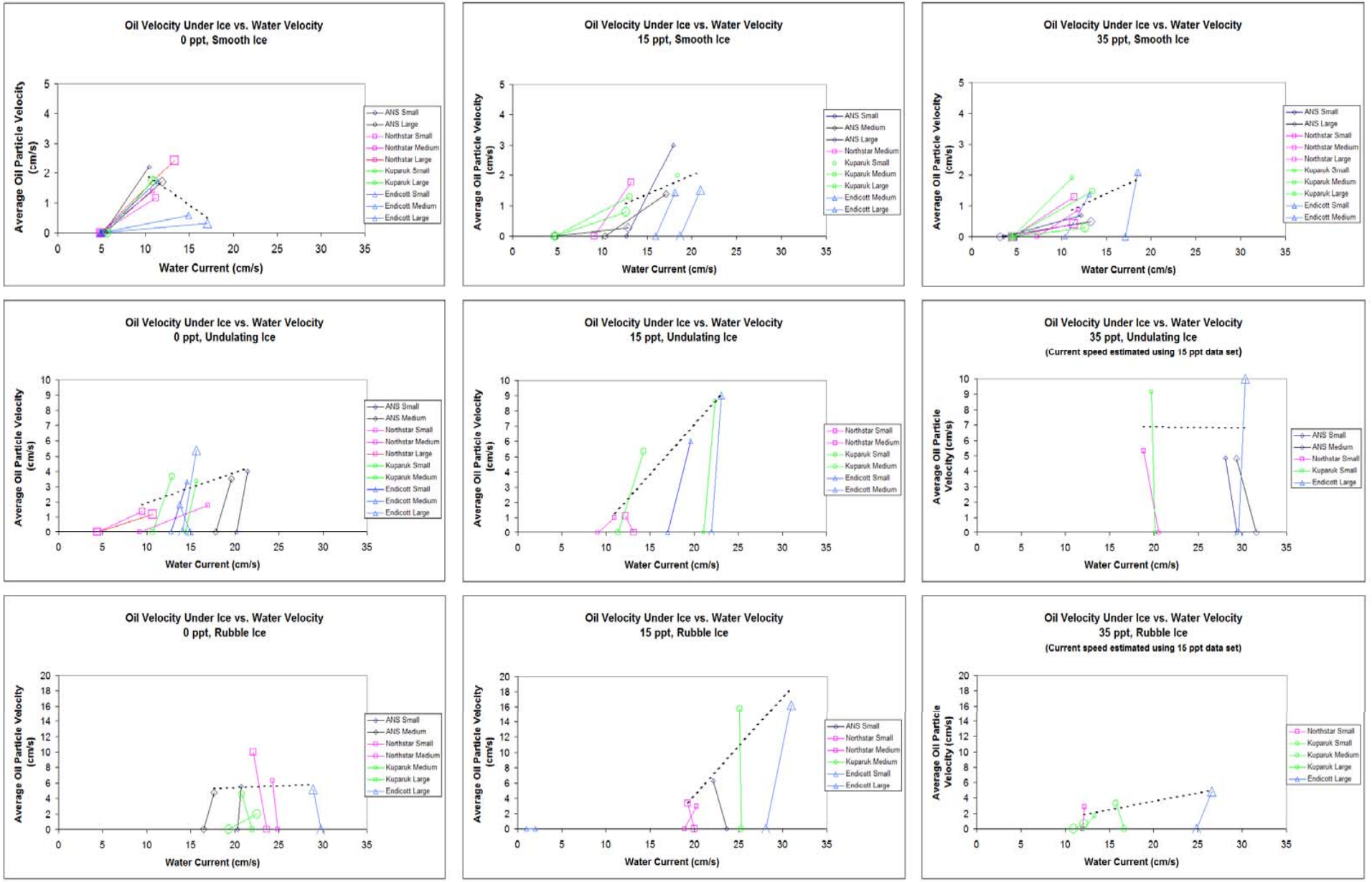

Figure 58. Results of Oil Under Ice Movement Experiments

Not surprisingly, the roughness of the refrozen rubble sheets masks any effects of ice salinity on "stripping" velocity. Again, no transient water velocity measurements were recorded under the 35‰ ice sheet and the current speeds were estimated from the 15‰ transient current data set rendering the 35‰ data set less reliable.

Cox and Schultz (1980) present the following empirical dimensional formula, based on flume tests, relating "stripping" velocity beneath smooth ice to oil viscosity:

$$U_{th} = \frac{305.79}{88.68 - \mu_o} \qquad \textbf{(19)}$$

Where: $U_{th} \equiv$ threshold ("stripping") velocity (cm/s)

$\mu_o \equiv$ oil viscosity in Poise

Table 17 shows the predictions of Equation 19 for the test oils in this study. The predictions are in reasonable agreement with the experimental data for the smooth, freshwater ice sheet.

Table 17. "Stripping" Velocity Predicted by Equation 19

	Crude Oil			
	ANS	Endicott	Northstar	Kuparuk
Oil viscosity at 0°C (Poise)	0.176	19.84	0.036	2.11
Threshold Velocity (cm/s)	3.5	4.4	3.4	3.5

Cox and Schultz (1980) also showed that mm-sized under-ice roughness caused an increase in the "stripping" velocity from 4 to 12 cm/s and cm-sized roughness further increased the "stripping" velocity to 22 cm/s. Although their experiments only measured slick velocities when the oil was in motion, Puskas and McBean (1986) noted a significant increase in the drag on a slick moving under saline ice, compared to freshwater ice. Since the characterization of under ice roughness is extremely difficult in the field, the following simple dimensional algorithm, based on Equation 19, is suggested:

$$U_{th} = C_i \left(\frac{305.79}{88.68 - \mu_o} \right) \qquad \textbf{(20)}$$

Where: $C_i \equiv$ under-ice roughness factor

= 2 for saline ice

= 3 for undulations under freshwater ice

= 4 for undulations under saline ice

= 6 for any refrozen rubble ice

Table 18 gives the predictions of Equation 20 for the various oils and ice sheets in the experiments. Although far from perfect, Equation 20 does roughly capture the trends in the data,

as demonstrated in Figure 59 (after Cox and Schultz 1980). Note that the data for the experiments where the transient currents were inadvertently not measured have not been included in Figure 59.

Table 18. Predictions of Equation 20 for Experimental Conditions

	Crude Oil			
	ANS	Endicott	Northstar	Kuparuk
Threshold Velocity under smooth freshwater ice (cm/s)	3.5	4.4	3.4	3.5
Effect of smooth saline ice (2x)	7	9	7	7
Effect of undualtions on freshwater ice (3x)	10	13	10	11
Effect of undulations on saline ice (4x)	14	18	14	14
Effect of rubble (6x)	21	27	21	21

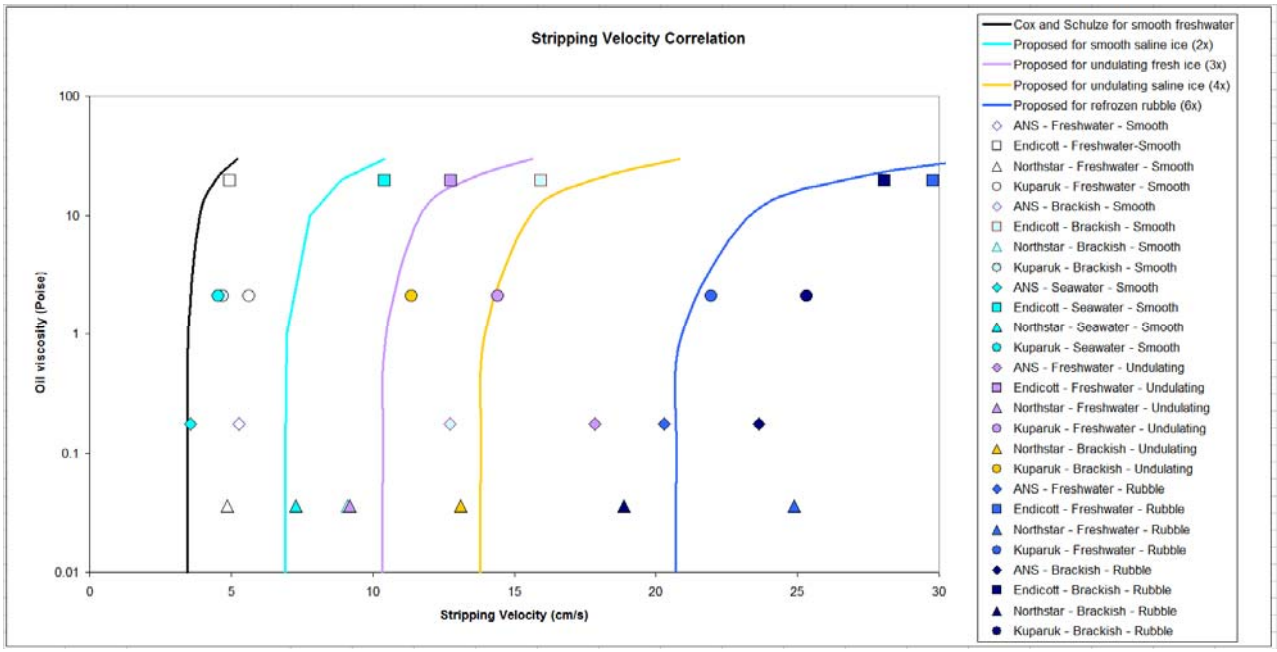

Figure 59. Comparison of Equation 20 Predictions with Experimental Data (after Cox and Schultz 1986)

9.0 EVAPORATION ON ICE, IN SNOW AND AMONG DRIFT ICE

The purpose of this series of experiments was to quantify evaporation rates from oil spilled on solid ice with and without snow, and in broken ice as a function of oil properties and ice characteristics. First, experiments were carried out at temperatures as low as –30 °C to determine the effects of very low temperatures on crude oil evaporation on solid ice. This was accomplished by placing test slicks of different thicknesses of the four crudes on the ice in the refrigerated wind/wave tank. Next, a series of experiments was carried out to quantify the effects of snow cover on evaporative flux. It is impossible to simulate the characteristics of snow in the laboratory, so these experiments were completed outdoors. Samples were taken over time from the spreading experiment plots described in the Section 7.5. The results were correlated with snow characteristics and on-site weather measurements to provide data on evaporation rates for the four crude oils spilled under snow of various thickness and type. Finally, samples were taken during the series of tests on emulsification (see the next section) to measure the effects of ice cover (area coverage, distribution, etc.) on evaporation rates in drift ice conditions.

9.1 State of the Art

Evaporation on Ice at Low Temperatures

Glaeser and Vance (1971) present the results of a series of crude oil evaporation experiments on sea ice and melt ponds at average temperatures of 3.3°C near Barrow, AK. Chen (1972) and McMinn (1972) report on the evaporation of a series of releases of North Slope crude oil (some on snow-covered sea ice and some on bare lake ice) undertaken near Port Clarence in January 1972 during which the temperatures were in the –25° to –9°C range. Tebeau *et al.* (1982) present the results of a series of weathering experiments with Prudhoe Bay crude on ice conducted in Groton, CT during December and January 1980/81. At most times the temperatures were below freezing. Stiver and Mackay (1983) present the "Mackay evaporative exposure" model for estimating hydrocarbon evaporation rates. This approach has become a standard in oil spill modeling. SL Ross and DF Dickins (1987) report evaporation rates for crude oil released on ice at –10°C. SL Ross and DMER (1988) and Berger and Mackay (1994) discuss how to modify the classic Mackay evaporation algorithms to account for the development of internal resistances to mass transfer due to increasing viscosity and gelling of higher pour point slicks. Fingas (1995) presents the results of parametric tests with one crude oil evaporating at temperatures ranging from –20° to 40°C. SL Ross (2003) present the results of evaporating a Russian crude oil at temperatures ranging from –20° to 0°C.

Evaporation in Snow

McMinn (1972) reports on a series of releases of North Slope crude oil (some on snow-covered sea ice) undertaken near Port Clarence in January 1972. SL Ross and DF Dickins (1988) conducted mid-size experiments to measure oil evaporation in snow on ice. Bech and Sveum (1991) report on a series of five large experiments with 1 m^3 each of diesel or crude released onto or under snow on sea ice.

Evaporation in Drift Ice

Scott and Chatterjee (1975) report on a series of experiments to monitor oil behavior on water, including evaporation, in ice-forming conditions. Deslauriers *et al.* (1977) report on evaporation of No.2 heating oil spilled in broken ice in Buzzards Bay. Payne *et al.* (1988) report a series of extensively sampled test tank experiments conducted to quantify crude oil weathering on cold water, and in ice-forming conditions. Tebeau *et al.* (1982) present the results of a series of weathering experiments with Prudhoe Bay crude on ice conducted in Groton, CT during December and January 1980/81. SL Ross and DF Dickins (1987a) conducted three 1-m^3 experimental releases of crude oil in pack ice during which they measured oil evaporation over several hours. SL Ross and DF Dickins (1987b) report a series of experiments on oil evaporation from slicks on leads cut in a sheet of ice on an outdoor test tank. Wilson and Mackay (1987) report on a series of small-scale, cold-room crude oil evaporation experiments in freezing situations. Singsaas *et al.* (1994) report on evaporation measurements taken over several days from a 10-m^3 experimental crude oil spill in a marginal ice zone.

9.2 Evaporation on Ice Methods

The experiments were carried out on an ice sheet grown from 35‰ salt water in the wind/wave tank (Figure 60). The tank was maintained at nominal temperatures of –10°, -20° and –30°C (actual average temperatures recorded over the tests were –10.5°±3.1°, –18.4°±6.0° and -25.7°C±6.8°) by the chiller. Two types of on-ice evaporation experiments were conducted: plastic rings were frozen and sealed in the ice, then filled with crude oil to different depths (1, 5 and 10 mm) and pre-weighed glass Petri dishes were filled with two thicknesses of crude (1 and 10 mm) and placed on the ice. Periodically (after 4 hours, 24 hours, 2 days and 5 days), the cover would be removed from the wind/wave tank and samples taken from the plastic rings and the Petri dishes removed and weighed using a Denver Instrument Model TR-4102D digital scale. The samples from the plastic rings were sealed in 5-mL glass vials with screw caps and frozen at –25°C. The density of the samples at room temperature was measured later with an Anton Parr digital densitometer and select samples were sent to ESTD for GC-TPH and n-alkanes compositional, BTEX and PAH analyses. The sample density was compared to the density of the wind tunnel weathered samples (Section 5.5) to estimate evaporative loss. Pre-weighed Petri dishes containing toluene were also placed in the tank and weighed periodically to determine of the airside mass transfer coefficient needed to calibrate the data for use in the evaporative exposure algorithms. Figure 61 gives the air velocity profile measured in the tank.

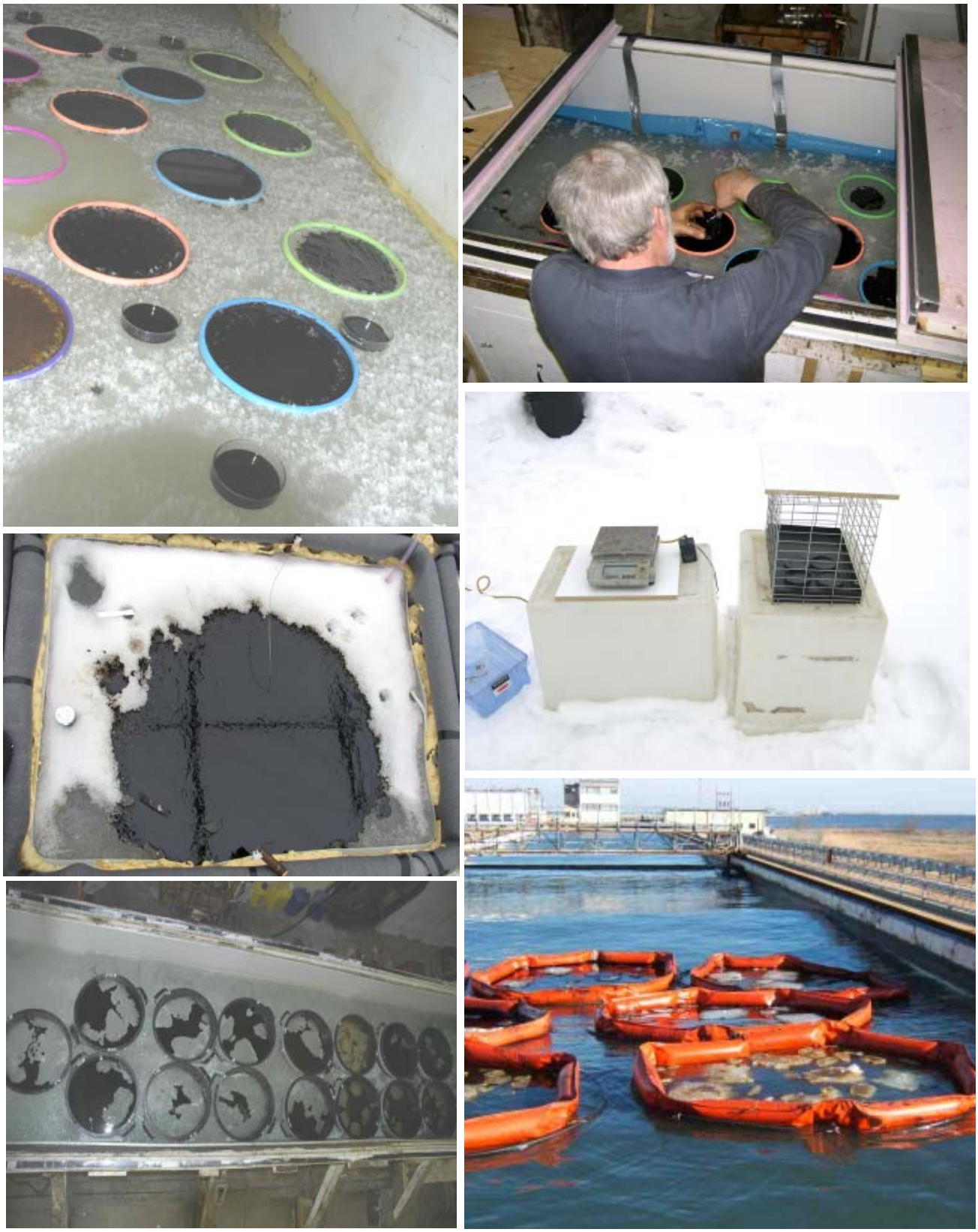

Figure 60. Various Evaporation Experiments

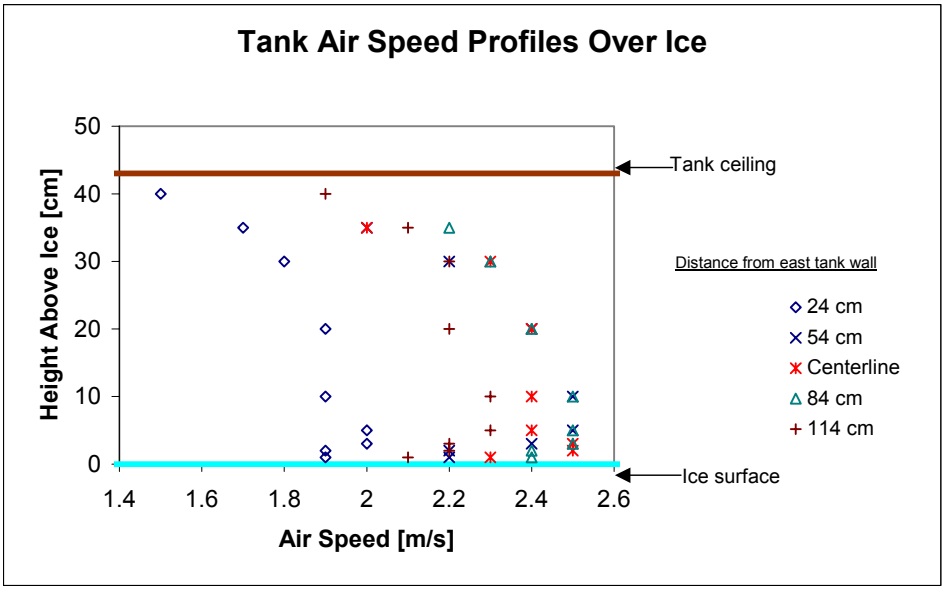

Figure 61. Air Velocity Profiles Over Ice in Tank for Evaporation Experiments on Ice

9.3 Evaporation on Ice Results

The percent evaporation data for the evaporation from the Petri dishes is presented in Figure 62. All the data may be found in Appendix F. Only the Petri dish data is presented for now, as it is the most reliable, depending only on a direct measurement of the weight loss of the sample. On the graph, the different crudes are grouped by symbol (◊ for ANS, □ for Endicott, ○ for Kuparuk and △ for Northstar); the 10-mm slick data is represented by a filled symbol and the 1-mm by an open symbol; and, the three nominal temperatures are represented by different colors (black for –10°, red for –20° and green for –30°C). Other than a general increase in percent evaporated with time, there are no obvious trends in the data.

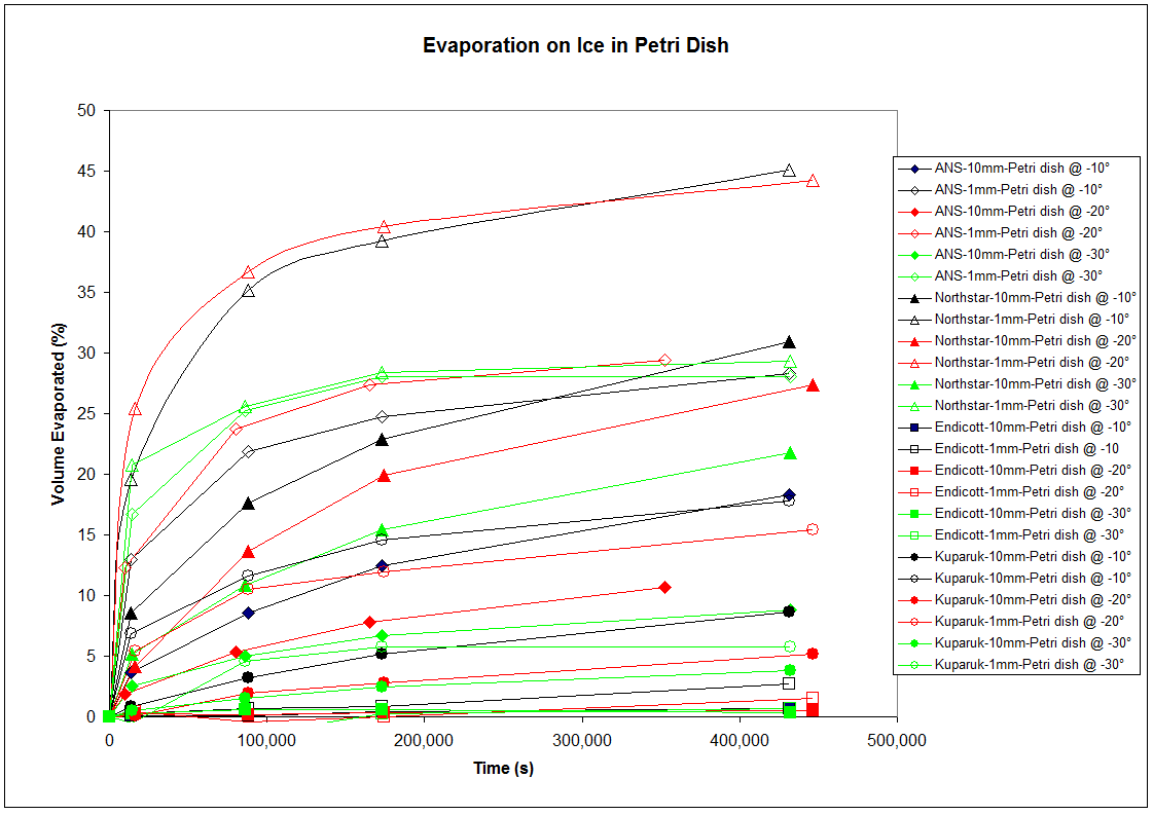

Figure 62. Percent Evaporated Data from On-ice Studies vs. Exposure Time

9.4 Evaporation on Ice Discussion and Algorithm Selection

Stiver and Mackay (1983) presented the classic treatment of oil evaporation on water. They proposed the following equation, with oil-based constants that are determined by small-scale wind tunnel evaporation experiments and a modified ASTM distillation (modified in that the liquid temperature is recorded as opposed to the vapor):

$$F_v = \ln\left[1 + \frac{BT_G}{T}\theta\exp\left(A - \frac{BT_0}{T}\right)\right]\frac{T}{BT_G} \qquad \textbf{(21)}$$

Where: $F_v \equiv$ volume fraction of the oil evaporated

T_0, $T_G \equiv$ the intercept and slope of the modified ASTM distillation [°K]

$T \equiv$ environmental ambient temperature [°K]

B, $A \equiv$ dimensionless, oil-specific constants equal to the least-squares slope and intercept of a plot of the natural logarithm of the Henry's Law constant (H = Pv/RT, which is numerically equal to the slope of the tangent to the curve of a plot of F_v vs. □ at the given point) vs. T_b/T

$T_b \equiv$ boiling point of weathered crude oil at atmospheric pressure [°K]

P ≡ vapor pressure of the weathered crude oil [Pa]

v ≡ liquid's molar volume [m^3/mol]

R ≡ gas constant 8.314 [Pa m^3/mol °K]
□ ≡ dimensionless evaporative exposure
= $kAt/V_0 = kt/x$
k ≡ mass transfer coefficient [m/s]
A ≡ area of slick [m^2]
t ≡ elapsed time since oil release [s]
V_0 ≡ initial volume of oil released [m^3]
x ≡ slick thickness [m]

Figure 63 shows the evaporation data from the Petri dish tests plotted against □ calculated using the value of the airside mass transfer coefficient (k) measured by evaporating pure toluene in the tank at the test temperatures. Using □ as the x-axis removes the effect of slick thickness and generally groups the oils by type. Figure 64 shows the Petri dish data plotted against the predicted evaporation from Equation 21, using the value of the airside mass transfer coefficient (k) measured by evaporating pure toluene in the tank at the test temperatures. The solid line shows where the measured evaporation is equal to the prediction. It is clear that, although the data generally fall on a straight line, Equation 21 greatly over predicts the actual evaporation.

Several researchers have demonstrated that a simple airside mass transfer coefficient may not be suitable for use in some situations, particularly in the case of viscous and waxy oils or emulsions at colder temperatures (SL Ross and DMER 1988, SL Ross 1994 and Berger and Mackay 1994). Berger and Mackay (1994) suggest that an overall mass transfer coefficient be used to account for resistances to molecular movement in the liquid phase. Using a "resistances in series" form:

$$\frac{1}{k_T} = \frac{1}{k_a} + \frac{K_{oa}}{k_o} \qquad \textbf{(22)}$$

Where: k_T ≡ overall mass transfer coefficient [m/s]
k_a ≡ air side mass transfer coefficient [m/s]
k_o ≡ liquid phase mass transfer coefficient [m/s]
K_{oa} ≡ air-oil partition coefficient

For liquid oils that are well mixed, K_{oa}/k_o is small compared to $1/k_a$ and only the airside coefficient need be considered. This gives the classic form of the equation given by Stiver and Mackay (1983). When the resistance to mass transfer in the liquid becomes significant and the term K_{oa}/k_o approaches, and then exceeds the value of $1/k_a$ the evaporation rate will be controlled by the rate at which molecules can reach the liquid/air interface. Figure 65 shows the Petri dish data plotted against the predictions of Equation 21 using a value of k_T =0.001 (since the value of k_a measured by toluene evaporation was on the order of 0.015 this means that the evaporation is being controlled by the liquid, or internal, mass transfer coefficient). The fit is much better than in Figure 64. Considerable effort was spent attempting to correlate a value for k_o with oil viscosity, as suggested by Berger and Mackay (1994) and with a "waxy crust" resistance as suggested by SL Ross and DMER (1988) but none of the attempts improved the overall fit of the data to Equation 21. Improvements to the fit could be made by slightly adjusting the value of k_T, but this was not felt to be justified, considering the likely accuracy of environmental data available at a spill site.

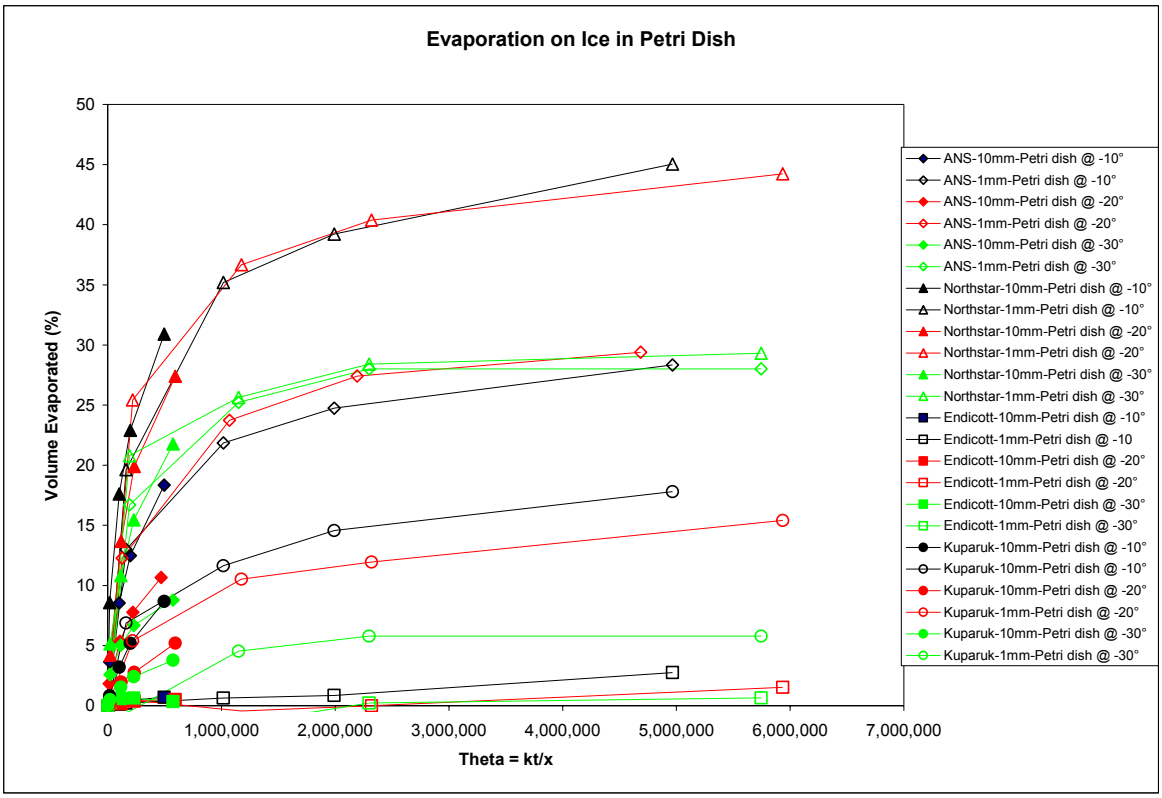

Figure 63. Petri Dish Evaporation Data Plotted Against Dimensionless Time

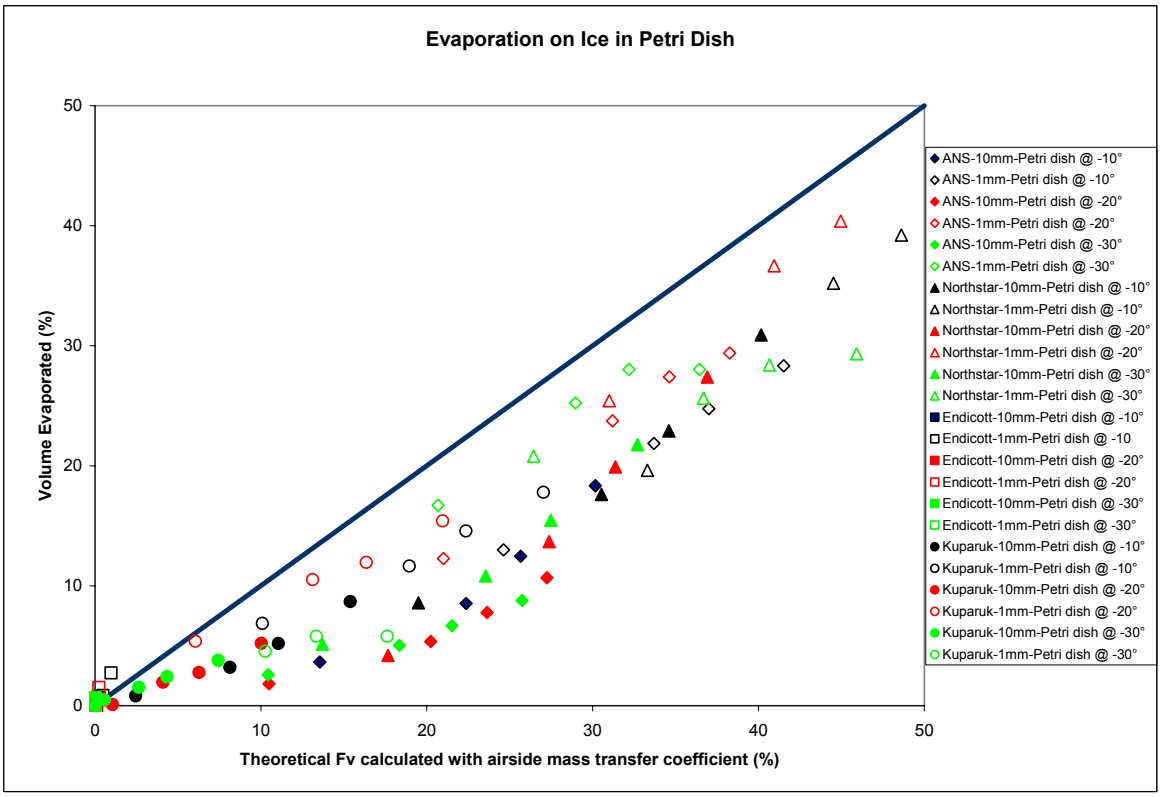

Figure 64. Petri Dish Evaporation Data vs. the Evaporation Predicted by Equation 21, using an Airside Mass Transfer Coefficient

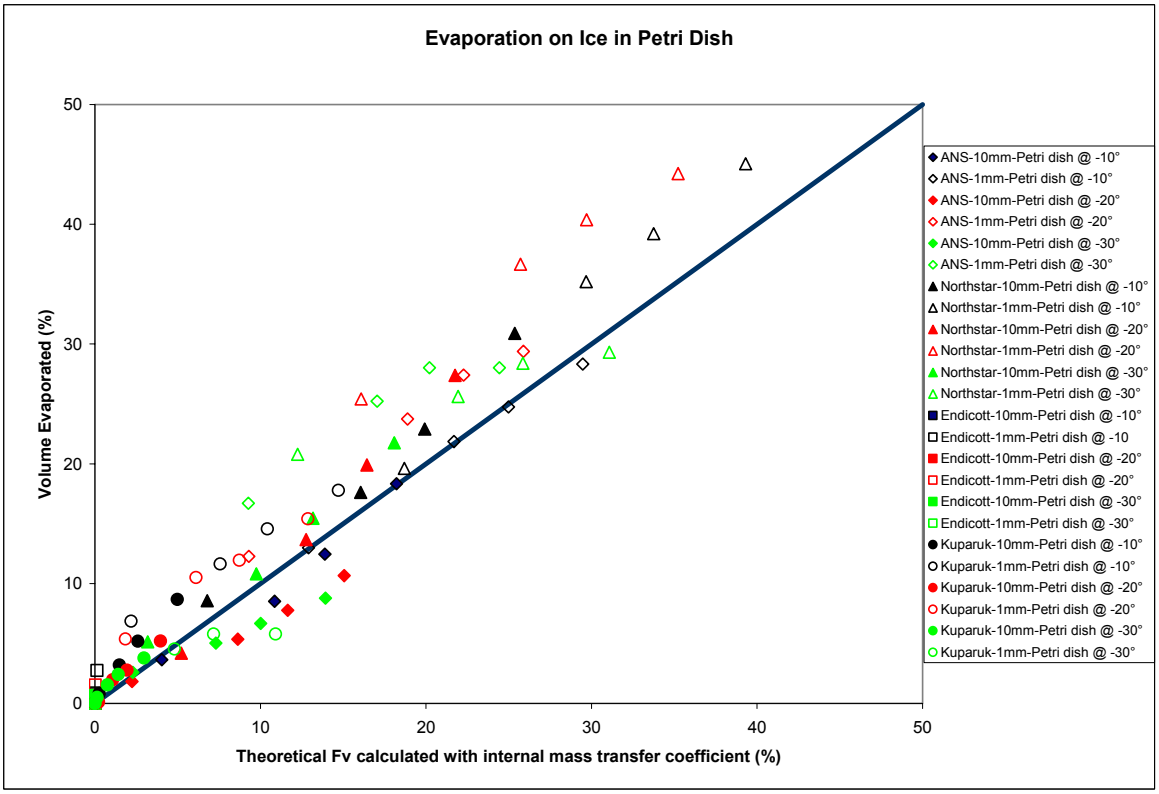

Figure 65. Petri Dish Evaporation Data vs. the Evaporation Predicted by Equation 21, using an Internal, Liquid-phase Mass Transfer Coefficient k_T = 0.001 m/s

Figure 66 shows the evaporation data from the slicks in rings on the ice sheet compared to Equation 21 with k_T =0.001. The equation appears to predict the general trends reasonably well, but the scatter in the data is much greater than in Figure 65. This is likely because the method used to measure evaporative loss for these samples (measuring their density at 15°C and correlating this with the change in density for a given crude with its evaporation measured in the wind tunnel - see Section 5) introduces additional errors in the determination of evaporative loss.

During the evaporation experiments, several aliquots of samples from the rings were subjected to chemical analysis at the ESTD laboratory. One of the series of analyses (see Section 5) involved the determination of individual n-alkanes and isoprenoids by GC-FID. Wang and Fingas (1994) developed a technique, called the Weathering Index that uses ratios of sums of smaller and larger n-alkanes to predict evaporative loss from samples of a crude that has been quantitatively weathered in the lab. The index is calculated by:

$$WI = \frac{(nC_8 + nC_{10} + nC_{12} + nC_{14})}{(nC_{22} + nC_{24} + nC_{26} + nC_{28})} \qquad \textbf{(23)}$$

Where: $WI \equiv$ weathering index
$nC_x \equiv$ the concentration of the n-alkane with x carbon atoms in the sample [mg/g]

Wang and Fingas (1994) also offer a simpler technique to determine the evaporation of a sample, employing the ratios of the concentration of one C_{20+} n-alkane in the sample, but this did not provide sufficient discrimination for some oils, particularly the Endicott crude.

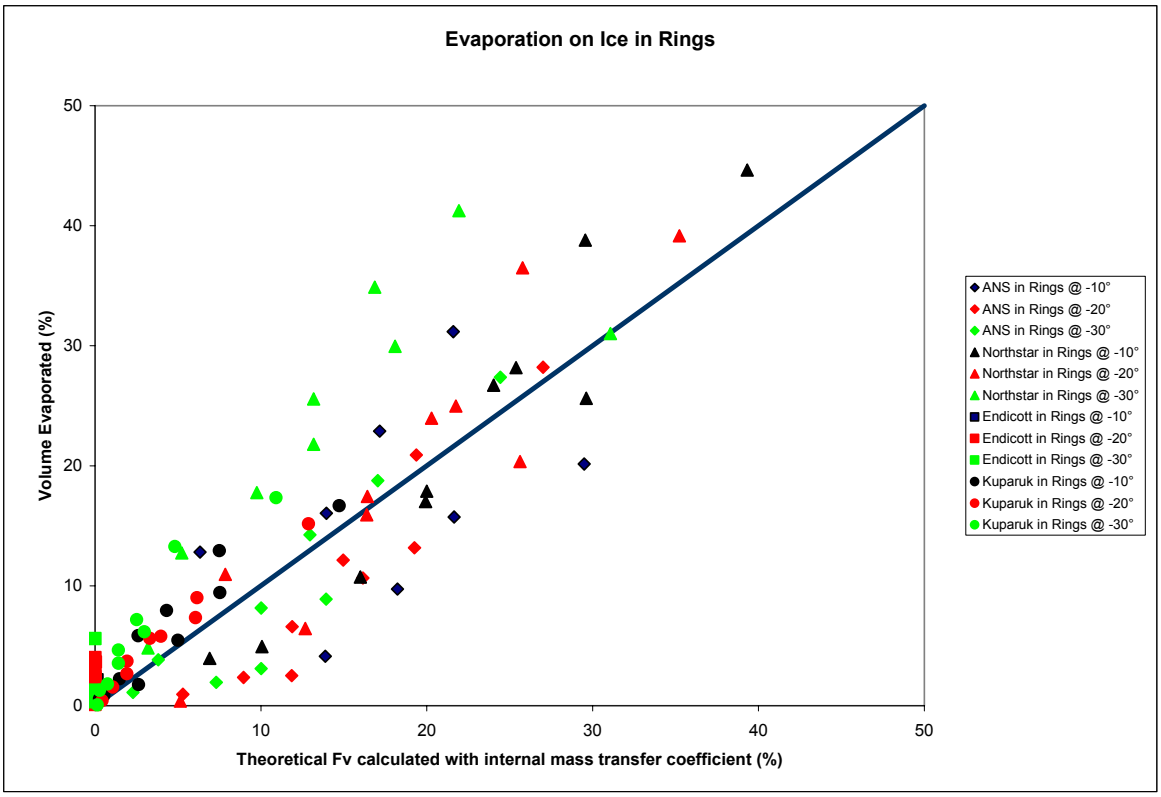

Figure 66. Ice Ring Evaporation Data vs. the Evaporation Predicted by Equation 21, using an Internal, Liquid-phase Mass Transfer Coefficient k_T = 0.001 m/s

Figure 67 shows the evaporative loss measured by the WI technique against the prediction of Equation 21 using an internal, liquid-phase mass transfer coefficient k_T = 0.001 m/s. The fit is quite good with the least squares fit to the data having a slope of 0.932, an intercept of 1.71 and an R^2 of 0.84.

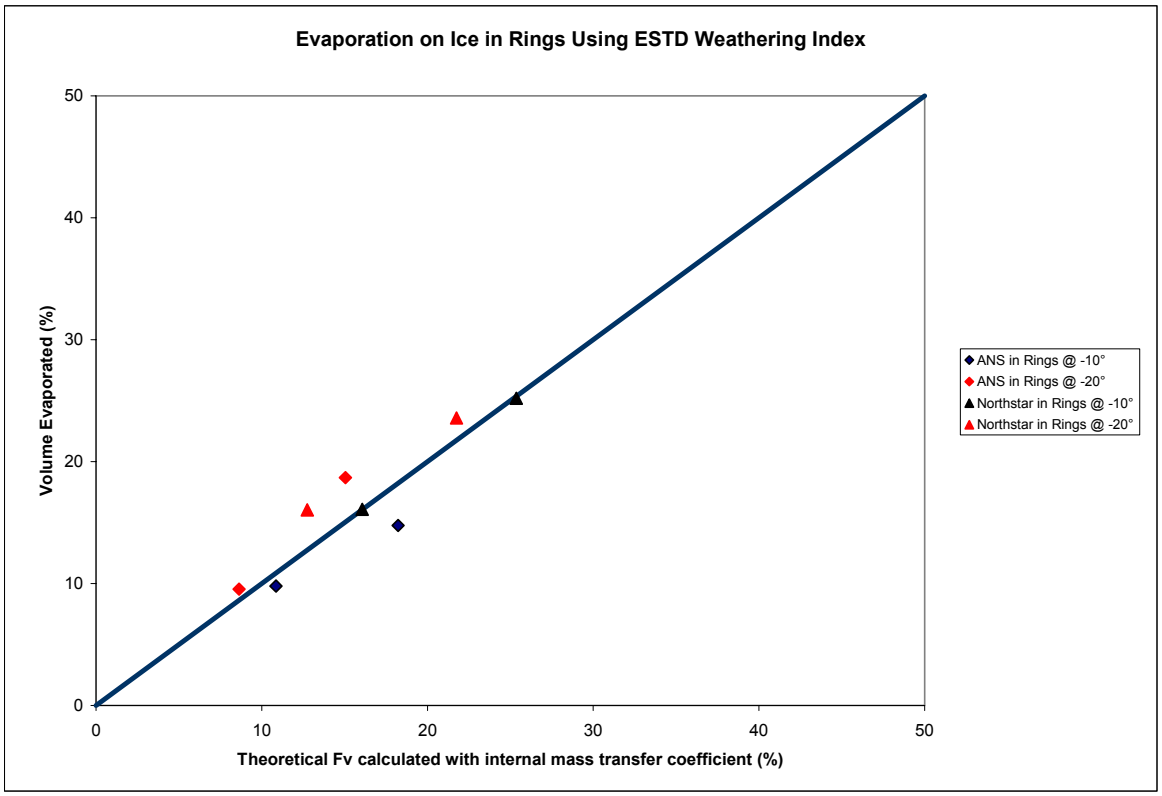

Figure 67. Comparison of Measured Evaporation Using ESTD Data with that Predicted by Equation 21, using an Internal, Liquid-phase Mass Transfer Coefficient k_T = 0.001 m/s

9.5 Evaporation in Snow Methods

The experiments were carried out using the slicks used to measure spreading rates in snow (see Section 7). Oil samples were collected from beneath the snow during the February 2005 test series and during the March 2005 test series (Figure 60). Samples were also collected during the February 2007 spreading experiments. The samples were placed in acrylic jars with snap lids and frozen at -25°C until they were analysed by melting them at room temperature, decanting the water and measuring their density at 15°C. The density was used to determine evaporative loss as described in Section 9.2. Some samples were sent to ESTD for chemical analysis.

At the same time as the oil was weathering in the snow plots, pre-weighed Petri dishes containing samples of each crude were placed in a covered cage outdoors at the test site (Figure 60) and weighed periodically with an electronic balance (see Section 9.2 for details). This was to provide a control (i.e., a known thickness not covered by snow) evaporative data set for each crude. The Petri dishes were weighed during the February 2005 test series after 1, 2, 3, 5, 6 and 8 days exposure and during the March 2005 test series after 1, 2, 3, 5 and 10 days exposure.

9.6 Evaporation in Snow Results, Discussion and Algorithm Selection

All the data from the oil evaporation in snow experiments can be found in Appendix F with the spreading data. Figure 68 shows the Petri dish evaporation results plotted against the prediction of Equation 21 at the average recorded temperatures of –3.8°C for February 2005 and –7.1°C for March 2005. The value of the airside mass transfer coefficient was calculated as k_a = 0.003 m/s for the average recorded wind speed at the site of 1.3 m/s in February 2005 and k_a = 0.0045 m/s for the average recorded wind speed at the site of 2.2 m/s in March 2005. This approach provided the best fit, except for two samples, the ANS crude in March 2005 and the Endicott crude. For the ANS crude, a better fit was obtained by using the internal mass transfer coefficient of k_T = 0.001 m/s, presumably because the cold ANS was beginning to gel at the ambient temperatures. It is apparent that Equation 21, with the proper mass transfer coefficient used to calculate □, can adequately predict evaporation rates outdoors.

Figure 69 shows the measured evaporative loss for the samples under snow compared to the prediction of Equation 21 using the appropriate airside mass transfer coefficient (k_a = 0.003 m/s for February 2005 and k_a = 0.0045 m/s for March 2005). It is clear that the measured evaporation is much less than predicted. This is because the snow adds another resistance to mass transfer. Using Equation 22 as a basis, the full "resistance in series" equation for calculating the overall mass transfer coefficient is:

$$\frac{1}{k_T} = \frac{1}{k_a} + \frac{K_{oa}}{k_o} + \frac{x}{D_s} \qquad \textbf{(23)}$$

Where: $D_s \equiv$ diffusivity of oil vapor in snow [m^2/s]
$x \equiv$ thickness of snow [m]

SL Ross and DF Dickins (1988) analyzed data from a series of crude oil evaporation experiments in snow and recommended a value for D_s of 2 x 10^{-5} m^2/s. Figure 70 shows the measured data compared to the prediction of Equation 21 using Equation 23 to calculate the mass transfer coefficient used to determine □. Although there is considerable scatter (likely due to the errors in using density measurements to estimate evaporative loss) the prediction is much better than in Figure 69.

Several samples of the oil from under snow were sent to ESTD for chemical analysis. Figure 71 shows the evaporative loss of these samples, calculated using the Weathering Index method described in Section 9.4 against the prediction of Equation 21 using the snow resistance term. The fit is reasonable. The reader is cautioned that the samples analyzed by ESTD from the February 2007 experiments were done using a different gas chromatograph that the earlier samples. This introduced a certain, unquantified degree of uncertainty in the 2007 data due to the lack of a GC trace for each fresh crude with the new chromatograph.

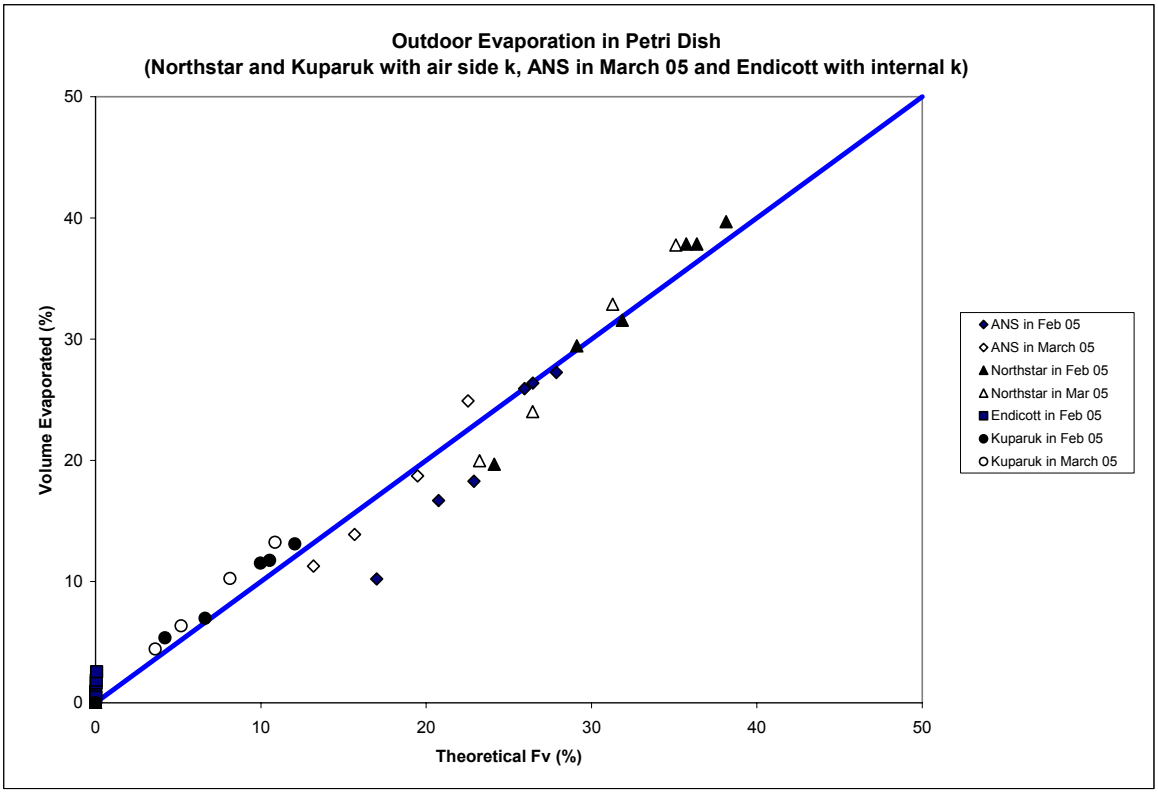

Figure 68. Comparison of Evaporation Measured From Petri Dishes Outdoors with Prediction of Equation 21

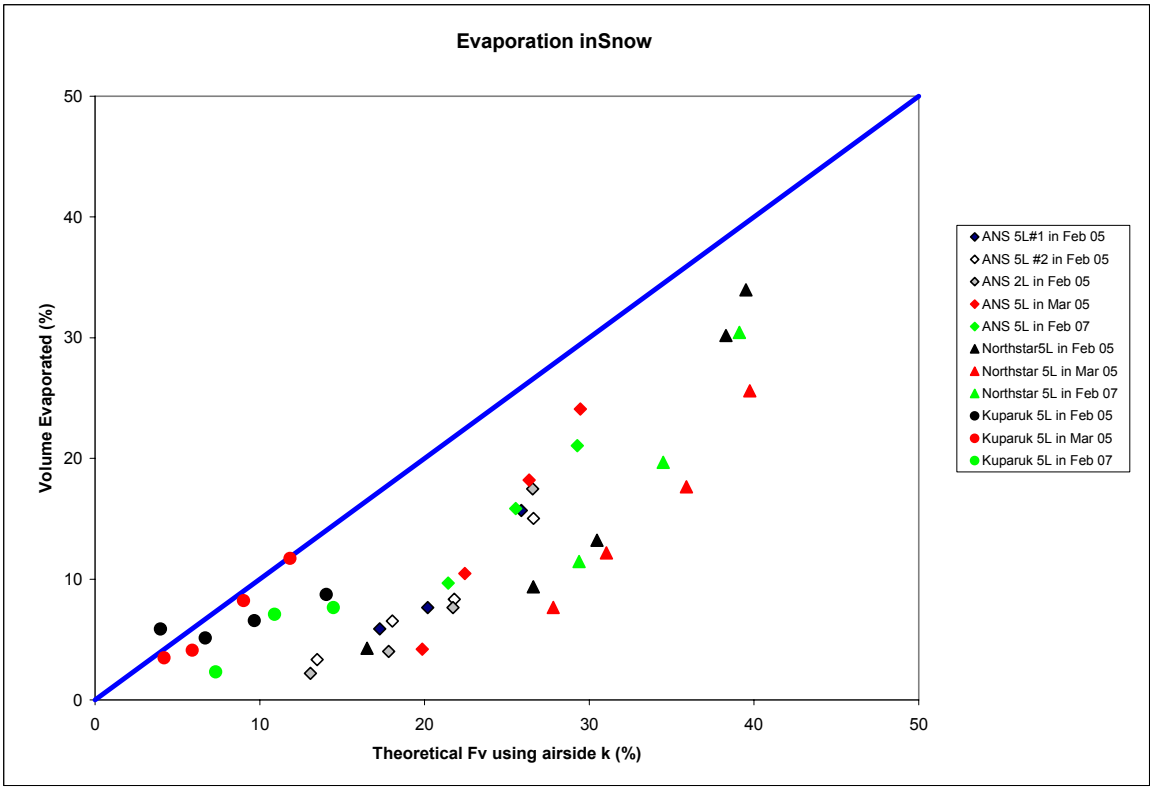

Figure 69. Comparison of Evaporation Measured in Snow with Prediction of Equation 21

9.7 Evaporation in Drift Ice Methods

During the experiments on emulsification in drift ice (see Section 10 below) samples were taken from the test rings (bottom left of Figure 60) to determine the evaporation of the oils. The samples were stored at –25°C until analyzed. This involved warming the oils to 15°C, removing all the water (both free and emulsified, by addition of an emulsion breaking surfactant) and measuring the density of the oils. Aliquots of some samples were also sent to ESTD for analysis.

Samples were also taken during the mid-scale emulsification tests at Ohmsett and analyzed using the same techniques as ESTD.

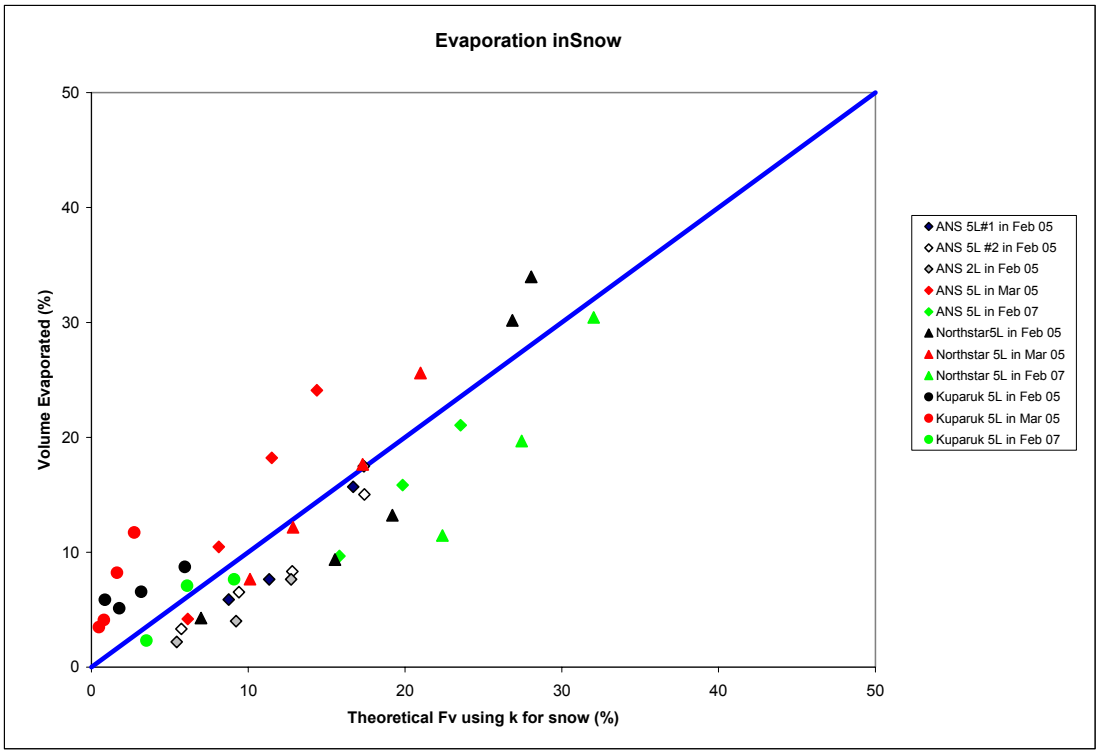

Figure 70. Comparison of Evaporation Data to Prediction of Equation 21 Using Snow Mass Transfer Coefficient

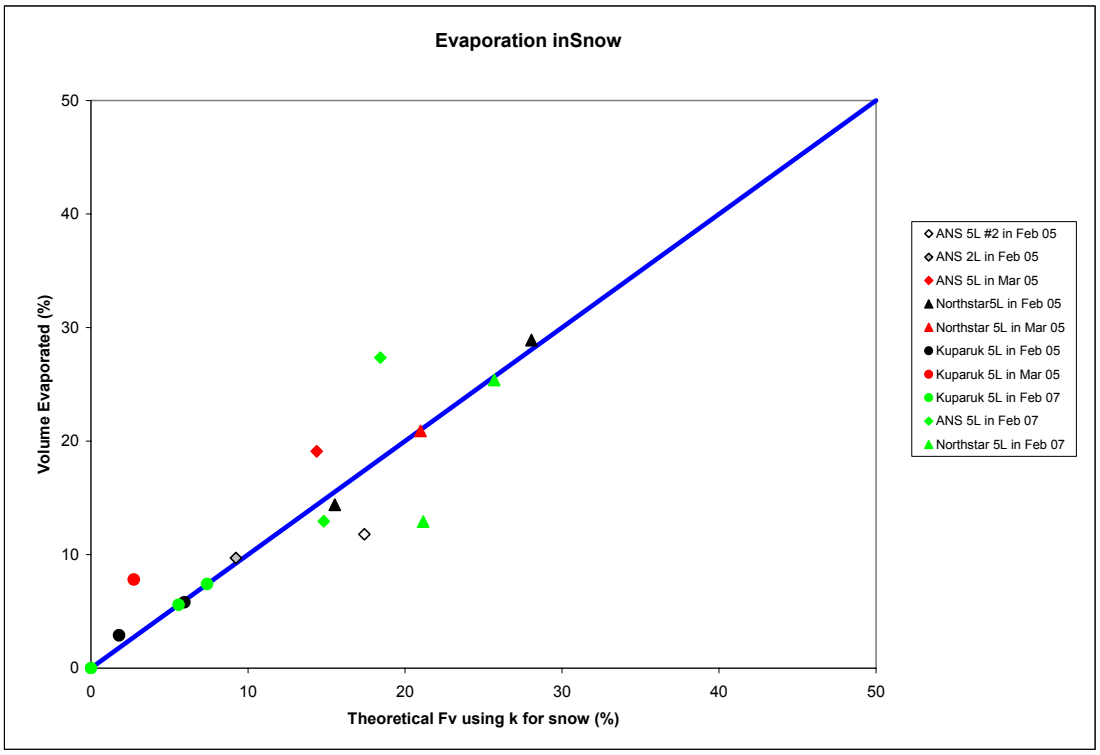

Figure 71. Comparison of WI-derived Evaporation Data to Prediction of Equation 21 Using Snow Mass Transfer Coefficient

9.8 Evaporation in Drift Ice Results, Discussion and Algorithm Selection

Full data are presented in Appendix F. Figure 72 shows the evaporative loss from the samples taken from the rings in the tank at SL Ross compared to the predictions of Equation 21 using an airside mass transfer coefficient of k_a = 0.0115 m/s, measured by toluene evaporation, at an average temperature of –2.5°C. The fit is quite reasonable. The fit of the data to equation 21 with the internal mass transfer coefficient was also checked, but it was considerably worse than Figure 72. This is likely because the experiments involved waves constantly agitating the slicks, which would prevent, or delay, the onset of gelling and the development of a significant internal resistance to mass transfer.

Also shown on Figure 72 are the evaporative loss estimates from two test rings during the second week of larger-scale emulsification tests at Ohmsett. The evaporative loss of these samples (from 5-mm slicks of Northstar and Kuparuk crude in 18-m^2 test rings containing a nominal 30% ice cover with higher waves – see the next section) was calculated from GC-FID n-alkane analysis of samples taken from the rings over four days. Despite the fact that the wind and temperature were quite variable over the five-day experiments, and that the GC-FID analysis was done at a local New Jersey lab, with the weathering index calibration curve was taken from ESTD analysis, the data fits the prediction reasonably well. The measured evaporative loss for the

Kuparuk crude in 30% drift ice was slightly less than predicted and the measured evaporative loss for the Northstar crude in 30% drift ice was slightly more than predicted.

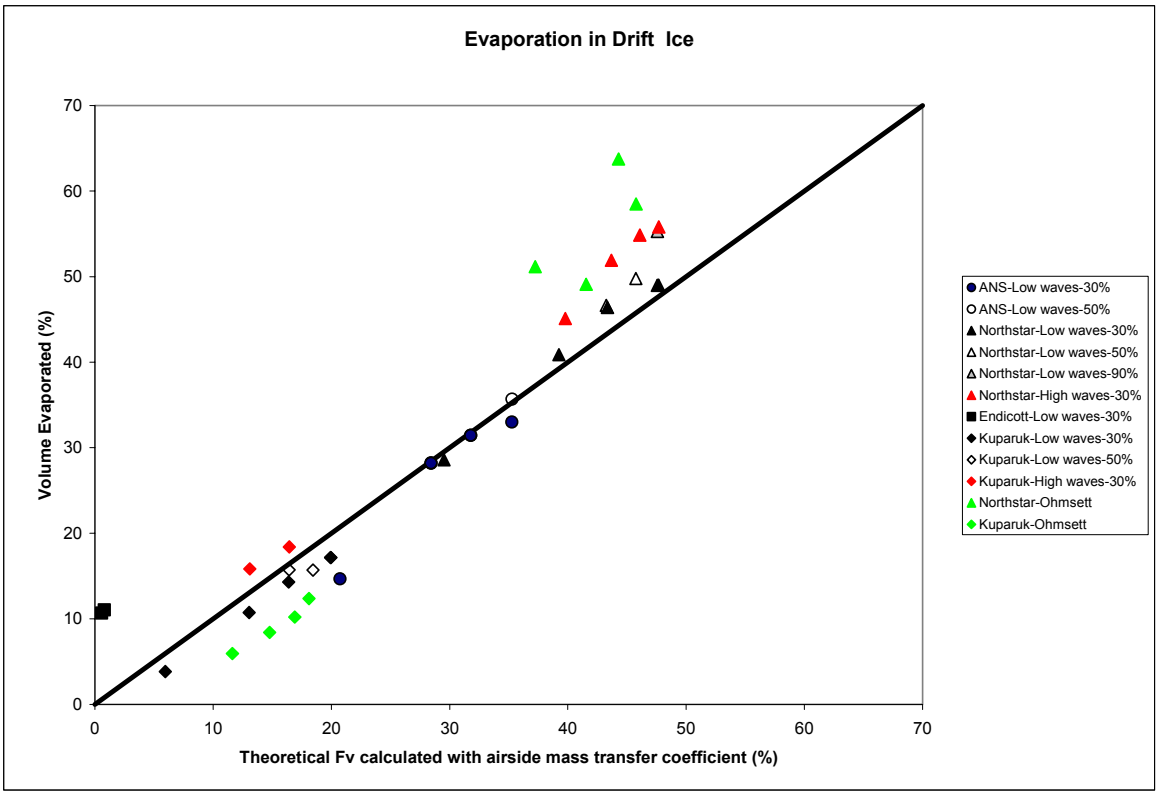

Figure 72. Measured Evaporative Loss During Emulsification Experiments in SL Ross Tank and at Ohmsett vs. that Predicted by Equation 21 using an Airside Mass Transfer Coefficient

10.0 FORMATION OF WATER-IN-OIL EMULSIONS IN DRIFT ICE

The formation of water-in-oil emulsions by spilled oil (colloquially known as emulsification) is an important process that may define the "window-of-opportunity" for many alternative countermeasures that have applicability in ice-covered waters. The formation of a stable emulsion also usually defines the cessation of natural dispersion, the key natural process that accounts for the disappearance of oil from the sea surface once evaporation has slowed to negligible rates. Quantitative tests in drift ice conditions subjected to representative wave action were used to establish the effect of oil properties and physical environmental conditions on the initiation and rate of emulsification. The experiments involved small-scale tests in the refrigerated wind/wave tank in a range of simulated drift ice concentrations and larger-scale tests at Ohmsett in a range of simulated drift ice concentrations.

10.1 State of the Art

When spilled at sea, most crude oils tend to eventually form water-in-oil emulsions. Emulsification occurs in the presence of mixing energy such as that provided by wave action. During emulsification, seawater is incorporated into the oil in the form of microscopic droplets. This water uptake results in several undesirable changes to the oil. First, there is a significant increase in the bulk volume of the slick (usually up to a four- or five-fold increase), greatly increasing the amount of oily material that must be pumped and stored. Secondly, there is a marked increase in fluid viscosity. The much higher viscosities greatly inhibit the chemical or natural dispersion of oil, and if high enough, can reduce skimmer recovery and pump transfer rates.

The mechanisms and rates of the emulsification of oils spilled at sea are still poorly understood, despite being the subject of research for many decades (e.g., Berridge *et al*. 1968). Through some mechanism, the mixing energy associated with waves causes small water droplets to become entrapped in the oil layer. Several theories have been advanced about the main chemical mechanisms involved in the process (Bobra 1990 and 1991, Walker *et al.* 1993). Most experts believe that precipitates of asphaltenes in the oil act as surface-active agents to stabilize the smaller water droplets in the forming emulsion. These natural surfactants form a "skin" around the smaller water droplets, preventing them from coalescing to form larger droplets. Without such stabilizing agents the small water droplets in the oil layer tend to combine into larger droplets that would sink through and leave the oil slick. An increase in the number of water droplets retained in the slick increases its viscosity, which in turn decreases the rate at which water droplets settle out, thus emulsification tends to occur rapidly once the appropriate conditions for forming a stable emulsion are reached. In any case, emulsification inhibits natural dispersion because the process greatly increases slick viscosity. Spills of some crude oils (generally those with higher concentrations of asphaltenes) will start to form an emulsion within a few minutes of being spilled, and will form a highly viscous and stable emulsion within hours. On the other hand, some crude oils must lose some of their lighter components through evaporation before the concentrations of their asphaltenes and resins are raised to the levels required to stabilize emulsions. Most distilled petroleum products do not easily emulsify at all.

Oil spill emulsification is one of the most difficult processes to model or predict on a spill-specific basis. Except perhaps for a few oils that have been tested extensively, such as ANS, it is virtually impossible to quantitatively predict when a particular crude oil will start to emulsify once spilled in a particular environment, and, once the emulsification process begins, to predict how long it will take for the spilled oil to form a "stable", highly viscous emulsion. Nonetheless, modellers of spill behavior have to deal with the problem of spill emulsification because it is such an important process. The usual tactic is to take advantage of a laboratory test, called the Mackay-Zagorski Test (Mackay and Zagorski 1982) that was developed to measure: (1) an oil's tendency to form an emulsion and, (2) the stability of the emulsion once formed. The test provides some indication of oil's emulsion forming characteristics, but does not predict rates of spill emulsification in the field. More recently, Fingas *et al.* (1998) have developed a new scheme for categorizing the type and stability of emulsions formed by oils; however, it employs complex, expensive rheological measurements in order to define an emulsion's stability, and has thus not seen wide use as yet.

There are very few references to emulsification in broken ice in the literature. Payne *et al.* (1987) report on a series of tank tests on Prudhoe Bay crude oil fate in sea ice. At the end of the tests, the ice was allowed to warm, manually fractured to simulate break-up, and then wave action was applied to the broken ice/oil mixture. In the case of "first year" ice that had been frozen only once, the grinding action of the rotten floes and frazil and grease ice caused rapid emulsification of the oil, much faster than had been measured in open water conditions. In the case of "multi-year" ice, which had been subjected to several freeze-thaw cycles before melting, the oil did not form water-in-oil emulsions nearly as fast nor with as high a water content, presumably because of the absence of slush ice between the melting "multi-year" ice. The relative rates and degrees of emulsification were:

- In open water, a steady increase in water content to 50% over 6 days;
- In "first year" ice at break-up, a rapid increase to 64% in one hour then maintaining that water content for 6 days; and,
- In "multi-year" ice at break-up a slow increase to 28% over 6 days.

SL Ross and DF Dickins (1987) performed a series of 1-m^3 experimental spills in dynamic pack ice off the east coast of Canada and sampled the slicks for water content. Despite the energetic conditions (3 to 4 m swell with 35 to 45 km/hr winds) and the fact that the crude oil used was known to form stable emulsions at cold temperatures, no emulsification was measured. It was surmised that the presence of the ice floes damped out the spectrum of wave energy required to form water-in-oil emulsions. Even though floes repeatedly bumped against each other in the swell, this did not cause emulsification to occur.

Hirvi *et al.* (1993) conducted a series of spill behavior tank tests with the crude oil spilled by the MT *Antonio Gramsi* in the Baltic Sea in the winter of 1987. In calm conditions in pack ice, the water content of the oil did not increase appreciably over a 20-day period. Once wave action was started (low frequency waves) the water content began to slowly increase, reaching 28% after 34 days. A second series of tests were conducted in a separate flume, fitted with a beach and wave paddle. In these tests, the pre-evaporated oil (14 days exposure) was placed among free-floating ice blocks and exposed to steeper, more energetic waves. Stable emulsions with water contents of 75% were created within hours in the beach zone of the tank where the waves were breaking.

Singsaas *et al.* (1994) report on two sets of recirculating flume trials and a 10 m^3 experimental spill in the marginal ice zone of the Barents Sea, all with the same crude oil blend. In the first flume experiment in 70% ice cover the water uptake was low for the first 12 hours (from 0 to 10%) in low frequency, non-breaking waves, and then increased dramatically (45% after 24 hours and 65% after 96 hours) when the wave frequency was increased and breaking waves were generated. In the second flume trial, on open water, the oil rapidly emulsified to 75% in only a few hours, similar to offshore trials in open water with the same oil. In the presence of 90% ice cover with similar conditions to the previous open water test, the emulsification was significantly reduced, with maximum water contents of 40 to 50% reached after about 10 hours. In the experimental spill, the ice cover was 90+% for the first few days with no wave action, and then decreased to 70% as the experimental site began to drift towards the ice edge. The wave conditions remained low throughout the 7-day sampling period. The water content of samples only began to increase after about 100 hours, reaching a maximum of 20% after 7 days.

10.2 Emulsification Methods

Small-scale Experiments in the SL Ross Tank

The first series of experiments was carried out in the refrigerated wind/wave tank at the SL Ross laboratory in January 2006. A 5-mm slick of each of the four crude oil types was placed carefully on the surface of the wind/wave tank in 0.16-m^2 (45-cm diameter) test rings containing ice grown on the tank and subjected to two different levels of wave action at three ice concentrations (3, 5 and 9 tenths) over 5-day test periods (Figure 73). During the test periods the tank was covered and the chiller maintained the air at sub-zero temperatures. Periodically samples were taken from each of the 15 rings to determine water content, emulsion stability (via a 24-hour settling test) and to characterize the water droplets (via photo microscopy). Surrogate oil that is known to strongly emulsify (Hydrocal 300 containing 5% IFO 380) was included in each test series as an indicator.

The emulsion samples were withdrawn from each ring with an oleophilic plastic surface (to eliminate the collection of free water) and drained into 10 mL calibrated glass vials. The vials were allowed to sit undisturbed for 24 hours and the height of water that settled in the bottom was recorded. Then the samples were treated with a few drops of Alcopol emulsion breaker, shaken vigorously, and then placed in a constant temperature bath at 50□C for at least 24 hours to separate. The vials were then removed from the bath, wiped and the heights of water and oil in the vials measured with a steel rule. The water content of the emulsion could then be estimated. Emulsion samples were also smeared on a microscope slide and photographed using an OM88T Trinocular microscope with a digital camera mounted on it. The scale of the photographs was determined by taking the photographs through an eyepiece reticule. The reticule scale is superimposed on the photos. The reticule scale was calibrated by taking a photograph of a blank stage micrometer slide with an etched scale on it. The water droplet size distribution in the photograph was determined using the digital photo analysis computer software Image J.

Figure 73. Laboratory Emulsification Experimental Setup

Larger-scale Experiments at Ohmsett

A two-week test program was also conducted at Ohmsett. The Ohmsett water was cooled using an industrial chiller and maintained at approximately –1.5°C. The slicks and ice were contained in eight test rings made from 50-foot sections of oil containment boom held in a circular shape using PVC pipe bent around the outside (Figure 74) creating a contained area of 17.75 m^2. The test circles were held in a group away from the tank walls using loose guy ropes. Six boom circles contained 5-mm slicks of the Northstar and Kuparuk crudes at three different ice concentrations (30, 50 and 90% coverage). The surrogate oil (Hydrocal 300 with 5% IFO 380) was included in one ring and one ring was intended for a randomly selected duplicate. Each crude oil was heated to 45°C or more and stirred in its drum prior to being added to ensure that it was reconditioned to its original form. The waves were generated 24 hours a day.

The artificial sea ice placed in the rings was grown at the US Army Cold Regions Research and Engineering Laboratory (CRREL) in Hanover, NH. One 330-m^2 sheet of 20-cm thick ice grown from urea-doped water was delivered to Ohmsett prior to the tests, pre-cut into 1.1 m x 1.2 m slabs. The pallets, each holding four slabs of ice, were stored in refrigerated shipping containers at Ohmsett until needed. When required, a pallet was brought to the edge of the tank and a test ring was pulled to the edge. The slabs were dropped into the water and manoeuvred into the pings using boathooks. Some of the slabs were quartered and some turned into rubble with an axe to give a distribution of ice piece sizes. The amounts of ice put into each ring were:

- For a 30% ice cover: 2 whole slabs, 1 quartered slab and one half slab of rubble;
- For a 50% ice cover: 3 whole slabs, 2 quartered slabs and one slab of rubble; and,
- For a 90% ice cover: 6 whole slabs, 3 quartered slabs and two slabs of rubble.

After the first day of experiments with the test rings stretched across the tank, it became clear that the sunlight was causing the ice to melt rapidly, despite the chilled water. After this, positioning two of the bridges over top of the rings and tying large plastic tarpaulins on to the bridges shaded the rings.

Samples were removed periodically from the rings using a ladle, and transferred to sample jars and glass vials. The glass vials were placed in a refrigerator at 4°C for 24 hours, then the height of any water and the oily layers was measured to determine the stability of the emulsion. Ten of these samples were selected and sent to a local lab for the same chemical analyses as conducted by ESTD to document weathering. The water content of the emulsion samples was determined using the procedures specified in ASTM D1796. The method involved splitting a well-shaken, 100-mL emulsion sample into two aliquots. Each aliquot was poured into a graduated, centrifuge tube containing 50 mL of toluene, filling the tube to the 100-mL mark. The tube was shaken vigorously, warmed and then placed in the centrifuge and spun for 10 minutes. The volume of water in the tubes was read directly from the graduations.

Photographs of the emulsion samples were taken through a microscope (the same model and camera as used at the SL Ross lab) and analyzed for droplet size distribution using the same techniques and software as for the photographs from the lab experiments.

Figure 74. Ohmsett Emulsification Experimental Setup

10.3 Results

The data from the lab and Ohmsett tests are summarized below. Full data may be found in Appendix G. See Section 10.4 for a discussion of the challenges of measuring wave energy.

Small-scale Results from the SL Ross Tank

Figure 75 shows the increase in water content of the samples taken from the rings in the SL Ross tank over time at the lower wave setting (generating waves with a frequency of 0.22 Hz with a height of 2 cm near the wave paddle, declining to 1 cm by the end of the 15 rings, and a wavelength of approximately 35 cm). Figure 76 shows the increase in water content of the samples taken from the rings over time at the higher wave setting (generating waves with a frequency of 0.23 Hz with a height of 7 cm near the wave paddle, declining to 5 cm by the end of the 15 rings, and a wavelength of approximately 15 cm). The open data points on both figures indicate the samples were unstable emulsions that spontaneously lost considerable amounts of water on standing for 24 hours. Table 19 gives the water droplet size distributions measured for the low energy wave experiments and Table 20 gives the same for the higher energy wave experiments. There are fewer results for the high-energy wave experiments because many of the slicks dispersed completely early in the tests.

Larger-scale Results from Ohmsett

Figure 77 presents the increase in water content of the samples taken from the rings Ohmsett over time at the lower wave setting (generating waves with a frequency of 0.17 Hz with a height of 29 cm). There are only data from five rings because, during an initial dry run with ice only in the rings, the ice melted completely from the eight rings in the first 24 hours. In order to conserve the remaining ice, the actual set of low wave experiments was reduced to five rings. On the last night of the low wave experiments a heavy rain fell, which may be responsible for the sharp increase in water content observed in the 72-hour samples.

Figure 78 shows the increase in water content of the samples taken from the eight rings over time at the higher wave setting (generating waves with a frequency of 0.22 Hz with a height of 32 cm). The key difference between the waves at the lower and higher wave setting is that the frequency at the higher setting is 30% greater (or, the period is 30% less). The open data points on both figures indicate the samples were unstable emulsions that spontaneously lost considerable amounts of water on standing for 24 hours.

Table 21 gives the water droplet size distributions measured for the low energy wave experiments at Ohmsett and Table 22 gives the same for the higher energy wave experiments. There are fewer results for the high-energy wave experiments because many of the slicks emulsified to such an extent that the droplets could not be made out clearly.

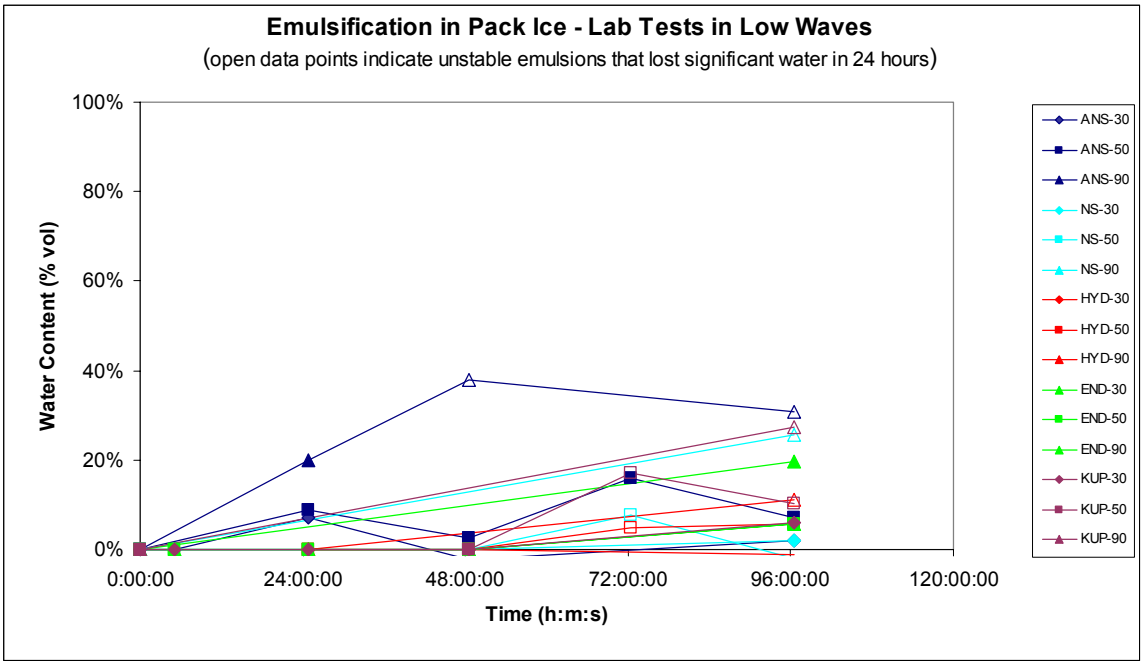

Figure 75. Water Content of Emulsions in SL Ross Tank at Low Wave Setting

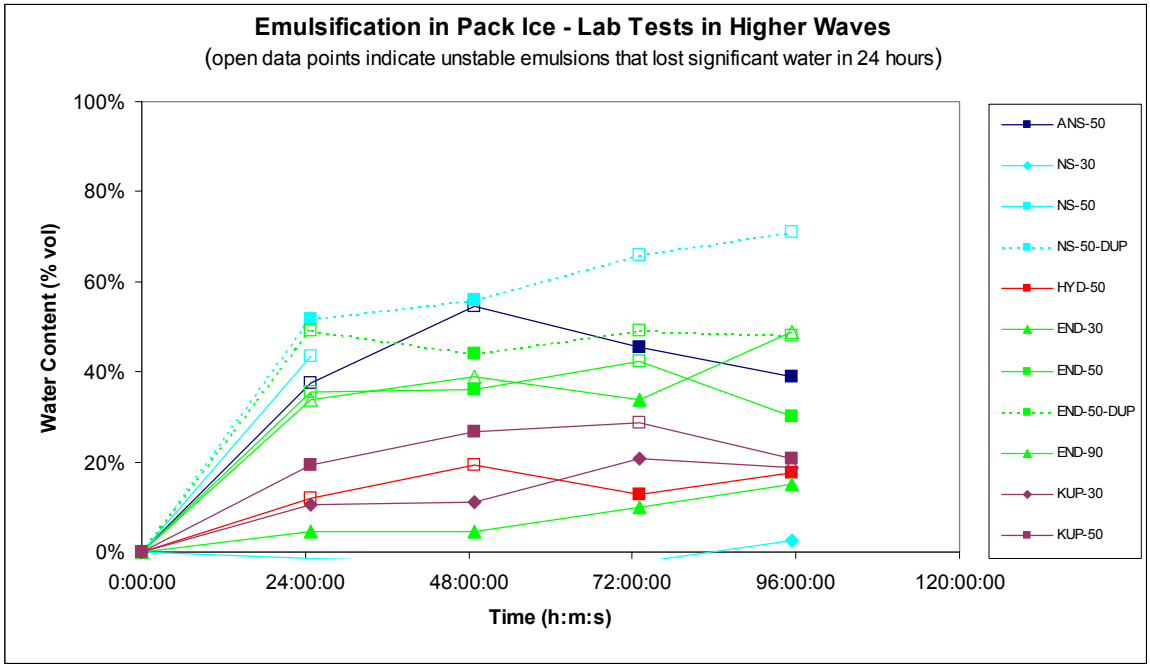

Figure 76. Water Content of Emulsions in SL Ross Tank at High Wave Setting

Table 19. Water Droplet Size Distributions for Low-energy Wave Experiments in SL Ross Tank

			All particles			Particles >= 5 µm diameter				
Crude	Ice (%)	Time (h:m:s)	Mean diam. (µm)	Std dev. (µm)	Count	Mean diam. (µm)	Std dev. (µm)	Count	Min diam. (µm)	Max diam. (µm)
ANS	30	5:24:00	undef.	undef.	0	undef.	undef.	0	undef.	undef.
ANS	30	25:00:00	163.5	181.8	3	163.5	181.8	3	19.7	367.9
ANS	30	48:26:00	318.3	188.3	2	318.3	188.3	2	185.1	451.5
ANS	30	96:10:00	54.3	62.4	14	54.3	62.4	14	9.0	205.8
ANS	50	24:02:00	128.3	205.2	3	128.3	205.2	3	7.9	365.3
ANS	50	48:28:00	58.2	69.5	12	63.4	70.4	11	1.1	232.9
ANS	50	72:25:00	583.7	undef.	1	583.7	undef.	1	583.7	583.7
ANS	50	96:20:00	89.0	126.9	15	89.0	126.9	15	10.6	403.8
ANS	90	24:04:00	10.7	15.3	264	14.8	18.0	167	3.1	170.5
ANS	90	48:32:00	8.0	10.0	257	10.8	12.2	152	3.1	120.9
ANS	90	24:00.0	84.0	103.0	23	84.0	103.0	23	14.9	501.9
Northstar	30	5:20:00	undef.	undef.	0	undef.	undef.	0	undef.	undef.
Northstar	30	25:12:00	undef.	undef.	0	undef.	undef.	0	undef.	undef.
Northstar	30	48:32:00	30.0	37.8	12	48.5	40.8	7	3.2	104.9
Northstar	30	96:27:00	39.7	23.5	23	41.4	22.5	22	1.9	94.3
Northstar	50	48:34:00	35.4	19.6	2	35.4	19.6	2	21.6	49.3
Northstar	50	72:25:00	40.7	24.5	7	40.7	24.5	7	17.0	74.4
Northstar	50	96:32:00	54.5	48.8	8	54.5	48.8	8	8.9	151.9
Northstar	90	48:34:00	60.7	21.8	4	60.7	21.8	4	42.0	92.1
Northstar	90	96:33:00	undef.	undef.	0	undef.	undef.	0	undef.	undef.
Hydrocal	30	47:50:00	260.6	undef.	1	260.6	undef.	1	260.6	260.6
Hydrocal	30	96:19:00	25.6	16.7	12	27.6	16.1	11	4.5	61.7
Hydrocal	50	48:23:00	12.4	undef.	1	12.4	undef.	1	12.4	12.4
Hydrocal	50	72:14:00	170.5	298.9	4	170.5	298.9	4	13.2	618.8
Hydrocal	50	96:22:00	50.0	undef.	1	50.0	undef.	1	50.0	50.0
Hydrocal	90	48:28:00	14.1	8.7	272	14.2	8.7	270	1.0	85.9
Hydrocal	90	96:25:00	10.4	9.3	178	12.7	9.9	131	3.5	78.3
Endicott	30	4:45:00	11.5	5.8	52	12.4	5.1	48	1.0	25.8
Endicott	30	24:36:00	172.7	undef.	1	172.7	undef.	1	172.7	172.7
Endicott	30	48:10:00	23.8	16.2	28	25.3	15.7	26	2.1	64.1
Endicott	30	96:08:00	15.9	20.7	29	15.9	20.7	29	5.1	96.0
Endicott	50	48:12:00	9.7	23.5	321	12.1	27.8	224	3.7	417.0
Endicott	50	71:58:00	102.6	57.9	2	102.6	57.9	2	61.6	143.5
Endicott	50	96:10:00	186.8	undef.	1	186.8	undef.	1	186.8	186.8
Endicott	90	48:13:00	63.3	82.1	15	63.3	82.1	15	10.1	240.2
Endicott	90	96:12:00	12.9	10.7	36	13.9	10.8	32	3.8	58.8
Kuparuk	30	5:04:00	undef.	undef.	0	undef.	undef.	0	undef.	undef.
Kuparuk	30	24:49:00	50.2	4.2	2	50.2	4.2	2	47.3	53.2
Kuparuk	30	48:26:00	273.3	undef.	1	273.3	undef.	1	273.3	273.3
Kuparuk	30	96:26:00	91.0	167.3	5	113.2	184.5	4	2.2	389.5
Kuparuk	50	48:34:00	497.9	undef.	1	497.9	undef.	1	497.9	497.9
Kuparuk	50	72:15:00	258.6	undef.	1	258.6	undef.	1	258.6	258.6
Kuparuk	50	96:32:00	27.9	26.5	7	27.9	26.5	7	6.4	68.0
Kuparuk	90	48:38:00	19.4	29.0	44	19.4	29.0	44	5.1	158.1
Kuparuk	90	96:37:00	18.2	12.7	24	18.8	12.6	23	3.8	56.2

Table 20. Water Droplet Size Distributions for Higher-energy Wave Experiments in SL Ross Tank

			All particles			Particles >= 5 µm diameter					
Crude	Ice (%)	Time (h:m:s)	Mean diam. (µm)	Std dev. (µm)	Count	Mean diam. (µm)	Std dev. (µm)	Count	Min diam. (µm)	Max diam. (µm)	
Northstar	30	24:37:00	6.0	5.7	1265	10.5	7.3	481	2.1	48.4	
Northstar	30	48:42:00	4.8	2.9	1625	7.7	3.2	544	2.2	37.7	
Northstar	30	72:53:00	4.3	2.6	1934	7.0	3.5	543	2.3	64.5	
Northstar	30	95:50:00	4.7	2.4	1593	6.7	3.2	529	2.8	41.4	
Northstar	50	23:45:00	5.8	5.2	1399	9.7	6.5	255	2.1	47.9	
Northstar	50	48:45:00	8.5	8.4	647	13.0	8.8	362	1.1	47.3	
ANS	30	95:45:00	17.7	14.5	132	19.6	14.5	117	3.0	85.3	poor image quality
Northstar	50	72:00:00	6.9	4.2	369	9.3	4.4	202	3.4	28.4	
Endicott	50	24:00:00	36.9	34.5	86	36.9	34.5	86	5.9	196.6	
Endicott	50	48:00:00	24.6	35.9	48	30.1	38.6	38	3.5	161.2	poor image quality
Endicott	50	72:04:00	9.4	22.4	236	17.1	32.4	103	0.6	231.2	
Endicott	50	95:54:00	11.3	29.1	156	13.1	32.3	125	2.3	348.0	
Hydrocal	50	24:00:00	9.6	15.6	142	13.0	19.2	87	1.1	125.5	no cover slide
Hydrocal	50	24:00:00	8.5	4.8	152	9.5	4.8	125	2.4	35.1	
Hydrocal	50	48:05:00	8.5	6.2	138	10.1	6.5	102	2.9	59.9	
Hydrocal	50	95:00:00	9.9	5.2	53	11.5	4.6	42	2.4	22.1	no cover slide
Hydrocal	50	95:00:00	4.8	4.5	96	13.2	6.8	15	1.6	27.5	
Endicott	30	24:00:00	21.0	8.3	423	21.0	8.3	423	10.5	50.9	
Endicott	30	48:00:00	7.5	12.2	225	13.1	17.9	90	2.3	151.0	
Endicott	30	72:00:00	46.6	46.2	61	49.6	46.3	57	3.4	261.0	
Endicott	30	96:00:00	15.1	36.6	212	18.6	41.2	163	1.5	436.5	
Endicott	50	24:00:00	14.3	21.9	180	14.7	22.2	173	3.5	287.8	
Endicott	50	48:00:00	20.4	31.2	158	21.3	31.8	150	2.6	366.7	
Endicott	50	72:00:00	8.3	15.2	477	12.5	20.3	245	0.8	283.6	
Endicott	50	96:00:00	7.3	8.5	141	13.9	11.8	49	2.1	59.6	
Endicott	90	24:00:00	12.3	23.5	492	13.2	24.5	447	1.6	464.2	
Endicott	90	48:00:00	21.6	38.3	10	21.6	38.3	10	5.2	130.1	
Endicott	90	72:00:00	6.8	17.4	222	14.0	28.5	76	1.4	236.5	
Endicott	90	96:00:00	9.9	5.2	46	11.0	4.6	40	1.4	25.1	
Kuparuk	30	24:00:00	26.7	29.9	518	26.7	29.9	517	4.9	382.0	
Kuparuk	30	48:00:00	11.2	10.7	147	11.5	10.9	140	3.4	108.5	
Kuparuk	30	72:00:00	9.1	10.1	127	12.5	11.7	78	2.5	91.6	
Kuparuk	30	24:00:00	15.6	15.2	153	15.8	15.3	150	3.5	175.3	
Kuparuk	50	48:00:00	16.5	15.5	86	17.0	15.6	83	3.4	70.6	
Kuparuk	50	48:00:00	18.0	18.9	84	18.5	19.0	81	3.3	103.6	
Kuparuk	50	96:00:00	15.3	7.0	78	15.3	7.0	78	6.5	46.8	

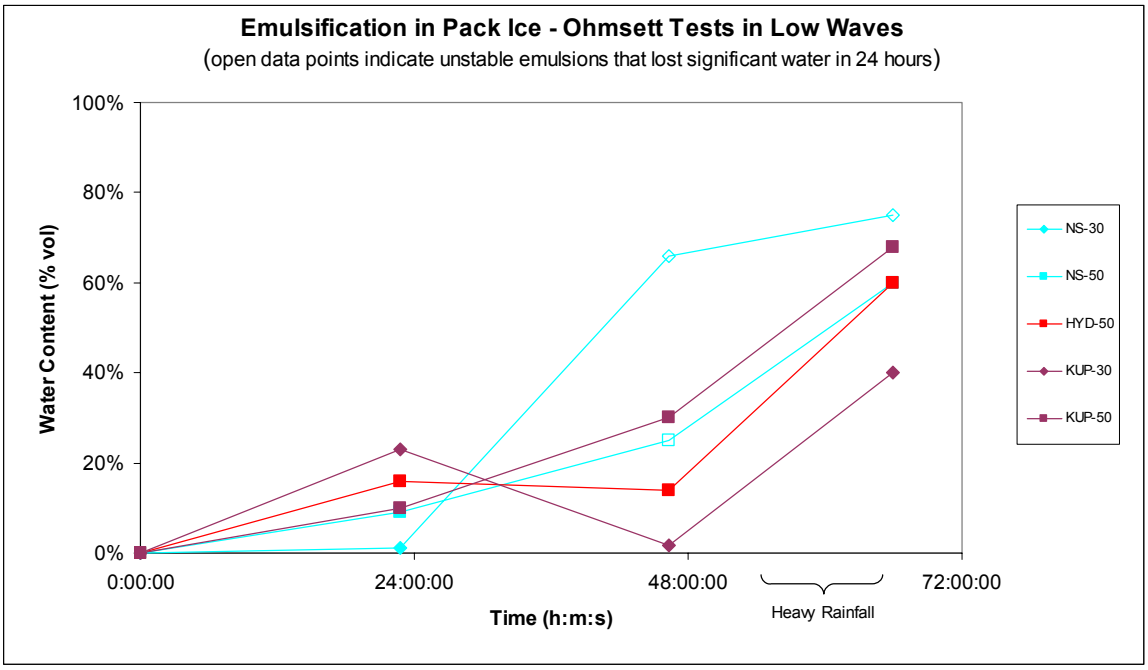

Figure 77. Water Content of Emulsions in Ohmsett at Low Wave Setting

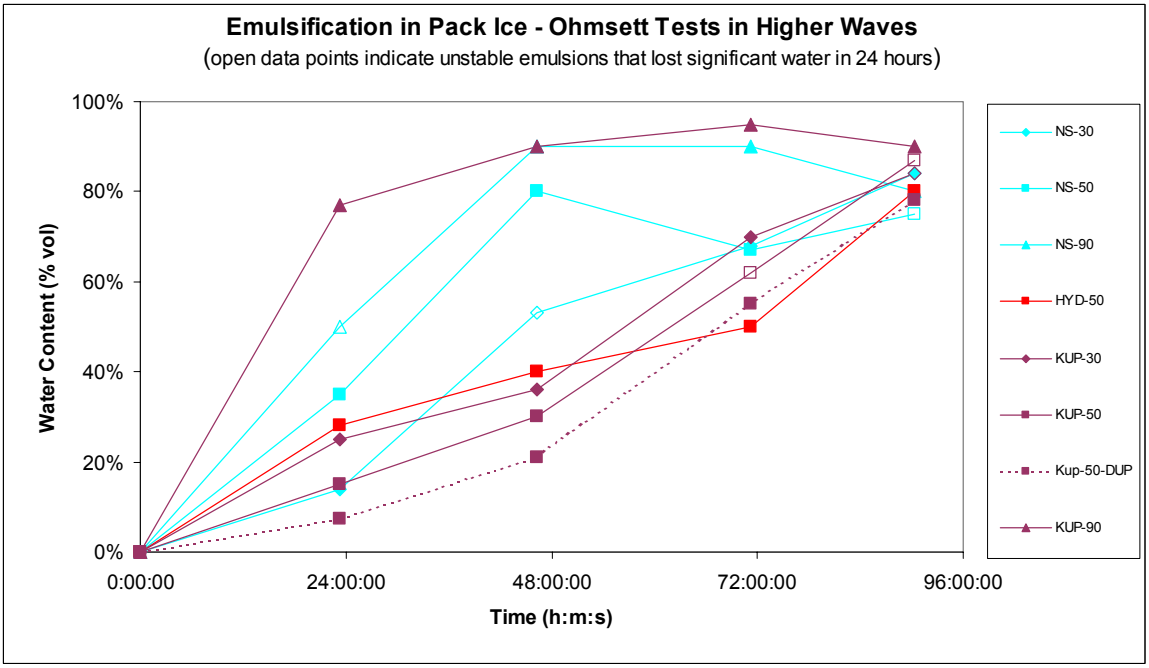

Figure 78. Water Content of Emulsions in Ohmsett at Higher Wave Setting

Table 21. Water Droplet Size Distributions for Low-energy Wave Experiments in Ohmsett

Crude	Ice (%)	Time (h:m:s)	All particles: Mean diam. (µm)	All particles: Std dev. (µm)	All particles: Count	Particles >= 5 µm diameter: Mean diam. (µm)	Particles >= 5 µm diameter: Std dev. (µm)	Particles >= 5 µm diameter: Count	Min diam. (µm)	Max diam. (µm)	
Northstar	30	0:00:00	undef.	undef.	0	undef.	undef.	0	undef.	undef.	
Northstar	30	22:50:00	14.7	13.8	162	21.2	13.8	102	2.2	104.5	
Northstar	30	46:51:00	14.7	22.6	229	27.3	28.3	107	1.6	148.2	
Northstar	30	66:53:00	20.3	31.5	65	27.2	35.2	46	0.5	177.5	poor image
Northstar	50	22:40:00	15.2	11.2	176	17.7	10.7	145	0.5	85.5	
Northstar	50	46:33:00	6.6	8.3	559	14.9	12.7	151	0.5	75.7	
Northstar	50	66:45:00	6.4	8.7	499	18.4	12.6	111	1.6	78.7	
Kuparuk	50	0:00:00	undef.	undef.	0	undef.	undef.	0	undef.	undef.	
Kuparuk	50	46:26:00	18.0	11.3	122	18.1	11.2	121	0.5	81.5	
Kuparuk	50	67:05:00	3.4	1.3	1981	6.3	1.5	177	0.5	17.0	
Kuparuk	30	22:50:00	9.7	9.2	111	9.9	9.3	106	2.4	99.4	
Kuparuk	30	46:25:00	4.0	2.1	1989	7.2	3.6	307	1.3	39.3	
Kuparuk	30	66:36:00	6.2	1.8	227	6.7	1.7	181	3.5	17.8	
Hydrocal	50	21:50:00	13.6	15.1	126	15.1	15.7	109	3.2	156.4	
Hydrocal	50	45:45:00	5.3	4.4	491	9.0	6.4	155	1.9	72.5	
Hydrocal	50	66:56:00	6.1	15.2	363	13.2	29.4	91	2.3	231.2	

Table 22. Water Droplet Size Distributions for Higher-energy Wave Experiments in Ohmsett

Crude	Ice (%)	Time (h:m:s)	All particles: Mean diam. (µm)	All particles: Std dev. (µm)	All particles: Count	Particles >= 5 µm diameter: Mean diam. (µm)	Particles >= 5 µm diameter: Std dev. (µm)	Particles >= 5 µm diameter: Count	Min diam. (µm)	Max diam. (µm)	
Northstar	90	23:14:00	9.0	15.5	813	16.2	21.5	352	1.1	200.7	
Northstar	90	46:42:00	24.9	25.2	115	30.0	25.5	93	2.3	103.2	poor image
Northstar	90	71:10:00	17.1	15.2	281	19.7	15.3	235	0.5	129.0	poor image
Northstar	50	23:35:00	13.4	12.0	270	15.1	12.3	228	1.8	105.3	
Northstar	50	46:33:00	17.0	16.0	206	22.0	16.1	151	0.5	95.2	
Northstar	50	71:32:00	15.4	11.8	151	17.0	11.7	133	0.5	90.5	
Northstar	30	23:17:00	15.1	56.5	155	17.2	61.5	130	1.1	707.8	
Northstar	30	47:17:00	15.0	19.6	224	20.4	21.9	151	2.5	179.3	
Northstar	30	71:18:00	24.1	24.6	139	28.2	25.1	116	2.7	164.5	
Kuparuk	50	24:06:00	8.3	13.2	325	12.0	17.0	177	2.1	141.3	
Kuparuk	50	47:55:00	12.5	15.4	245	13.7	16.1	216	0.5	149.7	
Hydrocal	50	0:00:00	7.0	4.4	209	9.5	4.7	113	2.3	40.1	
Hydrocal	50	23:40:00	8.6	16.9	283	13.8	23.4	135	2.7	218.0	
Hydrocal	50	46:21:00	11.7	21.2	154	21.3	28.7	70	2.7	184.6	
Hydrocal	50	71:39:00	17.0	20.4	209	19.6	21.4	174	3.0	247.5	
Hydrocal	50	91:25:00	17.7	25.4	206	20.9	27.1	168	1.0	225.5	
Kuparuk	90	24:53:00	13.8	21.7	205	18.7	25.1	138	2.2	169.8	
Kuparuk	90	47:07:00	12.4	15.3	284	18.1	17.3	172	0.5	172.6	
Kuparuk	90	72:52:00	17.8	16.5	102	20.8	16.8	83	1.8	86.5	
Kuparuk	90	91:50:00	19.3	21.1	128	19.9	21.3	123	4.0	175.5	large non-circular droplets
Kuparuk	50	25:08:00	31.7	63.4	48	53.4	76.2	28	0.9	326.7	poor image
Kuparuk	50	48:06:00	9.3	16.4	383	13.1	20.5	225	2.8	232.4	
Kuparuk	50	91:18:00	20.5	29.4	99	21.2	29.8	95	3.1	233.0	
Kuparuk	30	25:23:00	9.0	21.0	297	11.8	25.7	191	2.8	321.1	
Kuparuk	30	48:23:00	22.9	32.4	246	24.0	33.0	233	2.6	373.2	

10.4 Discussion and Algorithm Selection

There are three factors that dictate when a crude oil will emulsify: its asphaltene content, the amount and intensity of mixing energy available and the viscosity of the oil at the ambient temperature. The relevant, emulsification-specific data from the characterization of the four crudes is reproduced below in Table 23 from Section 5 for reference.

The data presented in Figure 75 show that very little emulsification occurred over 96 hours in the low energy environment of the low wave experiments in the SL Ross tank. Even the oils that would be expected to be prone to emulsify (particularly the doped Hydrocal, Endicott and ANS) did not. In the higher wave level in the SL Ross tank (Figure 76) the Endicott crude did form lower water content "entrained" water emulsions as did the one experiment with ANS that did not disperse completely. The doped Hydrocal also picked up more water than in the lower wave tests. The Northstar crude did pick up water, but the emulsions were unstable. Comparison of the water droplet size distributions shows that, as expected, the mean droplet size in the higher wave energy conditions was generally much smaller than the mean size in the lower waves. Perhaps the most surprising result was that, despite having nearly 10% asphaltenes, the Kuparuk crude did not form stable emulsions, either in the Mackay-Zagorski test or the wave tank. There does not appear to be any correlation between ice concentration and emulsification in these data.

Figure 77 shows that very little emulsification occurred with the oils in the low waves at Ohmsett (the increase in water content at the end of the experiment was more than likely due to heavy rains overnight). The droplet size distributions indicate that the emulsions contained relatively small water droplets. Figure 78 shows that, at the higher wave energy level all the oils formed high (80%) water content emulsions. Only two did not form stable emulsions (Northstar and Kuparuk in 50% ice – although the duplicate experiment with Kuparuk in 50% ice did form a stable emulsion). There also appears to be a trend that emulsification occurred more rapidly in higher ice concentrations. The water droplet size distributions in the samples from these tests had consistently small mean droplet sizes. In these tests, it appears that there could be a trend in increasing emulsification rate with increasing ice concentration, although after 96 hours all the experiments had resulted in high water contents in the 80% range.

The formation of stable emulsions by the Kuparuk and Northstar crudes was not expected, based on the characterization test results (Table 23) and the other tank test results. One likely explanation for the anomalous results is that the Ohmsett tests took place outdoors, in sunlight. Solar radiation has been shown by several researchers (e.g., Bocard and Gatellier 1981, Payne and Phillips1985, Mackay 1981, Brandvik and Daling 1991) to be a strong contributing factor to water-in-oil emulsion stability, through the formation of photolysed surfactant compounds in the parent oil. The combination of increased mixing energy and the production of photolysed surfactants in the oil could have resulted in stable emulsions being formed.

At present there are no satisfactory algorithms to predict emulsification of oil slicks at sea. There are two basic reasons for this:

1. There is still a lack of understanding of the basic mechanisms by which emulsification occurs; and,

Table 23. Summary of Emulsification Characterization Data for the Crude Oils

ANS

Time in Wind Tunnel	0	2 days	2weeks
Evaporation (vol %)	**0**	**30.8**	**38.2**
Emulsion Formation-Tendency and Stability @		0 °C	
Tendency Index	Very unlikely	Very likely	Very likely
Stability	Unstable	Entrained	Entrained
Water Content	0%	44%	29%
Emulsion Formation-Tendency and Stability @		15 °C	
Tendency Index	Very unlikely	Very likely	Very likely
Stability	Unstable	Unstable	Entrained
Water Content	0%	20%	29%
Asphaltenes (w/w%)	3.8	5	5.5

Endicott

Time in Wind Tunnel	0	2 days	2weeks
Evaporation (vol %)	**0**	**0.8**	**5.3**
Emulsion Formation-Tendency and Stability @		0 °C	
Tendency Index	Very likely	Very likely	Very likely
Stability	Entrained	Entrained	Entrained
Water Content	39%	39%	43%
Emulsion Formation-Tendency and Stability @		15 °C	
Tendency Index	Very unlikely	Very unlikely	Very likely
Stability	Unstable	Unstable	Entrained
Water Content	0%	13%	29%
Asphaltenes (w/w%)	5.1	5.2	5.5

Kuparuk

Time in Wind Tunnel	0	2 days	2weeks
Evaporation (vol %)	**0**	**9.5**	**20.3**
Emulsion Formation-Tendency and Stability @		0 °C	
Tendency Index	Very unlikely	Very unlikely	Very unlikely
Stability	Unstable	Unstable	Unstable
Water Content	13%	29%	0%
Emulsion Formation-Tendency and Stability @		14 °C	
Tendency Index	Very unlikely	Very unlikely	Very unlikely
Stability	Unstable	Unstable	Unstable
Water Content	0%	17%	0%
Asphaltenes (w/w%)	8.5	9	10.3

Northstar

Time in Wind Tunnel	0	2 days	2weeks
Evaporation (vol %)	**0**	**43.7**	**52**
Emulsion Formation-Tendency and Stability @		0 °C	
Tendency Index	Very unlikely	Very unlikely	Very unlikely
Stability	Unstable	Unstable	Unstable
Water Content	0%	0%	0%
Emulsion Formation-Tendency and Stability @		15 °C	
Tendency Index	Very unlikely	Very unlikely	Very unlikely
Stability	Unstable	Unstable	Unstable
Water Content	0%	0%	0%
Asphaltenes (w/w%)	0	0.1	0

2. There is a basic lack of understanding how to measure and quantify the energy levels in various test tanks and the sea. Although equations exist to estimate the total energy contained in a given wave, based on characteristics such as height, length, frequency and velocity, the parameter of interest to emulsification is the amount of small-scale mixing energy (or turbulence) imparted to the slick by the passing waves. This parameter is also crucial to understanding the mechanisms and rates of dispersion of oil slicks (natural and/or chemical) and is the subject of much ongoing research. At present there is no accepted standard method to measure the small-scale turbulence imparted to a slick by waves, nor is there a clear understanding of how wave energy measured in test tanks relates to wave energy at sea.

Until these issues are resolved, it is not fruitful to try to develop algorithms to predict emulsification rates at sea. The state of the art today is to conduct small-scale bench or tank tests with quantitatively evaporated oil samples at representative environmental temperatures to predict when oil will be come susceptible to forming stable emulsions. In open water conditions it is generally agreed that, once oil weathers to this state, emulsification will proceed to completion relatively rapidly, in a few hours. The results of the experiments reported here do not contradict this approach. There appears to be a trend in the Ohmsett data that increasing ice concentration and increasing wave energy level increase emulsification rate and exposure to sunlight increases emulsion stability, but until the rate of emulsion formation in open water is understood and modelled, it is not possible to model the effects of drift ice on the processes.

11.0 MIGRATION RATES THROUGH BRINE CHANNELS

This section describes a series of quantitative experiments using a the outdoor tanks to investigate the effects of environmental conditions, oil properties, ice salinity and sediment loading on the migration rates of oil spilled under a solid sea ice sheet. Migration refers to the process of oil rising naturally through connected brine channels that gradually form a continuous pathway to the surface as the ice warms.

11.1 State of the Art

Brine Entrapment in Sea Ice

Brine is entrapped within an ice sheet during the freezing process in the form of fine pockets of fluid between platelets of pure ice. The amount of salt trapped in the ice is principally dependent on the rate of freezing. As the ice thickens, the growth rate decreases and brine is expelled more efficiently. At any given temperature, the fluid within the brine channels is always at a salt concentration such that it exists in equilibrium with the surrounding pure ice crystals. The predominant salt in seawater, $NaCl.H_2O$, precipitates out at -22.9°C (Sanderson, 1988). This means that in order for the brine pockets to exist in a primarily crystalline (non fluid) state, the ice temperature needs to be below this value. In most areas outside the High Arctic, air temperatures are such that only the upper ice layer will experience temperatures below this threshold for any length of time. Consequently, most of the entrapped brine will exist in a concentrated fluid state. The gross brine volume fraction brine volume (V_b) within any sea ice sheet is approximated (Frankenstein and Garner, 1967) by a relatively simple function of temperature and salinity expressed as:

$$V_b = 0.001S(0.53 - \frac{49}{T}) \qquad \textbf{(24)}$$

Where: $S \equiv$ Salinity [‰]
T ≡ Temperature [°C]

Crude oil spilled underneath a sea ice sheet will immediately penetrate the soft, porous skeletal layer of fragile and separate ice crystals projecting downwards at the freezing interface (Figures 79 and 80). Once this initial saturation process has occurred and the oil spreading has stabilized, the oil will either remain static, or begin to migrate vertically through brine channels. The actual sequence of events in any given spill will depend primarily on the degree of connectivity between individual brine pockets.

In a cold sea ice sheet with a close to linear temperature profile connecting the cold surface (<<0°C) and relatively warm ice water interface (-1.9°C) the brine exists in discontinuous pockets with no clear pathway for the oil to migrate any significant distance. Over the course of the winter ice growth period, brine pockets naturally migrate downwards as a result of the normal winter temperature gradient. Energy considerations favor continual melting of the ice at the warmer end of the brine pocket and refreezing at the colder end. As a result, the pocket tends to migrate towards the higher temperatures, becoming larger and longer as they pass into progressively warmer surrounding ice at greater depth (Zubov, 1945). Eventually, the pockets coalesce to form major continuous channels in the order of 0.1 to 10 mm diameter. In the spring, the ice normally experiences a reversal in temperature gradient with both the upper and lower ice surfaces being warmer than the interior (Sanderson, 1988). In this situation, brine is expelled

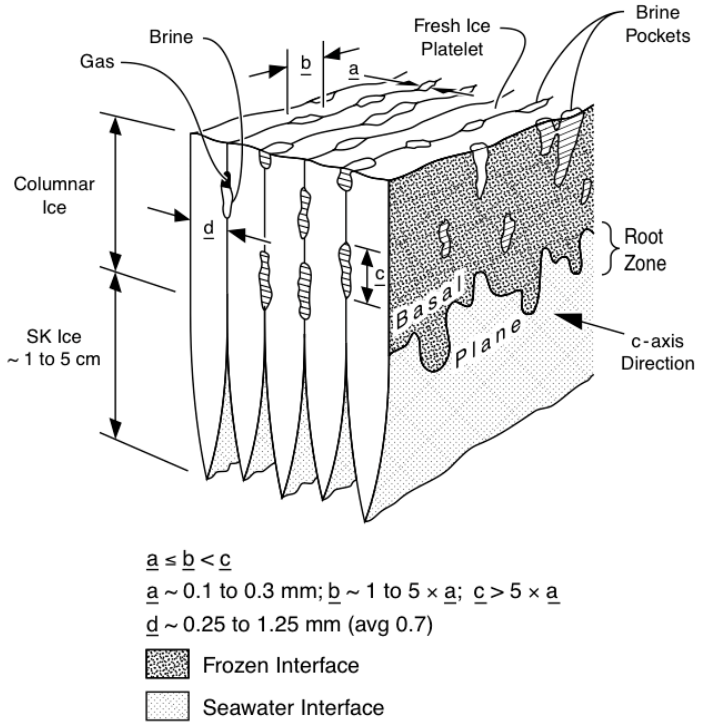

Figure 79. Sea Ice Crystal Structure Source: Kovacs (1996)

Figure 80. Trapped Oil Lens Visible in a Large Block of Sea Ice Cut Out of an Experimental Spill in Alaska Photo: A. Allen

from the sheet in both directions. As a result, the gross salinity (total salt content) of the sheet decreases with time and the brine channels remain to form a continuous pathway from a trapped oil layer to the ice surface. Once the ice reaches this state of deterioration, the rate of oil migration can be extremely rapid. For example, Norman Wells crude oil released under two meters of ice in the Balaena Bay experiment on the Arctic coast reached the ice surface within one hour in late May (Norcor, 1975).

When brine channels become continuously connected through the full sheet in late winter, the rate of vertical oil migration is thought to depend on a number of factors, including: oil viscosity, degree of emulsification at the time of the spill (viscosity), trapped film thickness, and the area distribution of the oil (isolated particles vs. substantial pools).

Past Studies: Field Spills

The Balaena Bay Project involved a series of spills under sea ice over the course of one winter (1974/75) and represents the most detailed historical study of crude oil migration (Norcor, 1975). Oil spilled in early winter remained static as a discrete lens until February, at which time the ice surface temperatures gradually rose from –20°C to –12°C. The transient reduction in temperature gradient combined with increased ice salinity immediately above the oil lens, led to an initial migration of 10 to 15 cm even in mid-winter while new ice was forming rapidly beneath the oil layer. During the winter period, the vertical depth of the main oil lens at the time of the spill had little or no effect on the extent of migration.

During March and April, the brine channel network within the ice sheet became progressively more connected and the oil gradually rose through the sheet to within 10 to 15 cm of the surface layer. The average brine channel diameter at this point was 4 mm. The final penetration to the surface was blocked for a short time by the upper layer of clear frazil ice that lacked a cohesive brine channel network (randomly oriented crystals) but once the air temperatures remained consistently above freezing, the oil from all the test sites broke through to the surface with a similar timeline, regardless of the depth of the oil within the ice.

Nelson and Allen (1981) reported observations from a series of 18 spills of diesel and crude under natural first-year ice from 15 to 57 cm in thickness. All of the diesel spills migrated very quickly, never having time to formed trapped lenses in the ice. Crude oil tended to migrate to the surface earlier than at Balaena Bay (described above). The difference in behavior was linked to the presence of abnormally deep snowdrifts over the spill sites, resulting in internal ice temperatures more typical of spring conditions.

Dome Petroleum sponsored an experiment involving three spills of Prudhoe Bay crude with compressed air under fast ice during the winter of 1979/80 at McKinley Bay NWT. Much of the oil appeared on the surface in June, as the ice surface ablated to expose the trapped oil layer. Brine channel migration was much more pronounced in the spill where the gas volume was substantially lower (quickly leading to defined oil pools as opposed to scattered oil particles under the ice). See Figure 81 below. The greater oil viscosity was also though to be a factor in explaining the difference in migration behavior from the earlier spill at Balaena Bay. The presence of gas injected with the oil had a major effect in decreasing or eliminating the process of oil migration. The McKinley Bay spills showed that trapped oil residing as widely scattered

droplets within the ice is only exposed in large volumes when the surface has completely melted down to the level of the originally trapped oil (Dickins and Buist, 1981).

Figure 81. Initial Surface Appearance of Crude Oil Migrating Through the Ice at the Dome Oil and Gas Under Sea Ice Experiment in Early June 1980

Dickins *et al.* (2008) describe a recent experimental spill conducted with SINTEF and UNIS on Svalbard in March 2006 and the subsequent documentation of oil behaviour. Ice thickness averaged 65 cm at the time of the spill and the spill volume was 3,400 L inside a 100 m^2 circular area contained within a plastic skirt. The weathering of the oil under the ice with respect to vertical migration, evaporative loss and water content was monitored through oil and ice sampling at regular intervals throughout the field period. The oil was first observed on the ice surface under the snow inside the skirted area on April 20 after 24 days under the ice (March 27 to April 20). The rate of bulk oil migration through the ice was monitored by visual inspection of the ice and by analyzing the oil content in ice cores.

The rate of oil surfacing observed in this experiment on Svalbard (Figure 82) makes an interesting comparison with a previous oil-under-ice experiment in the Canadian Beaufort Sea carried out in 1979/80 (Dickins *et al*., 1981). Oil from the first spill in that experiment rose through a similar ice thickness (60 to 70 cm) to reach 100% exposure in approximately 40 days from first appearance under the snow, results very similar to the timing of oil appearance documented at Svea.

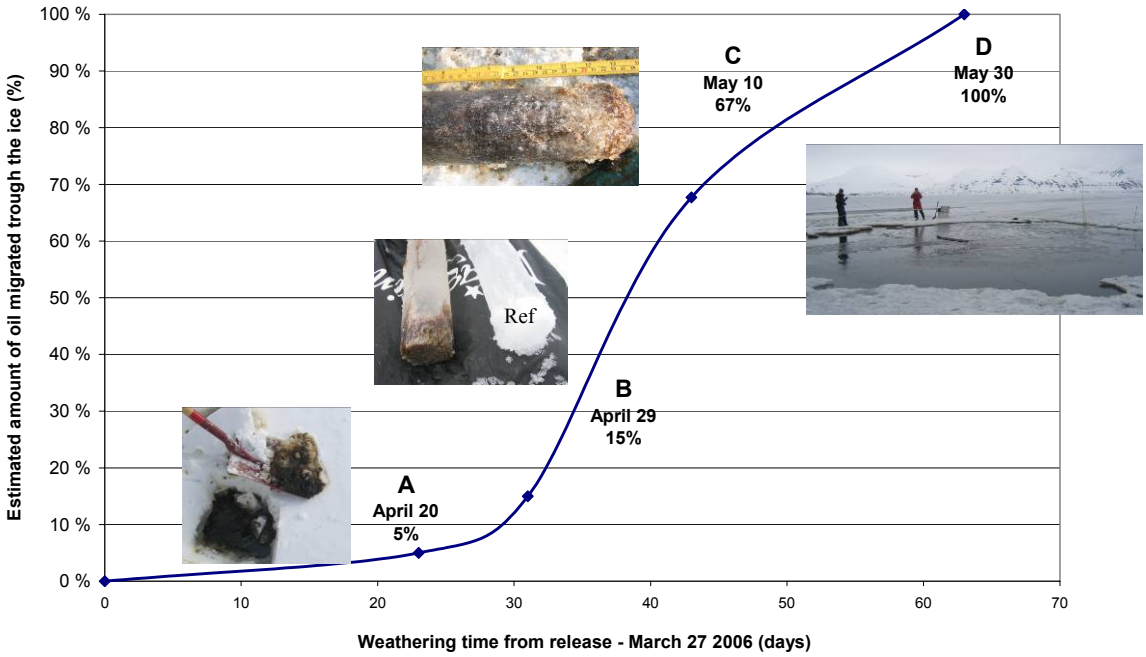

Figure 82. Estimated Amount of Oil Penetrated Through the Brine Channels in the Ice and Available on the Ice Surface during SINTEF's Experimental Spill Under Ice in 2006 Photos show appearance of core at different stages in the migration cycle Source: SINTEF/UNIS

Past Studies: Laboratory and Tank Tests

Numerous other researchers have conducted laboratory and tank tests to complement the limited number of field spills in natural sea ice. Selected examples are highlighted briefly here.

Purves (1978) presents the results of spilling crude oil and methane gas under laboratory grown saline ice. Oil and gas were rapidly released from the sheet when the minimum ice temperature reached –3.6°C. Kisil (1981) conducted a series of small-scale experiments using an 11-liter aquarium, adding oil after first releasing air under the ice. She developed an expression to predict the oil migration rate as a function of ice thermal conductivity, temperatures at the surface and depth of the oil layer, and distance from the trapped oil to the surface. She found that the sheet became porous first to gas and then oil, once the minimum ice temperature reached between –2 and –6°C.

Payne *et al.* (1984) examined the chemical and physical weathering behavior of oil released under a thin sheet (8 cm grease/frazil underlain by 8 cm columnar ice) of simulated first-year ice in refrigerated tank. Once a 5 mm layer of solid columnar ice beneath the oil encapsulated the spill, a thaw cycle was initiated to promote migration. Oil flow rates through the brine channels were measured and compared to theoretical predictions by Cox *et al.* (1980). Cox calculated the minimum brine channel that would allow effective oil migration in seawater as a function of oil/water interfacial tension, contact angle, oil lens thickness, and oil density. The calculated channel diameter in the case of Payne's experiment was 3.6 mm that agrees well with field

observations at Balaena Bay (Norcor, 1975). The rise velocity was determined to be 0.35 mm/sec, agreeing reasonably with an experimental value of 0.7 mm/sec determined by Martin (1979), based on observations of oil rising through 2 m of ice in May 1975 at the Balaena Bay site.

Dickins *et al.* (2005) describes recent experiences with oil spilled beneath a 40 cm sheet of urea ice (artificial sea ice mimicking the natural crystal structure) at CRREL. These tests demonstrated that significant (15 to 18 cm) vertical migration of a low viscosity crude (in this case South Louisiana) could occur within a young, growing ice sheet while air temperatures are still well below freezing (in this case –17°C). Internal ice temperatures at the upper level of oil migration were in the range –3 to –4°C.

Sediment Effects on Oil Migration

The interaction of sediments with sea ice along the Alaskan North Coast is described in detail by Osterkamp and Gosink (1984). Payne *et al.* (1989) conducted a detailed laboratory and literature study of frazil ice and sediment interactions during freeze-up and break-up as part of a NOAA/ MMS OCSEAP sponsored research program. It had been intended to conduct a series of experiments with oiled sediment, but this was replaced with a study of sediment/oil interactions in open water.

High concentrations of sediments in ice routinely occur through a variety of processes thought to include ice keel gouging, flotation by anchor ice releasing from the bottom, direct freezing to the seabed in shallow water with subsequent re-floating, and entrainment of suspended sediments in frazil ice throughout the water column (Figure 83).

Figure 83. Underwater Photograph Showing Extremely Fragile Frazil Ice Crystals Hanging Beneath Fast Ice During an Experimental Spill of Emulsified Oil (visible hanging below the ice in the background) Large partly agglomerated drops of emulsified crude are visible in the foreground Source: Buist *et al.* (1983)

Sediments incorporated within the ice sheet will potentially affect the light transmittance (with potential effects on solar gain and temperature-related oil migration in the spring), mechanical strength and possibly other parameters.

This study focused on documenting any measurable effects of incorporated sediments on vertical oil migration that could be distinguished from the natural variability inherent in dealing with such an inhomogeneous material as sea ice. Apart from a possibility of direct interference to migration by physically blocking individual brine channels, the most likely effect in a natural environment could involve changes to the thermal gradient in the ice sheet during the warming period (related to the increased albedo of contaminated ice). High sediment concentrations could lead to an accelerated warming of the upper levels of the sheet due to solar radiation absorption. This effect could in turn lead to an earlier appearance of oil on the ice surface, especially in the case where a spill occurred early in the growth cycle, resulting in an oil lens in the upper layers of the ice sheet.

11.2 Methods

Brine Channel Migration

Section 4.1 describes the original set of six outdoor tanks constructed outside of Ottawa prior to the winter of 2005/2006. Unfortunately, due to unusually warm winter temperatures, the ice thickness did not reach the specified amount (30 cm) until early March, too late for the oil migration experiments to take place. Some oil was injected beneath the ice in several of the tanks to check the test procedures. A no-cost extension to the contract was requested, and received, to allow the brine channel experiments to be repeated in the winter of 2006/2007. Two additional tanks were obtained to expand the outdoor test tank facility for the add-on study "Sediment Effects on Oil Migration". The expansion to eight tanks was completed and the two new tanks were fitted with submersible pumps for suspending sediment in the water during freeze-up (see Figures 84 and 85). The tanks were sheltered under a raised, opaque tent cover to minimize snowfall on the ice, and to prevent sunshine from melting the ice prematurely. Each tank had a loop of stainless steel wire installed that, when heated by electrical resistance, allowed measurement of the ice thickness with minimal disturbance.

The oil migration experiments utilized eight test pools of four different fresh crude oils placed under meso-scale realistic sea ice sheets grown from water of two salinities of interest: full-salinity sea water (i.e., in the neighborhood of 30‰) and brackish water (15‰) representative of near-shore Beaufort Sea areas such as off the Colville River in Alaska. Two of the tanks contained ice grown with suspended sediments in the water.

Sediments simulating Alaskan North Slope bottom material (1000 ppm of a 50/50 mixture of Cedar Heights ball clay and commercial potting soil) were introduced into tanks 7 and 8 and maintained in suspension through low level turbulent mixing (e.g. a submersible pump) while the water-cooled. Frazil ice was created in the water by adding 125 L of snow to the water in the tanks, and then the mixing was stopped. The frazil was then allowed to rise and accumulate on the surface. This process scavenged a portion of the suspended sediment as the frazil crystals rose, thereby concentrating the sediment in a band of randomly oriented crystals in the upper layers of the sheet. See Figures 86 and 87.

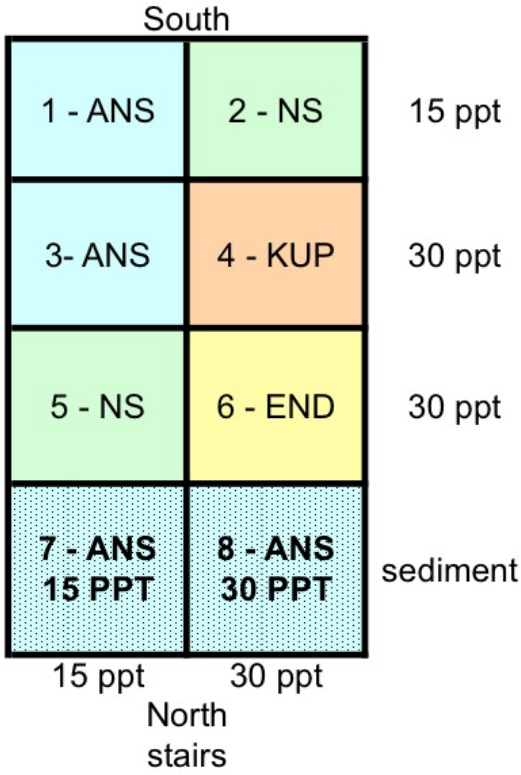

Figure 84. Test Layout for Brine Channel Migration Experiments

Figure 85. View of All Eight Tanks as Utilized During the Winter 2006/07 with Two New Tanks Added After the First Year to Incorporate the Sediment Add-on

Figure 86. Mixing Sediment into Agitated Tanks Prior to Adding Snow

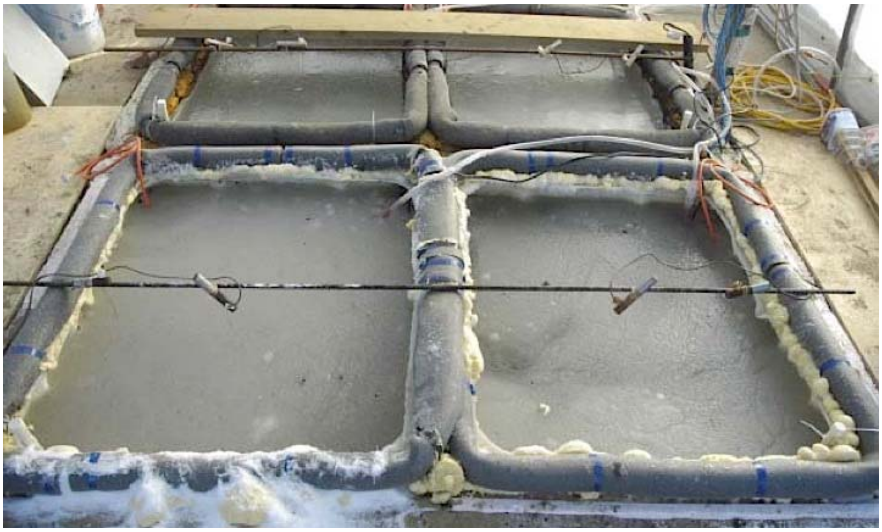

Figure 87. Frazil Ice Accumulated at Surface after 125 L of Cold Snow Added and Pumps Turned Off
Refer to photographs of ice thin sections from the upper ice surface in Tank #7 (left) for a view of the small grain size and random crystal orientation associated with the rapidly freezing frazil layer

Approximately one litre (an average under-ice coverage of 1 mm) of each of the oils was placed under ice in the tanks on February 7, 2007. In practice, the ice surface was not flat and the oil tended to congregate into thicker films in the centre or around the tank edges depending on the under-ice curvature. The variability in ice thickness at the time is discussed below.

The oil was encapsulated by further natural ice growth of 15-20 cm below the oil in response to the ambient sub-zero environment until the melt phase began (see climate records under Results following). The ice thickness was monitored at regular intervals. The initial intent was to attempt *in situ* oil sampling during the migration process by drilling into the oil layer. This technique was later judged to present too great a risk of disturbing the natural processes and not executed. A second set of experiments was conducted in the SL Ross indoor tank to collect data on weathering of encapsulated crude oil in brackish and sea ice.

An independent examination of the ice structure was carried by the National Research Council Canada in February 2007 (Johnston, 2007). A series of cores extracted from the SL Ross indoor tank and the outdoor tanks were used for temperature (in situ), salinity measurements (melted sections), and horizontal and vertical thin section analysis (grain size and crystal orientation with depth). Freezing thin pieces of ice to a glass plate and polishing the uppermost surface of ice with a microtome prepared thin sections. The sections were then photographed through a polarizing filter to delineate the crystal structure (see examples following and in Appendix H). This is a standard procedure used for decades by Arctic engineers and scientists in evaluating the internal structure of ice sheets.

Figures 88 and 89 show examples of the coring activities on February 15, 2007 at the outdoor tanks. Cores were deliberately limited to 30 cm in order not to penetrate the ice water interface and potentially create a pathway for premature oil surfacing. One 28 cm long core (#5) taken in Tank #7 showed oil at the bottom of the ice and resulted in oily water rising in the drill hole (no flooding of the surface).

Figure 88. Extracting Cores from the Outdoor Test Tanks

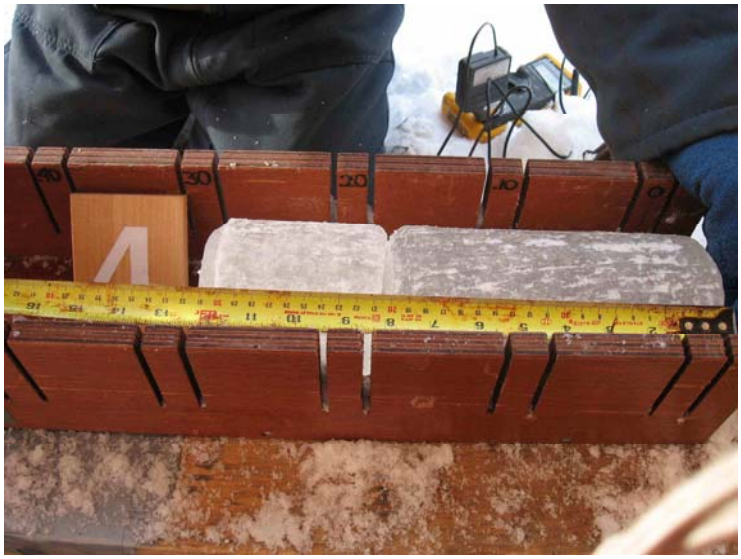

Figure 89. Example Ice Core #4 Extracted from Tank #3, 30‰ Water

Time-lapse video cameras were mounted to document the surface appearance of the ice in each tank from March 1 through April 29, 2007 as the oil was appearing on the surface. The videos are split into 4 time periods March 1-15, March 16-31, April 1-15 and April 16-29. Two Web cams were used to each cover groups of four tanks (Annexes). As oil accumulated on the surface of each tank, It was recovered using pre-weighed sorbent pads, which were subsequently reweighed to determine the mass of oil on the surface of the ice.

Evaporation of Encapsulated Oil

It had originally been planned to drill small holes into the ice in the outdoor tanks and recover samples of oil for analysis at ESDT to quantify the amount that evaporated during the encapsulation period. Once the oils were placed under the ice at the outdoor tanks it was decided to not disturb those samples and let them appear naturally (a hole drilled to obtain samples may have artificially accelerated appearance of the oil on the surface). Instead, the indoor refrigerated tank was used to encapsulate the oils under ice sheets of different salinities for a period of 50 days.

In order to accomplish this, six plastic-lined cells of 1 m^3 volume were positioned in the tank containing 15‰ salt water. The cells were constructed using a cubic frame of ¾-inch plastic water pipe inserted into large, industrial clear plastic film bags. Figure 90 shows the construction of the cells and their positioning in the tank. Once the cells were positioned in the tank, additional salt was added to three of them and mixed with an air bubbler to increase the salinity to 30‰. The lids were then placed on the tank and the chiller started to freeze an ice sheet. Once the sheet reached 30 cm thick, three crudes (ANS, Kuparuk and Northstar) were injected under the ice in the cells (one crude in each 15 and 30‰ cell). After 50 days encapsulation, a chain saw was used to dig down to the oil (Figure 91) and samples were collected for analysis at ESTD.

Figure 90. Construction and Installation in Tank of Cells for Evaporation in Ice Experiments

Figure 91. Extraction of Oil Samples for Evaporation Analysis after 50 Days Encapsulation

11.3 Results and Discussion

Ice Growth and Climate Data

Figure 92 shows the air temperature record at the outdoor test site from January to the end of April 2007. Apart from an unusually warm period at the beginning of the winter, temperatures were consistently below freezing from mid-January to February 28. There was no appreciable accumulation of thawing-degree days (TDD) until March 15 at which point the ice melt phase began, as indicated In Figure 93 in a combined plot of ice thickness and TDD.

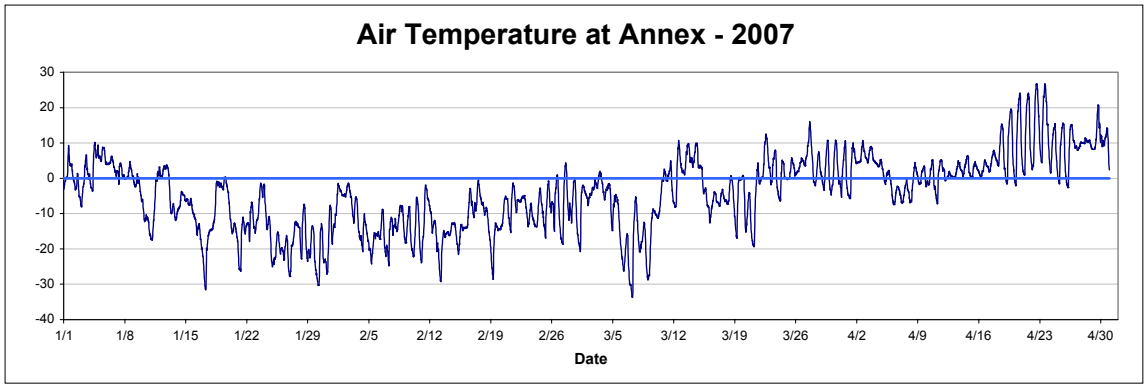

Figure 92. Air Temperature Record from the On-site Weather Station

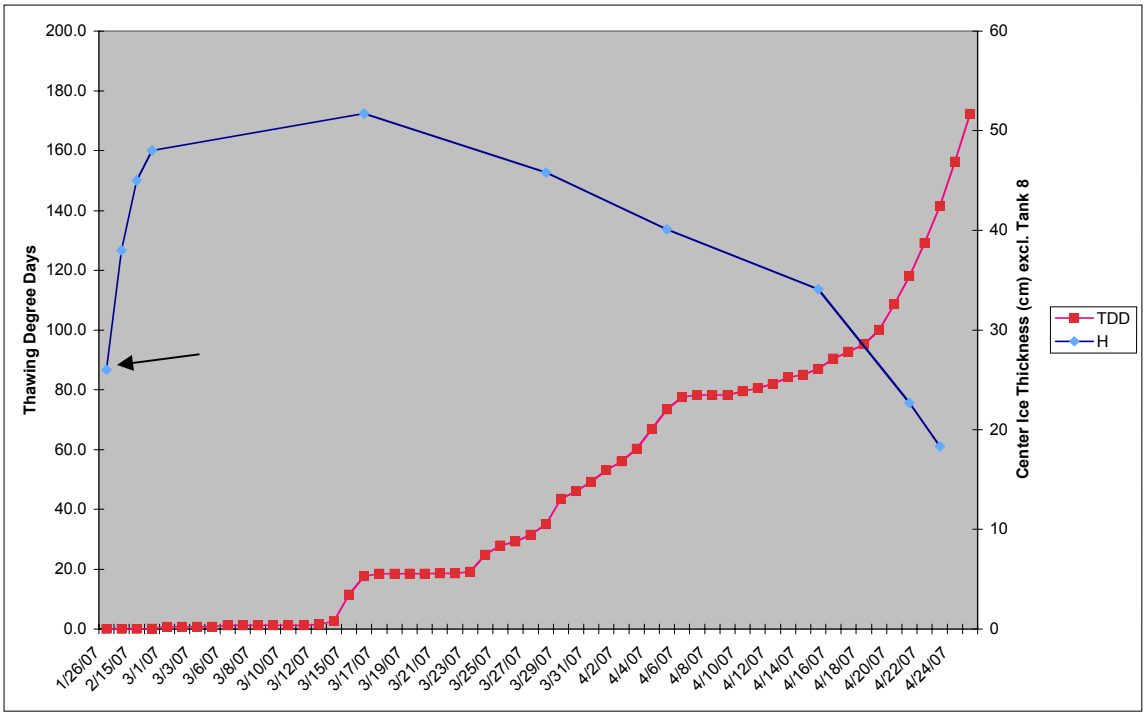

Figure 93. Plot of Thawing Degree Days (C°) Derived from On-site Weather Station Records and Ice Thickness (average of center tank readings excl. Tank 8)

Table 24 summarizes the variability in ice thickness at the centre and corner of each tank at the time of oil introduction on February 7, 2007 (indicated by the arrow in Figure 93 above). The two thickness readings are important in that they provide some indication of the likely oil distribution under the ice following injection. In several cases, the natural tendency of the oil to pool in the under-ice hollows greatly clearly affected the migration patterns observed on video cameras.

Table 24. Ice Thickness Readings at Time of Discharge – February 7, 2007

Test Tank #	Center Ice Thickness (cm)	Side Ice Thickness (cm)
1	36	35
2	40	41
3	43	41
4	31	33
5	45	43
6	32	33
7	36	64 - ERROR
8	30	27

The relative thickness readings in Table 24 indicate that at least a portion of the oil could have pooled towards the center in Tanks # 2, 4 and 6 and towards the sides in Tanks # 1, 3, 5 and 8. Note: The side thickness measurements in Tank #7 are suspect due to a problem with the thickness wire system.

Table 25 summarizes the maximum ice thickness attained at the peak of the ice growth period, mid-March, in each of the tanks.

Table 25. Ice Thickness Readings at the End of the Growth Period – March 16, 2007

Test Tank #	Center Ice Thickness (cm)	Side Ice Thickness (cm)
1	53	50
2	54	56
3	54	52
4	45	48
5	55	52
6	48	48
7	55	ERROR
8	37	40

In comparing Tables 24 and 25 it is interesting to note that the ice thickness became less variable towards the end of the growth cycle, after the oil injection. The pattern of significantly thicker ice in Tanks 2, 3 and 5 in early February was not apparent at the end of the winter. The most noticeable deviation from the "typical" growth pattern occurred in Tank # 8 with significantly thinner ice throughout the experiment. There is no apparent reason for this difference given the similarity in preparing the two sediment tanks, #7 and 8 and lack of any measurable difference in ice thickness related to water salinity in the other six tanks.

Ice Structure

Five ice cores were extracted from Tank #'s 1, 3 and 7 (Johnston, 2007 – in Appendix H). Overall, the ice that was grown in outdoor tanks was found to closely mimic the first-year ice observed in the Arctic. When the ice was allowed to develop undisturbed, columnar grained ice formed within several centimeters of the uppermost ice surface, as it does in nature. The ice that formed in the 15‰ water was comparable to sea ice grown from brackish water, with its larger grains, less entrapped salt and smoother grain/sub-grain boundaries. Sea ice that was grown from 30‰ water as expected, had smaller grains; more entrapped brine; and, jagged grain boundaries. The 30‰ water resulted in ice that was more representative of the Arctic first-year ice that forms in undisturbed, sheltered bays, than the ice grown from 15‰ water. When sediment and frazil were introduced to the tank, the columnar grains developed later (further from the top ice surface), and were smaller than when the water was left undisturbed. As such, the frazil-induced ice was similar to the first-year ice that forms under turbulent conditions in the Arctic.

There were differences between the ice grown in the outdoor tanks and in the indoor tank at the SL Ross lab. This is not surprising, considering the sensitivity of ice structure to growth rate and growing conditions. Grain size of the ice formed in the 30‰ water was similar for both the indoor and outdoor tanks, but the ice formed from the 15‰ water was different comparing the two locations. The surface layer of ice from the outdoor 15‰ tanks had much larger grains and a lower salinity than ice in the indoor 15‰ cells. The ice grown in the 30‰ indoor cells had salinities similar to Arctic first-year ice (in the range of 4 to 6‰); however, the 30‰ outdoor tanks produced lower ice salinities. The ice with the frazil and suspended sediment had higher salinities towards the surface (8 to 10‰), which is in keeping with Arctic first-year ice that has a surface layer of frazil.

Results indicate that the model ice can be made effectively either indoors or outdoors. That said, the limited measurements made with a small sample set of cores seem to indicate that the indoor cells provided more repeatable results, where the conditions were more easily controlled. The main difference between the model ice examined here and naturally grown sea ice is that the model ice did not exhibit the characteristic "C-shaped" salinity profile that is commonly observed in Arctic first-year ice (higher at top and bottom than the center). This is most likely because at the time of sampling, the ice sheet was already relatively warm and more representative of an Arctic spring than winter condition. The mid-sheet (17-23 cm depth) internal ice temperatures in the outdoor tanks on the day of sampling was $\geq$ -7°C. Under these conditions, much of the internal brine has already drained through the sheet explaining the relatively low salinity at the surface and elevated salinities at depth measured in the two cores from clean ice in Tanks 1 and 3 (no sediments). In the core taken through the sediment –laden

ice, the salinities in the upper 15 cm of the sheet were 4-6‰ higher than the ice at depth. This corresponds to the region of randomly oriented crystal structure clearly visible in the thin sections prepared by Johnson (2007). This band of very different structure in the upper layers of the sediment-contaminated ice is caused by the presence of suspended frazil at freeze-up (Figure 87 above). Even with the relatively warm ice, it appears that brine is more effectively trapped and temporarily prevented from draining down by the lack of a defined vertical brine channel network. Full details of the ice core analysis are provided in the NRC report in Appendix H. Examples of the thin section photographs and salinity/temperature profiles are extracted from that report and provided below in Figures 94, 95, 96, 97, 98 and 99.

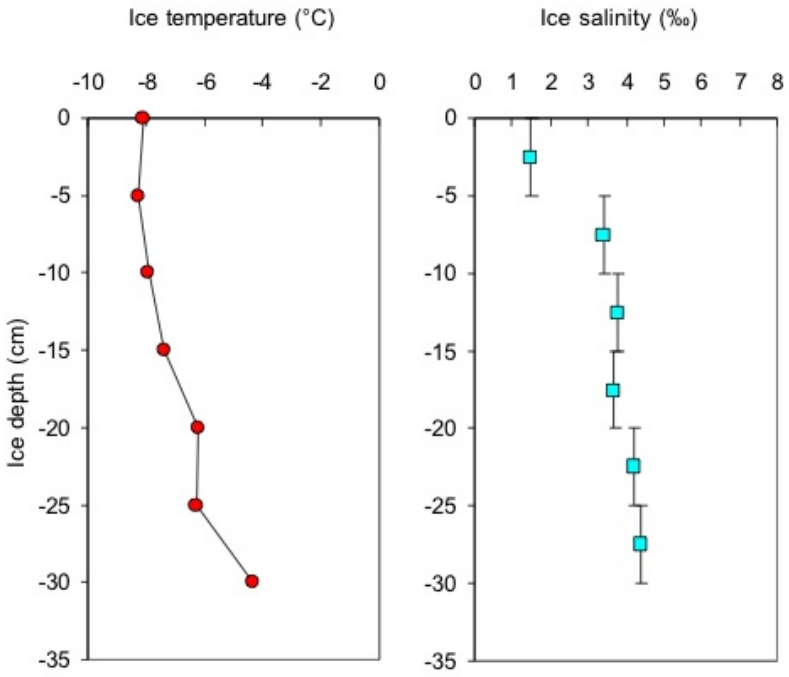

Figure 94. Tank #1 Ice Salinity and Temperature
Lack of substantial difference in internal ice salinity with 15‰ water vs. 30‰ water (figure following) can be explained by relatively warm internal ice temperatures giving rise to substantial brine drainage before the cores were extracted

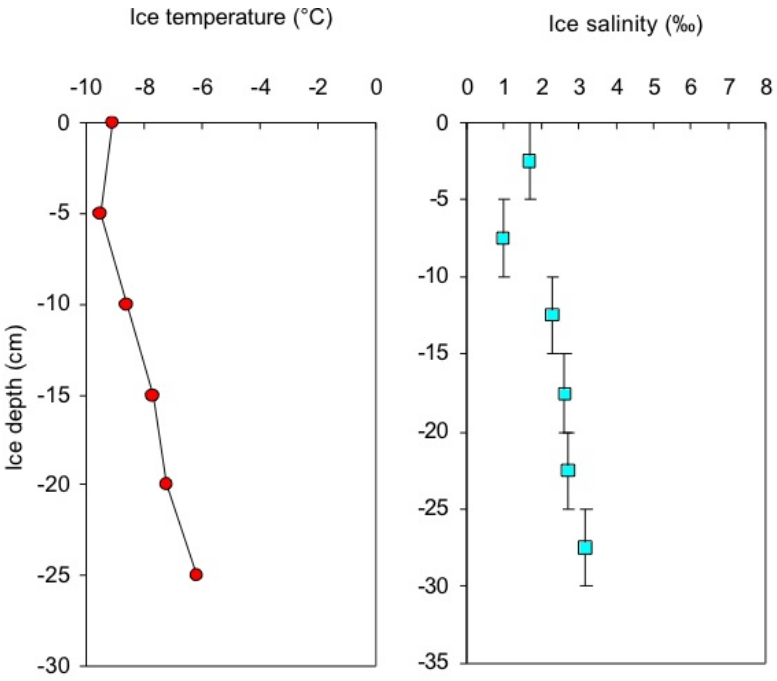

Figure 95. Tank #3 Ice Salinity and Temperature
Low overall bulk salinity and elevated relative salinities in the lower levels indicate significant brine drainage has already occurred

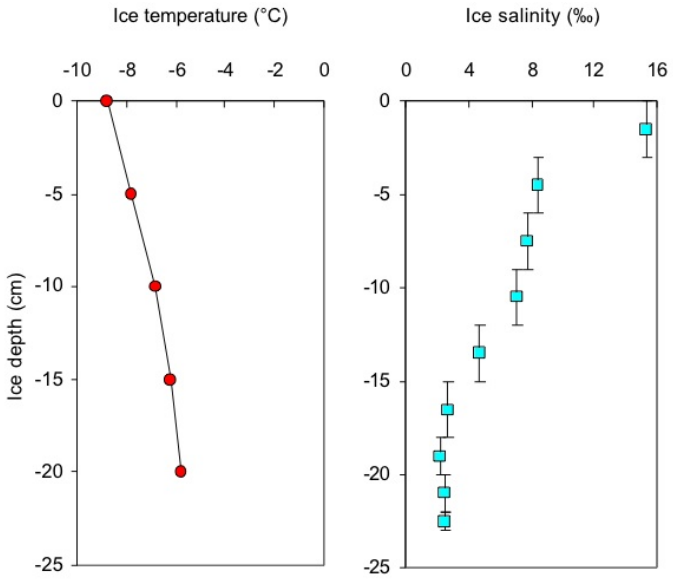

Figure 96. Tank #7 Ice Salinity and Temperature
Note the elevated salinities in the upper 13 cm corresponding to the region of random crystal structure shown in the thin section photograph

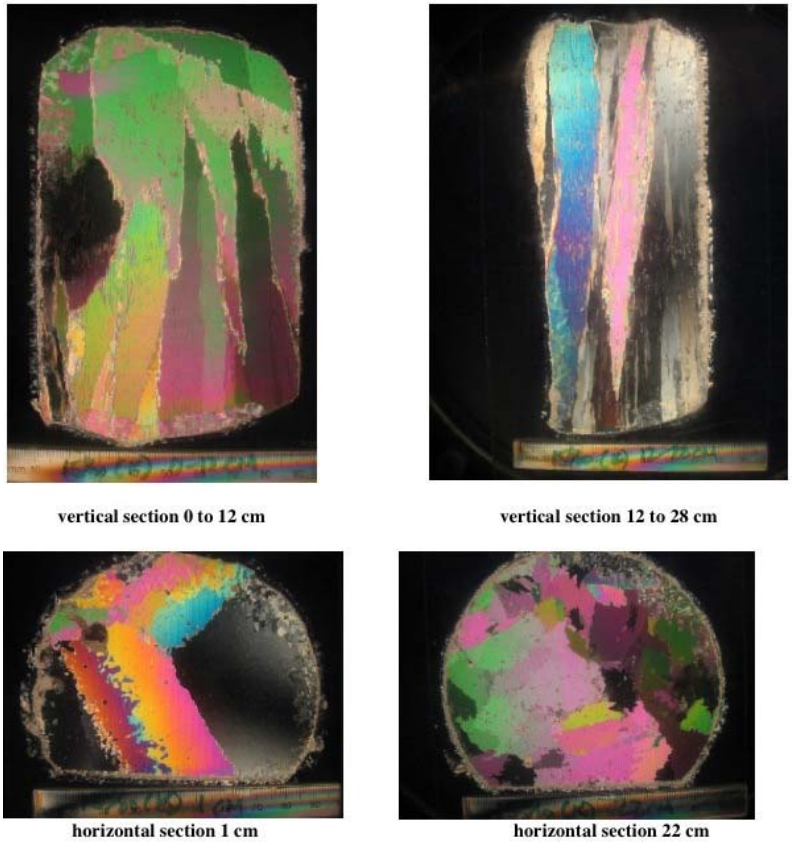

Figure 97. Tank #1 (15‰) Ice Microstructure
Note the significantly larger crystal size and less jagged grain boundaries than ice grown from 30‰ water (below)

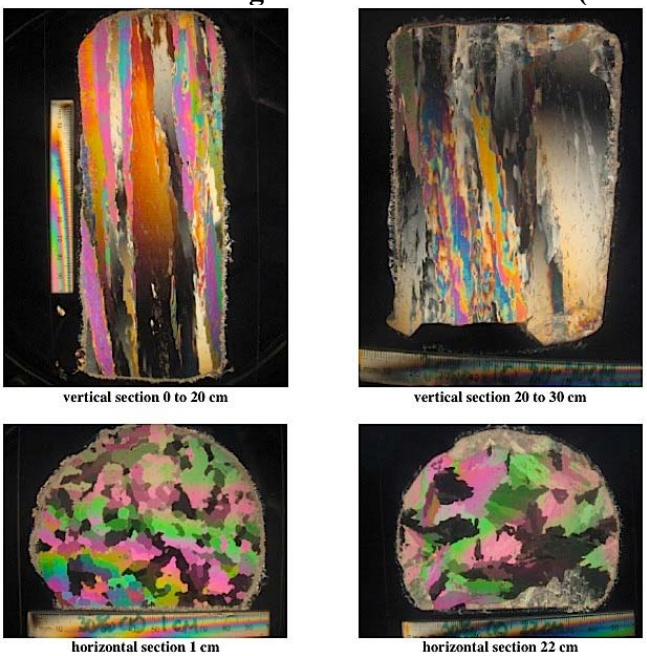

Figure 98. Tank #3 (30‰) Ice Microstructure
Compared with the brackish ice in Tank #1 (previous figure) the crystals are smaller in size and more jagged in terms of grain boundaries

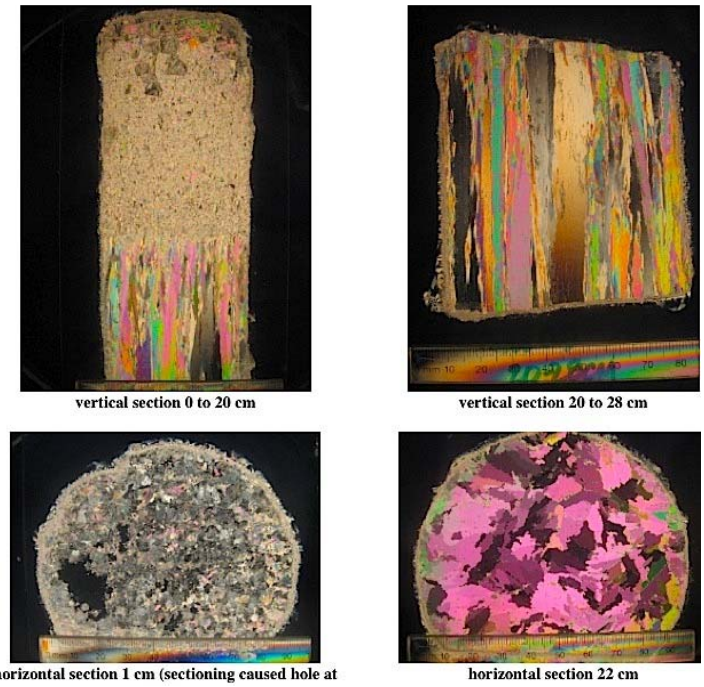

Figure 99. Tank #7 (15‰) Ice Microstructure

Note the randomly oriented crystal structure associated with frazil ice in the upper 12-13 cm. Crystal structure at lower depths resembles thin sections of 30‰ ice grown without frazil or sediment (Tank 2). This could be explained by a more rapid initial growth initiated by the frazil and giving rise to smaller grain size and elevated salinities (faster growing ice traps more salt).

Migration Data Analysis

One of the six ice cores extracted on February 15, 2007 in Tank 7 (ANS with sediment) encountered small volumes of oil at the 26-28 cm depth. The ice thickness at time of oil introduction into this tank on Feb 7 was ~36 cm (center reading only available). This indicates that an initial migration corresponding to the skeletal layer depth of 8-10 cm probably occurred immediately during or soon after spillage. This phenomenon of skeletal layer saturation has been observed in previous field and tank spills.

Interestingly, a 30 cm core taken in Tank # 1 on the same day did not encounter any evidence of oil even though according to records taken on day of oil injection, the ice thickness in both tanks (1 and 7) were almost identical. A possible explanation is that the ice thickness at the side of Tank 7 (no data available) was more than a few cm thinner than the centre leading to a slightly elevated level of initial migration (just enough to show on the bottom of 28 cm core) compared to Tank #1.

Beginning on February 25, 2007 and continuing to April 29, oil was sorbed from the surface of the ice in each tank on up to 20 occasions and a running tally kept of the cumulative % volume surfaced from each spill (see data spreadsheet in Appendix H.

The video camera footage was examined to understand the evolution and progress of the migration and to distinguish between two very different phenomena:

1. Natural surfacing indicated by the oil visibly appearing from one or more holes in the central area of the tank (away from the side walls); and
2. Oil surfacing at the interface between the ice sheet and the plastic tank walls, interpreted as an unavoidable artifact of the test set-up.

Table 26 shows the results of analyzing the video footage to distinguish between periods of natural and unnatural (side leakage) surfacing. The results of this analysis were then applied to the overall database of % oil surfacing (referred to above). In some cases, these findings led to a decision to completely eliminate two tanks (#2 and #5) from further analysis. In three cases (#1, 3 and 4) it became necessary to subtract the oil volumes that were observed to surface primarily through side leakage and then normalize the totals to correct for this unnatural pathway. Subsequent plots embody these corrections.

Table 26. Video Camera Interpretation of Migration Pathways and Timing

Dates	Tank Numbers							
	1	2	3	4	5	6	7	8
3/4 to 3/12	Not natural	Not natural	Not natural	minor ~0	Not natural	None	None	None
3/13	Not natural	Not natural	Not natural	Side - 55%	Not natural	None	None	Natural
3/15	Side - 56%	Not natural	Side - 56%		Not natural	None	None	Natural
3/16 to 3/21	No surfacing	Not natural	Natural	Natural	Not natural	None	None	Natural
3/22 to 3/24	Side leaks	Not natural	Natural	Natural	Not natural	None	None	Natural
3/24 to 3/31	No surfacing	Side - 68%	Natural	Natural	Not natural	None	None	Natural
4/1 to 4/15	Most natural	None	Most natural	Most natural	Not natural	None	Natural	Natural
4/16 to 4/31	Most natural	Not natural	Most natural	Most natural	Not natural	Natural	Natural	Natural
Est. Date when melt = H at spill - 10 cm	20-Apr	24-Apr	24-Apr	15-Apr	23-Apr	17-Apr	18-Apr	15-Apr
Total % Remaining at end of migration	>>17	>>25	>>2	>>8	>>46	100	84	44
	Data used to plot surfacing (normalized to only include periods with natural surfacing)							
	Data invalidated due to lack of any natural migration observed on video							

In the same table, an effort was also made to compute the % of residual oil remaining at the point where the ice surface had melted to within 10 cm of the original oil layer (incorporating the porous ice zone of initial oil migration observed soon after oil release in previous field trials). Not surprisingly, the results were highly variable and in some cases could only be expressed as >> than a certain value, reflecting the fact that a substantial amount of oil surfaced at the ice tank side wall, thereby artificially depressing the true residual volume at final exposure.

Once the valid time period was identified when natural migration occurred in each tank, the following two plots were prepared to compare and contrast natural oil surfacing rates.

- % Surfacing vs. Date (can also be viewed vs. TDD accumulation)
- % Surfacing vs. the Distance to the Original Oil Layer (assuming all melt from the top down)

It is difficult to interpret the affect of oil type (viscosity) on migration rates in a simple chronological plot (Figure 100), because of the inherent variability in ice thickness at the time the oil was spilled (27 to 45 cm) and the subsequent melt rates between the various tanks. This variability led to significant differences between tanks in the vertical path length (distance the oil had to travel to reach the surface) on any given date. Consequently, a simple comparison of oil surfacing as function of time is misleading.

Figure 101 was prepared in an effort to remove the ice variability factor and place each tank on a level baseline by relating the cumulative volume of oil on the surface to the distance from the original oil layer (ice thickness on February 7) to the ice surface, recognizing that equivalent distances will occur on significantly different dates (±5 days) according to the individual melt rates etc.

Principal observations gained from the migration data analysis comparing three oils (ANS, Kuparuk and Endicott) are that:

- The most rapid migration rate is clearly associated with the lightest, least viscous oil and ice formed from 30‰ water: ANS. This finding makes intuitive sense in that ice formed from true seawater has a higher area density of brine channels than brackish ice and the oil with the least viscosity and density will move more freely through those channels to the surface.
- The lowest migration rate (essentially zero) is associated with the oil having by far the greatest viscosity and density: Endicott. In this case, there was no migration in the true sense of the word, and exposure of the oil all took place in the last few days of the project when the ice melted sufficiently from the surface to expose the oil still trapped at its original position in the sheet. Note: that Endicott has a pour point of 12°C making it impossible for the oil to flow through any vertical channel in the ice.
- Kuparuk in ice formed from 30‰ water experienced a slower migration rate than ANS in similar ice. This observation fits with the relative oil properties, Kuparuk at 0°C being more dense (s.g. 0.93 vs 0.88) and more viscous (211 vs. 17.6) than ANS.
- The thin section analysis clearly showed the effect of water salinity on the subsequent crystal structure with many more brine channels being potentially available in ice formed from water of higher salt content. This difference is borne out in the plot

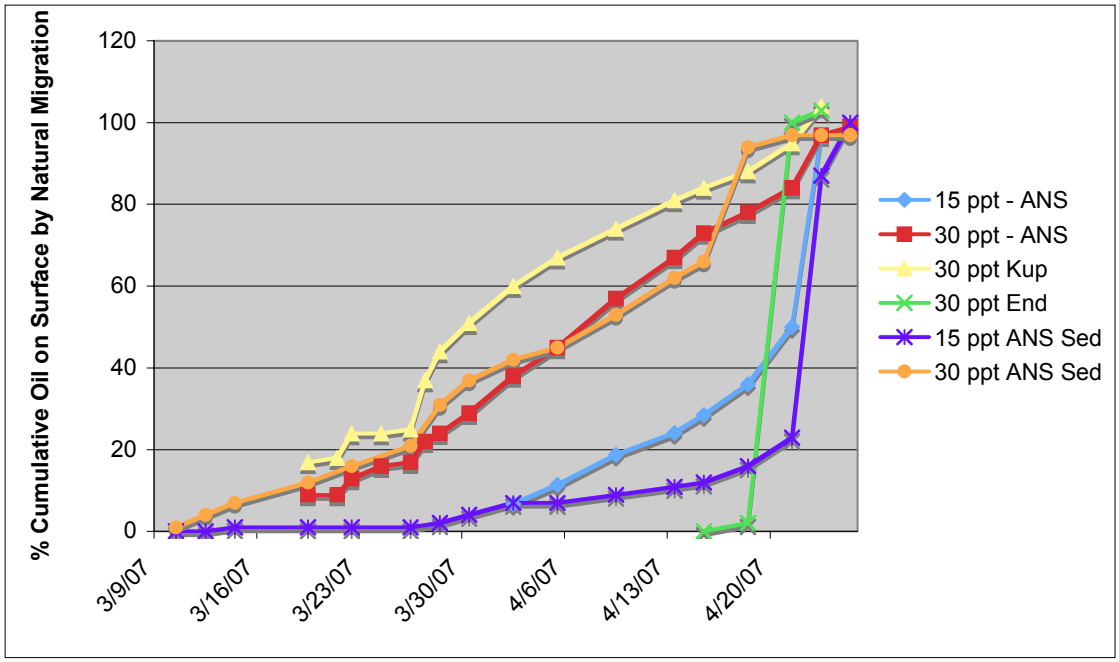

Figure 100. Cumulative Oil Volume on the Surface (natural migration only) Corrected for Periods of Predominantly Side Leakage at the Tank Walls, vs. Time
The same plot is also available with TTD instead of date on the bottom

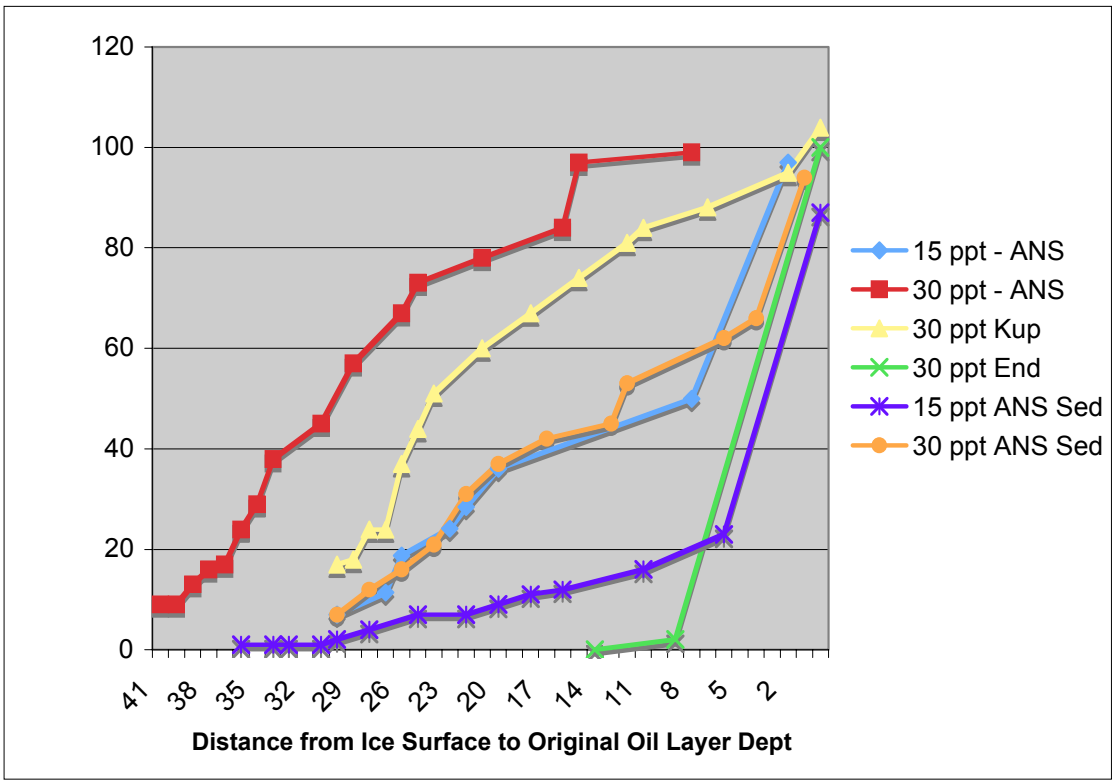

Figure 101. Cumulative Oil Volume on the Surface (natural migration only) Corrected for Periods of Predominantly Side Leakage at the Tank Walls, vs. the Distance From the Ice Surface to the Original Oil Layer Depth (assuming all melt from the top down)

comparing the two ANS migration rates with 30 and 15‰ water. It appears that the effect of salinity on migration rate is equivalent to the effect of incorporating sediment into the ice (comparing ANS 15‰ clean ice to ANS 30‰ with sediment).

- The combination of low salinity water and sediment produced the lowest actual migration rate (discounting Endicott where the oil was exposed in batch mode at the end of the melt phase). The 12-5 cm cap of frazil ice in the sediment tanks likely played an important role in blocking or inhibiting oil migration for the first three weeks of the melt cycle (mid-March to early April).

As shown in Table 26 above, a substantial amount of oil (>25%) can remain as a residual volume associated with the original oil layer. This oil is only exposed at the surface in the final few days of the melt process as the ice surface physically melts down to meet (within 10 cm) the oil. The greatest residual volume (excluding Endicott at 100%) was associated with Tank #7 (ANS 15‰ with sediment) with 84% of the oil exposed through this final melt process rather than migration.

Evaporation of Encapsulated Oil

As discussed earlier (Section 9.6), the analysis of the samples sent to ESTD in 2007 was done with different GC equipment than the samples sent to ESTD in 2005. Unfortunately, samples of the fresh crudes were not re-analyzed with the newer GC and thus no baseline trace was available with which to calculate the Weathering Index for the 2007 sample set. In order to save as much of the 2007 data as possible, the GC results from the encapsulated crude oil in the 15‰ ice were employed as the "fresh" oil baseline from which the Weathering Index for the other 2007 samples were calculated. It was not possible, therefore, to calculate meaningful Weathering Index values for the samples of crude encapsulated in the ice in the SL Ross tank.

Alternatively, the degree of weathering of the encapsulated samples was estimated qualitatively by visually comparing the GC traces of the 2007 samples with the traces of the fresh crudes done in 2005.

Figures 102, 103 and 104 compare the fresh oil GC traces done in 2005 with the traces for the oil samples removed from the ice in the SL Ross tank after being encapsulated for 50 days. In each case, the GC trace on the bottom left is for the sample encapsulated in 15‰ ice, and the GC trace on the bottom right is for the sample encapsulated in 30‰ ice. By carefully examining the highlighted area of the trace at the left (the region of the lightest, most volatile hydrocarbons) it is evident that very little evaporation occurred over the time that the oil was encapsulated.

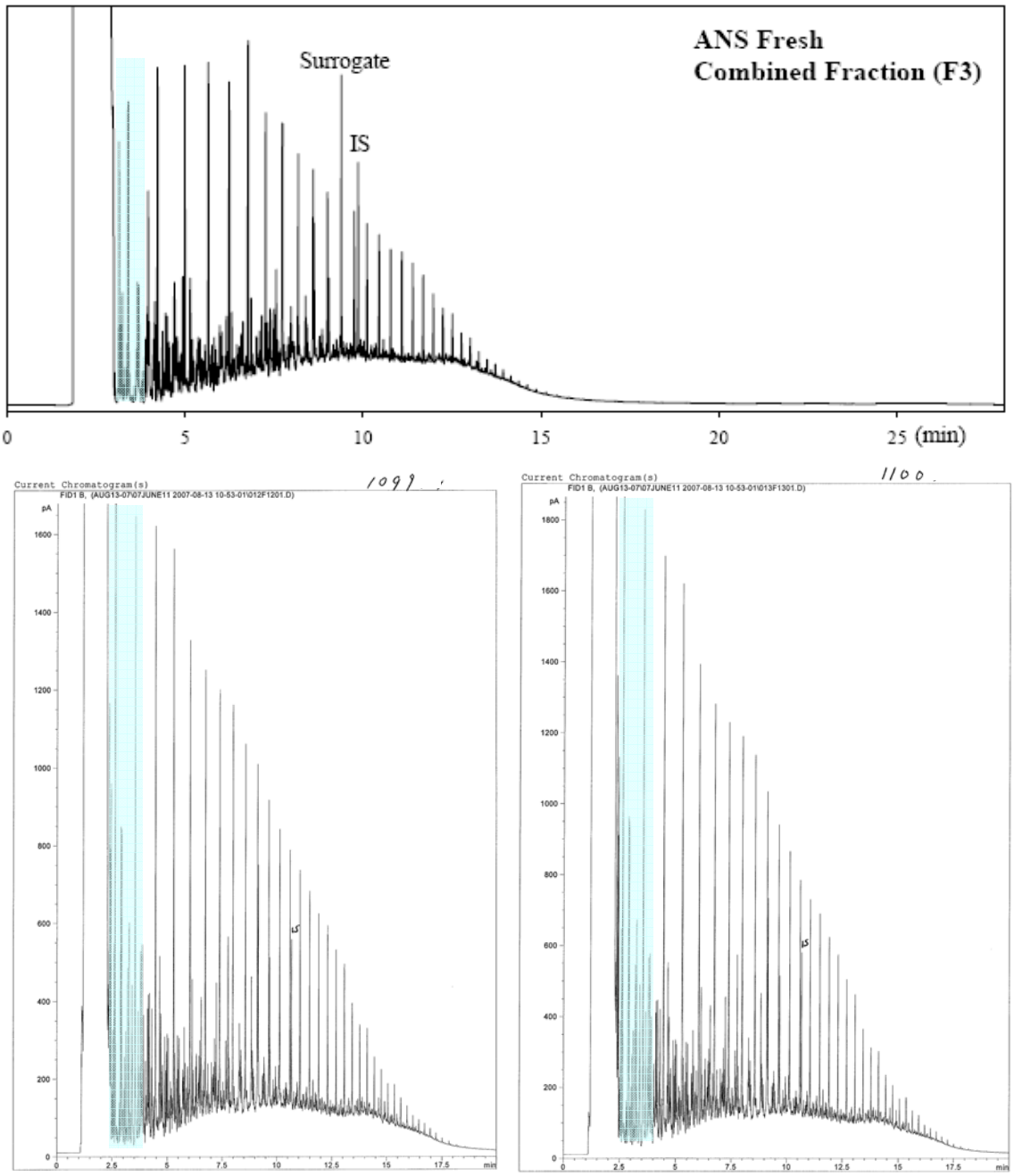

Figure 102. Comparison of GC traces for Fresh ANS Crude Oil from 2005 with ANS Crude Oil Samples Removed from Ice after 50 Days in 2007

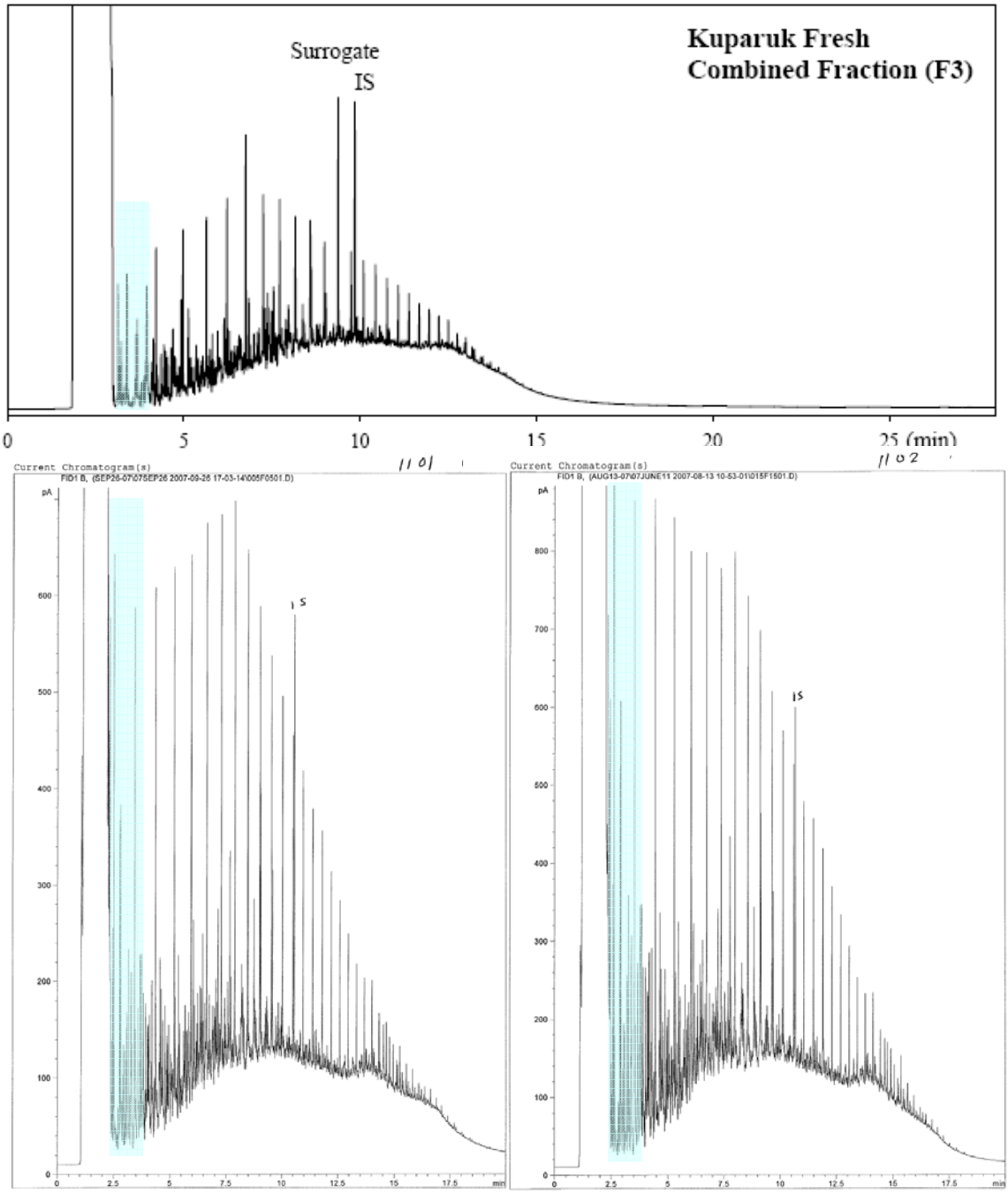

Figure 103. Comparison of GC traces for Fresh Kuparuk Crude Oil from 2005 (top) with Kuparuk Crude Oil Samples Removed from Ice after 50 Days in 2007 (bottom)

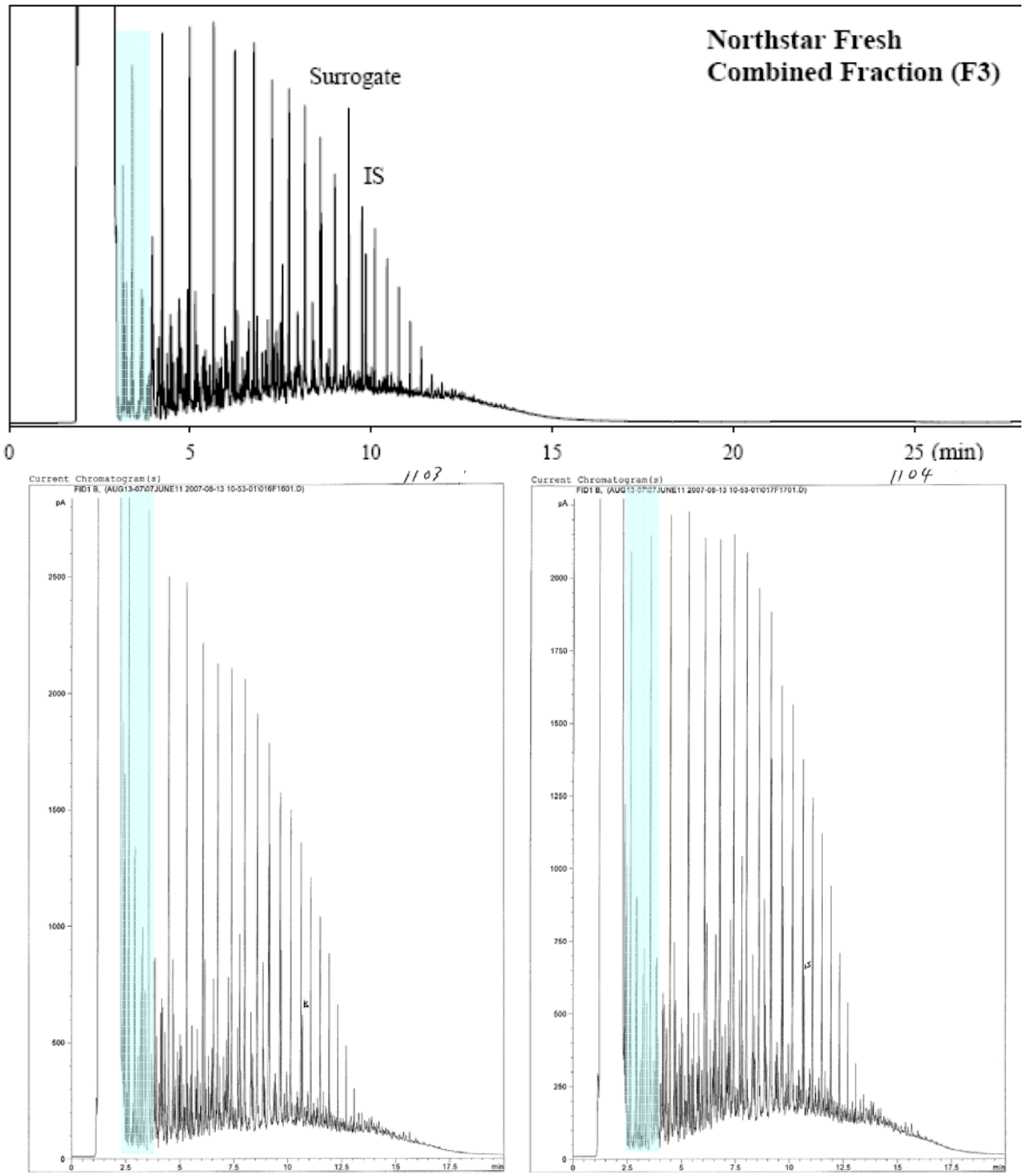

Figure 104. Comparison of GC traces for Fresh Northstar Crude Oil from 2005 (top) with Northstar Crude Oil Samples Removed from Ice after 50 Days in 2007 (bottom)

12.0 SUMMARY

The objective of this research was to generate experimental data that could be used to validate weathering algorithms and computerized oil weathering models in the presence of ice and snow. More specifically the goals of the experiments were:

1. For low and high pour point oils, to measure emulsification, evaporation, spreading, under-ice movement, slick thickness, and oil composition in an ice field and in snow on top of sea ice.
2. To develop a database on oil weathering in ice fields for use in model validation.
3. Use these data in concert with other oil-ice weathering data to validate and enhance or develop new algorithms of oil weathering in ice.

The study goals were achieved by conducting five series of small-scale experiments, over a period of three years, to generate data on:

1. Slick Thickness on Cold Water
2. Spreading on Ice and in Snow
3. Evaporation in Ice and Snow
4. Migration Rates through Brine Channels
5. Formation of Water-in-Oil Emulsions in Broken Ice

The experiments were preceded by a comprehensive spill-related characterization of fresh and wind tunnel weathered samples of each of the four crude oils utilized. The four crude oils were obtained from the North Slope of Alaska and represented a wide range of physical properties: Alaska North Slope sales crude from Pump Station #1 on the TAPS pipeline, Northstar sales crude, Endicott sales crude, and Kuparuk sales crude. The samples were collected in the fall of 2004 and used for all the experiments over the three-year experimental period.

These experiments were conducted at three facilities:

i. An outdoor test facility near Ottawa constructed using insulated, IBC shipping containers as the test tanks each containing 1 m^3 of salt water.
ii. An indoor, 11-m^3 wind/wave tank at the SL Ross Lab specially modified: to incorporate a refrigerated cold air system to allow precise air temperature control to –30°C; to allow the growing of substantial thicknesses of sea ice; and, to generate under-ice water currents.
iii. The 10,000-m^3 Ohmsett Facility in Leonardo, NJ, outfitted with large-capacity industrial water chillers to ensure freezing water temperatures.

12.1 Pour Point Effects

In many of the small-scale experiments (primarily the spreading and evaporation test series), particularly at colder test temperatures, one or more of the crude oils had a pour point (the temperature at which the oil ceases to flow in a test tube tipped sideways) above the ambient temperature. The results of these tests often do not correlate with the results of the experiments with the other crude oils and the results were not used in the algorithm selection process. This is because oils whose pour point exceeds ambient temperature have unusual physical characteristics. As these oils cool wax particles begin to precipitate from solution in the bulk oil

and eventually, in the absence of external mixing energy, form a polymer-like matrix in the oil that renders it a gel-like semi-solid. This has two major effects from the perspective of the tests conducted here:

- The oils develop a resistance to starting to flow (called a yield stress) and become non-Newtonian fluids (typically they exhibit pseudoplastic rheology – shear thinning, and become thixotropic – their viscosity is time dependant). These changes greatly reduce, or prevent, spreading of the oil on water, on ice and through snow. At present there is no way to model this; however, in most situations the gelled oil just does not spread at all.
- The onset of the internal wax matrix greatly restricts diffusive movement of the volatile molecules through the slick to the air/oil surface that changes the way in which the oil evaporates. This reduced evaporation can be effectively modeled by using an internal resistance to mass transfer.

12.2 Recommended Algorithms

The following algorithms are recommended, based on the best fit of the experimental data from the respective experiments to various theoretical equations.

Equilibrium Thickness of Oil on Quiescent Cold Water after Fay (1969)

$$h_\infty = \left(\frac{\rho^2 \nu D^3 V^2}{\sigma^2} \right)^{1/8}$$

Where: $h_\infty \equiv$ final slick thickness [cm]
V ≡ Volume of oil [g/cm^3]
D ≡ Molecular diffusivity of oil [cm^2/s]
≈ 1 x 10^{-4} cm^2/s
ν ≡ kinematic viscosity of oil [cm^2/s]
ρ ≡ density of water [g/cm^3]

Spreading on Cold Water Fay and Hoult (1971)

	One-dimensional	**Axi-symmetric**
Gravity-Inertia	$l = k_{1I}(\Delta g A)^{1/3} t^{2/3}$	$r = k_{2I}(\Delta g V)^{1/4} t^{1/2}$
Gravity-Viscous	$l = k_{1V}\left(\frac{\Delta g A^2}{\nu^{1/2}}\right)^{1/4} t^{3/8}$	$r = k_{2V}\left(\frac{\Delta g V^2}{\nu^{1/2}}\right)^{1/6} t^{1/4}$
Surface Tension-Viscous	$l = k_{1T}\left(\frac{\sigma^2}{\rho^2 \nu}\right)^{1/4} t^{3/4}$	$r = k_{2T}\left(\frac{\sigma^2}{\rho^2 \nu}\right)^{1/4} t^{3/4}$

	One-dimensional	Axi-symmetric
Gravity-Inertia	$k_{1I} = 1.5$	$k_{2I} = 1.14$
Gravity-Viscous	$k_{1V} = 1.5$	$k_{2V} = 1.45$
Surface Tension-Viscous	$k_{1T} = 1.33$	$k_{2T} = 2.30$

Where: $l \equiv$ the length of a 1-dimensional slick [cm]
$r \equiv$ the radius of a 2-dimensional slick [cm]
$k \equiv$ proportionality constants
$\Delta \equiv$ ratio of the density difference between water and oil to the density of water
$g \equiv$ acceleration of gravity [cm/s^2]
$A \equiv$ volume of oil per unit length normal to the direction of spread (initial thickness x initial length) [mL]
$V \equiv$ volume of oil [mL]
$\nu \equiv$ kinematic viscosity of water [cm^2/s]
$\rho \equiv$ density of water [g/cm^3]
$\sigma \equiv$ spreading coefficient, or net surface tension [g/cm s^2]
$= \sigma_{w/a} - \sigma_{w/o} - \sigma_{o/a}$

The reader is cautioned that neither of the above two algorithms incorporate the effects of wind, waves and oceanic turbulent eddies on oil slicks. These factors will break a slick up into many small patches, or slicklets, surrounded by clean water, and greatly increase the overall size of a slick and reduce the average final thickness.

Equilibrium Oil Thickness on Ice after Kawamura *et al*. (1986)

$$h_f = 0.04 V^{0.15} \mu^{0.24}$$

Where: $h_f \equiv$ final slick thickness [cm]
$V \equiv$ volume of oil [mL]
$\mu \equiv$ dynamic viscosity of oil [g/cm s]

Oil Spreading on Ice after McMinn (1971)

	One-dimensional		Axi-symmetric	
Gravity-Inertia	$l = k(gA)^{1/3} t^{2/3}$	**(12)**	$r = k(gV)^{1/4} t^{1/2}$	**(13)**
Gravity-Viscous	$l = k\left(\frac{\rho_o g A^3}{\mu}\right)^{1/5} t^{1/5}$	**(14)**	$r = k\left(\frac{\rho_o g V^3}{\pi^3 \mu}\right)^{1/8} t^{1/8}$	**(15)**

Where: $l \equiv$ the length of a 1-dimensional slick [cm]
$r \equiv$ the radius of a 2-dimensional slick [cm]
$k \equiv$ proportionality constants ≈ 1.0 for 1-D gravity viscous

$g \equiv$ acceleration of gravity [cm/s^2]
$A \equiv$ volume of oil per unit length normal to the direction of spread (initial thickness x initial length) [mL]
$V \equiv$ volume of oil [mL]
$\mu \equiv$ dynamic viscosity of oil [g/cm s]
$\rho_o \equiv$ density of oil [g/cm^3]
$\sigma_i \equiv$ spreading coefficient, or net surface tension of oil on ice [g/cm s^2]
$= \sigma (1-\cos \theta)$, where θ is the contact angle between ice and oil, assumed to be between 25° and 45° and σ is assumed to be 30 g/cms^2 after McMinn (1971)

Oil Spread in Snow after SL Ross and DF Dickins (1987)

$$r = \left(\frac{2K\rho_o g V}{\pi E^2 \mu} \right)^{1/4} t^{1/4}$$

Where: $K \equiv$ specific permeability of snow [cm^2]
$= 7.7 \times 10^{-2} d_o^2 e^{(-7.8\rho_s/\rho_i)}$
$d_o \equiv$ mean snow grain size [cm]
$E \equiv$ porosity (void fraction) of snow
$= (1-\rho_s/\rho_i)$
$\rho_s \equiv$ snow density [g/cm^3]
$\rho_i \equiv$ ice density [g/cm^3]

Stripping Velocity for Small Oil Forms under Ice adapted from Cox and Schultz (1980)

$$U_{th} = C_i \left(\frac{305.79}{88.68 - \mu_o} \right)$$

Where: $U_{th} \equiv$ threshold ("stripping") velocity (cm/s)

$\mu_o \equiv$ oil viscosity in Poise
$C_i \equiv$ under-ice roughness factor
= 1 for smooth, freshwater ice
= 2 for saline ice
= 3 for undulations under freshwater ice
= 4 for undulations under saline ice
= 6 for any refrozen rubble ice

Evaporation on Ice, Under Snow and Among Drift Ice after Stiver and Mackay (1983)

$$F_v = \ln\left[1 + \frac{BT_G}{T} \theta \exp\left(A - \frac{BT_0}{T} \right) \right] \frac{T}{BT_G}$$

Where: F_v ≡ volume fraction of the oil evaporated
T_0, T_G ≡ the intercept and slope of the modified ASTM distillation [°K]
T ≡ environmental ambient temperature [°K]
B, A ≡ dimensionless, oil-specific constants equal to the least-squares slope and intercept of a plot of the natural logarithm of the Henry's Law constant (H = Pv/RT, which is numerically equal to the slope of the tangent to the curve of a plot of F_v vs. □ at the given point) vs. T_b/T
T_b ≡ boiling point of weathered crude oil at atmospheric pressure [°K]
P ≡ vapor pressure of the weathered crude oil [Pa]
v ≡ liquid's molar volume [m^3/mol]
R ≡ gas constant 8.314 [Pa m^3/mol °K]
□ ≡ dimensionless evaporative exposure
= $kAt/V_0 = kt/x$
k ≡ mass transfer coefficient [m/s]
A ≡ area of slick [m^2]
t ≡ elapsed time since oil release [s]
V_0 ≡ initial volume of oil released [m^3]
x ≡ slick thickness [m]

And, for the mass transfer coefficient used to calculate □:

$$\frac{1}{k_T} = \frac{1}{k_a} + \frac{K_{oa}}{k_o} + \frac{x}{D_s}$$

Where: k_T ≡ overall mass transfer coefficient [m/s]
k_a ≡ air side mass transfer coefficient [m/s]
k_o ≡ liquid phase mass transfer coefficient [m/s]
K_{oa} ≡ air-oil partition coefficient
k_o/K_{oa} = 0.001 m/s
D_s ≡ diffusivity of oil vapor in snow [m^2/s]
= 2 x 10^{-5} m^2/s
x ≡ thickness of snow [m]

Emulsification in Drift Ice

At present there are no satisfactory algorithms to predict emulsification of oil slicks at sea. There are two basic reasons for this:

1. There is still a lack of understanding of the basic mechanisms by which emulsification occurs; and,
2. There is a basic lack of understanding how to measure and quantify the energy levels in various test tanks and the sea.

Until these issues are resolved, it is not fruitful to try to develop algorithms to predict emulsification rates at sea. The state of the art today is to conduct small-scale bench or tank tests

with quantitatively evaporated oil samples at representative environmental temperatures to predict when oil will be come susceptible to forming stable emulsions. In open water conditions it is generally agreed that, once oil weathers to this state, emulsification will proceed to completion relatively rapidly, in a few hours. The results of the experiments reported here do not contradict this approach. There may be an effect of ice concentration on emulsification rate, but until the rate of emulsion formation in open water is understood and modelled, it is not possible to model the effects of drift ice on the processes.

The experimental data showed that very little emulsification occurred over 96 hours in the low wave experiments in the SL Ross tank. Even the oils that would be expected to be prone to emulsify (particularly the doped Hydrocal, Endicott and ANS) did not. In the higher wave level in the SL Ross tank the Endicott crude did form lower water content "entrained" water emulsions as did the one experiment with ANS that did not disperse completely. The doped Hydrocal also picked up more water than in the lower wave tests. The Northstar crude did pick up water, but the emulsions were unstable. Comparison of the water droplet size distributions shows that, as expected, the mean droplet size in the higher wave energy conditions was generally much smaller than the mean size in the lower waves. Perhaps the most surprising result was that, despite having nearly 10% asphaltenes, the Kuparuk crude did not form stable emulsions. There does not appear to be any correlation between ice concentration and emulsification in these data.

Very little emulsification occurred with the oils in the low waves at Ohmsett. The droplet size distributions indicate that the emulsions contained relatively small water droplets. At the higher wave energy level all the oils formed high (80%) water content emulsions. Only two did not form stable emulsions (Northstar and Kuparuk in 50% ice – although the duplicate experiment with Kuparuk in 50% ice did form a stable emulsion). The water droplet size distributions in the samples from these tests had consistently small mean droplet sizes. In the higher wave experiments at Ohmsett, it appears that there could be a trend in increasing emulsification rate with increasing ice concentration, although after 96 hours all the experiments had resulted in high water contents in the 80% range. The formation of stable emulsions by the Kuparuk and Northstar crudes was not expected, based on the characterization test results and the other tank test results. One likely explanation for the anomalous results is that the Ohmsett tests took place outdoors, in sunlight. Solar radiation has been shown to be a strong contributing factor to water-in-oil emulsion stability, through the formation of photolysed surfactant compounds in the parent oil. The combination of increased mixing energy and the production of photolysed surfactants in the oil could have resulted in the stable emulsions being formed.

Brine Channel Migration

It was not possible to develop algorithms for the rate of appearance of oil on the surface of melting ice in spring; however, the following key conclusions were formed from analyzing results from the migration study:

1. Oil viscosity/pour point/density play a major role in controlling the rate of migration in a given ice salinity.
2. Brackish ice provides fewer pathways for migration and slows down the surfacing rate with an effect equivalent to introducing sediment into the tanks.

3. It is not clear if the main effect observed in the sediment experiments is directly related to the presence of particle inclusions at the grain boundaries or the substantial cap of frazil ice in the upper layers of the sheet, providing no aligned brine channels for direct oil migration.
4. Regardless of oil type, water salinity or the presence of sediments, the difference in timing when most of the oil was exposed (80% or better) amounted to less than ten days. From an oil spill response point of view timing differences in migration rates due to these variables would likely be much more significant in the case of spills under much thicker ice in a true Arctic climate.

REFERENCES

Bech, C. and P. Sveum, 1991. Spreading of Oil in Snow. In Proceedings of the Fourteenth AMOP Technical Seminar. Environment Canada, Ottawa. Pp 57-71.

Berger, D. and D. Mackay, 1994. The Evaporation opf Viscous or Waxy Oils – When is a Liquid Phase Resistance Significant? In Proceedings of the Seventeenth AMOP Technical Seminar. Environment Canada, Ottawa. Pp 77-92.

Berridge, S., M. Thew and A. Loriston-Clarke, 1968. The Formation and Stability of Emulsions of Water in Crude Petroleum and Sililar Stocks. Journal of the Institute of Petroleum. Vol. 54, pp 333-357.

Bobra, M., 1990. A Study of the formation of water-in-oil emulsions. Proceedings of the Thirteenth Arctic and Marine Oilspill Program Technical Seminar. Environment Canada, Ottawa, Ontario. pp. 87-117.

Bobra, M. 1991. Water-in-oil Emulsification: A Physicochemical Study. Proceedings of the 1991 International Oil Spill Conference. American Petroleum Institute, Washington, D.C. pp. 483-488.

Bobra, A.M., and M.F. Fingas, 1986. The Behavior and Fate of Arctic Oil Spills. Water Science Technology, Vol. 18 No. 2, pp 13-23.

Bocard, C. and C. Gatellier, 1981. Breaking of Fresh and Weathered Emulsions by Chemicals. In Proceedings of the 1981 Oil Spill Conference. API, Washington. pp 601-607.

Brandvik, P.J., and P.S. Daling. 1990. W/O Emulsion Formation and W/O Emulsion Stability Testing – An Extended Study with Eight Oil Types. IKU SINTEF DIWO Report No. 10. Trondheim.

Cammaert, A., 1980. Oil and Gas Under Laboratory IceLaboratory Study. Beaufort Environmental Impact Statement RWC17. Environment Canada, Ottawa.

Chen, E., B. Keevil and R. Ramsier, 1976. Behaviour of Crude Oil Under Fresh Water Ice. Journal of Canadian Petroleum Technology. Vol. 15, pp 79-83.

Chen, E.C., J.C.K. Overall and C.R. Phillips. 1974. Spreading of crude oil on an ice surface. Can. J. Chem. Eng. February 1974.

Cox, J.C. and L.A. Schultz, 1980.The Transport and Behaviour of Oil Spilled Under Ice. Proceedings of the Third Arctic Marine Oilspill Program Technical Seminar, Environment Canada, Ottawa, pp 45-61.

Cox, J.C. and L.A. Schultz, 1981.The Containment of Oil Spilled Under Rough Ice. Proceedings of the 1981 International Oil Spill Conference. API. Washington. Pp 45-61.

Cox, C., Schultz, L.A., Johnson, R.P. and R.A. Shelsby. 1980b. Transport of and Behavior of Oil Spilled in and Under Sea Ice. Report prepared by ARCTEC for NOAA/OCSEAP, Research Unit 568, Final Report, 170 p.

Deslaurier, P.C., S. Martin, B. Morson and B. Baxter. 1977. The physical and chemical behavior of the Bouchard No. 65 oil spill in the ice covered waters of Buzzards Bay. NOAA OCSEAP Report. Boulder.

Dickins. D.F., Brandvik, P.J., Bradford, J., Faksness, L-G., Liberty, L. and R. Daniloff. May 2008. Svalbard 2006 Experimental Oil Spill Under Ice: Remote Sensing, Oil Weathering Under Arctic Conditions and Assessment of Oil Removal by In-situ Burning. Paper accepted for presentation at the 2008 International Oil Spill Conference, Savannah, Georgia.

Dickins, D., Liberty L., Hirst W., Bradford J., Jones V., Zabilansky L., G. Gibson G., and J. Lane. 2005. New and Innovative Equipment and Technologies for the Remote Sensing and Surveillance of Oil in and Under Ice. Proceedings 28 th Arctic and Marine Oilspill Program Technical Seminar, Calgary, June 2005. (MMS Contract 1435-01-04-36285)

Dickins, D.F. and I.A. Buist, 1981. Dome Petroleum's Study of Oil and Gas Under Sea Ice. Proceedings International Oil Spill Conference, American Petroleum Institute, Wash. D.C., pp 183-189 (see also full Report Published Under COOSRA).

D F Dickins Associates Ltd., and Fleet Technology Limited. Behavior of Spilled oil at Sea (BOSS): Oil-in-Ice Fate and Behavior; report submitted to Environment Canada, U. S. Minerals Management Service and American Petroleum Institute. 1992 (DRAFT)

Dome Petroleum Limited. 1981. Oil and gas under sea ice study. Report to the Canadian Offshore Oil Spill Research Association, Calgary.

Fay, J.A. 1969. The spread of oil slicks on a calm sea. Fluid Mechanics Laboratory, Department of Mechanical Engineering, Massachusetts Institute of Technology, Cambridge, Massachusetts.

Fay, J.A. and D.P. Hoult, 1971. Physical Processes in the Spread of Oil on a Water Surface. MIT - NTIS report #AD726281.

Fazal, R. and J. Milgram, 1979. The Effects of Surface Phenomena on the Spreading of Oil on Water. MIT Report MITSG-79-31. Cambridge, MA.

Fingas, M., 1994. The Evaporation of Oil Spills. In Proceedings of the Eighteenth AMOP Technical Seminar. Environment Canada, Ottawa. Pp 43-60.

Fingas, M., B. Fieldhouse and J. Mullin. 1998. Studies of Water-in-Oil Emulsions: Stability and Oil Properties. Proceedings of the 21st Arctic and Marine Oilspill Technical Seminar. Environment Canada, Ottawa. pp 1-26.

Frankenstein, G. and Garner, R. 1967. Equations for Determining the Brine Volume of Sea Ice from -0.5°C to -22.9°C. Journal of Glaciology 6(48), 943-944.

Glaeser, J.L. and G.P. Vance. 1971. A study of the behavior of oil spills in the Arctic. U.S.C.G. Report CG-D-53-74. Washington.

Hirvi, J-P, J. Koponen and H. Vespa, 1993. A Case Study of the M/T Antonio Gramsci Oil Accident in Ice Infested Waters: Comparison Between the Observations and Results for a Coupled 3D Hydrodynamic Oil Spill Model. In Combating Marine Oil Spills in Ice and Cold Conditions. National Board of Waters and the Environment. Helsinki. pp 163-173.

Hollebone, B., M. Fingas, D. Pearlmann and J. Mullin, 2000. The Fate and Behaviour of Oil in Freezing Environments. Environment Canada Report. Ottawa.

Hokstad, J. and P. Daling. 1993. Methodology for Testing Water-in-Oil Emulsions and Demulsifiers. Description of Laboratory Procedures. In Formation and Breaking of Water-in-Oil Emulsions: Workshop Proceedings Marine Spill Response Corporation, Washington DC, MSRC Technical Report Series 93-108, pp 239-254

Johnston, M.J. October 2007. Description of Ice Grown in Indoor and Outdoor Tanks, Winter 2007. Report prepared for this study under subcontract by the Canadian Hydraulics Centre, National Research Council Canada, Ottawa.

Kawamura, P., D. Mackay and M. Goral. 1986. Spreading of chemicals on ice and snow. Report to Environment Canada, EETD, Ottawa.

Kisil, C.A. 1981. A Study of Oil and Gas in Fresh and Salt Water-Ice Systems. University of Toronto, MSc. Thesis.

Kovacs, A. 1996. Bulk Salinity Versus Floe Ice Thickness. CRREL Report 96-7, Hanover, NH.

Kovacs, A., R.M. Morey, D.F. Cundy, and G. Decoff, 1981. Pooling of Oil Under Sea Ice. Proceedings, POAC 81: Sixth International Conference on Port and Ocean Engineering under Arctic Conditions, Quebec, pp 912-922.

Mackay, D., 1987. Formation and Stability of Water-in-Oil Emulsions. Environment Canada Report EE-93. Ottawa.

Mackay, D., M.E. Charles and C.R. Phillips. 1975. The physical aspects of crude oil spills on northern terrain (final report). Department of Indian and Northern Affairs. Report ALUR 1974-75. Ottawa.

Mackay, D. and W. Zagorski. 1982. Studies of water-in-oil emulsions. Environment Canada Report EE-34, Ottawa.

Malcolm, J. and A. Cammaert, 1981. Movement of Oil and Gas Spills Under Sea Ice. In Proceedings of the Sixth International Conference on Port and Ocean Engineering Under Arctic Conditions, pp 923-936.

Martin, S. 1979. Field Study Of Brine Drainage And **Oil** Entrainment In First-Year Sea Ice. Journal Of Glaciology, Vol 22, No.88, 1979, Pp.473-501.

McMinn, T.J. 1972. Crude Oil Behaviour on Arctic Winter Ice. U.S. Coast Guard, NTIS-AD-754261.

Moir, J. and Y. Lau, 1975. Some Observations of Oil Slick Containment by Simulated Ridge Keels, Environment Canada, Burlington.

Nelson, W.G., and A.A. Allen. 1981. Oil Migration and Modification Processes in Solid Sea Ice. Proceedings 1981 Oil Spill Conference, API.

NORCOR Engineering and Research Ltd. 1975. The Interaction of Crude Oil with Arctic Sea Ice. Beaufort Sea Project Technical Report No. 27, Canada Department of the Environment, Victoria, British Columbia.

Osterkamp, T.E, and J.P. Gosink. 1984. Observations and Analysis of Sediment-Laden Sea Ice. Pp. 73-93 in The Alaskan Beaufort Sea: Ecosystems and Environments, Ed. by Barnes, P.W., Schell, D.M., and E. Reimnitz, Academic Press, London.

Payne, J.R. and C.R. Phillips. 1985. Petroleum spills in the marine environment - the chemistry and formation of water-in-oil emulsions and tar balls. Lewis Publishers Inc. Chelsea, Michigan.

Payne, J., J.R. Clayton, Jr., G.D. McNabb, B.E. Kirstein, C.L. Clary, R.T. Redding, J.S. Evans, E. Reimnitz, and E.W. Kempema. 1989. Oil-ice-sediment interactions during freezeup and breakup. Pp. 1-382 in Outer Continental Shelf Environmental Assessment Program, Final Reports of Principal Investigators. NOAA/OCSEAP Vol. 64, Washington, DC.

Payne, J.R., G. McNabb, L. Hachmeister, B. Kirsten, J. Clayton, C. Phillips, R. Redding, C. Clary, G. Smith and G. Farmer, 1987. Development of a Predictive Model for the Weathering of Oil in the Presence of Sea Ice. Pp. 147-461 in Outer Continental Shelf Environmental Assessment Program, Final Reports of Principal Investigators. Vol 59, NOAA/OCSEAP, Washington, DC.

Purves, F. 1978. The Interaction Of Crude Oil And Natural Gas With Laboratory Grown Saline Ice. Prepared by ARCTEC Canada for Environment Canada, EPS-4-EC-78-9, Ottawa, Ontario.

Puskas, J. and E. McBean, 1986. The Transport of Crude Oil Under Saline Ice. In Proceedings of the Fourth International Conference on Cold Region Engineering. ASCE. NY, NY, pp 670-684

Puskas, J., E. McBean and N. Kouwen, 1987. Behaviour and Transport of Oil Under Smooth Ice. Canadian Journal of Civil Engineering. Vol 14, pp 510-518.

Rosenegger, L.W. The Movement of Oil Under Sea Ice, 1975. Prepared by Imperial Oil Limited for the Beaufort Sea Project, Department of the Environment Canada, Victoria, Beaufort Sea Technical Report No. 28.

Sanderson, T.J. 1988. *Ice Mechanics: Risks to Offshore Structures*. Graham and Totman, London.

Scott, B.F. and R.M. Chatterjee. 1973. Behaviour of oil under Canadian climate conditions. Part 1 - Oil on Water Under Ice-Forming Conditions. Scientific Series No. 50, Environment Canada, Ottawa.

Singsaas, I., P.J. Brandvik, P.S. Daling, M. Reed and A. Lewis. 1994. Fate and behaviour of oils spilled in the presence of ice - a comparison of the results from recent laboratory, meso-scale flume and field tests. Proceedings of the Seventeenth Arctic and Marine Oil Spill Program (AMOP) Technical Seminar. Environment Canada, Ottawa.

S.L. Ross Environmental Research Limited, 2003. Laboratory Analysis of the Spill-Related Properties of Chayvo Crude Oil on Cold Water and Broken Ice. Report to ExxonMobil Upstream Research, Houston.

S.L. Ross Environmental Research Limited and DF Dickins Associates Ltd., 1987.Field Research Spills to Investigate the Physical and Chemical Fate of Oil in Pack Ice. Environmental Studies Revolving Funds, Report No. 062, Ottawa.

S.L. Ross Environmental Research Limited and D.F. Dickins Associates Ltd. 1988. Modelling of oil spills in snow. Report to Environment Canada, EETD. Ottawa.

S.L. Ross Environmental Research Limited and D. Mackay Environmental Research Limited. 1988. Laboratory studies of the behaviour and fate of waxy crude oil spills. Environmental Studies Research Funds, Report 084. Ottawa.

S.L. Ross Environmental Research Limited and Energetex Engineering, 1986. In-situ burning of uncontained oil slicks. Environmental Emergencies Technology Division, Environmental Protection Service, Environment Canada, EE-60.

Stiver, W. and D. Mackay. 1983. Evaporation rate of spills of hydrocarbons and petroleum mixtures. Environmental Protection Service, Environment Canada, Report EE-8. Ottawa.

Tebeau, P.A., T.M. Meehan and J.C. Myers. 1982. A laboratory experiment on oil weathering under Arctic conditions. U.S. Coast Guard Report CG-D-34-82. Washington.

Tebeau, P.A., T.M. Meehan and S.A. Saspoff. 1984. A laboratory study of oil spreading under Arctic conditions. United States Coast Guard R&D Centre. Groton, CT.

Tekmarine, Inc., Polar Alpine, Inc. and OCTL, 1985. 1984 Beaufort Sea Multiyear Ice Floe Trackingh Study. AOGA Project 280, Sierra Madre, CA.

Timco, G. and M. Davies, 1995. Laboratory Tests of Oil Fate in Cold Water, Ice and Waves. National Research Council of Canara Report HYD-TR-002. Ottawa.

Tsang, G. and E. Chen, 1978. Laboratory Study of Diversion of Oil Spilled Under Ice Cover. Environment Canada. Burlington.

Uzuner, M., F. Weiskopf, J. Cox and L. Scultz, 1979. Transport of Oil Under Smooth Ice. USEPA Report EPA-600/3-79-041. Washington.

Vefsnmo, S. and B.O. Johannessen, 1994. Experimental Oil Spill in the Barents Sea - Drift and Spread of Oil in Broken Ice. Proceedings 17th Arctic and Marine Oil Spill Program Technical Seminar, Vancouver.

Walker, M., M. McDonaugh, D. Albone, S. Grigson, A. Wilkinson and G. Baron, 1993. Comparison of observed and predicted changes to oil after spills. Proceedings of the 1993 Oil Spill Conference, American Petroleum Institute, Washington, D.C. pp 389-393.

Wang, Z. and M. Fingas. Study of the Effects of Weathering on the Chemical Composition of a Light Crude Oil. In Proceedings of the Seventeenth AMOP Technical Seminar, Environment Canada, Ottawa. Pp 133-172.

Wilson, D. and D. Mackay, 1987. The Behaviour of Oil in Freezing Situations. Environment Canada Report EE-92. Ottawa.

Wotherspoon, P.D. and J.J. Swiss. 1985. Oil-in-ice computer simulation model. Proceedings of the 8th Annual Arctic Marine Oilspill Program Technical Seminar. Edmonton.

Zubov, N.N. 1945. Arctic Ice. Izdatel'stvo Glavsermorputi, Moscow. English translation by US Navy Oceanographic Office/American Meteorological Society.

APPENDICIES

Please see enclosed CD for information for Appendix A through H.

Appendix A – Crude Oil Physical Property Data
Appendix B – Crude Oil Chemical Property Data
Appendix C – Oil Spreading on Cold Water Data
Appendix D – Oil Spreading on Ice and Snow Data
Appendix E – Oil Under Ice Stripping Velocity Data
Appendix F – Oil Evaporation Data
Appendix G – Oil Emulsification in Pack Ice Data
Appendix H – Brine Channel Migration Data